Liège Université
Faculty of Applied Sciences
Department of Electrical Engineering and Computer Science

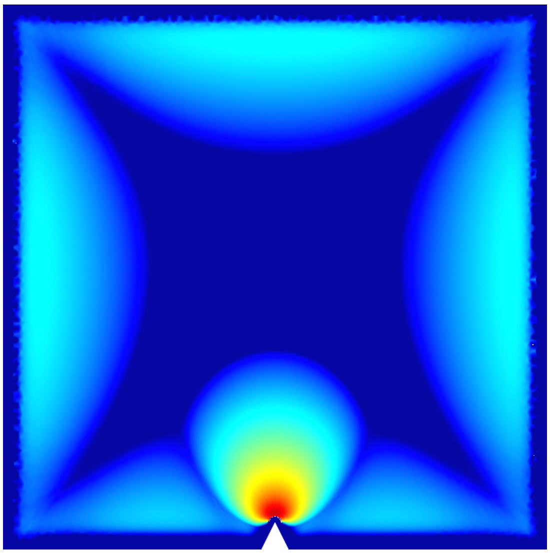

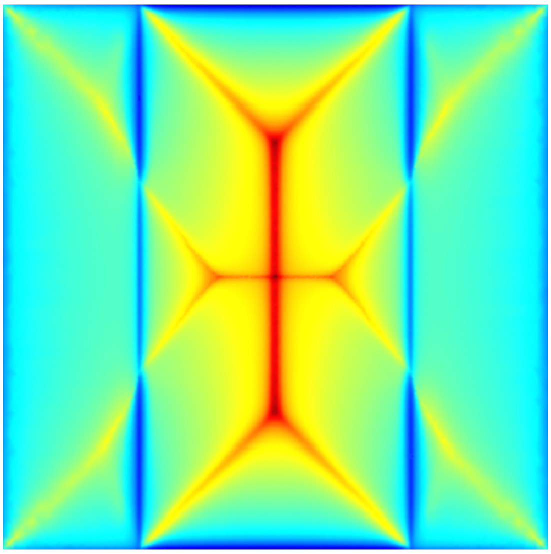

Numerical investigation of the magnetic field distributions in structured superconducting film systems

Loïc Burger
Supervisor: Benoît Vanderheyden

Thesis submitted in partial fulfilment of
the requirements for the degree of
Doctor of Philosophy (PhD) in Engineering Science

November 2021

Liège Université
Faculty of Applied Sciences
Department of Electrical Engineering and Computer Science

Numerical investigation of the magnetic field distributions in structured superconducting film systems

Jury:
Prof. Dr. Ir. C. Geuzaine (Chairman, ULiège, Belgium)
Prof. Dr. Ir. P. Vanderbemden (ULiège, Belgium)
Prof. Dr. A. V. Silhanek (ULiège, Belgium)
Prof. Dr. A. Badía Majós (University of Zaragoza, Spain)
Prof. Dr. M. V. Milošević (University of Antwerp, Belgium)
Prof. Dr. Ir. B. Vanderheyden (Supervisor, ULiège, Belgium)

Thesis submitted in partial fulfilment of
the requirements for the degree of
Doctor of Philosophy (PhD) in Engineering Science by

Loïc Burger

November 2021

Résumé

Les films supraconducteurs et les empilements de rubans supraconducteurs font partie intégrante de nombreuses applications, parmi lesquelles on retrouve des magnétomètres de haute sensibilité, des détecteurs de photons uniques, les ordinateurs quantiques, les câbles de transmission à faibles pertes, les moteurs supraconducteurs, ou encore des systèmes de stockage d'énergie magnétique. Comprendre comment le champ magnétique et les courants induits qui en résultent sont distribués à l'intérieur des films supraconducteurs est essentiel au développement de telles applications. Pour ce faire, la recherche s'est récemment focalisée sur la visualisation en temps réel de la réponse magnétique des systèmes sur base de films supraconducteurs soumis à un champ externe transverse.

Cette thèse cherche à déterminer les raisons physiques à l'origine de distributions de champ magnétique inattendues au sein de systèmes supraconducteurs structurés soumis à un champ transverse. Par 'systèmes supraconducteurs structurés', on fait ici référence à des systèmes composés d'un ou plusieurs films supraconducteurs assemblés ou usinés de sorte à influencer la distribution du champ magnétique. A cette fin, l'emploi de méthodes numériques rend possible le test d'hypothèses physiques, la réalisation d'études paramétriques concernant les structures étudiées, ou l'évaluation de champs électromagnétiques dont la mesure est difficile, voire impossible, expérimentalement. En particulier, la méthode par éléments finis est une technique numérique polyvalente et adaptée à la modélisation des systèmes physiques non-linéaires dont la géométrie tridimensionnelle peut devenir complexe.

Avant toute chose, une formulation **H**-ϕ sur base des éléments finis est développée pour modéliser les différents contextes expérimentaux rencontrés. Afin de réduire le nombre de degrés de liberté nécessaires, on considère des transformations de domaine, qui consistent en des bijections faisant correspondre tout point d'un domaine d'extension infinie à un point d'un domaine de dimension finie au travers d'un changement de coordonnées. Les performances d'une telle approche sont testées pour des transformation sphériques, trapézoïdales et unidirectionnelle. L'influence de la qualité du maillage et des paramètres géométriques de la transformation unidirectionnelle est étudiée avec pour but de choisir un ensemble de paramètres limitant le nombre de degrés de liberté tout en assurant une précision suffisante des résultats. D'une part, il apparaît que quelle que soit la forme du domaine transformé et de la section du film parmi celles considérées, la précision des méthodes de transformation de domaine est comparable à celle obtenue dans le cadre d'une méthode de troncature, plus répandue en pratique, qui consiste à placer la frontière du domaine de simulation à une distance élevée mais finie des domaines conducteurs. D'autre part, dans le cas des disques supraconducteurs minces, les transformations sphériques sont capables de réduire les temps de simulation de 35% par rapport aux durées de calcul requises par la méthode de troncature. Cependant, l'intérêt computationnel des transformations de domaine devient marginal lorsqu'on emploie une transformation unidirectionnelle ou dans le cas de films rectangulaires.

Par la suite, l'accent est mis sur la modélisation et l'interprétation de l'observation des distributions de champ magnétiques particulières. Dans un premier temps, la formulation $\mathbf{H}$-ϕ est utilisée afin de confirmer si des variations locales de la barrière de surface peuvent être responsables de l'ouverture des lignes de discontinuité autour d'indentations à la suite d'une élévation de température. Les barrières de surface sont modélisées au travers de régions périphériques où le pinning est renforcé. Il est démontré numériquement qu'un abaissement de la barrière de Bean-Livingston aux environs de la pointe d'une indentation entraîne (1) l'ouverture des lignes de discontinuité paraboliques qui se développent autour de l'indentation, et (2) un excès de pénétration de flux magnétique par rapport à la position du front de pénétration attendu dans un film sans indentation. Les concavités et les excès de pénétration obtenus numériquement sont respectivement inversement et directement proportionnels à l'amplitude de la réduction de la barrière de surface. Ces tendances restent valables que l'on soit dans une géométrie longitudinale ou dans une géométrie de film. Toutefois, pour relier sans ambigüité l'élévation de température à l'ouverture des lignes de discontinuité qui entourent les indentations dans des films de niobium, davantage d'études expérimentales sont nécessaires.

Dans un second temps, la méthode des éléments finis est utilisée pour motiver la tendance qu'ont les avalanches de flux magnétique à se déclencher préférentiellement le long des bords lisses plutôt qu'au niveau des indentations. Les simulations numériques montrent que les indentations provoquent une élévation simultanée des niveaux des champs magnétique et électrique par rapport à ceux atteints le long des bords du film. Cependant, contrairement à ce qui est usuellement admis, il apparaît que la présence d'indentation ne s'accompagne pas systématiquement d'une concentration des lignes de courant dans le voisinage direct des sommets de l'indentation. En effet, un tel phénomène ne survient que si la densité de courant critique est indépendante du champ magnétique. A l'inverse, si la densité de courant critique dépend du champ magnétique, les lignes de courant ont tendance à s'espacer davantage les unes des autres près de l'indentation qu'ailleurs dans le film. En outre, lorsqu'une dépendance de type $J_c(\mathbf{B})$ est prise en compte, il est suggéré que le renforcement du champ électrique au niveau de l'indentation se traduit par de légères variations du niveau seuil de champ magnétique théorique auquel la première avalanches de flux se déclenche. Dans certains cas, le champ seuil devient plus bas au niveau des bords lisses qu'au niveau de l'indentation, ce qui favorise la nucléation des avalanches le long de ces bords lisses.

Finalement, des simulations numériques sont réalisées afin de mettre en exergue le rôle primordial que joue la dépendance en champ magnétique de la densité de courant critique sur la structure des lignes de discontinuité observées dans deux configurations distinctes : (1) dans des films minces dont l'épaisseur est modulée par un réseau régulier de trous triangulaires de formes identiques, et (2) dans diverses superpositions de films minces de sections carrées et rectangulaires. Dans les deux cas, les résultats délivrés par imagerie magnéto-optique illustrent clairement une dépendance de la position des lignes de discontinuité en fonction du champ appliqué.

Dans le premier système, il est soutenu que la symétrie C_3 des trous triangulaires se traduit par une densité de courant critique asymétrique, ce qui est corroboré par les résultats de simulations exploitant les équations de Ginzburg-Landau dépendantes du temps, à l'échelle des trous de taille microscopique. Ces propriétés valables à l'échelle microscopique sont transposées à l'échelle macroscopique au travers d'une loi **E**-**J** anisotrope et dépendante de la valeur du champ magnétique qui est ensuite inclue dans la formulation **H**-ϕ. Compte tenu de cette modélisation, les simulations éléments finis permettent alors de reproduire qualitativement les distributions de champ magnétique et les états critiques observés durant les expériences.

Dans le cas du second système, la modélisation numérique met en lumière un mécanisme physique qui permet de reproduire la dépendance en champ appliqué de la forme des états critiques dans des structures bi-couches formées d'un film carré et d'un film rectangulaire. Sur base des résultats numériques, on montre que la différence de sections définit une région centrale où le champ de réaction du film rectangulaire affecte le film carré, en conséquence de quoi se génère une distribution non-uniforme de la densité de courant critique dans les films, pour peu que l'on prenne en compte la dépendance de la densité de courant critique par rapport au champ magnétique. De là, tenant compte des prédictions d'un modèle d'état critique réduisant la géométrie tridimensionnelle de la structure en une géométrie bidimensionnelle, il est montré comment cette non-uniformité mène à des états critiques dont l'allure est proche de ceux observés expérimentalement. Finalement, une étude paramétrique faisant varier (1) les paramètres de la loi de Kim, et (2) les paramètres géométriques de la structure est réalisée, illustrant plus finement comment la dépendance en champ magnétique de la densité de courant critique, d'une part, et, le couplage magnétique entre les films, d'autre part, modulent la forme des lignes de discontinuité.

Abstract

Superconducting films and stacks of tapes are used in many applications, among which sensitive magnetometers, single-photon detectors, quantum computers, low-loss transmission cables, trapped-field magnets, superconducting single-photon detectors, superconducting motors, and superconducting magnetic energy storage systems. They also provide interesting perspectives for novel electronics, spintronics, or fluxonics devices. Understanding how magnetic flux and the associated induced current density are distributed in the superconducting films is essential to develop these applications. To this aim, an important research effort has been devoted to the in-situ visualization of the response of superconducting film systems subjected to a perpendicular applied field.

This thesis aims at explaining the origin of several unexpected magnetic flux distributions that have been recently observed in structured superconducting film systems subjected to an out-of-plane magnetic field. 'Structured superconducting film systems' here refer to single-film or multilayer superconducting systems that are patterned in such a way to influence the penetration of magnetic field. To this aim, numerical methods allow one to test hypotheses, run parametric investigations, or evaluate electromagnetic fields that cannot be accessed by experimental means. In particular, the finite-element method is a versatile numerical approach that is adapted to the efficient modelling of non-linear physics in complex three-dimensional geometries.

A finite-element $\mathbf{H}$-ϕ formulation is developed to tackle the modelling of the different experimental contexts. In an attempt to reduce the number of degrees of freedom of the simulations, the relevance of shell-transformation techniques, which consist in mapping the infinite space surrounding the superconducting domains onto a shell domain of finite extension, is investigated. Spherical, trapezoidal, and unidirectional shell transformations are considered. The influence of the mesh and geometrical parameters for the unidirectional shell transformation is discussed in order to select a set of parameters that limits the number of degrees of freedom, while achieving a satisfactory accuracy. On the one hand, for all shell geometries and for various film cross sections, it is shown that the accuracy of the shell-transformation techniques is comparable to that of the more common truncated-geometry approach, where the boundary of the simulated domain is placed at a large but finite distance from the conducting domain. On the other hand, for thin superconducting disks, it appears that spherical shell transformations can reduce the simulation times by 35% compared to those of the truncated-geometry approach. By contrast, the interest of using shell transformations becomes marginal with unidirectional shell transformations, or in the case of rectangular films.

Then, the focus is put on modelling and explaining the various peculiar magnetic flux distributions observed experimentally. First, the **H**-ϕ formulation is used to verify whether surface barriers can explain the opening of discontinuity lines around edge indentations upon a temperature increase. Surface barriers are modelled by means of an enhanced pinning region that lies in the periphery of the film. It is numerically shown that a depletion of the Bean-Livingston barrier in the vicinity of the indentation sharp tip indeed leads to (1) an opening of the parabolic discontinuity lines around the indentation, and (2) to an excess flux penetration with respect to the position of the flux front obtained in a non-indented film. The simulated concavities and excess penetration depths are found to be respectively inversely and directly proportional to the magnitude of the surface barrier depletion. These conclusions hold true in both the longitudinal and film geometries. However, without further experimental work, it remains difficult to correlate unambiguously the raising of the temperature to the opening of the discontinuity lines that surround edge indentations in niobium films.

Second, the finite-element method is used to explain why magnetic flux avalanches are sometimes triggered along smooth borders rather than at the edge indentations. Numerical simulations outline the simultaneous enhancement of the electric field and the magnetic field levels at the indentation, with respect to their levels along the smooth edges. However, contrary to what is usually assumed, it seems that the presence of an indentation is not systematically concomitant with current crowding in the direct surroundings of the indentation tip. In fact, current crowding arises when the critical current density does not depend on the local magnetic field intensity, while the current lines are otherwise less densely concentrated around the indentation in comparison to the rest of the film. Besides, it is argued that the enhancement of the electric field at the indentation when a $J_c(\mathbf{B})$ dependence is taken into account leads to small differences of the threshold magnetic field at which the first flux avalanche is triggered. In some instances, this threshold field may become lower along the smooth edges than at the indentation, which favours the nucleation of flux avalanches along the smooth borders of the film.

Finally, numerical simulations are performed to evidence the essential role played by the magnetic field dependence of the critical current density on the shape of the discontinuity-lines observed in two different structured systems: (1) in thin films where a regular array of micron-size triangular holes is etched, and (2) in three-dimensional assemblies of superimposed square and rectangular films. In both cases, magneto-optical imaging displays applied-field-dependent discontinuity-line patterns.

In the first system, it is argued that the C_3 symmetry of the equilateral triangles leads to an asymmetry of the critical current density, as evidenced by time-dependent Ginzburg-Landau simulations at the scale of the holes of microscopic size. At the macroscopic scale, a magnetic-field-dependent anisotropic **E**-**J** model that encapsulates the main micro-scale properties of the system is developed and included in the **H**-ϕ formulation. The finite-element simulations then show similar magnetic field distributions and critical state patterns than those reported in the experiments, provided both the anisotropy of the critical current density and its magnetic field dependence are taken into account.

For the second system, numerical modelling reveals a mechanism that replicates the applied-field-dependent shapes of the critical states in two-layer assemblies made of a square film and a rectangular one. With the help of numerical simulations, it is demonstrated how the dissimilar cross sections of the two films delimit a region where the reaction field of the rectangular film affects the square film, which in turn, accounting for the magnetic field dependence of the critical current density, results in a non-uniform distribution of the critical current density in the square film. Then, based on the results of a simplified critical state model, it is shown how such non-uniform critical current density distributions can lead to the formation of the observed discontinuity-line patterns. A systematic investigation of (1) Kim's law parameters, and (2) the variations of the geometrical characteristics of the assembly, is carried out, and illustrates how both the magnetic field dependence of the critical current density and the magnetic coupling between the films shape the architecture of the discontinuity lines.

Acknowledgements

The past six years have been quite the journey, enriching from a scientific but also personal viewpoint. This journey ends with the redaction of the present thesis. Although it is only a modest contribution to the field of superconductivity, I sincerely hope that this work will inspire many others to pursue the exploration and the elucidation of the secrets of superconductors. Before digging into the scientific content of the manuscript, I would like to take the time to give a proper shout-out to the people that supported me all this time and to those who directly contributed to this work.

I would first express my gratitude to the jury for taking the time to read throughout the manuscript, and for attending to my defence.

The numerical models that were elaborated required to be confronted to experimental evidence to be validated. For this reason, I would like to acknowledge the contribution to this work of the people who designed and fabricated the samples, but also the experimentalists that carried out the experiments and collected the experimental data. In particular, I would like to thank Ivan Veshchunov and Tsuyoshi Tamegai (University of Tokyo, Japan) for having carried out the magneto-optical measurements on the two- and three-layer assemblies of superimposed niobium films, and for the fruitful discussions that followed. Similarly, I wish to express my gratitude to Jeremy Brisbois, Sylvain Blanco-Alvarez and Alejandro Silhanek (ULiège, Belgium), for their measurements of the discontinuity lines in indented thin niobium and YBCO films. Finally, I wish to share my sincere appreciation to Alejandro Silhanek (ULiège, Belgium) and Maycon Motta (Universidade Federal de São Carlos, Brazil) for sharing the magneto-optical images of the superconducting samples with arrays of antidots.

Similarly, I wish to present my deepest thanks to Jesús González Acosta, Željko Jelić, and Milorad Milošević (University of Antwerp, Belgium) who carried out time-dependent Ginzburg-Landau simulations and let me use their data to collect precious information for my own finite-element model. My gratitude also goes to François Henrotte, Julien Dular and Christophe Geuzaine for their valuable insight about the finite-element method and numerical techniques in general, especially about shell transformations. Most crucially, I could also rely on their expertise and vast knowledge about GetDP and Gmsh.

More particularly, I would like to thank Alejandro Silhanek, for the depth of his knowledge about the subtleties of superconductivity and the limitations and possibilities offered by experimental techniques. His inventive mind allowed for rich scientific exchanges, and he always came up with refreshing scientific ideas and intriguing results to discuss, some of them being presented in this work.

A particular thought as well to Philippe Vanderbemden, who gave me invaluable advice and authentic inspiration when it comes to teaching. He was also the first person to introduce me to superconductivity, and also the one who got me hooked in this complex but wonderful field. I cannot stress out enough how essential people like him are for cultivating vocations among the future generations, and I am glad to have crossed paths with him.

I am also indebted to my supervisor Benoît Vanderheyden, with who I had the privilege to work for all these years. He is a humble, demanding and careful supervisor, who always took the time to investigate each scientific hint every nook and cranny. He encouraged me to permanently strive for excellence and honesty, which are paramount to research. My understanding of superconductivity has drastically improved by being around him, and this thesis is also the illustration of all the time and faith he put in me. I cannot remember a single time when he left his door closed when I needed advice or to discuss about science (or anything else, actually). Truly, I am very privileged to have met such an admirable scientist, supervisor, and person.

I would also like to acknowledge my fellow teaching assistants, with who I shared a lot of good memories during all these hours of teaching. So, to Michel, Sébastien, Laurent, Clara, Anaïs, Delphine, Anthony and Nicolas, I wish you all the best for the future. I would also like to thank Julien Dular, Alejandro Silhanek, and of course Benoît Vanderheyden, for reading my manuscript and commenting it.

I cannot forget my parents and my sister for their unconditional support throughout the past 10 years, and for teaching me to be hard-working and persevering, among other things. Evolving in a caring, non-judgemental, supportive environment was a true chance. In their own personal way, both of them contributed to this thesis, and for this, I can barely show enough gratitude. I am also extremely grateful to Isabelle, my mother-in-law, for having kindly offered me accommodation to work on my thesis during the pandemic. Her encouragements and her presence lifted my spirits more than once.

Finally, I could not finish these acknowledgements without mentioning Léopold who supported me for the complete duration of this demanding but enriching experience. He is the person who I could rely on when I felt discouraged, and who constantly pushed me to give my best. Together, we forged unforgettable memories, on many levels, and I cannot wait for those to come. On a personal note: I hope that you will take the time to read through my thesis, and finally be convinced that I have not been working on quantum mechanics for the past few years!

I dedicate this work to Léopold and my father.

Contents

List of Figures

List of Tables

Introduction

Context

In the last decades, type-II superconducting films and tapes have been used in many applications. Superconducting films are mainly used in Josephson junctions, which consist in three-layer assemblies made of two superconducting films separated by a metallic or insulating layer. When subjected to a DC voltage, they generate an AC current with a voltage-dependent frequency that can exceed 10 THz for some materials [1], hence their relevance for high-frequency applications. These heterostructures can then be arranged in rings to form superconducting quantum interference devices (SQUID), that are magnetometers able to reach a magnetic field resolution as low as ~ 4 fT/$\sqrt{\text{Hz}}$ at 77 K [2]. To this day, SQUID are the most sensitive magnetometers that have ever been devised. Josephson junctions have also been successfully used for designing qbits [3], and have recently allowed to reach quantum supremacy thanks to the 53-qubit Sycamore processor, by reducing the time needed to sample the output of a pseudo-random quantum circuit to 200 s, while it is estimated that it would otherwise have taken 10000 years with a classical supercomputer [4]. Thin films are also used to make superconducting radio frequency (SRF) cavities with a very high quality factor. Typically, the cavities are made of bulk niobium coated with thin magnesium diboride films to increase the penetration field and avoid the entrance of parasitic vortices [5]. These cavities are of particular interest for future accelerators.

Superconducting tapes are structured assemblies that include a thin high-temperature superconducting film, generally made of rare-earth barium copper oxide (REBCO), which is placed in between non-superconducting buffer and stabilizer layers. Owing to their ability to carry very large current densities with very limited dissipation [6], tapes are particularly adapted for current transport applications [7]. Several tapes can also be stacked on top of each other, forming superconducting assemblies that present many advantages over bulk samples: larger critical current densities, enhanced mechanical flexibility, improved homogeneity of the electrical properties, and better thermal properties, to enumerate a few [8, 9]. The high values of the critical current density and the advantageous mechanical properties of the stacks of tapes are paramount for the design of trapped-field magnets [10]. At the time of writing this thesis, a record 17.7 T has been trapped with stacks of REBCO tapes, without the need of any mechanical reinforcement around the tapes [10]. Similarly, the various advantages of tapes over bulks have opened the path for machining contactless bearings based on stacks of superconducting tapes that would prove useful for low-loss levitating high-speed trains [11, 12]. Finally, tapes can also be used in the form of coils, which widely contribute to the design of many existing or future electrotechnical applications such as superconducting motors [13, 14, 15, 16], transformers [17], superconducting magnetic energy storage (SMES) systems [18], or accelerator magnets [7, 19].

Another field of application of thin superconducting structures concern superconducting nanowires, which are used for superconducting single-photon detectors (SSPD). The principle of operation of the SSPD is based on the propagation of a hot spot that is generated by the absorption of a photon in a superconducting nanowire. The hot spot generates a local transition from the superconducting to the normal state, and progressively grows until it covers the whole width of the nanowire, which ultimately results in a measurable voltage across the device. SSPD require reliable photon absorption, reliable generation of an output voltage upon photon absorption, and fast recovering times from the normal to the superconducting states to reset the detector [20]. Lately, it has been experimentally demonstrated that NbN nanowires SSPD are capable of detecting incident photons with an efficiency over 90% [21], and a temporal resolution that goes below 3 ps [22].

In parallel with these well-established applications, a lot of research effort has been put in developing structures with new properties. Superconducting films can be coupled to films with different electromagnetic properties, aiming at controlling the motion of magnetic flux inside the superconductor. For example, the energy dissipation that results from the eddy currents generated by the motion of vortices in the vicinity of a metallic film induces a magnetic-braking mechanism that hampers their motion. This damping force depends on the magnetic flux velocity, and on the electromagnetic properties of the metallic and superconducting layers [23, 24]. Therefore, metallic layers and sheaths are often presented as practical means to deflect magnetic flux avalanches, effectively limiting their entry in the region capped with the metallic layer [24, 25]. They can also serve as a way to provide better thermal stability and prevent the superconductor from quenching [26].

Similarly, a lot of work has been recently dedicated to the investigation of the interactions between ferromagnetic structures and superconducting films. While magnetic flux is channelled into ferromagnetic materials, superconducting domains tend to expel it, owing to their diamagnetic behaviour. Studying the coupling between these two categories of materials turns out to be an ideal playground to discover rich and intriguing physics. Upon changing the orientation of the in-plane magnetization of the magnetic domains [27, 28], or by means of polarized structures placed in the vicinity of the superconducting films [29], it is possible to gain control over the entrance and the exit of magnetic flux in the heterostructures. Moreover, it has recently been shown that the ferromagnetic-superconducting interaction enables the manipulation of skyrmions in the ferromagnetic layer through the motion of vortices [30, 31]. The interactions at play in metallic-superconducting and magnetic-superconducting heterostructures pave the way for manufacturing controllable topological hybrid materials, while revealing the existence of new magnetic flux dynamics at the same time. It might also lead to progress concerning the development of new devices in spintronics (based on carriers of spin degrees of freedom, as opposed to charge carriers) and in fluxonics (based on carriers of magnetic flux), or else broaden the realm of possibilities for memory devices or in the field of information theory.

Finally, superconducting films are involved in the conceptualization of novel hybrid materials and metamaterials. For example, magnetic phases or nanorods can be included to generate spin textures that might be useful for future nano-scale spintronics devices [32]. Metamaterials are also considered for promising applications, such as magnetic cloaking [33, 34, 35], magnetic flux concentrators [36, 37, 38] and distance coupling [39]. Prototypes have already been realised at the macroscopic scale, but the possibility of reducing their size to the microscopic scale for novel, responsive, compact, and low-consumption devices remains a very interesting open question.

Objectives of the thesis

In regard with the design and the optimization of technological devices, understanding how magnetic flux diffuses within the superconducting films is crucial to improve or optimize the functionality of a given application. This thesis concerns the numerical investigation of the magnetic field distributions in structured superconducting film systems. The term 'structured superconducting film systems' here refers to multilayer assemblies that include some thin superconducting layers or single superconducting films that are patterned in such a way to influence the magnetic flux penetration in the investigated system. To this aim, an important endeavour has been devoted to the in-situ visualization of the response of structured superconducting film systems subjected to a perpendicular applied field [24, 27, 40, 41, 42, 43, 44, 45, 46, 47, 48, 49]. In particular, recent magneto-optical imaging (MOI) of three different structured superconducting film systems have evidenced peculiar distributions of magnetic field [41, 44, 48].

The first investigated system concerns a superconducting film with an edge indentation [41]. Two unexpected observations were reported. The first one concerns the shape of the discontinuity lines (d-lines) around edge indentations in niobium films. The d-lines mark the location where the current lines bend abruptly, as they bypass the indentation. As long as the magnetic flux penetration is smooth, experiments show that the parabolic d-lines forming around the indentation open up more than predicted by the theory, and with a temperature dependence that cannot be explained by the theory. The second observation concerns the location of the sudden magnetic flux avalanches that can occur in niobium films. According to a common view held in the literature, the onset of magnetic flux avalanches is facilitated at the indentation. However, in some instances, this fact is invalidated in niobium films, as flux avalanches were instead observed to be preferentially triggered along the smooth and non-indented borders.

In the second and third systems, the attention is switched towards the formation of unexpected and evolving networks of d-lines in (a) films with a regular array of triangular antidots [48], and (b) assemblies of several superposed films with different cross sections [44]. The asymmetric motion of vortices along the easy and hard axis of the array, and the non-symmetric arrangement of the films in the out-of-plane direction, imply that the two structured superconducting film systems present inherent geometrical characteristics that break the symmetry of these systems. In both cases, the d-lines do not remain static structures that are dictated by the geometry of the sample. Instead, the d-line networks change with respect to the strength of the applied field, and their shape is not the same upon increasing or decreasing the applied field, which, to the best of my knowledge, has not been previously observed.

Unfortunately, it is impossible to conclude about the physical origin of the magnetic field distributions reported in [41, 44, 48] from the sole inspection of the experimental data. By contrast, numerical modelling is a flexible and powerful tool when it comes to testing different model hypotheses. Numerical modelling is also very efficient if ones wishes to carry out a systematic investigation of the influence of diverse geometrical or physical parameters, or to assess some physical quantities that are difficult to evaluate experimentally. Due to demagnetization effects that result from the thin-film geometry and the superconducting nature of the film, the penetration of magnetic field in superconducting thin films is (1) highly non-local, since the magnetic field at a given position is determined by the distribution of the current density over the whole film, and (2) non-linear, as the electric field is a non-linear function of the current density. The finite-element (FE) method is one of the methods capable of handling such a non-linear and complex physics efficiently, while being adapted to a large number of complex geometries.

This thesis addresses, by means of finite-element simulations, the modelling of the peculiar magnetic flux distributions that were exposed above. Therefore, the aim is to propose models that are then evaluated numerically to help in elucidating the fundamental questions that were raised by the experimental data in [41, 44, 48]. In particular, we will investigate how the magnetic field dependence of the critical current density and the surface barriers can influence the distribution of the magnetic field and the shape of the resulting critical states. Indeed, while both aspects usually modify the field levels only, it will be shown here that they play a much more consequential role in some structured geometries. Although the results of this work directly concern much more fundamental questions than the development of matured applications, the relevance of these aspects is believed to be important in structures where a precise control of the penetration of the magnetic field is required, such as in metamaterials or heterostructures.

Outline

The manuscript is organized as follows. Chapter **1** provides an overview of the basic theoretical concepts about superconductivity that pave the way for the results presented in the rest of the manuscript. The basis of the macroscopic penetration of magnetic field inside type-II superconducting samples and the specificities of the thin-film geometry are reminded. Finally, since the main experimental results that have motivated the upcoming numerical simulations are based on MOI, a short overview of the technique is given.

Chapter **2** is devoted to the elaboration of the numerical method on which the simulations of the subsequent chapters rely. Bearing in mind the reduction of the number of degrees of freedom required to mesh the domain that surrounds the superconducting films, the relevance of a shell-transformation approach is investigated and compared to the usual domain truncation of the non-conducting regions.

Chapter **3** concerns the study of the influence of surface barriers on the opening of the parabolic d-lines that develop around a triangular indentation. A way of modelling surface barriers is proposed, while the dependency of the opening of the d-lines around triangular indentations on the temperature is discussed. The theme of this chapter is inspired from the experimental results of [41].

Chapter 4 focuses on the rearrangement of current lines around defects and indentations, and discusses the occurrence of the current-crowding effect that is normally expected to happen in the vicinity of an indentation. The effects of the magnetic field dependence of the critical current density on the distributions of the magnetic field, the current density, and the electric field, are discussed in the case of a square thin film with a triangular indentation cut along one of its edge. Finally, in an attempt to answer the questions raised in [41], the location of the nucleation of the first magnetic flux avalanche is discussed from a conceptual standpoint, based on the conclusions of the previously simulated results.

Chapter 5 concerns the distribution of the magnetic field in superconducting thin films containing a square array of identical triangular antidots, based on the configuration that is described in the experiments in [48]. It is explained how the magnetic-field-dependent anisotropy of the critical current density, which stems from the asymmetry of the antidots, is responsible for the apparition of a central d-line and for its reversal that follows the change of direction of the out-of-plane applied field.

Chapter 6 tackles the investigation of the penetration of magnetic field in superposed assemblies of superconducting films with unequal cross sections, as in [44]. The investigation first concerns the applied-field-dependent critical states in two-layer assemblies that consists in the superposition of a square and a rectangular films. Then, the analysis is extended to three-layer assemblies made of two rectangular and one square films. A systematic parametric investigation of the geometrical parameters of the assembly is carried out afterwards, with the aim of having a better grasp on the role of the three-dimensional coupling between the films and the magnetic-field-dependent critical current densities that characterize the films.

Finally, a conclusion chapter closes the manuscript by summarizing the main findings and discussing the perspectives of this work.

Chapter 1

Theoretical overview of the magnetic field penetration in thin superconducting films

This thesis aims at explaining several magnetic-field distributions in superconducting films that were measured by means of magneto-optical imaging. Before analysing the experimental results and proceeding with their numerical modelling, it is important to introduce the basic concepts of superconductivity and to understand how magnetic flux diffuses in superconducting films.

Section **1.1** introduces the main parameters that are commonly used to describe superconductivity. First, an overview of the T-H-J phase diagram highlights the main critical parameters that determine the limit between the superconducting and the normal states. The definition of the London penetration depth, λ, and the coherence length, ξ, are illustrated within the formalism of the London and the Ginzburg-Landau equations for simple study cases. This in turn leads to the distinction between the Meissner phase and the Shubnikov phase (mixed state). The temperature dependence and orders of magnitude for the superconductivity parameters at $T = 0$ K are also given.

Section **1.2** focuses on the vortex dynamics in the Shubnikov phase, starting from the interaction between two individual vortices and leading to their collective behaviour in the presence of randomly distributed pinning sites. In particular, the critical-state model is introduced in the context of the Bean and the Kim models as convenient, but simplified, tools to understand flux and current distributions in an infinitely long superconducting slab subjected to a transverse applied field. Explanations about the physical origins of the flux-flow and flux-creep regimes are provided. The influence of the current-density anisotropy and of the surface barriers on the entrance and the propagation of in-plane and out-of-plane vortices are also discussed.

Section **1.3** evidences the main differences that arise in the thin-film geometry in comparison with bulk samples, as far as the micro- and macro-scale magnetic-field penetration are concerned. The notion of discontinuity lines and their location in the framework of the critical-state model in several typical thin-film cases are also covered. An overview about

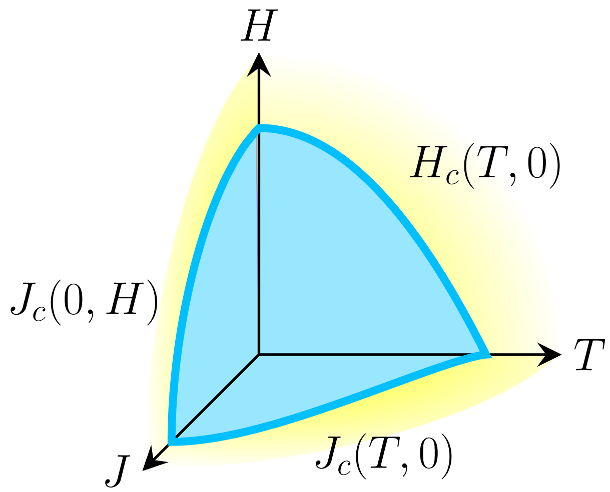

Figure 1.1: T-H-J surface that separates the superconducting phase, in light blue, from the normal conducting phase, in yellow. The bold light blue curves represent the critical parameters in each principal plane, $H_c(T,0)$, $J_c(0,H)$ and $J_c(T,0)$, which roughly outline the superconducting phase.

thermomagnetic avalanches, which occur much more frequently than in bulk samples, closes the section.

Finally, Section **1.4** is devoted to the magneto-optical imaging technique, on which relies the in-situ visualization of both the smooth penetration of magnetic flux and the dramatic thermomagnetic flux avalanches that are triggered in niobium thin films. The key physical principles on which the method is based are recalled, before the experimental set-up, the main challenges to which the experimentalists are confronted and the practical answers to these issues are briefly highlighted.

1.1 Electrodynamics of superconductors and fundamental parameters

1.1.1 The T-H-J phase diagram

Historically speaking, superconductivity has been experimentally evidenced by the observation of an abrupt drop of the resistivity of metallic compounds below a critical temperature, T_c. Superconductivity results from the creation of Cooper pairs, i.e. pairing of electrons that condense into a state of lower energy [50], this state being separated from a dissipative state by an energy gap, Δ_s. When the temperature, T, approaches T_c, the energy of thermal fluctuations, which is $k_B T$ with k_B being the Boltzmann constant, becomes comparable to Δ_s. Cooper pairs start to dissociate, leading to the suppression of the superconducting phase in favour of the normal phase. In fact, superconductivity is not only limited by T_c, it is also suppressed when the magnetic field is higher than a critical value, H_c, or if a transport current that exceeds an upper bound, J_c, is forced through the superconductor. J_c is always lower than the depairing current, J_{dep}, which is the current density beyond which Cooper pairs are no longer energetically favourable and split, marking the loss of superconductivity. The definition of T_c, H_c and J_c delimits a closed region in the T-H-J diagram where the material is superconducting. A schematic illustration of such a phase diagram is indicated in Figure 1.1. Note that T_c, H_c and J_{dep} are intrinsic characteristics of a given superconductor.

1.1.2 The London equations and the London penetration depth

On the microscopic level, the magnetic-field landscapes inside a superconducting material can be characterized with the help of two main spatial parameters. The first one is the London penetration depth, λ. The first feat of superconductivity that was discovered consists in its ability to transport current with no heat dissipation. It was also discovered that superconductors act as perfect diamagnetic materials. Supercurrents shield the superconducting volume from the external applied magnetic field, efficiently preventing its entrance. This last property is usually referred to as the Meissner effect. Perfect conductivity and diamagnetism can be modelled by the London constitutive laws [51]

$$\mathbf{E} = \frac{\partial}{\partial t}\left(\frac{m_e}{n_s e^2}\mathbf{J}\right), \tag{1.1}$$

$$\nabla \times \left(\frac{m_e}{n_s e^2}\mathbf{J}\right) = -\mathbf{B}, \tag{1.2}$$

where m_e is the electron mass, e is the electron charge, n_s is a density of superconducting carriers, $\mathbf{J}$ is the current density, $\mathbf{E}$ is the electric field, and $\mathbf{B}$ is the induction field. Both equations stem from the basic phenomenology of superconductivity. The first London law, Equation 1.1, translates the perfect conductivity of superconductors. It can be inferred from the Drude model, in the limit where the carrier scattering rate vanishes, which effectively models perfect conductivity. The second London law, in Equation 1.2, is supported by the resilience of the Cooper pairs to perturbations, which is enhanced with respect to the case of single electrons [51]. Furthermore, the second London law can be combined to Ampere's law, $\nabla \times \mathbf{H} = \mathbf{J}$, yielding

$$\nabla^2\mathbf{B} = \frac{1}{\lambda^2}\mathbf{B}, \tag{1.3}$$

$$\lambda = \sqrt{\frac{m_e}{\mu_0 n_s e^2}}. \tag{1.4}$$

where μ_0 is the vacuum permeability, while λ is the London penetration length, which measures the spatial screening of magnetic field inside a superconducting phase. For the sake of illustration, if an infinitely long superconducting slab of width W is subjected to a uniform static field, $\mathbf{H}_a$, $\mathbf{H} = H_z\mathbf{e_z}$ that is parallel to the sample's border, Equation 1.3 and Equation 1.4 yield a magnetic-field distribution

$$H_z = H_a \frac{\cosh(x/\lambda)}{\cosh(W/2\lambda)}, \tag{1.5}$$

where x is the distance from the median plane of the sample, see panel (a) of Figure 1.2. Equation 1.5 shows the exponential decay of magnetic field, evidencing the screening of magnetic field caused by the Meissner currents.

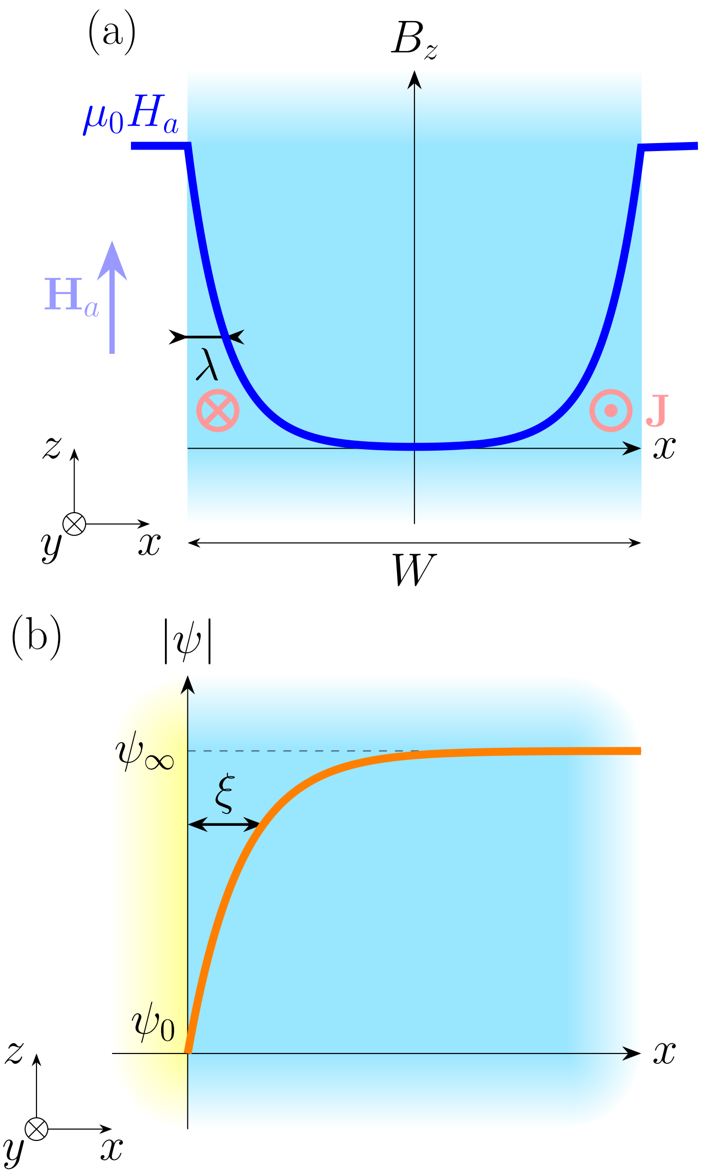

Figure 1.2: (a) Distribution of the transverse magnetic field, B_z, in an infinitely long superconducting slab of width W under a transverse field, H_a, as a function of the distance from its transverse median plane. The London penetration depth, λ is the screening characteristic length of the magnetic field, $\mathbf{B}$. (b) Order parameter, ψ, in the juxtaposition of two semi-infinite phases as a function of the distance from the interface between both phases, x. The superconducting phase is highlighted in blue and the non-superconducting one is in yellow. In the superconducting phase, the norm of the order parameters goes from ψ_0 at the interface between both phases, to ψ_∞ at an infinite distance from it. The coherence length, ξ, is the characteristic length of variation of ψ.

1.1.3 The Ginzburg-Landau equations and the coherence length

The second parameter that shapes the microscopic distribution of the magnetic field in superconductors is the coherence length, ξ. As it will be shown below, ξ is closely related to a theory of superconductivity that was devised by Ginzburg and Landau [52]. The

Ginzburg-Landau theory relies on a variational method that minimizes the free energy of the system, expressed as a function of a pseudo wave-function, which is called the order parameter, ψ. Remarkably, $|\psi|^2$ is the density of superconducting electrons. The Ginzburg-Landau equations for Cooper pairs read as

$$\frac{1}{4m_e}\left[\frac{\hbar}{i}\nabla - 2e\mathbf{A}\right]^2\psi + \alpha\psi + \beta|\psi|^2\psi = 0, \tag{1.6}$$

$$\frac{1}{\mu_0}\nabla\times\nabla\times\mathbf{A} = \frac{e}{m_e}\mathrm{Re}\left\{\psi^*\left[\frac{\hbar}{i}\nabla - 2e\mathbf{A}\right]\psi\right\}, \tag{1.7}$$

with $\hbar$, the Planck constant, $\mathbf{A}$, the vector potential, that verifies the relation $\mu_0\mathbf{J} = \nabla\times\nabla\times\mathbf{A}$, while Re stands for the real part of the expression surrounded by braces. The expressions in brackets consist in operators, and the square corresponds to a repeated application of the operator. Equation 1.6 has a form that is very close to Schrödinger equation, while Equation 1.7 reproduces exactly the quantum-mechanical expression of a current density carried by Cooper pairs which effective charge and mass are $2e$ and $2m_e$, respectively. These similarities explain why ψ is assimilated as a pseudo wave-function. The constants α and β are intrinsically related to the spatial distribution of ψ. One can indeed define the coherence length as $\xi^2 = \hbar^2/2m|\alpha|$, and the characteristic order of magnitude of the superconducting electron density as $\psi_\infty^2 = -\alpha/\beta > 0$. The physical meaning of ξ can be understood as the typical length that is required to mitigate a perturbation of ψ that stems from the transition between a superconducting phase and non-superconducting phase, going from ψ_0 at the interface between both phases, to ψ_∞ at an infinite distance from it [53]. In particular, it characterizes the spatial extension of the transition from a superconducting phase to an adjoining normal phase. This is illustrated in panel (b) in Figure 1.2.

Importantly, Equations 1.6 and Equation 1.7 can be generalized into a time-dependent scheme, which is known as the time-dependent Ginzburg-Landau (tdGL) equations, which are given as [54, 55]

$$\frac{\hbar^2}{4m_eD}\left[\frac{\partial}{\partial t} + i\frac{2e}{\hbar}V\right]\psi + \frac{1}{4m_e}\left[\frac{\hbar}{i}\nabla - 2e\mathbf{A}\right]^2\psi + \alpha\psi + \beta|\psi|^2\psi = 0, \tag{1.8}$$

$$\frac{1}{\mu_0}\nabla\times\nabla\times\mathbf{A} = \frac{e}{m_e}\mathrm{Re}\left\{\psi^*\left[\frac{\hbar}{i}\nabla - 2e\mathbf{A}\right]\psi\right\} - \sigma_n\left(\frac{\partial\mathbf{A}}{\partial t} + \nabla V\right), \tag{1.9}$$

where D is a phenomenological diffusion constant [56], σ_n is the normal conductivity of the material in the normal state and V is the scalar electric potential.

1.1.4 Type-I and Type-II superconductors

The magnetic properties of a superconducting material change radically depending on the value of the Ginzburg-Landau parameter, $\kappa = \lambda/\xi$. On the one hand, when $\kappa < 1/\sqrt{2}$, the material is a type-I superconductor. In such superconductors, the magnetic field is shielded by superconducting currents, according to the Meissner effect. Applied fields that exceed the thermodynamic field, $H_c(T)$, destroy superconductivity as shown in panel (a) in Figure 1.3. On the other hand, if $\kappa > 1/\sqrt{2}$, the material is considered as a type-II superconductors. In these superconductors, a normal phase and a superconducting

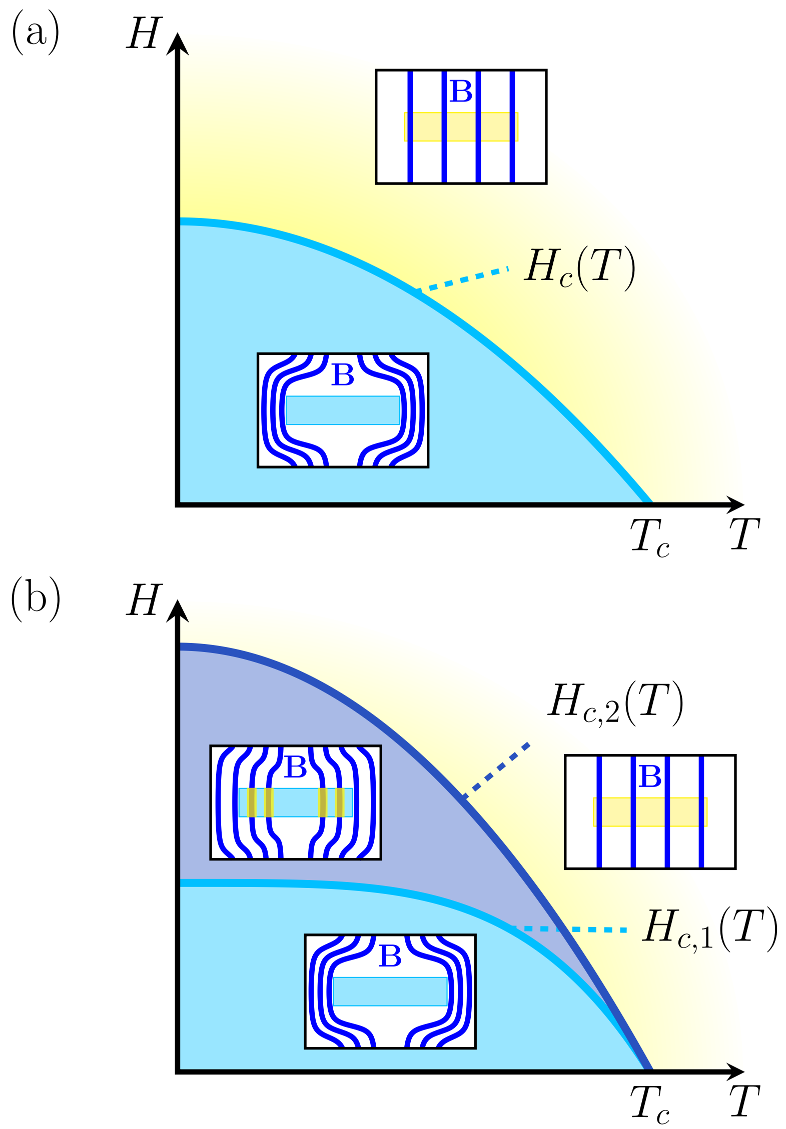

Figure 1.3: H-T diagrams in (a) type-I superconductors ($\kappa < 1/\sqrt{2}$), and (b) type-II superconductors ($\kappa > 1/\sqrt{2}$). Type-I superconductors are characterized by a sole Meissner phase, which holds for $H < H_c$, H_c being the thermodynamic critical field. H_c demarcates the conducting and the Meissner phases. Type-II superconductors are divided in a Meissner phase when $H < H_{c,1}$, and a Shubnikov phase for $H_{c,1} < H < H_{c,2}$. In the latter phase, magnetic field is allowed in the superconductor in the form of vortices, each of them carrying a constant magnetic flux, ϕ_0. The first vortex becomes energetically favourable at $H_{c,1}$, while $H_{c,2}$ delimits the transition from the Shubnikov phase to the normal phase.

phase can coexist. The sample is then said to be in the Shubnikov or mixed state. In other words, magnetic flux can penetrate inside the material, in the form of quantized magnetic flux bundles that are named vortices. A single vortex is composed of a core where superconductivity is locally suppressed, while it remains maintained outside it. Commonly, a vortex is thus represented as a cylinder that extends over the thickness of the sample, and which radius is comparable to ξ. Each vortex individually carries a fixed amount of magnetic flux, which is called the flux quantum, $\Phi_0 = h/2e = 2.07 \times 10^{-15}$ T/m^2.

Unlike type-I superconductors, type-II superconductors are characterized by two critical fields. The first one represents the limit between the Meissner and the mixed states and indicates the field at which the first vortex is allowed into the sample. At this value of the applied field, the Gibbs free energy that is required to introduce the first vortex in the sample, and which comes from the magnetic energy of the vortex and the kinetic energy from the surrounding superconducting currents, is equal to the Gibbs energy of the sample free of magnetic flux. The threshold field is called the lower critical field and is denoted by $H_{c,1}$. Below $H_{c,1}$ a type-II superconductor experiences a pure Meissner phase, like the one described for type-I superconductors. The second threshold outlines the boundary between the mixed state and the normal state. It is called the upper critical field and is denoted as $H_{c,2}$. Above $H_{c,2}$, superconductivity is destroyed. Alternatively, for decreasing applied fields, $H_{c,2}$ coincides with the nucleation of superconductivity inside a normal phase. Both $H_{c,1}$ and $H_{c,2}$ are schematically shown as a function of the temperature in the right image of panel (b) in Figure 1.3.

Analytical expressions for $H_{c,1}$ and $H_{c,2}$ can be derived and are given by

$$H_{c,1} = \frac{\Phi_0}{4\pi\mu_0\lambda^2}\log\kappa, \tag{1.10}$$

$$H_{c,2} = \frac{\Phi_0}{2\pi\mu_0\xi^2}, \tag{1.11}$$

while the thermodynamic field, H_c, is given by

$$H_c = \frac{\Phi_0}{2\sqrt{2}\pi\mu_0\lambda\xi}. \tag{1.12}$$

Comparing Equation 1.12 to Equation 1.11, one finds $H_{c,2}/H_c = \sqrt{2}\kappa$ and understands the origin of the threshold value $\kappa = 1/\sqrt{2}$, that distinguishes type-I and type-II superconductors. Similarly, Equation 1.12 and Equation 1.10 lead to $H_c/H_{c,1} = \sqrt{2}\kappa/\log\kappa$. H_c can then be roughly considered as the geometrical mean between $H_{c,1}$ and $H_{c,2}$. Type-II superconductors are then much useful in practice, since they can be utilized at much larger working magnetic fields than their type-I counterparts.

1.1.5 Temperature dependence of the London penetration length, the coherence length and the critical fields

Material	T_c	$\lambda(0)$	$\xi(0)$	$\mu_0 H_{c,1}(0)$	$\mu_0 H_{c,2}(0)$
Nb	9.2 K [57]	39 nm [57]	38 nm [57]	160 mT [58]	450 mT [59]
$YBa_2Cu_3O_7$	92 K [60]	150 nm [60]	1.5 nm [60]	180 mT [61]	125 T [62]

Table 1.1: Principal bulk parameters of superconducting Nb and $YBa_2Cu_3O_7$. For the latter material, which presents an anisotropic crystal structure, critical fields are determined along the out-of-plane direction to the CuO_2 planes, and $\lambda(0)$ and $\xi(0)$ correspond to the values along the same CuO_2 planes, when the sample is subjected to an external magnetic field in a direction perpendicular to the CuO_2 planes.

As it can be expected from Subsection **1.1.1**, the critical fields and the spatial characteristic lengths of a superconductor are temperature-dependent. However, based on the relations that relate H_c, $H_{c,1}$ and $H_{c,2}$ to λ and ξ, see Equation **1.12**, Equation **1.10** and Equation **1.11**, the knowledge of the temperature dependence of only two among these five quantities is necessary. For instance, one can rely on the variations of λ and H_c with temperature to deduce the temperature dependence of $H_{c,1}$, $H_{c,2}$ and ξ. The exact temperature dependences of H_c and λ depend on the material [63] and the theoretical model that is considered to fit the experimental data, such as the the two-fluid model [64], the BCS model [65], or the electron-phonon model [66], but more elaborated models and empirical fits are also possible [63, 67]. Since the experimental results exposed in this thesis mostly concern thin niobium films, using the two-fluid model [64] to explain the temperature dependence of H_c and λ is appropriate, as evidenced by convincing fits to the experimental data [68, 69]. In summary, we will use the following temperature dependences for bulk niobium [64]:

$$\lambda(T) \sim \left[1 - \left(\frac{T}{T_c}\right)^4\right]^{-1/2},\ \xi(T) \sim \left[1 - \frac{T}{T_c}\right]^{-1/2}, \tag{1.13}$$

$$H_c(T) \sim 1 - \left(\frac{T}{T_c}\right)^2,\ H_{c,1}(T) \sim 1 - \left(\frac{T}{T_c}\right)^4,\ H_{c,2}(T) \sim 1 - \left(\frac{T}{T_c}\right)^2. \tag{1.14}$$

Typical values of the superconducting parameters at $T = 0$ K for Nb and $YBa_2Cu_3O_7$ compounds are given in Table **1.1**, with the associated references. Note that these values are valid for bulks and can change drastically for thin films [70, 71, 72, 73], depending on the fabrication process, the microstructure or the presence of impurities [74, 75, 76]. Also, note that the temperature dependences in $YBa_2Cu_3O_7$ differ a lot from the ones above [63]. Nevertheless, it is still useful to keep in mind these expressions, as a reference to compare to more realistic and detailed experimental studies of these parameters.

1.2 Magnetic properties of type-II superconductors

1.2.1 Magnetic-field distribution around an isolated vortex

Since niobium is a type-II superconductor, gaining additional insight about the distribution of magnetic field and current density around an isolated vortex and how they interact with each other is crucial. The magnetic field and current density around a single vortex can be extracted from the Ginzburg-Landau formalism, using numerical methods to solve this system of non-linear coupled differential equations. However, a first approximation can be derived in the high-κ limit, i.e. $\kappa \gg 1$. This assumption allows one to consider the vortex as a normal cylindrical core of radius ξ, around which supercurrents circulate and shield the core magnetic field. Assuming magnetic field to be directed in the out-of-plane direction, the generated magnetic field decreases along the radial direction, r, so that $\mathbf{B} = B_z(r)\mathbf{e}_z$, and the subsequent Meissner current are azimuthal, $\mathbf{J} = J_\theta(r)\mathbf{e}_\theta$. In this

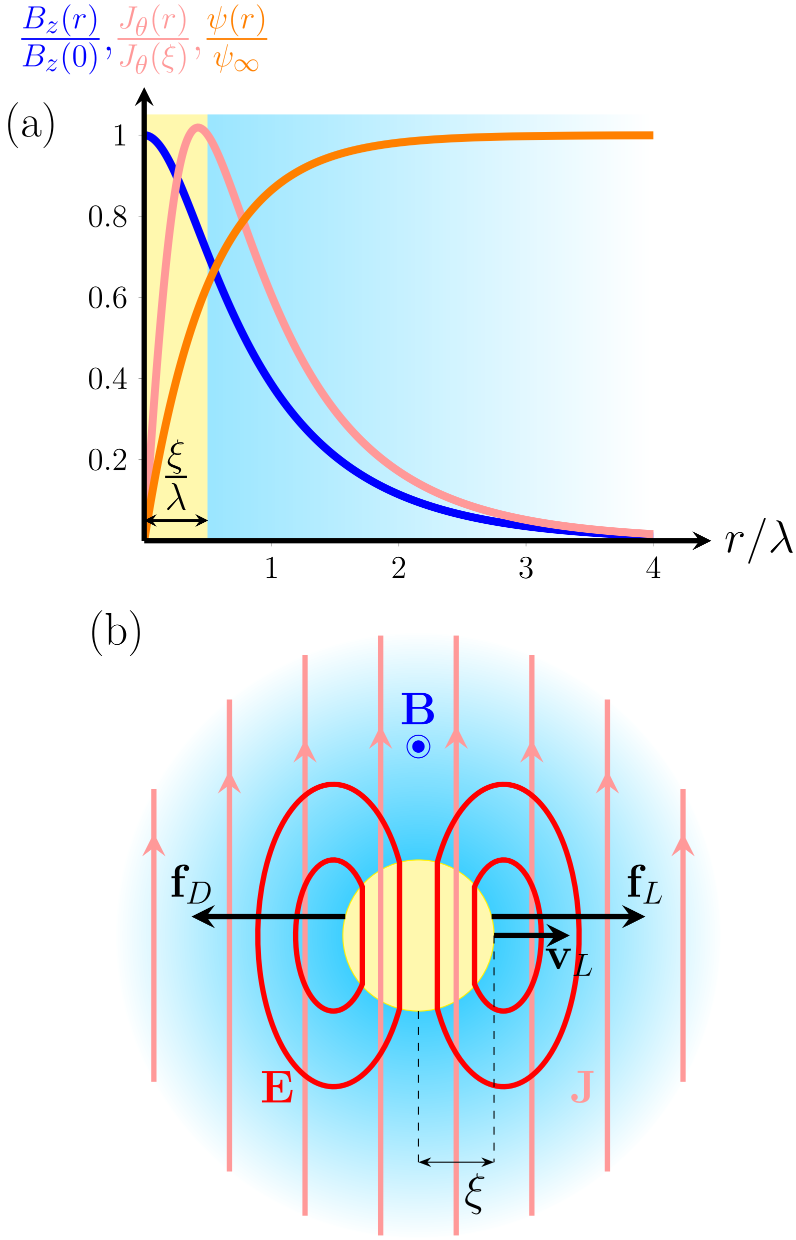

Figure 1.4: (a) Distributions of the out-of-plane component of the magnetic field, $B_z(r)/B(0)$, the azimuthal current density, $J_\theta(r)/J_\theta(\xi)$, and the order parameter, $\psi(r)/\psi_\infty$, as a function of the radial distance from the vortex centre of an Abrikosov vortex, r/λ, in the specific case $\kappa = 2$. The normal core region is represented in yellow, and the superconducting region, where Meissner currents extend, is coloured in light blue. (b) Electric field inside and around an Abrikosov vortex and the Lorentz force that drives the vortex forward, $\mathbf{f}_L = \mathbf{J} \times \mathbf{B}$. In the steady state, the vortex moves at the velocity $\mathbf{v}_L$. The motion of the normal core, in yellow, of lateral extension ξ, results in Joule-effect energy losses that can be modelled by a dissipative force opposing the vortex motion, $\mathbf{f}_d = \eta \mathbf{v}_L$.

context, Equation 1.6 yields [77]

$$B_z(r) = \frac{\Phi_0}{2\pi\lambda^2} \frac{K_0\left(\sqrt{r^2+\xi'^2}/\lambda\right)}{K_1\left(\xi'/\lambda\right)}, \tag{1.15}$$

$$J_\theta(r) = \frac{\Phi_0}{2\pi\mu_0\lambda^3} \frac{K_1\left(\sqrt{r^2+\xi'^2}/\lambda\right)}{K_1\left(\xi'/\lambda\right)} \frac{r}{\sqrt{r^2+\xi'^2}} \tag{1.16}$$

where K_0 and K_1 are the zeroth- and first-order modified Bessel functions of the second kind, and ξ' is a variational parameter of the order of magnitude of ξ. Note that Equation 1.15 is supposed to diverge as $\log(\lambda/r)$ close to the center of the vortex. In practice, this divergence is cut-off, because $|\psi|^2 \to 0$ in the normal core and the superconducting currents drop to zero. As a result of this, the magnetic field reaches a maximum at the center of the core and one can estimate

$$B_z(0) \approx \frac{\Phi_0}{2\pi\lambda^2} \log \kappa. \tag{1.17}$$

The B_z and J_θ profiles of a so-called Abrikosov vortex as a function of r/λ are schematically represented in panel (a) of Figure 1.4, in the case $\kappa = 2$. From the magnetic-field decay from a single vortex, it is then possible to deduce its energy per length unit, ϵ_0. Neglecting the normal core of the vortex, ϵ_0 is the sum of the magnetic and the kinetic energies of the Meissner currents [77]

$$\epsilon_0 \approx \frac{\Phi_0^2}{4\pi\mu_0\lambda^2} \log \kappa. \tag{1.18}$$

1.2.2 Interactions between vortices

In a real sample, not only one but many vortices penetrate the sample and interact with each other. The presence of other neighbouring vortices results in additional contributions to the system free-energy. These additional terms can be interpreted as the presence of forces that act on each vortex on behalf of every other surrounding vortices. In order to illustrate the kind of force that the vortices undergo, let us consider the simplest case of a vortex pair. Starting from the results of Equation 1.15 in the limit $\kappa \gg 1$, the force acting on vortex 2 on behalf of vortex 1, $\mathbf{f}_{12}$, is given by

$$\mathbf{f}_{12} = -\nabla F_{12} = (J_\theta \mathbf{e}_\theta) \times (\phi_0 \mathbf{e}_z) \tag{1.19}$$

where F_{12} is the free-energy characterizing the interaction between both vortices, and J_θ is the current density associated with vortex 1. Similarly, one can estimate the force governing the interaction of a vortex with an antivortex, which carries a fluxon of opposite sign. The force is then the opposite of that in Equation 1.19.

The first observation that can be made about Equation 1.19 is that the force that undergoes the vortex takes a form similar to a Lorentz force, even though it is limited to the superconducting currents, and while the current is the cause of vortex motion and not the magnetic field [78]. Equation 1.19 generalizes easily to samples that contain many vortices

$$\mathbf{f}_L = \mathbf{J}_{sc} \times \mathbf{\Phi_0}, \tag{1.20}$$

with $\mathbf{f}_L$ being the Lorentz force to which the vortex is subjected, and $\mathbf{J_{sc}}$ being the total superconducting current density that reaches the target vortex and generated by every other vortices. The second observation is that $\mathbf{f}_{12}$ is repulsive, whereas the force acting between a vortex and an antivortex is attractive. A vortex and an antivortex then attract each other, until they annihilate. On the other hand, in the presence of a multitude of vortices that carry fluxons of the same polarity, the vortices are bound to spontaneously move because of the repulsive Lorentz forces. Ultimately, in a bulk sample, vortices will arrange themselves into a stable triangular lattice known as the Abrikosov vortex lattice [79].

1.2.3 Flux flow and critical current density due to pinning

The situation is completely different when an external current is forced through the superconductor. Then, the driving Lorentz force is not only generated by the superconducting current density of the vortices, but also takes the external supplied current into account. This additional contribution to the total current forces the vortex lattice out-of-equilibrium, undergoing a net force that sets the vortices into motion, at a speed $\mathbf{v}_L$. In turn, the flux quanta in motion induce an electric field, $\mathbf{E}$. According to the Bardeen-Stephen model [80], which assumes that the core of the vortex acts as a normal state region, the electric field generated inside a moving vortex is parallel to the current density passing through the core. A sketch of the electric field inside and around the normal core of the vortex, when superconductivity is supposed to act locally, is shown in panel (b) of Figure 1.4. As a consequence of the induced $\mathbf{E} \parallel \mathbf{J}$, energy is dissipated locally in the form of heat because of Joule effect, at a rate $\mathbf{E} \cdot \mathbf{J}$. This regime, where vortices move, carrying their fluxons and dissipating energy simultaneously, is called the flux-flow regime. Flux flow can be characterized by a flux-flow resistivity, ρ_{ff}, that emerges from equating the driving Lorentz force, $\mathbf{f}_L = \mathbf{J} \times \mathbf{\Phi_0}$, to a viscous drag of the form $\mathbf{f}_D = -\eta \mathbf{v}_L$, which models the energy losses stemming from Joule heating and opposes the vortex motion, as represented in panel (b) in Figure 1.4. Here, η is a drag coefficient that reflects the effect of heat dissipation of the medium. From the expression of the induced electric field $\mathbf{E} = \mathbf{v}_L \times \mathbf{B}$, one directly finds that [80]

$$\rho_{ff} = \frac{\Phi_0}{\eta} |\mathbf{B}| \approx \frac{n_v \Phi_0^2}{\eta}, \tag{1.21}$$

where n_v is the density of vortices in the material and depends on the applied field. The dissipated power by unit length of the normal core, P_D, and the flux-flow resistivity can be related to the resistivity of the material in the normal state, ρ_n, according to [80]

$$P_D = \frac{|\mathbf{v}_L|^2 \Phi_0^2}{4\pi \xi^2 \rho_n} \tag{1.22}$$

$$\frac{\rho_{ff}}{\rho_n} \approx \frac{|\mathbf{H}|}{H_{c,2}}, \tag{1.23}$$

Flux flow particularly undermines the usefulness of type-II superconductors for applications, especially at high applied field, as witnessed by Equation 1.23, since current cannot be transported without heat dissipation any more. In order to counteract the deleterious consequences of the flux-flow regime, vortices need to remain immobile. This can be done by introducing artificial defects and inhomogeneities in the sample such as normal phases, dislocations, inclusions, arrays of antidots or holes, vacancies or grain boundaries. These defects locally suppress the order parameter and reduce the energy of the vortices, so that it becomes beneficial to them to pass through the defects, partially or completely, instead of bypassing them. The pinning sites thereby act as potential wells where vortices tend to hook on and remain trapped. This potential landscape is denoted by ϵ_P. A local pinning force, $\mathbf{f}_P$, can be derived from the pinning potential as

$$\mathbf{f}_P = -\nabla\epsilon_P. \tag{1.24}$$

A vortex remains pinned to a given pinning center as long as $\mathbf{f}_P$ can balance the driving force, $\mathbf{f}_L$. A straightforward force balance outlines a local critical current density, $J_c = |\mathbf{f}_{P,max}|/\Phi_0$, above which the vortex detaches from the pinning center and keeps moving until it pins to another pinning site, provided the local current density is not too intense, i.e. $|\mathbf{J}| \leq J_c$. Bear in mind that $J_c < J_{dep}$ and cannot exceed this value, as mentioned in Subsection **1.1.1**.

1.2.4 The critical state model

The Ginzburg-Landau model has proved its efficacy in describing the penetration of magnetic field in superconductors at the scale of the coherence length and the vortices. However, being able to probe the magnetic landscapes at such a small length scale becomes quickly heavy in terms of numerical workload when the size of the investigated system increases. Moreover, it is not necessary to probe the magnetic field in such details to appreciate the main features that manifest at the macroscopic scale. Instead, one can average the electromagnetic quantities over several vortex spacings and use the Maxwell equations. This approach is more adapted to macroscopic systems, which size typically extends over several hundreds of micrometers or more. Macroscopic models are then needed to investigate superconducting properties.

Critical state models (CSM) constitute a class of macroscopic models that aim at explaining the distribution of magnetic field in type-II superconductors. The main assumption of this category of models is the strong pinning hypothesis, that supposes that pinning is sufficiently strong to prevent any flux leakage from the pinning sites, once the external applied field is kept constant. As stated in Subsection **1.2.3**, vortices remain attached to their pinning centres and cannot move as long as $|\mathbf{J}| \leq J_c$. As soon as $|\mathbf{J}|$ exceeds J_c, the vortices are set into motion and reorganize until a new equilibrium configuration is reached. This situation occurs once the condition $|\mathbf{J}| \leq J_c$ holds for every vortex. Each vortex is then anchored to a pinning site, until the external field changes again. This delimits a region where vortices have penetrated, where the condition $|\mathbf{J}| = J_c$ holds. By contrast, the remaining part of the sample remains flux-free, since no vortex has progressed thus far. For infinitely long bulk sample, $\mathbf{J} = \mathbf{0}$ in the flux-free region.

Among the CSM, the Bean model [81, 82] neglects the possible non-uniformities in the pinning landscape, so that J_c is supposed to be uniform in the whole sample. Considering $H_{c,1}$ to be zero and $H_{c,2}$ infinitely large, the Bean model allows an easy description of the magnetic field distribution in an infinitely long superconducting slab of width W which is subjected to a uniform out-of-plane magnetic field, $\mathbf{H}_a = H_a\mathbf{e}_z$. The problem is then

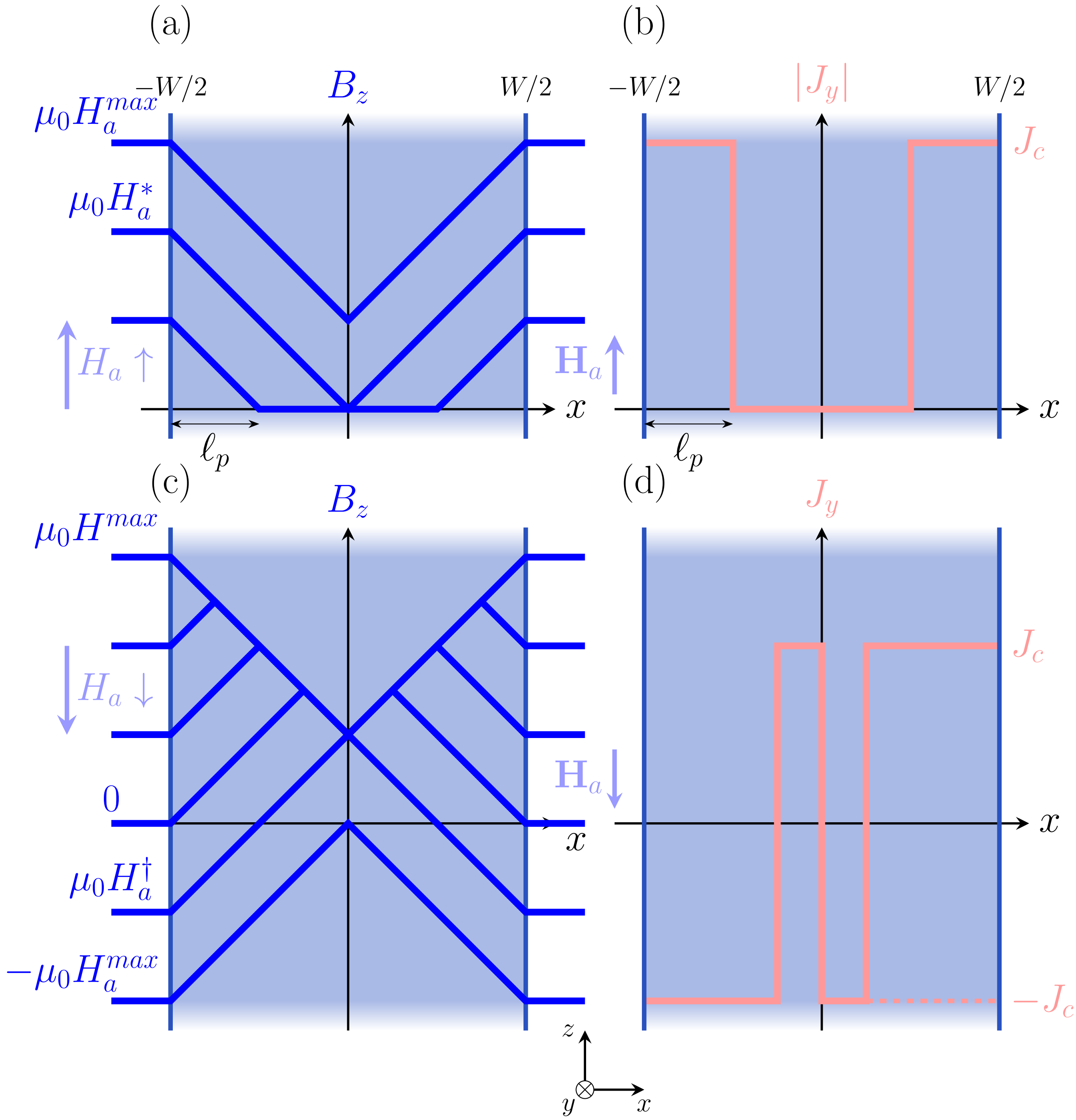

Figure 1.5: Critical states in an infinitely long superconducting slab of width W in the framework of the Bean model. The applied field, H_a, is directed along the z-direction. (a) Distributions of the magnetic field, B_z, as a function of the distance from the centre when the applied field is ramped up from 0 to a maximal field H_a^{max}. H_a^* is the applied field that is required to force the flux front at the centre of the slab. ℓ_p is the penetration length of the flux front. (b) Distribution of the norm of the current density, $|J_y|$, corresponding to the first B_z profile highlighted in panel (a). (c) B_z profiles when the applied field is ramped back from H_a^{max} to $-H_a^{max}$. $H_a^\dagger = H_a^{max} - 2H_a^*$ is the applied field for which $J_y = \mathrm{sgn}(x)\, J_c$ in the whole sample for the first time. (d) J_y that corresponds to $H_a = 0$, back from H_a^{max}.

reduced to a one-dimensional problem, and the induced currents are directed toward the y-axis, $\mathbf{J} = J_y(x)\mathbf{e}_y$. The magnetic field profiles, B_z, at different values of the external field, H_a, are illustrated in panel (a) in Figure 1.5, increasing H_a from a virgin state up to a maximum applied field, H_a^{max}. Since $H_{c,1} = 0$, vortices enter the sample as soon as $H_a > 0$, and $\mathbf{B} = \mu_0\mathbf{H}$ holds throughout the magnetization process. Moreover $H_z = H_a$ at $x = \pm W/2$ for any H_a. According to Ampere's law, $\mathbf{J} = \nabla \times \mathbf{H}$, B_z decreases linearly with x with a slope that is equivalent to J_c until $B_z = \mathbf{0}$. This occurs at a distance ℓ_p, the penetration length, as illustrated in panel (b) of Figure 1.5. The higher H_a, the higher ℓ_p, until a threshold field, H_a^* is reached for which $\ell_p = W/2$. In this case, $J_y = -\mathrm{sgn}(x)\, J_c$ in the whole slab, and the relation $H_a^* = J_c W/2$ holds. When $H_a \geq H^*$, vortices occupy every pinning centres, the magnetic response of the slab remains unchanged, and the profiles of H_z are simply shifted by a constant $H_a - H_a^*$.

Once H_a^{max} has been reached, H_a is decreased back to $-H_a^{max}$. The B_z and J_y profiles are shown in panels (c) and (d) of Figure 1.5. Now, antivortices that carries fluxons of opposite polarity immediately enter the sample, since $H_{c,1} = 0$, and progressively replace the anchored vortices. The superconductor is thus divided into a region where $J_y = -J_c$, and another region where $J_y = J_c$ is still holding, see for instance panel (d) of Figure 1.5. At $H_a^\dagger = H_a^{max} - 2H^*$, for the first time, $J_y = \mathrm{sgn}(x)\, J_c$ everywhere in the infinitely long bulk. The magnetic response then stays as it is, although H_a still decreases until $H_a = -H_a^{max}$. The remanent state displays a rooftop-like profile, which is a completely different magnetic field landscape than the original virgin state.

The critical state model can also account for magnetic-field-dependent J_c. Among diverse available empirical fits, this dependence can in general be faithfully described by the generalized Kim model, which states [83]

$$J_c(\mathbf{B}) = \frac{J_c(0)}{(1 + |\mathbf{B}|/B_0)^\alpha}, \tag{1.25}$$

where B_0 is a characteristic magnetic field that describes the variations of J_c with $|\mathbf{B}|$, $J_c(0)$ is the critical current density at $\mathbf{B} = \mathbf{0}$ and α is a fitting parameter. Kim's model is obtained for the particular case $\alpha = 1$ [84]. Upon a magnetization from a virgin state, and considering the same longitudinal geometry as for the Bean model, the profiles of B_z in the region filled with vortices as a function of H_a can, in the context of Kim's model, be obtained from the relation

$$(B_z + B_0)^2 - (\mu_0 H_a + B_0)^2 = 2\mu_0 J_c(0) B_0 \left(|x| - \frac{W}{2} \right), \tag{1.26}$$

and the associated current-density distributions in the penetrated region are given by

$$\frac{J_c(0)}{|J_y(x)|} = \sqrt{\left(1 + \frac{\mu_0 H_a}{B_0}\right)^2 + \frac{2\mu_0 J_c(0)}{B_0}\left(|x| - \frac{W}{2}\right)}. \tag{1.27}$$

The B_z and $|J_y|$ profiles are respectively outlined in panel (a) and panel (b) in Figure 1.6 in the particular case $\alpha = 1$, $B_0 = \mu_0 J_c(0) W/2$ and for various applied fields, $B_a/B_0 = 0.5$, 1 and 1.5. The flux front stops at a distance ℓ_p from the edges, which value can be obtained from Equation 1.26 with $B_z = 0$. The penetration length ℓ_p for a given H_a is thus

$$\ell_p = \frac{H_a}{J_c(0)} \left(1 + \frac{\mu_0 H_a}{2B_0} \right), \tag{1.28}$$

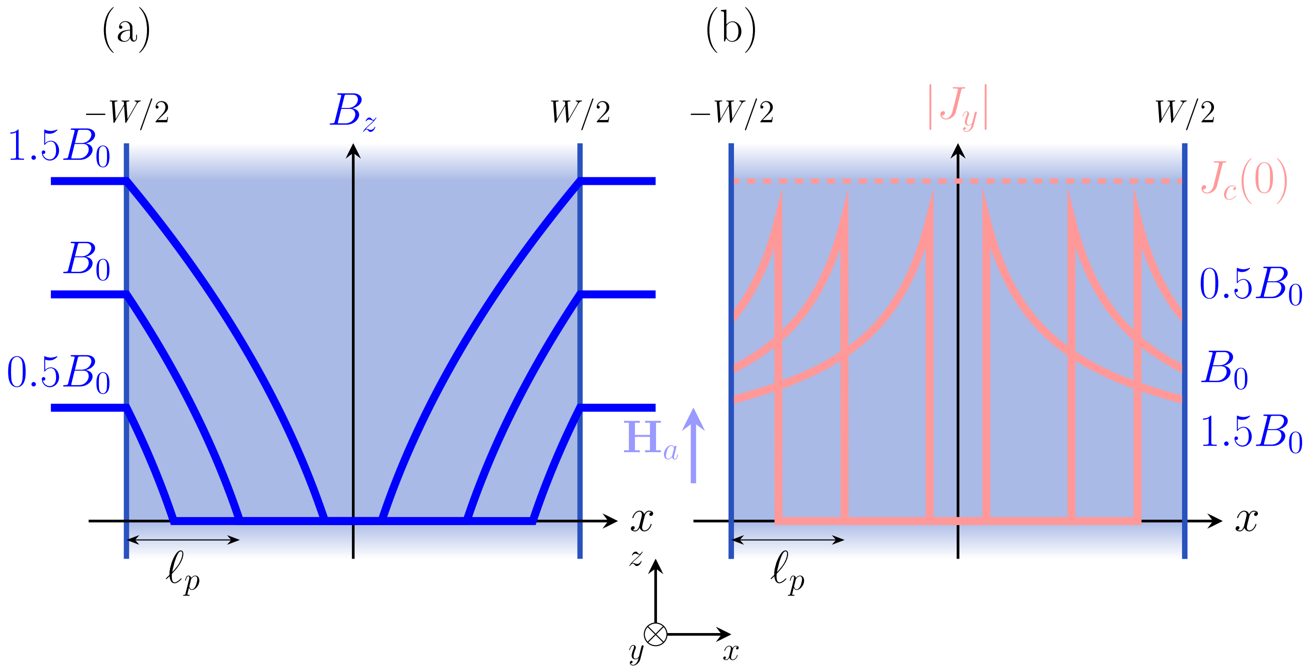

Figure 1.6: Critical states in an infinitely long superconducting slab of width W in the framework of the Kim model. The applied field, H_a, is directed along the z-direction. (a) Distributions of the magnetic field, H_z, and (b) the corresponding distributions of the norm of the current density, $|J_y|$, as a function of the distance from the centre of the slab when the applied field is ramped up from 0 to a given maximal field. The magnetic field dependence is given by Equation 1.25, with $\alpha = 1$. The B_z and $|J_y|$ profiles are given for $B_0 = \mu_0 J_c(0)W/2$, and for applied fields $\mu_0 H_a$ equal to $0.5B_0$, B_0 and $1.5B_0$. ℓ_p is the penetration length of the flux front and is indicated in the case $\mu_0 H_a = B_0$ for the sake of illustration.

which is a larger value than the penetration length that is expected in the Bean model with $J_c = J_c(0)$, i.e. $\ell_p = H_a/J_c(0)$. This is expected, since J_c decreases with $|\mathbf{B}|$. J_c is thus depleted close to the lateral surface of the slab and increases as one gets closer to $|x| = W/2 - \ell_p$, as evidenced in panel (b) of Figure 1.6. The magnetic field variations are then smoother and the flux front progresses further than in the Bean model. When $|x| \leq W/2 - \ell_p$, $B_z = 0$ and $J_y = 0$, as dictated by the CSM. Note that in the extreme case $B_0 \to \infty$, Equation 1.26, Equation 1.27 and Equation 1.28 yield the same analytical expressions as the Bean model.

1.2.5 Surface barriers

The critical state models focus on the dynamics of vortices once the vortices have entered the superconductor, but are not dedicated to how their entrance unfolds, which is a surface effect in essence. In fact, the entrance of the first vortex is not immediate and a minimal intensity of the applied field is required so that the formation of a single vortex becomes favourable in terms of the free energy of the system. Under this threshold field, a vortex cannot exist in the superconductor, which corresponds to the Meissner state. In practice,

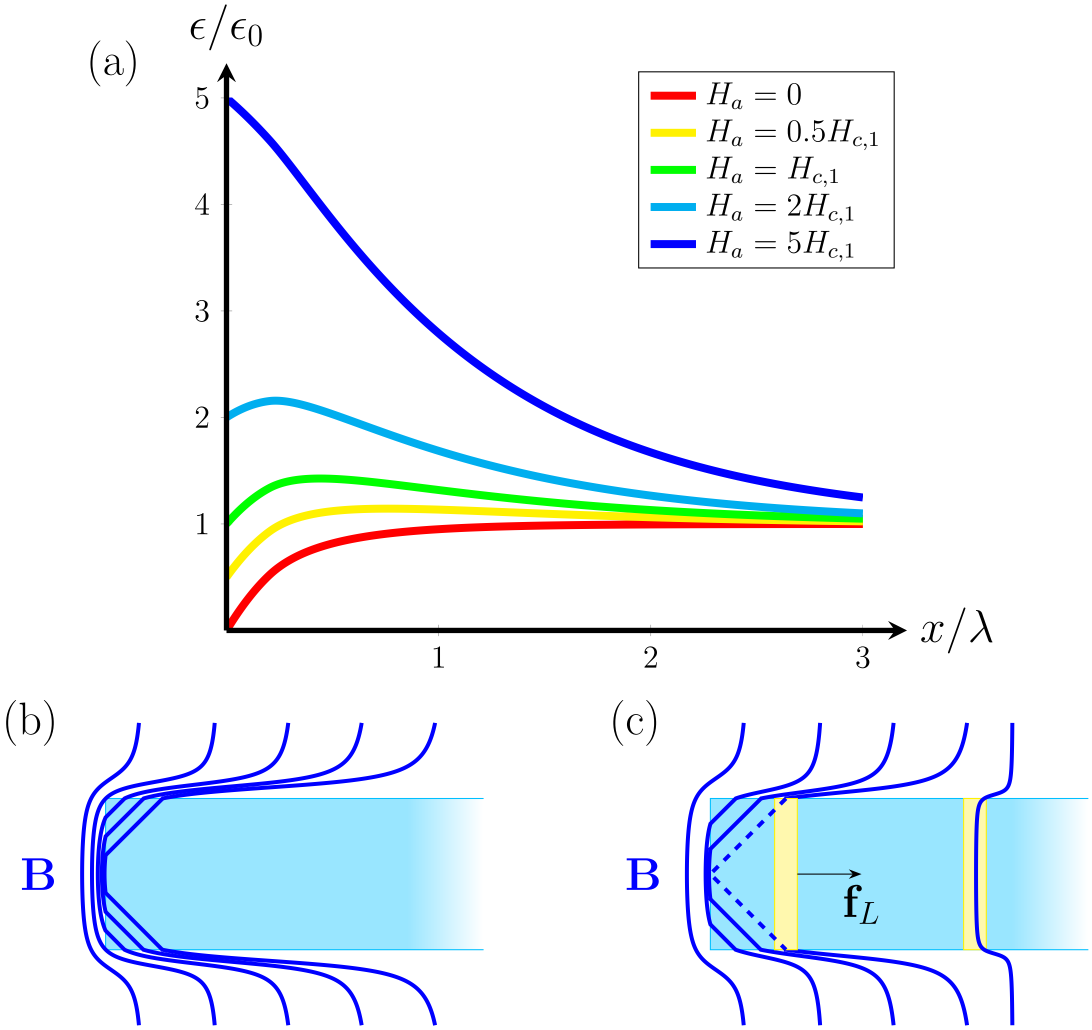

Figure 1.7: (a) Free energy of the vortex, ϵ/ϵ_0, as a function of the distance from the edge of an infinitely long superconducting slab, x/λ, for various strengths of the applied field, H_a, and in the case $\lambda = 10\,\xi$. The energy barrier that opposes the entrance of vortices above $H_a = H_{c,1}$ is called the Bean-Livingston barrier. (b) Enlargement of the magnetic flux lines, in dark blue, close to the sharp corners of a superconducting film when $H_a < H_{GB}$. (c) Enlargement of the magnetic flux lines, in dark blue, close to the sharp corners of a superconducting film when $H_a > H_{GB}$.

this lower threshold can differ from the lower critical field $H_{c,1}$. Two main phenomena can explain a modification of the actual penetration field, $H_p \neq H_{c,1}$.

The Bean-Livingston barrier

The first type of barrier that a vortex must overcome to enter a sample is known as the Bean-Livingston barrier [85]. When a vortex lies close to the surface of a superconductor of infinite lateral extension, it undergoes two opposing forces. The first one stems from the zero normal current condition across the border of the superconductor. This conditions is equivalent to create a fictive antivortex that is the image of the targeted vortex, according to a mirror symmetry with respect to the film border. Based on Equation 1.19, for $x \gg \xi$, this generates an attractive force towards the border and contributes to its energy per unit length as

$$\epsilon_B = -\frac{\phi_0^2}{4\pi\mu_0\lambda^2} K_0\left(\frac{2x}{\lambda}\right) \tag{1.29}$$

where x stands for the distance of the vortex from the border. The second force stems from the interaction between the vortex and the field inside the superconductor. If the internal flux lines and the entering vortex point towards the same direction, the interaction between the Meissner currents and the vortex results in a Lorentz force that pushes the vortex away from the border. This mechanism contributes to the energy per unit length of the vortex as a Zeeman energy

$$\epsilon_Z = \phi_0 H_a \exp\left(-\frac{x}{\lambda}\right). \tag{1.30}$$

Combining Equation 1.29 and Equation 1.30, one can estimate the dimensionless energy per unit length of a vortex, ϵ/ϵ_0, with respect to the normalized distance from the border, x/λ, with $\epsilon = \epsilon_0 + \epsilon_B + \epsilon_Z$ and ϵ_0 is the energy per length unit of a single vortex far from the border, see Equation 1.18. This is plotted in panel (a) in Figure 1.7 for different applied fields in the particular case of $\lambda = 10\,\xi$. When $H_a < H_{c,1}$, the line energy of the vortex is the lowest close to the border of the film, so that the formation of a vortex is unfavourable and does not occur. If $H_a \geq H_{c,1}$, the line energy becomes lower at sufficiently long distances from the border than at the border itself. However, it increases over a finite distance form the border, reaching a maximal value, which means that the vortex has to overcome a potential barrier to enter the sample. Such barrier prevents the vortex entrance inside the superconductor. This barrier is called the Bean-Livingston barrier, and its height decreases as H_a increases, until it reaches the value of H_{BL} above which the line energy is strictly decreasing with x, meaning that the first vortex is allowed to enter the sample freely.

The aforementioned developments assume a perfectly smooth surface. In practice, however, the roughness of the borders involves small defects where magnetic pressure may locally be enhanced, which facilitates flux entrance even for $H_a < H_{BL}$, so that the defects act as tiny flux faucets. However, upon a reduction of the applied field, these same locations, where the magnetic field flux lines concentrate locally, block and delay the exit of vortices, which remain trapped inside the sample [85]. The Bean-Livingston barrier is thus an non-symmetric barrier. The hysteretic behaviour of magnetization in weak-pinning or close-to-T_c samples is the signature of such surface barriers and has mostly been observed in single crystals [86, 87].

Geometrical barrier

The other kind of surface barrier that can delay the entrance of vortices is the geometric barrier [88, 89]. It results from a balance between the line tension of a vortex that keeps it anchored to the edges of the sample and the Lorentz force that drives it to the centre of the film [90]. The onset of vortex penetration is represented for an infinitely long sample of rectangular transversal section, in panels (b) and (c) of Figure 1.7, which show close-up views on the magnetic flux lines around the corners of the sample [91]. In analogy to the flux-concentrating property of small irregularities along rough borders that was mentioned when discussing the Bean-Livingston barrier, the sharp corners of a sample are also locations of magnetic flux concentration. Since $H_{c,1}$ is first reached there, vortices nucleate through the corners, in such a way that they are at first not parallel to the applied field and stay attached to the boundary because of their line tension, see panel (b) of Figure 1.7. The vortex undergoes two opposing forces. One the one hand, the line tension of the vortex tends to minimize the length of the vortex and prevents its progression inside the superconducting film. On the other hand, the Lorentz force pushes the vortex towards the interior of the sample. The balance between both forces determines the length of the vortex, which progressively increases as the applied field increases. This balance is maintained until both the upper and lower part of the vortices merge and form a single vortex that straightens and becomes parallel to the applied field, see panel (c) of Figure 1.7. At this moment, the length of the vortex suddenly reaches its minimum value, the line tension becomes minimal, and the Meissner currents drive the vortex to the center of the superconductor, in the absence of pinning, or until $|\mathbf{J}| = J_c$, in the presence of pinning. This can lead to the formation of magnetic flux domes [88, 90]. These domes vanish outside a given range of applied current and applied field [92]. The geometrical barrier also implies an hysteretic behaviour of the magnetization of the superconductor, because the field of first vortex entry is not the same as the field that is required to exit the superconducting material [90, 91].

The applied field at which the vortex detaches from the boundary and is carried away by Meissner currents is the penetration field related to the geometrical barrier, H_{GB}. This penetration field is highly dependent on the geometry of the sample, which determines the line tension of the vortex. In the case of an infinitely long strip of rectangular cross section with rounded borders, and in the absence of the Bean-Livingston barrier, it can be shown that [90]

$$H_{GB} = H_{c,1} \frac{1}{\sqrt{2W/d + 1}}. \tag{1.31}$$

Thereby, the geometric barrier reduces the applied field that is necessary to let a vortex in the superconductor. Equation 1.31 immediately demonstrates that geometrical barriers are much more prominent in thin films that are subjected to a transverse field than in bulks. In fact, if $W/d \approx 1000$, H_{GB} is effectively reduced by a factor of 45, while it is only divided by a factor of 2 when $W/d \approx 1$. For a niobium thin film of aspect ratio $W/d \approx 1000$, taking $\mu_0 H_{c,1} = 160$ mT, this thus gives a first penetration field that is of the order of magnitude of 4 mT.

1.2.6 Anisotropic behaviour

The Bean and the Kim models, which were introduced in Subsection 1.2.4, assume uniform pinning, which is a very convenient hypothesis. Nevertheless, depending on the material or the microstructure, pinning is not always isotropic. Both out-of-plane and in-plane anisotropy can significantly deform the shape of the vortices, for instance causing the twisting and tilting of the flux lines [93]. Anisotropy can be divided into two types. Intrinsic anisotropy can stem from the crystal structure of the compounds, but also from the inclusion of pinning sites and anisotropic structural defects, such as columnar defects, extended defects [93]. $YBa_2Cu_3O_7$ is a known example of anisotropic superconductor. Its atomic structure, which consists in parallel CuO planes that sandwich barium and yttrium atoms alternatively, leads to very different effective electron masses along or normal the CuO planes, which in turn influences the superconducting and transport properties along each direction [93, 94]. Intrinsic anisotropy can also be instigated by ion-beam irradiations, which create oblique pinning centres [95].

Contrary to intrinsic anisotropy, extrinsic anisotropy can be induced by an external in-plane field, $H_{\parallel}$, that is superposed to an out-of-plane field, $H_{\perp}$ [96, 97]. Two main theories were proposed to explain the rise of anisotropic features under the application of an in-plane field. The first one is based on flux cutting. $H_{\parallel}$ gives rise to in-plane vortices (in the direction of $H_{\parallel}$) which interact with the usual out-of-plane or tilted vortices that penetrate because of $H_{\perp}$. The out-of-plane vortices that move perpendicular to the in-plane vortices must cross them and undergo successive cutting-and-reconnection processes that further hinder their passage, while the vortices that make their way parallel to the in-plane vortices remain unperturbed by their presence and only have to overcome bulk pinning [96]. The in-plane field thus begets an increase of the pinning force when the vortices move perpendicular to the direction of $H_{\parallel}$, while pinning in the same direction as $H_{\parallel}$ is preserved. A second theory was proposed just after the first and advocates for reduced pinning along the in-plane vortices, that act as preferential corridors for the motion of the out-of-plane vortices, while their motion remains roughly unaffected along the perpendicular direction [43]. In any case, both theories conclude that J_c is larger in the regions where the current density is parallel to the direction of $H_{\parallel}$ than those where it flows perpendicular to $H_{\parallel}$.

Extrinsic anisotropy steps in only when $H_{\parallel}$ exceeds a lower threshold value which coincides with the field at which in-plane vortices are allowed in the sample [96]. For this reason, for a given value of $H_{\parallel}$, extrinsic anisotropy is prevented if the sample is thinner than a threshold value [96, 97]. Extrinsic anisotropy becomes more significant as $H_{\parallel}$ is increased, so that extrinsic anisotropy has the benefit to be completely tunable [97]. One should be careful on the fact that critical states might radically differ depending on whether the anisotropy is intrinsic or extrinsic [95].

1.2.7 Thermally activated flux-creep

Subsection **1.2.3** emphasized that vortices remain pinned to defects until the local current density reaches its critical value, J_c. The temperature dependence of the critical current density, $J_c(T)$, can be estimated as [98, 99]

$$J_c(T) = J_c(0)\left(1 - \frac{T}{T_c}\right)^{3/2}, \tag{1.32}$$

where $J_c(0)$ is the critical current density at $T = 0$ K. Besides, due to thermal fluctuations, vortices happen to hop from their pinning center to another one, and then reorganize, meanwhile dissipating power, which increases the measured voltage drop across a sample, for a given value of the transport current. This thermally activated phenomenon is better known under the name of flux creep. From the perspective of modelling, flux creep relates

$\mathbf{E}$ and the local $\mathbf{J}$ according to a power law

$$\mathbf{E}(|\mathbf{J}|) = \frac{E_c}{J_c}\left(\frac{|\mathbf{J}|}{J_c}\right)^{n-1}\mathbf{J} \equiv \rho(|\mathbf{J}|)\,\mathbf{J}. \tag{1.33}$$

Equation 1.33 is formally explained by a logarithmic dependence on $\mathbf{J}$ of the activation energy, $U = U_0 \log(J_c/|\mathbf{J}|)$, where U_0 is an energy constant that may vary with temperature and magnetic field. The logarithmic shape is corroborated experimentally [100, 101] and then combined to the usual flux-creep model [102] to yield Equation 1.33. The choice of the logarithmic dependence of U with respect to $\mathbf{J}$ is motivated by a logarithmic shape of the potential wells within which vortices are trapped, which corresponds to the expected shape of the potential well for small defects that extend over distances that are comparable to the coherence length, ξ [100]. Strictly speaking, the value of E_c is an arbitrary chosen value that defines the value of J_c from the E-J curve of the studied sample. In this thesis, the very widespread value $E_c = 1\ \mu$V/cm is chosen. However, the choice of E_c is not expected to influence qualitatively the results of this thesis [103]. It is worth stressing out that the isotropic flux-creep model is not suited for treating the modelling of longitudinal currents [104, 105, 106]. In that case, one should refer to more elaborated models [105, 107, 108].

Determining a value of n can be achieved by either the direct measurement of the logarithmic scale plot of the $E-J$ curve or using the decay of the magnetization with respect to time [84, 109]. In fact, because of the thermal fluctuations that enable flux hopping from one pinning site to another, the array of vortices rearranges continuously and the total magnetization of the sample progressively decreases since some of these unpinned vortices exit the sample through the borders. Since vortex motion is driven by Lorentz forces and flux gradients, which are reduced as trapped vortices are released, flux creep slows down over time. In practice, this results in a logarithmic time decay of the total magnetization of the sample $\mathbf{M}$ and the persistent currents that are responsible for it. Denoting the normalized flux-creep rate by S, one can show that, at large times, [109]

$$S = -\frac{\partial \log(|\mathbf{M}|)}{\partial \log t} = \frac{1}{n-1}. \tag{1.34}$$

Notice that if $n \to \infty$, one recovers the critical state assumption, where the pinning centres are strong enough to prevent any thermally activated flux creep. In such a case, $\mathbf{E} = \mathbf{0}$ if $|\mathbf{J}| < J_c$, and the magnetization of the sample does not decay over time.

1.3 Magnetic properties of thin films

1.3.1 Penetration of magnetic field in thin superconducting films at the micro- and macro-scale

Up to this point, the focus was put on the main superconducting parameters and the general dynamics of vortices to explain the propagation of magnetic field in superconductors in the mixed state. However, the results of this thesis focus on thin films subjected to an external out-of-plane magnetic field. Thin films cover samples with a lateral extension, let us say L, much larger than its thickness, d, i.e. $L/d \gg 1$. Such a restriction has crucial implications regarding the magnetic field distribution around vortices. First, the magnetic field generated by vortices in bulk superconductors is characterized by an exponential asymptotic decay at distances $r > \lambda$, i.e. $B_z \sim \exp(-r/\lambda)$. In contrast to Abrikosov vortices, the so-called Pearl vortices, which arise in thin films with $d \leq \lambda$, generate a magnetic field that asymptotically decays as $1/r^3$, and the superconducting currents, that dictate the interaction range of the vortices stemming from the pseudo-Lorentz forces, decay as $1/r^2$ [72]. Pearl vortices then interact on much longer scales than Abrikosov vortices. Subsequently, the macroscopic profiles of the magnetic field in practical thin superconducting films are heavily impacted by the long-range interactions and ordering between vortices. Second, when $d \leq \lambda$, the Meissner currents that screen the magnetic field leaking through the vortices are confined over the film thickness, so that these induced current extend over typical distances of the order of $\Lambda = 2\lambda^2/d$ in the planar direction, instead of λ for bulk samples. Pearl vortices typically appear when $d \ll \lambda$, but are also reported when $d \sim \lambda$ [110].

Moreover, the thin-film geometry also involves much more prominent demagnetizing effects than in bulk samples, influencing even further the magnetic field penetration in thin superconducting films, which becomes strongly non-local. These demagnetizing effects and the sharp edges of the samples tend to concentrate the magnetic flux at the border of the film, as illustrated in the upper picture of panel (a) in Figure 1.8. Such a concentration means that vortices may enter the film although the magnitude of the applied field, H_a, is much lower than $H_{c,1}$ or H_{BL}, if the Bean-Livingston barrier is accounted for, as witnessed by Equation 1.31. Besides, for partially penetrated films with strong pinning, the current density is uniform along the thickness only where vortices have penetrated, while currents spreads non-uniformly across the thickness in the Meissner region [111], forming a meniscus-like shape. The sheet current density, $\mathbf{J}_s$, is therefore non-zero in the flux-free regions, as schematically illustrated in the lower part of panel (a) in Figure 1.8. Physics in thin films thus becomes non-local, which adds complexity to the already challenging non-linear behaviour of superconductors.

In order to have a better grasp of the typical distributions of the out-of-plane component of the magnetic field, H_z, and the current density, $\mathbf{J}$, in the thin-film geometry, analytical expressions can be obtained for thin disks of radius R and infinitely long thin strips of width W subjected to an out-of-plane external field, $\mathbf{H}_a = H_a\mathbf{e}_z$. These results rely on the thin-film approximation, which consists in recasting Maxwell's equations with the current density, $\mathbf{J}$, replaced by the sheet current density, $\mathbf{J}_s$, which is the integration of $\mathbf{J}$ over the thickness of the film, d, i.e.

$$\mathbf{J}_s(x,y) = \int_{-d/2}^{d/2} \mathbf{J}(x,y,z)dz. \tag{1.35}$$

The film is then treated as an infinitely thin layer, where the magnetic field in the film, $\mathbf{H}$, is strictly directed in the out-of-plane direction, while the current density remains strictly parallel to the cross section of the film. This assumption allows the three-dimensional eddy-current problem to be reduced to a two- or one-dimensional problem, which is based on the resolution of the Biot-Savart law. The results are obtained in the framework of the critical state model, with a critical current density equal to J_c. In the case of a thin

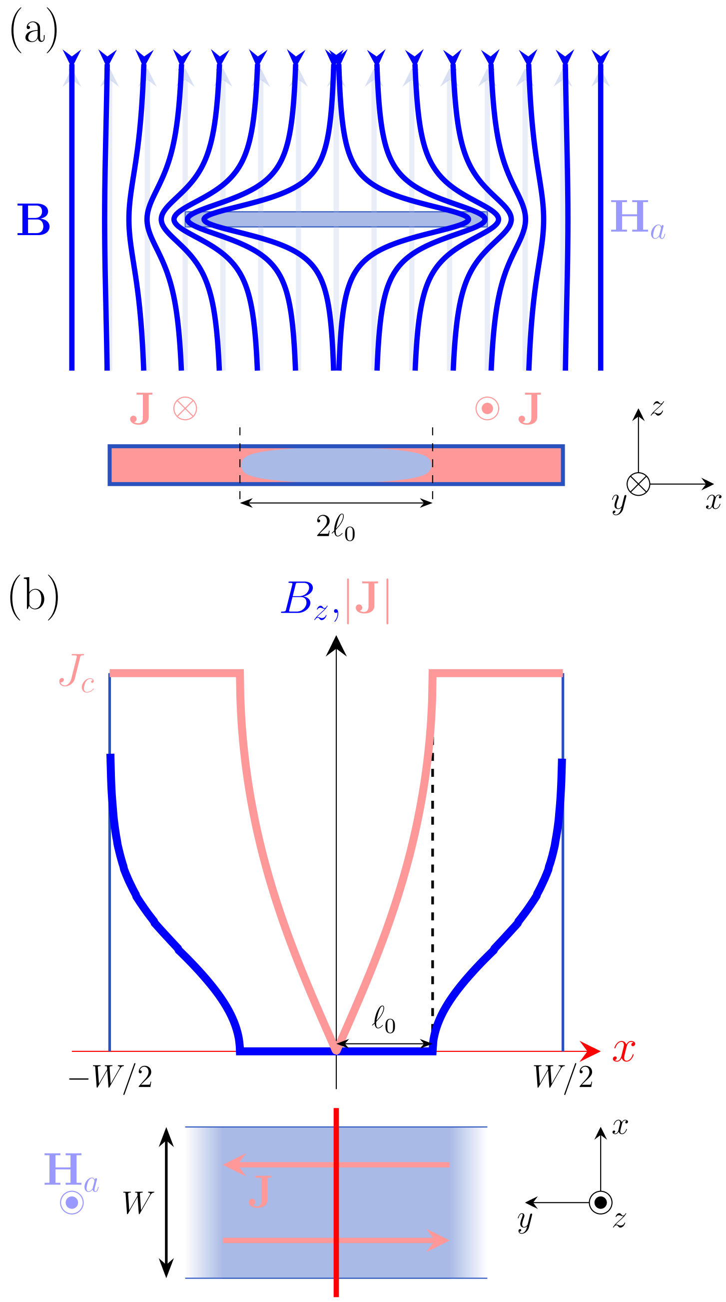

Figure 1.8: (a) Distribution of the magnetic field lines (in dark blue) in a superconducting film with strong pinning, which is subjected to a uniform out-of-plane applied field (in light blue). The associated distribution of the current density is sketched in the bottom drawing. This distribution is non-uniform in the flux-free regions, which extends over a length $2\ell_0$. (b) Distributions of B_z and $|\mathbf{J}|$ in an infinitely long thin superconducting strip of width W as a function of the distance from the centre of the strip, x, with $H_a/H_d = 1.5$. The profiles are taken along the red curve.

disk, the current density flows in the azimuthal direction, and one has [112, 113]

$$H_z(r) = \begin{cases} 0 & \text{if } 0 \leq |r| \leq \ell_0, \\ H_d \left[\operatorname{arccosh}\left(\frac{R}{\ell_0}\right) - \operatorname{arccosh}\left(\frac{R}{r}\right) + \right. & \\ \left. \int_{\arcsin(\ell_0/R)}^{\pi/2} \frac{2}{\pi} \frac{1-\theta\cot\theta}{\sqrt{1-(H_a/H_d)^2\sin\theta}} d\theta \right] & \text{if } \ell_0 \leq |r| \leq R, \end{cases} \tag{1.36}$$

$$|\mathbf{J}(r)| = \begin{cases} \frac{2J_c}{\pi} \arctan\left\{ \frac{r}{R}\sqrt{\frac{R^2-\ell_0^2}{\ell_0^2-r^2}} \right\} & \text{if } |r| \leq \ell_0, \\ J_c & \text{if } \ell_0 \leq |r| \leq R, \end{cases} \tag{1.37}$$

where r is the radial distance from the centre of the disk, $\ell_0 = R/\cosh(H_a/H_d)$ corresponds to the extension of half the flux-free region, and $H_d = J_c d/2$. Similarly, in the case of the infinitely long strip, the CSM in the thin-film approximation yields [114]

$$H_z(x) = \begin{cases} 0 & \text{if } 0 \leq |x| \leq \ell_0, \\ H_d \operatorname{arctanh}\left\{ \frac{\sqrt{x^2-\ell_0^2}}{c_0|x|} \right\} & \text{if } \ell_0 \leq |x| \leq W/2, \end{cases} \tag{1.38}$$

$$|\mathbf{J}(x)| = \begin{cases} \frac{2J_c}{\pi} \arctan\left\{ \frac{c_0|x|}{\sqrt{\ell_0^2-x^2}} \right\} & \text{if } 0 \leq |x| \leq \ell_0, \\ J_c & \text{if } \ell_0 \leq |x| \leq W/2, \end{cases} \tag{1.39}$$

where x is the distance along the width from the infinitely long median of the strip, $\ell_0 = W/(2\cosh(H_a/H_d))$, $c_0 = \tanh(H_a/H_d)$ and $H_d = J_c d/\pi$. The profiles of H_z and $|\mathbf{J}|$ are plotted versus x for $H_a = 1.5H_d$ in the strip geometry in panel (b) of Figure 1.8. Contrary to the CSM in bulk samples, the magnetic field diverges as a logarithm close to the borders of the film. Besides a region of constant $|\mathbf{J}| = J_c$, the current density is also non-zero outside this region, and decays progressively until $\mathbf{J} = \mathbf{0}$ at the centre of the film, as illustrated in the bottom figure of panel (a) of Figure 1.8. Note that the logarithmic divergence is cut off at the boundary of thin films of finite thickness, d, and reaches a level that scales as $\sim \log(L/d)$, where L is the typical in-plane size of the film [115, 116].

1.3.2 Discontinuity lines

In any superconductor in the mixed state, magnetic field enters the sample through the border of the sample as soon as it exceeds the surface barrier and progresses further towards the center as the external field is increased. The associated distribution of the current density also varies with the applied field, and the current loops that result from this distribution evolve accordingly, in a complex way. However, once the magnetic field has fully penetrated inside the film, the reaction field does not change any more and the induced current lines freeze into a definite shape [116]. The hypotheses of the critical state model then become relevant. The current density must flow parallel to the borders of the sample to obey current conservation, and the current streaming lines are equidistant from each other, in accordance with the CSM. If the boundary of the film cross section makes sharp turns, the current lines follow them, leading to abrupt changes of orientation of the current density. These current deflections occur at specific locations that are known as discontinuity lines (d-lines) [116].

Two kinds of d-lines can be identified [95]. The first kind regroups d-lines that demarcate two regions of unequal J_c, where current must bend sharply to obey current conservation. These d-lines are also labelled as d$^-$-lines. In particular, they include the borders of the film or the holes that may perforate the film cross section. As is obvious in the case of the film boundaries, vortices and magnetic flux can cross d$^-$-lines. The second kind of d-lines concerns those arising in a region of uniform J_c, but where the current density changes its direction abruptly. In contrast with d$^-$-lines, magnetic flux cannot traverse d$^+$-lines and moves along them instead. These d-lines are confounded with particular symmetry lines that are intricately related to the geometry of the sample. Note that the thin-film geometry exacerbates the levels of magnetic field around the d-lines, where B_z diverges logarithmically [116, 117]. If the magnetic landscapes are probed by means of magneto-optical imaging, see Subsection 1.4, the d-lines stand out in the thin-film geometry, and can be easily identified. This is in stark contrast with bulk samples, where such magnetic field divergence is non-existent, so that d-lines might be difficult to identify. Moreover, once the sample has been completely penetrated by the magnetic field, the d-lines do not change any more, and their shape is exclusively determined by the geometry of the film and the spatial distribution of the critical current density, whatever the strength of the external field that might be applied afterwards [116]. The difference between the d$^-$-lines and the d$^+$-lines is now illustrated in particular cases.

Discontinuity lines in a thin square film with uniform J_c

First, the case of a square film of length L is considered. The corresponding array of d-lines is shown in panel (a) of Figure 1.9. The d$^-$-lines coincide with the outer boundary of the film, since current density is zero outside the film, and suddenly becomes J_c on the other side of the boundary, inside the superconducting sample. The d$^+$-lines correspond to the diagonals of the square, because they separate two patches of currents, each of them flowing parallel to one of a pair of adjacent sides of the square, which form a $\pi/2$ angle. Current conservation then implies that a d$^+$-line emerges from the corner, making a $\pi/4$ angle with respect to each edge. Another way to explain this result is to observe that current lines are equidistant from the borders, so that the d$^+$-lines must be equidistant to each pair of adjacent edges, and thus follow the bisector line.

Discontinuity lines in a thin rectangular film with uniform J_c

In the case of a rectangular sample, the situation does not change much. d$^-$-lines still coincide with the outer boundary of the film, while d$^+$-lines still make a $\pi/4$ turn, starting from each corner of the rectangle, in accordance with current conservation. However, the bisector lines that start from each corner do not meet at a single point, as in the case of a square film. Instead, the two upper bisector lines meet at point, I_1, which is located on the longest median of the rectangle, in the upper half of the rectangle. Similarly, the two lower bisector lines meet at I_2, the point reflection of I_1 with respect to the barycentre of the rectangular film. The d$^+$-lines and the central vertical d$^-$-line thus imitate a 'double Y' shape, as represented in panel (b) of Figure 1.9.

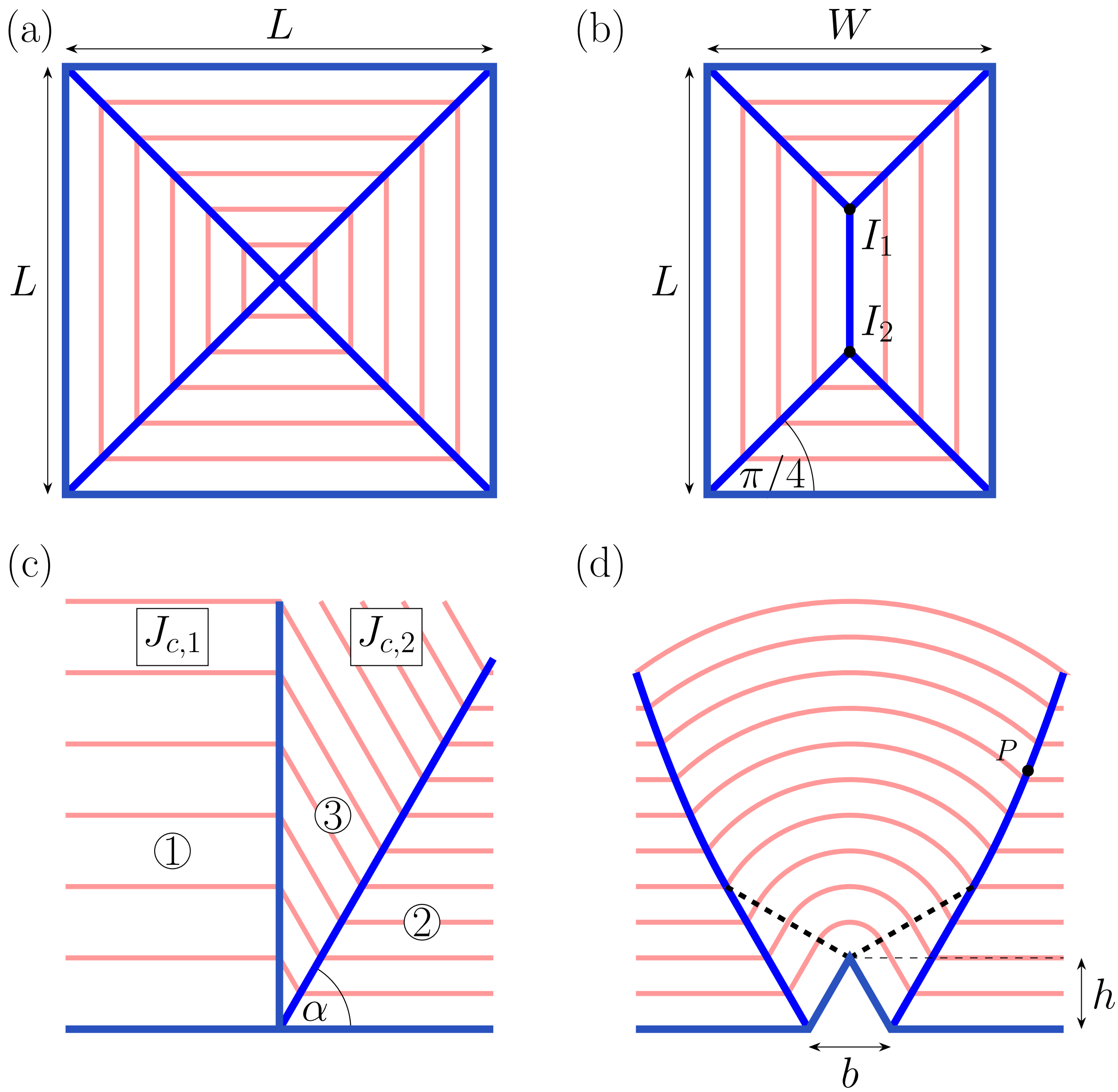

Figure 1.9: Discontinuity lines and current lines in different thin-film geometries subjected to an out-of-plane magnetic field, within the CSM assumptions. In all panels, the bold blue and cerulean lines correspond to d$^+$- and d$^-$-lines, respectively, while current lines are depicted in light red. Dashed lines are guides for the eye. (a) 'X'-shaped d-lines in a thin square superconducting film of side L. (b) 'Double Y'-shaped d-lines in a thin rectangular superconducting film of width W and length L. (c) Abrupt current reorientation in a semi-infinitely long sample which is characterized by a non-uniform critical current density distribution, with $J_c = J_{c,1}$ on the left side and $J_c = J_{c,2} > J_{c,1}$ on the right side. The d-lines are sketched in the particular case $2J_{c,1} = J_{c,2}$. (d) Parabolic d$^+$-lines around an isosceles triangular indentation of base b and height h. P is a point of the right branch of the parabolic d$^+$-lines. In the drawing, the triangle is equilateral, so that $h/b = \sqrt{3}/2$.

Discontinuity lines around an abrupt non-uniform J_c transition

Let us now consider the case of a semi-infinite film that is divided in two regions of uneven J_c, as schematically illustrated in panel (c) of Figure 1.9. Let us denote by $J_{c,1}$ the current density in the left region (sector 1) and $J_{c,2}$ the current density in the right region (sector 2 and 3), where $J_{c,1} < J_{c,2}$, without loss of generality. Unsurprisingly, d$^-$-lines are located along the flat border of the semi-infinite film. Since $J_{c,1} < J_{c,2}$, a mismatch between the location of current lines in the left and right regions arises. In particular, horizontal current lines in sector 1 have advanced deeper in the superconducting film than those in sector 2, where they are denser. In sector 3, the current lines take a sharp turn and become oblique in such a way that the mismatch can be gradually rectified. Current conservation along the limit between sector 1 and 3 yields

$$\frac{J_{c,1}}{J_{c,2}} = \cos(\pi - 2\alpha). \tag{1.40}$$

Several remarks are worth mentioning. First, because of the concurrent and sharp changes of both the orientation of the current lines and the value of the current density along the line that demarcates sector 1 and 3, a d$^-$-line is located there. Secondly, the d^+-line that separates sector 2 from sector 3 corresponds to the bisector line between the horizontal and oblique current lines in sector 2 and 3, respectively. This highlights once again the fact that d^+-lines coincide with symmetry lines. Last, α affects the strength of the logarithmic divergence that surrounds the d^+-line, according to the relation [116]

$$B_z \sim K_\alpha \frac{\mu_0 J_c d}{2\pi} \log(\delta x), \tag{1.41}$$

where $K_\alpha = 2\cos\alpha$ and δx here represents the distance from the monitored d-line. The smaller α, the larger the multiplying factor K_α, and the more the d-line stands out. In the limit $J_{c,1} = 0$, one recovers the $\pi/4$ d$^+$-line that emerges from a sharp right corner. By contrast, if $J_{c,1}/J_{c,2} \to 1$, one recovers the case of a uniform J_c sample, and the d$^+$-line vanishes.

Discontinuity lines around defects

Finally, let us consider the case of a plain isosceles triangular indentation that is cut along the border of a film, with a base length b and height h, as illustrated in panel (d) of Figure 1.9. As usual, d$^-$-lines are located along the border of the film and the indentation. Since current lines are parallel to these borders, they must change their direction along a d$^+$-line that is equidistant from the border of the film and the lateral border of the indentation. The d$^+$-line is thus located along the bisector line of the outer angles, at the basis of the indentation. The oblique current lines that develop parallel to both lateral edges of the indentation rejoin thanks to circular current lines, which are equidistant to the tip of the triangular indentation. The change of orientation of the current lines is continuous, so that no d-line is observed there.

The d$^+$-line does not however remain linear indefinitely. Far enough from the indentation, the circular current lines that originate from the tip of the indentation meet the horizontal current lines parallel to the border of the sample before the latter ones meet the oblique current lines that are parallel to the lateral sides of the indentation. The d$^+$-line now outlines the locus of points that are equidistant from the tip and the horizontal border of the film. The curve that satisfies such a requirement is a parabola. If one refers to an orthonormal basis which origin corresponds to the mid-point of the triangle basis, the parabolic part of the d$^+$-lines is described by the following equation:

$$y_P = \frac{x_P^2}{2h} + \frac{h}{2}, \tag{1.42}$$

where $P(x_P, y_P)$ is a point of the parabolic d$^+$-line. Equation 1.42 immediately shows that the longer the indentation height, the more open the parabola. For the sake of illustration, the network of d-lines and the current lines that form around a triangular indentation are represented in panel (d) of Figure 1.9, in the specific case of an equilateral triangular indentation, $h/b = \sqrt{3}/2$. The above reasoning can also be easily extended to the case of circular and square indentations [41]. Indistinctly of the indentation geometry, a parabolic d$^+$-line forms far enough from the indentation, and its opening is related to the height of the indentation [41].

1.3.3 Magnetic flux avalanches

The critical state model, an overview of which was given in Section 1.2.4, addresses the problem of how magnetic field is distributed in superconducting materials. Such an approach is not exclusive to superconductivity but can also be used to describe the physics of numerous other self-organized systems, such as sand piles, earthquakes or financial markets [118]. For instance, the vortex rearrangement upon an increase of the external magnetic field is similar to the reorganization of grains of sand that are deposited on top of a sand pile. In this context, the incoming amount of sand might force the slope of the pile to exceed a critical slope. The grains at the top of the pile are pulled downwards by gravity and rearrange until the slope is less than the critical value everywhere. These updates of the sand-pile structure occur in the form of several local sand avalanches that continue until an equilibrium is found where the slope of the pile is less than the critical slope. To this extent, it is worth noticing that the sand-pile equilibrium does not correspond to the lowest energy state, which is a flat surface where all the sand has spread over, but rather to a situation of local equilibrium where friction is balanced by gravity, which determines the critical slope. The analogy between the sand-pile problem and the penetration of vortices in superconductors is rather immediate if one relates the grains of sand to the vortices, the gravity to the Lorentz forces, and if the friction forces between the grains, which prevent them from further tumbling down the slope, are assimilated to the vortex pinning forces. The small and sometimes abrupt rearrangements of vortices are labelled under the name of dynamically driven flux avalanches, since they stem from the local balance between the opposing Lorentz and pinning forces and dissipate only low amounts of energy.

However, when temperature and thermal effects are taken into account, vortices might sometimes reorganize over larger length scales and smaller time scales. These kinds of avalanches are called thermally driven avalanches. The advent of thermally or dynamically driven events can be understood by comparing the magnetic and thermal diffusivity constants of the material. The magnetic diffusion constant assesses the ability of the

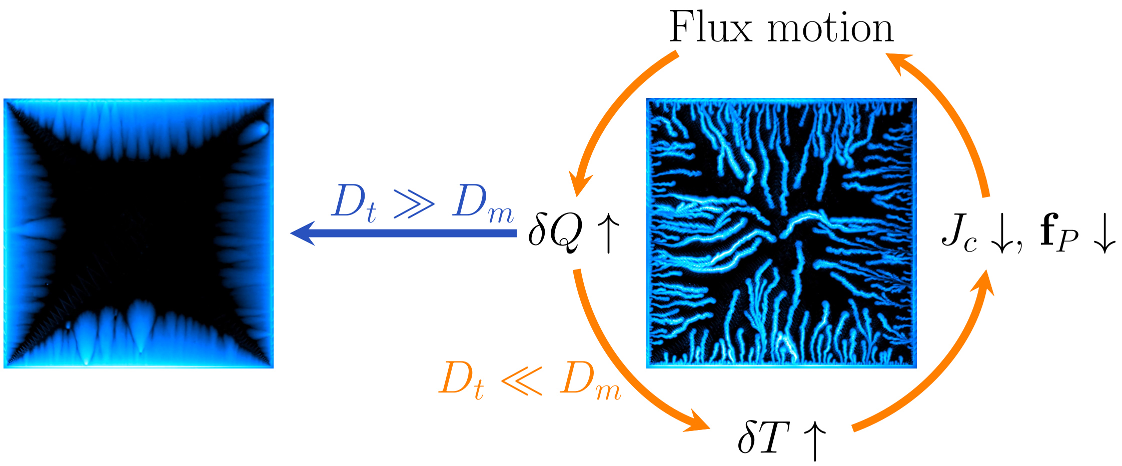

Figure 1.10: Illustrations of the dynamically driven and the thermally driven propagations of magnetic field inside a superconducting film. When heat is easily evacuated after a local generation of heat ($D_t \gg D_m$), magnetic flux penetrates smoothly in the sample. If heat cannot be removed efficiently ($D_t \ll D_m$), a positive feedback loop is initiated, leading to thermomagnetic avalanches. The magneto-optical images were provided with the courtesy of J. Brisbois and A. V. Silhanek.

material to smear a perturbation of magnetic nature. It is derived from Faraday's and Ohm's law and writes as

$$D_m = \frac{\rho_0}{\mu_0}, \tag{1.43}$$

with μ_0, the magnetic permeability, and ρ_0, the normal-state electric resistivity of the material. Similarly, the thermal diffusion constant, D_t, assesses the efficacy of the material to spread a thermal perturbation. It compares the heat conductivity of the material, κ_t, to the volumetric heat capacity, c_v, so that

$$D_t = \frac{\kappa_t}{c_v}. \tag{1.44}$$

If $D_t/D_m \gg 1$, heat diffuses much more rapidly than magnetic field. Each time vortices are set in motion, modifying the distribution of magnetic field, the heat generated by the motion of vortices is efficiently removed. Therefore, the superconducting properties remain stable, and one assists to a relatively smooth magnetic field penetration, such as showed in the left image of Figure 1.10.

By contrast, if $D_t/D_m \ll 1$, heat is smeared very slowly with respect to the motion of flux lines. As soon as vortices escape their pinning centres, the dissipated heat is not removed efficiently. As a result, a local heat excess, δQ, occurs and the resulting small temperature increase, δT, locally degrades the superconducting properties, such as the critical current density J_c and the pinning forces $\mathbf{f}_P$. This facilitates magnetic flux motion, which begets additional heat dissipation, degrading even more J_c and $\mathbf{f}_P$. A positive feedback loop is initiated and leads to the occurrence of extremely fast and sudden thermomagnetic flux avalanches, as illustrated in the rightmost picture of Figure 1.10. Eventually, these events stop spontaneously, since the Meissner currents that entail the motion of magnetic flux decrease when heat is released and temperature raises. In addition, as the large amount of vortices that contribute to the avalanche process is pushed forward, the flux gradient decreases close to the border of the sample. The incoming vortices end up being pinned again, which prevents further heat dissipation responsible for the onset of flux avalanches.

These thermally driven events are extremely deleterious to the superconducting sample, since they can locally elevate the sample temperature above T_c and completely suppress superconductivity there. This can damage the sample definitively [119]. Thermomagnetic avalanches events typically occur over a few nanoseconds and reach velocities that can go as high as 160 km/h [120]. They are also extremely erratic, are not triggered systematically at the same location along the border of the sample, while their number and morphology depend on the applied field and substrate temperature, T_0 [121, 122]. Following the same pedagogical incentive that motivated the analogy between sand piles and dynamically driven avalanches, thermodynamically driven avalanches can also be compared to other phenomena that can be observed in nature, such as snow avalanches or thunderstorms. Snow avalanches are triggered when the weight of the snow that has accumulated on a mountain flank is so high that a sudden release of this stacked up potential energy, which is converted into kinetic energy as snow tumbles down the slope, becomes inevitable. In the case of thunder, electric charges accumulate, building up large amounts of electrostatic energy, until a thunderous discharge unfolds, once the gradient of the electric potential reaches a critical threshold.

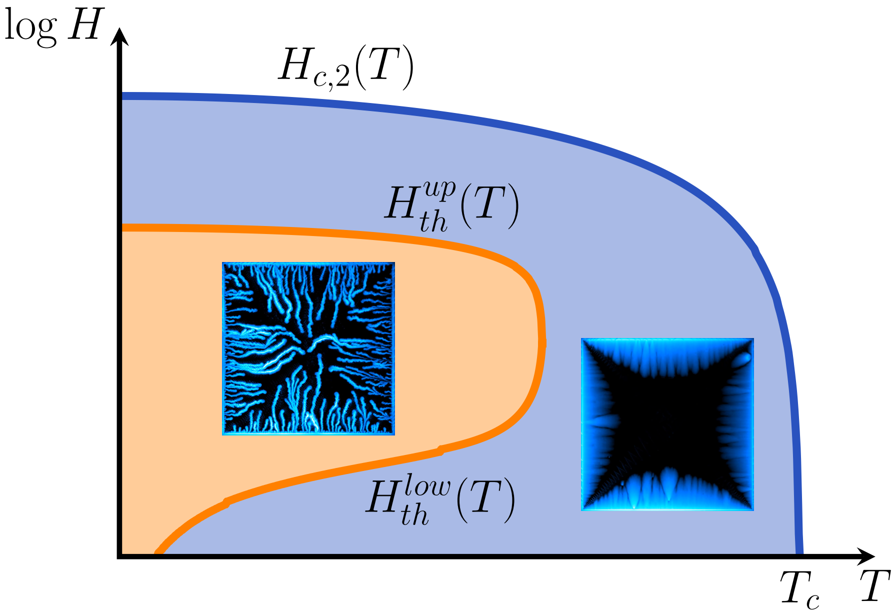

Figure 1.11: Threshold magnetic field for the onset of thermomagnetic avalanches, H_{th}, as a function of the temperature, T. The region of the H-T diagram where magnetic flux avalanches occur is delimited by an upper and a lower bound of H_{th}^{low} and H_{th}^{up}, respectively, and form a unique curve that is indicated in orange. Within the region coloured in cerulean, the magnetic field penetration is smooth, while flux avalanches occur in the orange region, see the insets. $H_{c,2}$ is indicated in cerulean for the sake of comparison and indicates the transition from the Shubnikov phase to the metallic phase. The magneto-optical images were provided with the courtesy of J. Brisbois and A. V. Silhanek.

From a more theoretical standpoint, the onset of avalanches has been extensively studied starting from a linear stability analysis of the coupled heat diffusion equation and the Maxwell equations, i.e.

$$\nabla \times \mathbf{H} = \mathbf{J} \tag{1.45}$$

$$\nabla \cdot \mathbf{B} = 0 \tag{1.46}$$

$$\dot{\mathbf{B}} = -\nabla \times \mathbf{E} \tag{1.47}$$

$$c_v \dot{T} = \nabla \cdot (\kappa_t \nabla T) + \mathbf{E} \cdot \mathbf{J}, \tag{1.48}$$

with the associated thermal boundary conditions, $(\kappa_t \nabla T) \cdot \mathbf{n} = h_0(T - T_0)$, where h_0 is the thermal heat exchange coefficient and $\mathbf{n}$ denotes the normal vector to the surface of the sample, and with $\mathbf{E}$ being related to $\mathbf{J}$ by Equation 1.33. This linear analysis of the propagation modes provides several threshold criteria for the onset of thermally driven events in bulks [123] and films [124, 125] and was successful in predicting the different morphologies of the thermally driven events [124]. In particular, for an infinitely long thin superconducting film of width W and thickness d, the threshold magnetic field that characterizes the onset of dendritic avalanches, H_{th}, is given by [126]

$$H_{th} = \frac{J_c d}{\pi} \operatorname{arccosh}\left(\frac{1}{1 - 2\ell_{th}/W}\right), \tag{1.49}$$

where

$$\ell_{th} = \frac{\pi}{2}\left(\sqrt{\frac{|\mathbf{E}| J_c}{\kappa_t T_{th}}} - \sqrt{\frac{2h_0}{nd\kappa_t}}\right)^{-1} \tag{1.50}$$

is the penetration length in the infinitely long strip just before the first avalanche is triggered, with n the flux-creep exponent from Equation 1.33. The parameters invoked in Equation 1.49 and 1.50 being temperature-dependent, Equation 1.49 provides a H-T curve for the onset of the first avalanche. In particular, there is an upper threshold for T, T_{th}, above which no avalanche can develop in the film, when the film is already fully penetrated, i.e. $\ell_{th} = W/2$. It is also worth mentioning that the linear analysis yields an onset electric field threshold, E_{th}, that is larger for bulks by several orders of magnitude than for thin films [124], which explains why thermomagnetic avalanches are much more frequent in the thin-film geometry. H_{th} as a function of T and the different morphologies of the magnetic field penetration are summarized on the H-T diagram in Figure 1.11.

1.4 Magneto-optical imaging

The experimental results which support the validity of the numerical modelling results exposed in this thesis were all obtained with the magneto-optical imaging (MOI) technique, which is a method that enables the in-situ visualization of the magnetic field distribution in a sample. The key idea behind MOI is to exploit the difference between the refraction indices of left- and right- circularly polarized light beams, n_L and n_R, respectively, that appears in circularly birefringent materials and results in a rotation of the polarization plane of the medium. This mismatch stems from the asymmetry of the unit cell of the material, which is intrinsic or can be induced by an external magnetic field. When the birefringence is induced by an external magnetic field, the medium is said to be Faraday-active. The magnetization of the material, $\mathbf{M}$, can be related to the phase shift according to [127]

$$\Delta\alpha_F = V(\omega) \int_{\mathcal{L}_o} \mu_0 \mathbf{M} \cdot \mathbf{dl}, \tag{1.51}$$

where $\Delta\alpha_F$ is the change of orientation of the polarization plane across the Faraday-active medium, $V(\omega)$ is the so-called frequency-dependent Verdet constant, and the integral is performed along the optical path taken by the light beam across the Faraday-active birefringent medium, $\mathcal{L}_o$.

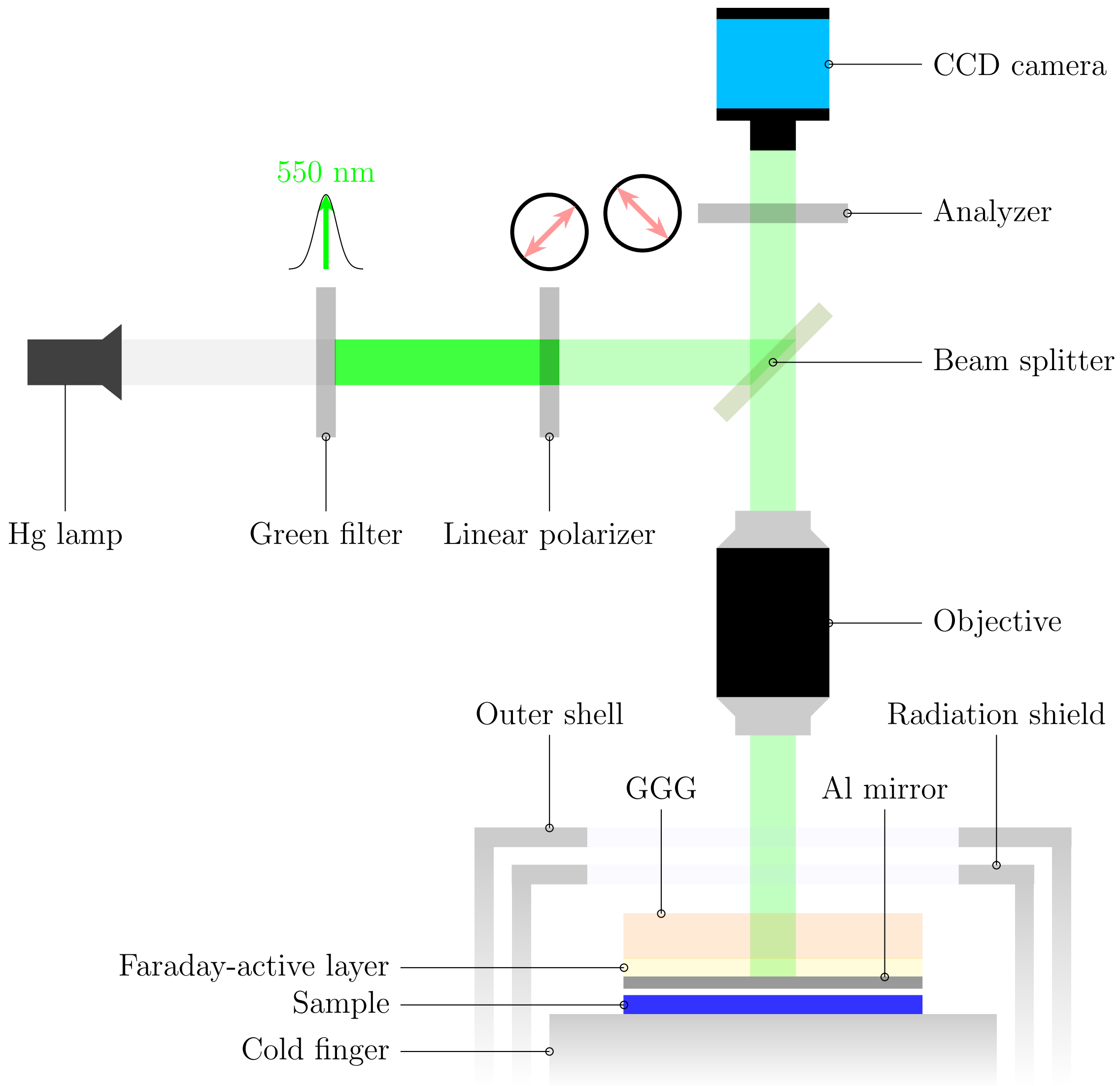

Figure 1.12: Front-view sketch of a magneto-optical imaging set-up. Non-polarized green light is extracted from a non-polarized natural light emitted from a Hg lamp. A linear polarizer selects a given polarization plane for the incident electric field, which is in turn deviated towards the Faraday-active layer placed in close proximity to the sample, within the cryostat. The changes of orientation of the polarization plane are recorded by the CCD camera, from which the magneto-optical images can be analysed afterwards.

An overview of the magneto-optical set-up is schematically depicted in Figure 1.12. Non-polarized green light is extracted from a non-polarized natural light source. A linear polarizer selects a given orientation of the polarization plane. The resulting beam then passes through a beam splitter that redirects it towards the Faraday-active medium placed on top of the superconducting sample. The reflected green light, which polarization plane orientation has changed under the effect of the Faraday-active layer, reaches the analyser, which is another linear polarizer. Its polarization plane is rotated by an $\pi/2$ angle with respect to polarization plane of the first linear polarizer, insofar that one wants the regions that were affected by the Faraday effect to stand out. Flux-free regions then appear pitch black, while regions where magnetic flux has penetrated are coloured in green, with an intensity that increases with the local field strength. The final luminous output signals are recorded by a high-resolution charge coupled device (CCD) camera, which provides the user with the experimental images of the magnetic field distributions. Since the magnetic landscapes are recorded with a high-resolution CCD camera, it allows for high-resolution imaging while covering a large field of view in comparison. For instance, the MOI can record samples that extend over several square millimiters, while offering a resolution that is as small as one micrometer. Being a non-destructive method that offers in-situ and real-time pictures, and being a particularly responsive technique [128, 129], the MOI is perfectly adapted for the visualization of extremely fast-paced dynamics, as in flux avalanches, or slower-paced magnetic field penetrations and the corresponding critical states in superconducting films [41, 46].

Several aspects can degrade the quality of the images collected with MOI. Thick garnets magnify the rotation of the polarization plane across the Faraday-active indicator, but this is done at the cost of a blurring of the images, since the polarization-plane rotation is an image of the mean magnetization across the Faraday-active indicator. Selecting a medium that optimizes the Verdet constant in the visible spectrum is thus paramount to recording qualitative images of the magnetic landscapes [130]. Besides, although the sensitivity of the technique is optimal at low applied fields, it decreases at fields that are of the same order of magnitude or larger than the anisotropic field [131]. It is also worth noticing that, because of the magnetic-field decay with the out-of-plane distance from the sample, the probed levels of magnetic field do not exactly correspond to those inside the film, even if the garnet is placed directly on top of the sample.

The magneto-optical garnet also highlights magnetic domains that progressively emerge upon magnetization and become visible on top of the magnetic landscapes that one actually wishes to visualize. These domains can be erased by applying an external in-plane field, at the expense of the sensitivity of the Faraday-active medium, while it can also impact the superconducting films due to extrinsic anisotropy, as discussed in Subsection **1.2.6**. Finally, a numerical post-processing procedure is needed to convert the qualitative light-intensity gradients into quantitative levels of magnetic field. The procedure is based on the combination of Malus' law and the magnetic-field-dependent Faraday phase shift that provides an essential relation between the incident light intensity and the local out-of-plane component of the magnetic field. Such a procedure is for instance detailed in [132]. The corresponding current density distribution can then be obtained from the magnetic field levels by inverting Biot-Savart law [133, 134]. Exact specifications about the instruments that were used in the MOI set-up of the Experimental Physics of Nanostructured Materials (Liège Université) group are also documented in [130, 132].

Chapter 2

Finite-element modelling of the magnetic field penetration in thin superconducting films with shell transformations

2.1 Introduction: A brief overview of the numerical modelling of high-temperature superconductors

The physics of electrodynamics in thin superconducting film being non-linear and non-local [117], numerical simulations are required to compute physical quantities that cannot be directly measured or to perform systematic parametric studies. Various complementary approaches shed light on different aspects of superconductivity. Its origin and inherent physical properties at the scale of the atoms can be evaluated with the help of the ab-initio formalism [135, 136] or in the framework of the BCS theory [65]. In the mixed state, the physics of superconductors is described by the dynamics of vortices, their interactions with neighbouring vortices, and the borders of the sample or defects. The time-dependent Ginzburg-Landau (tdGL) theory [137, 138] addresses the dynamic manifestations at the scale of a vortex. The fact that several millions of vortices might enter in a sample of realistic size requires a prohibitive amount of numerical resources for a single simulation. The behaviour of macroscopic samples can be modelled with less resources by solving Maxwell's equations. In that case, electromagnetic fields are averaged over the scale of several vortices. Superconductivity is then introduced by means of constitutive laws stemming from experimental observations or microscopic models and relating the different fields to each other, such as London's laws [51], critical model laws [81, 139, 140], surface barrier models [89, 90, 91], or the highly non-linear power law between **J** and **E** which is observed in transport measurements [100]. In the context of this thesis, since many experimental observations involve samples that typically extend over distances that range from a few hundreds of micrometers to a few millimeters, macroscopic models that rely on Maxwell's equations appear as natural candidates to model the penetration of magnetic field in thin superconducting films.

In the framework of the critical state model, analytical solutions of the magnetic field distribution in thin superconducting films exist, but only for a very restricted number of geometries, such as disks [113], strips [141], or ellipses [142]. For other geometries, numerical modelling is the only tool at disposal. When it comes to thin superconducting films, four main techniques have been exploited: integral methods, Fast Fourier Transform (FFT) methods, minimization techniques such as the Minimum Electro-Magnetic Entropy Production (MEMEP), and finite-element (FE) approaches.

In integral methods, the three-dimensional geometry of the film is simplified as a two-dimensional geometry by means of a thin-film approximation. The current density, $\mathbf{J}$, is assumed to be constant over the thickness of the sample and can consequently be replaced in Maxwell's equations by the sheet current density, $\mathbf{J}_s = \int_{-d/2}^{d/2} \mathbf{J}\,\mathrm{d}z = \mathbf{J}d$. An example of such contrivance is attributed to E. H. Brandt [143]. The method solves the coupling of Faraday's law with Biot-Savart law with respect to a scalar magnetization function, g, which is related to $\mathbf{J}_s$ as

$$\mathbf{J_s}(\mathbf{r}) = -\mathbf{e}_z \times (\nabla g(\mathbf{r}))\,, \tag{2.1}$$

where $\mathbf{r} = (x, y)$ are the in-plane coordinates and $\mathbf{e}_z$ points in the out-of-plane direction. Biot-Savart law is thereby tantamount to

$$\dot{g}(\mathbf{r}, t) = \int_{\Omega_c} Q^{-1}(\mathbf{r}, \mathbf{r}') \left[\frac{1}{\mu_0 d}\nabla \cdot [\rho(\mathbf{r}', t)\nabla g(\mathbf{r}', t)] - \dot{H}_a\right] \mathrm{d}\mathbf{r}', \tag{2.2}$$

with $Q^{-1}(\mathbf{r}, \mathbf{r}')$ being the inverse kernel, μ_0 is the vacuum magnetic permeability, $\dot{H}_a$ is the rate of variation of the applied field, and $\rho(\mathbf{r}', t)$ is the electrical resistivity given in Equation **1.33**. The integral is carried out over the superconducting film, which extends over a planar surface Ω_c. This model was successfully applied to thin films subjected to an external transverse field for various geometries such as plain square and rectangular samples [143], or square films with holes or slits that are required in flux-focusing geometries [144]. The method was also extended to the case of a finite London penetration length, λ [145], or to anisotropic current densities [95, 146, 147]. The computational complexity of the Brandt's method scales as $\mathcal{O}(N^2)$, with N being the number of degrees of freedom [148, 149]. In the context of this method, the conducting domain is generally meshed with regular grids, but it has also been extended to triangular meshes [150].

The FFT method is a straightforward variant of Brandt's method and has mostly been elaborated for modelling either thermomagnetic flux avalanches in thin superconducting films [119, 125] or smooth penetrations in two-dimensional or three-dimensional geometries [151, 152]. The core idea hence remains the same as in the integral method of Brandt, although the kernel inversion is carried out in the Fourier space. When the number of degrees of freedom equals a power of two, the FFT algorithm scales as $\mathcal{O}(N \log N)$ [149, 153]. However, the FFT also has its own challenges and limitations such as the complexity of implementing non-regular grids and the subsequent performance cost [154, 155, 156], the necessity of extending the domain beyond the boundary of the film and the associated treatment of the current-free regions [151, 152], the regularization of the kernel around $\mathbf{k} = \mathbf{0}$ [125, 151], or addressing the presence of holes in the superconductor and three-dimensional geometries [151].

The Minimum Electro-Magnetic Entropy Production (MEMEP), has been devised and applied to cubic and bulk superconductors [157, 158], stack of tapes [159, 160], coils and large magnets [161] or Roebel cables [162]. It consists in the minimization of the Euler-Lagrange functional describing Faraday's law, which gives the increment of magnetic field or current density at each time step [157]. It can be shown to be equivalent to the minimization of the entropy production in the system. Simulations are heavily sped up with the help of an algorithm performing an iterative parallelization by sector and accounting for the symmetry when possible. An adaptative time-step algorithm is also used for convergence. This approach has also been investigated in several other works in the context of the critical state [163, 164, 165, 166].

Last, the finite-element (FE) method consists in approximating the field as a linear combination of a finite set of M basis functions, whose coefficients become the unknowns of the problem. Furthermore, the simulated domain is partitioned in a finite number of smaller, non-overlapping, and generic building blocks, which are called elements. The basis functions are chosen in such a way that they are defined piecewise on every single element, so that the unknown field is locally approximated on each elementary subdomain with simple mathematical functions, such as polynomials. The coefficients of the linear combination are then computed by solving the weak form of the partial differential equation (PDE) that is addressed, which is tested against a set of M test functions. This amounts to solving an $M \times M$ matrix equation, for which the essential boundary conditions can be directly stipulated. Most of the time, the test functions are chosen to be the same as the basis functions. The motivation behind the FE method is two-fold. First, the $M \times M$ matrix that is assembled is sparse, and second, the method is very systematic and can be applied to a variety of meshes and very complex structures. The computational complexity of the FE method scales as $\mathcal{O}(N^\alpha)$, with $\alpha \in [1, 2[$ [150]. The FE method is thus a very versatile, efficient numerical scheme. It has been applied to a wide variety of situations and to numerous formulations, such as $\mathbf{H}$-formulation [36, 167, 168, 169, 170, 171, 172, 173, 174], $\mathbf{H}$-ϕ formulation [175, 176], $\mathbf{H}$-$\mathbf{A}$ formulation [177, 178], $\mathbf{A}$-V formulation [179, 180, 181, 182], $\mathbf{T}$ formulation [183], $\mathbf{T}$-Ω formulation [184, 185], $\mathbf{T}$-$\mathbf{A}$ formulation [186], $\mathbf{A}$-V-$\mathbf{J}$ formulation [187], $\mathbf{E}$ formulation [188] or even in the critical state [164, 189].

The FE method possesses several valuable attributes over other methods, which contribute to its versatility and popularity. For instance, it enables the refining of the mesh in the regions that require particular care, while relaxing the mesh elsewhere. This is of crucial importance for complex geometries, or if one needs to evaluate the behaviour of electromagnetic fields around structures that are much smaller than the size of the film, such as little holes or indentations. The other methods are mostly built for regular grids, and extending them to irregular ones or unstructured meshes does not always seem to be a trivial task, while the impact on the efficiency of the methods still needs to be elucidated.

The FE method also appear to be the most natural choice to simulate stacks of tapes. The FFT has been extended to the case of stacks of thin films by extending the Green's functions in the out-of-plane direction, which allows considering the influence of each film on all other ones, at the cost of extending the convergence issues for more closely packed stacks [152]. Similarly, Brandt's method would also need to be rewritten with these adapted Green's functions. As far as the MEMEP is concerned, the modelling of the non-conducting regions that separate the successive films has been addressed by means of a high spurious resistivity [160]. As a consequence of the uniform grid, if the spacing between the films is larger than the thickness of the films, many degrees of freedom are needed in the non-conducting regions. Besides, at the current state of the art, the FFT and the MEMEP are restricted to stacked tapes with identical cross sections. Finally, there exist numerous operational commercial or open-source FE softwares [190], such as ANSYS$^{\text{TM}}$, COMSOL$^{\text{TM}}$, GetDP [191], or FEMPAR [192], while the other methods consist in home-made codes that must be implemented from scratch. The advantages and the drawbacks of each technique are summarized in Table 2.1.

The numerical results of this thesis rely on the FE $\mathbf{H}$-ϕ formulation, which aims at evaluating the magnetic field, $\mathbf{H}$, from the weak form of Faraday's law, $\dot{\mathbf{B}} = -\nabla \times \mathbf{E}$. In order to solve this kind of problem, one can resort to h-conform or b-conform formulations. In h-conform formulations, $\mathbf{E}$ can be expressed in terms of $\mathbf{H}$ by combining Ampere's law and the constitutive law $\mathbf{E} = \rho(\mathbf{J})\mathbf{J}$, where ρ is the electrical resistivity, which is very low in superconductors. By contrast, b-conform formulations, among which the $\mathbf{A}$-V formulation, require the use of the electrical conductivity, $\sigma = 1/\rho$, which diverges when $\mathbf{E} \to \mathbf{0}$ in superconducting materials, and can be tricky to handle in some cases, especially when the magnetic field is on the verge of penetrating the sample [177]. Among the h-conform formulations, the $\mathbf{H}$-ϕ formulation uses the current-free property in the non-conducting region, $\mathbf{J} = \nabla \times \mathbf{H} = \mathbf{0}$, to imply $\mathbf{H} = \nabla\phi$, with ϕ being the magnetic scalar potential. Using ϕ instead of $\mathbf{H}$ in the non-conducting region has the merit of reducing the number of degrees of freedom with respect to the $\mathbf{H}$-formulation, which solves the problem with respect to the vectorial quantity $\mathbf{H}$, even in the non-conducting regions. Furthermore, the $\mathbf{H}$-ϕ formulation provides the user with a proper way to treat current-free regions, as there is no need to introduce some spurious resistivity such as in the $\mathbf{H}$-formulation.

In the context of the $\mathbf{H}$-ϕ formulation, a source of error of the three-dimensional FE method is the necessity to mesh a domain that extends beyond the conducting domain, since the essential boundary condition on the magnetic potential ϕ cannot be defined directly on its boundary. Ideally, the boundary condition $\phi = 0$ should be imposed at an infinite distance from the conducting regions. However, the simulated domain is of finite extension, so that a truncation error is inevitable. A rule of good practice is to mesh a domain that typically extends over more than five times the characteristic length of Ω_c, so that the effect of the finite extension of the domain is reduced as much as possible [193]. However, this leads to an increase of the number of degrees of freedom of the problem, hence longer simulations. Several options exist to overcome the issue of open boundaries in finite-element computations, such as mapped elements, iterative and integral numerical techniques, or hybrid methods [193, 194].

Among the possibilities that keep the assembled matrices sparse, infinite elements are an interesting option [195]. The key idea behind their use is to map the physical region of infinite extension into a shell of finite extension through a change of coordinates, hence the name of shell transformations. The outer infinite physical domain is mapped onto a finite region such as spherical or a truncated pyramidal shells. The boundary conditions are simply applied on the outer boundary of the shell.

In this chapter, the relevance, the efficiency and the accuracy of the shell-transformation approach for modelling the magnetic field penetration in thin superconducting films are tested against the usual truncated-geometry approach. The more classical spherical and truncated pyramidal shell transformations are considered, as much as the less common prismatic shell transformation. The idea that motivates the use of prismatic shells con-

Characteristics	Brandt	FFT	MEMEP	FEM
Mesh adaptability	2D regular grids / Triangular meshes [150]	2D regular or non-regular grids [154, 155, 156]	3D regular grids [157, 158, 160]	Fully adaptable meshes
Dedicated softwares	None	Open-source	Open-source	COMSOL™, GetDP [191], FEMPAR [192], ANSYS™
Mesh in the non-conducting regions	None	Yes	Partially [160]	Yes
Treatment of the non-conducting regions in stacks of tapes	3D Green functions	3D Green functions [152]	Spurious resistivity [160]	Spurious resistivity / Cohomology functions / **H**-ϕ formulation
Computational complexity	$\mathcal{O}(N^2)$ [149]	$\mathcal{O}(N \log(N))$ [149]	Unknown	$\mathcal{O}(N^\alpha)$, $1 \leq \alpha < 2$ [150]
Sparsity of the matrix	Full	Sparse	Full	Sparse

Table 2.1: Summary of the global characteristics of the diverse numerical techniques for modelling the penetration of magnetic field in superconducting films.

sists in reducing the extension of the non-conducting regions in the meshed domain, while ensuring that the boundary conditions are applied at an infinite distance from the conducting domains.

The chapter is structured as follows. Section **2.2** summarizes the formal concepts that are related to the finite-element method. In particular, the approximation spaces and the different formulations that can be exploited to solve eddy-current problems are described, among which the **H**-ϕ formulation. The strong form of the eddy-current problem with an appropriate set of constitutive laws for the superconductors in the mixed state is posed, and the corresponding weak form in the context of the **H**-ϕ formulation is derived from it. The linearisation of the non-linear **E**-**J** constitutive law and the time-discretization schemes that will be used throughout the numerical simulations are described as well. Section **A.1** of Appendix **A** further elaborates on the former point. Finally, a very general overview of how the finite-element method can be implemented from a weak formulation is recalled. Information about the test functions used in the **H**-ϕ formulation are then provided.

In Section **2.3**, the mathematical background about shell transformations is addressed. First, the sensitivity of the eddy-current distribution in thin superconducting films on the proximity of the boundaries of the truncated geometry is illustrated. Then, the main idea behind shell transformations is introduced, and mathematical details about the coordinate changes involved in spherical, truncated pyramidal, and prismatic shell transformations are given. A practical way to apply an external field of known distribution in a restricted domain despite the presence of the shell-transformation elements is mathematically derived.

Section 2.4 constitutes the core of this chapter. Emphasis is first put on the prismatic shell transformations, in the specific case of the magnetic field penetration inside a thin superconducting disk. The influence of the size of the shell region, which embeds the shell transformation, is illustrated by means of numerical simulations. A rationale for the choice of the shell size relies on the mathematical developments of Section B.1 of Appendix B. Then, a numerical investigation of the dependence of the quality of the finite-element scheme on the refinement of the mesh in the non-conducting region along the out-of-plane direction is carried out. This allows for the empirical determination of mesh parameters that achieve a good balance between accuracy of the numerical approximations and the computational cost. The computational complexity of the prismatic shell transformation with respect to the in-plane mesh quality is also investigated.

Afterwards, the various shell-transformation shapes are compared to the truncated geometry in terms of quality of the finite-element approximation and time performance. This comparison is done for thin disks, rectangular and square films, which are the film geometries that will be involved in the results of the following chapters. In Section B.2 of Appendix B, the results of Section B.1 of Appendix B are extended to the case of thin rectangular films of arbitrary in-plane aspect ratio. Throughout Section 2.4, the results are confronted to the analytical results of the critical state model or to the Brandt method, which serve as references to assess the quality of the finite-element approach.

Finally, Section 2.5 draws the main conclusions and further work that are brought up by this chapter.

2.2 The finite-element method

2.2.1 Strong form of the general eddy-current problem in the H-formulation

From a global standpoint, a magnetodynamic formulation consists in the simultaneous resolution of Faraday's law, Ampere's law, and Gauss's law, which are respectively

$$\dot{\mathbf{B}} = -\nabla \times \mathbf{E}, \tag{2.3}$$
$$\mathbf{J} = \nabla \times \mathbf{H}, \tag{2.4}$$
$$\nabla \cdot \mathbf{B} = \mathbf{0}, \tag{2.5}$$

with constitutive laws that relate $\mathbf{B}$ to $\mathbf{H}$ and $\mathbf{E}$ to $\mathbf{J}$, i.e.

$$\mathbf{B} = \mu \mathbf{H}, \tag{2.6}$$
$$\mathbf{E} = \rho \mathbf{J}, \tag{2.7}$$

where μ is the magnetic permeability and ρ is the electrical resistivity. Note that since the conductivity in superconductors is very large, the displacement current, $\dot{\mathbf{D}}$, is omitted in Equation 2.4 [196]. In addition to Equation 2.3, Equation 2.4 and Equation 2.5, one must also make sure that adapted boundary conditions are enforced on the boundary of the investigated domain to ensure the unicity of the solution. These boundary conditions involve one of the fields **B**, **E**, **H** or **J**, depending on the formulation that is used. For instance, in the so-called **H**-formulation, in the conducting regions, Equation 2.4 is substituted in Equation 2.3, so that, with the help of Equation 2.6 and Equation 2.7, one obtains

$$\frac{\partial}{\partial t}(\mu \mathbf{H}) + \nabla \times (\rho \nabla \times \mathbf{H}) = \mathbf{0}, \tag{2.8}$$

which only involves the magnetic field, **H**. In the non-conducting regions, which are current-free, one has instead

$$\nabla \times \mathbf{H} = \mathbf{0}. \tag{2.9}$$

Besides, in the non-conducting regions, combining Equation 2.5 and Equation 2.6 yields

$$\nabla \cdot (\mu \mathbf{H}) = 0. \tag{2.10}$$

In such a case, Equation 2.8, Equation 2.9, and Equation 2.10, with the appropriate associated boundary conditions, is the strong form of the magnetodynamic **H**-formulation. It is worth noticing that, although Equation 2.5 is not directly involved in Equation 2.8, Equation 2.3 implies

$$\nabla \cdot \dot{\mathbf{B}} = 0 \Rightarrow \nabla \cdot \mathbf{B} = C, \tag{2.11}$$

where C is a time-independent integration constant. Consequently, if one ensures $\nabla \cdot \mathbf{B} = 0$ as an initial condition, then Equation 2.5 is verified at all times in Ω.

2.2.2 Geometry of the magnetodynamic eddy-current problem

Next, the general strong form of the **H**-formulation is particularized to the case of the penetration of magnetic field inside a thin superconducting film subjected to a uniform applied magnetic field, $\mathbf{H}_a$, which is generated by some external sources. In the light of this, **H** can be decomposed into two contributions, i.e.

$$\mathbf{H} = \mathbf{H_a} + \mathbf{h}, \tag{2.12}$$

where **h** is the reaction field, i.e. the magnetic field that stems from the eddy currents induced in the conducting regions in response to $\mathbf{H}_a$.

The strong form of the magnetodynamic formulation is applied to a simulated domain of finite extension which is denoted by Ω, and which outer boundary is Γ. The vector field of the unitary normal to Γ and which points outwards is denoted by **n**. The conducting regions, which include the superconducting films, are denoted by Ω_c, which boundary is denoted by Γ_c. Finally, the non-conducting regions, which are by definition current-free, are denoted by $\Omega \setminus \Omega_c$ and will be assumed to be simply connected. In this case, Ampere's law, $\nabla \times \mathbf{h} = \mathbf{0}$, makes it possible to express the reaction field as the gradient of a magnetic scalar potential

$$\mathbf{h} = -\nabla \phi. \tag{2.13}$$

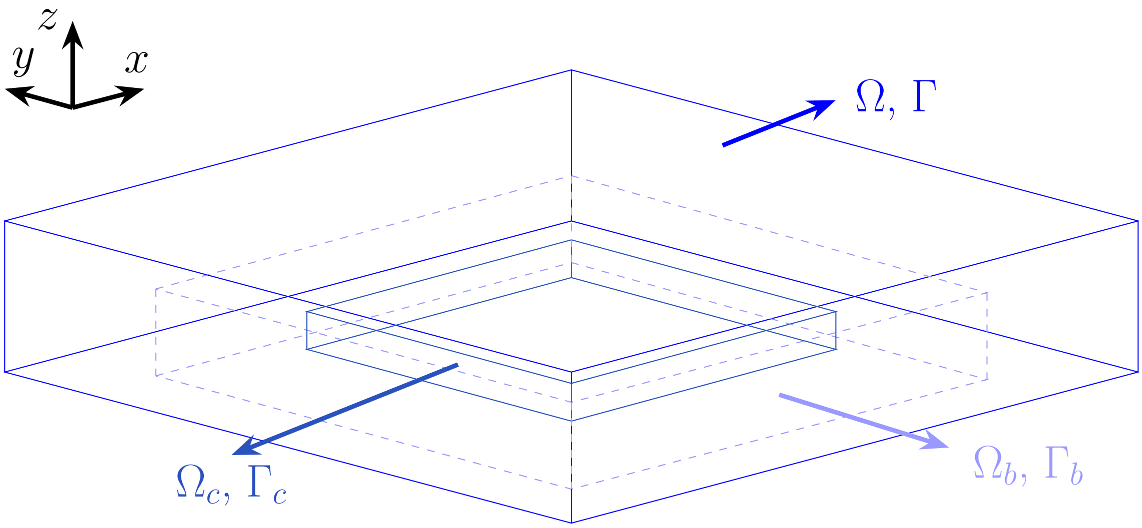

Figure 2.1: Definition of the different volumes and surfaces that are implied in the numerical $\mathbf{H}$-ϕ formulation. Ω, which appears in blue plain lines, corresponds to the simulated domain. Ω also includes the shell transformations, see Section **2.3**. Ω_c, which is delimited by the plain cerulean lines, corresponds to the conducting domain. Ω_b, which is the dotted box in light blue, is a domain of arbitrary shape, where the applied field will be forced to be uniform in the scope of this thesis, see Section **2.3.3**. The domain Ω_b is chosen such that $\Omega_c \subset \Omega_b \subset \Omega$. The boundaries of Ω, Ω_c, and Ω_b are denoted by Γ, Γ_c and Γ_b, respectively. In particular, the boundary conditions of the problem are set on Γ. The vector field of all the outward unitary normal vectors to Γ (resp. Γ_b) is denoted by $\mathbf{n}$ (resp. $\mathbf{n}_b$).

A schematic drawing of the different domains is shown in Figure 2.1. Now that the geometry of the problem has been formally introduced, the boundary condition associated to the **H**-formulation can be written explicitly as

$$\mathbf{n} \times \mathbf{h}|_{\Gamma} = \mathbf{0}. \tag{2.14}$$

In terms of ϕ, provided Equation **2.13** holds, Equation **2.14** automatically results from the essential boundary condition

$$\phi|_{\Gamma} = 0. \tag{2.15}$$

2.2.3 Constitutive laws in an isotropic superconductor

The constitutive laws, which were presented in their most general form with Equation **2.6** and Equation **2.7**, must be particularized to each medium or material that composes the system under scrutiny, Ω. In particular, different constitutive laws characterize the conducting domains, Ω_c, and the non-conducting ones, $\Omega \setminus \Omega_c$. If the latter domain is filled with a mix of cryogenic fluid, gas, or air, which are non-magnetic, one has

$$\mathbf{B} = \mu_0 \mathbf{H}. \tag{2.16}$$

If the conducting region consists in a superconductor in the mixed state, the effect of the surface barrier is neglected, and it is assumed that $H_{c,1} \ll |\mathbf{H}| \ll H_{c,2}$ [91, 197]. In this range of applied field, Equation 2.6 becomes

$$\mathbf{B} = \mu_0 \mathbf{H}, \tag{2.17}$$

where $\mu_0 = 4\pi \times 10^{-7}$ H/m is the vacuum magnetic permeability. Besides, the thermally activated flux-creep power law from Equation 1.33 is used

$$\mathbf{E}\left(|\mathbf{J}|\right) = \frac{E_c}{J_c}\left(\frac{|\mathbf{J}|}{J_c}\right)^{n-1}\mathbf{J} \equiv \rho\left(|\mathbf{J}|\right)\mathbf{J}, \tag{2.18}$$

with $E_c = 1$ μV/cm is the critical electric field, J_c is the current density and n is a dimensionless exponent. J_c can be either constant or magnetic-field-dependent, such as stated by Equation 1.25. Throughout the manuscript, the isothermal hypothesis is assumed, so that solving the heat equation is not required in the upcoming finite-element simulations.

2.2.4 The h-conform function spaces

This subsection is devoted to the definition of the functional spaces in which the electromagnetic fields belong. Maxwell's equations involve three key linear differential operators that will be used throughout the chapter: the gradient operator, grad, the curl operator, curl, and the divergence operator, div. For sufficiently smooth scalar (resp. vectorial) fields $f : \Omega \to \mathbb{R}$ (resp. $\mathbf{f} : \Omega \to \mathbb{R}^3$), which means that $f \in \mathrm{H}^1(\Omega)$ (resp. $\mathbf{f} \in \mathbf{H}^1(\Omega)$), where $\mathrm{H}^1(\Omega)$ (resp. $\mathbf{H}^1(\Omega)$) is the scalar (resp. vectorial) Sobolev space on Ω, these operators are defined as

$$\operatorname{grad} f = \nabla f = \left(\frac{\partial f}{\partial x}, \frac{\partial f}{\partial y}, \frac{\partial f}{\partial z}\right), \tag{2.19}$$

$$\operatorname{curl}\mathbf{f} = \nabla \times \mathbf{f} = \left(\frac{\partial f_z}{\partial y} - \frac{\partial f_y}{\partial z}, \frac{\partial f_x}{\partial z} - \frac{\partial f_z}{\partial x}, \frac{\partial f_y}{\partial x} - \frac{\partial f_x}{\partial y}\right), \tag{2.20}$$

$$\operatorname{div}\mathbf{f} = \nabla \cdot \mathbf{f} = \frac{\partial f_x}{\partial x} + \frac{\partial f_y}{\partial y} + \frac{\partial f_z}{\partial z}, \tag{2.21}$$

where x, y and z are the Cartesian coordinates of an orthonormal basis, and f_x, f_y and f_z are the three components of $\mathbf{f}$ along the x, y and z directions. The domain of definition of these operators are

$$\mathrm{H}\left(\mathrm{grad}, \Omega\right) = \{f \in \mathrm{L}^2\left(\Omega\right) ; \nabla f \in \mathbf{L}^2\left(\Omega\right)\}, \tag{2.22}$$

$$\mathrm{H}\left(\mathrm{curl}, \Omega\right) = \{\mathbf{f} \in \mathbf{L}^2\left(\Omega\right) ; \nabla \times \mathbf{f} \in \mathbf{L}^2\left(\Omega\right)\}, \tag{2.23}$$

$$\mathrm{H}\left(\mathrm{div}, \Omega\right) = \{\mathbf{f} \in \mathbf{L}^2\left(\Omega\right) ; \nabla \cdot \mathbf{f} \in \mathrm{L}^2\left(\Omega\right)\}, \tag{2.24}$$

where $\mathrm{L}^2(\Omega)$ (resp. $\mathbf{L}^2(\Omega)$) is the space of all scalar (resp. vectorial) fields that are square-integrable over Ω. The function spaces of each operator (Equation 2.22, Equation 2.23 and Equation 2.24) can further be limited to subspaces of functions that verify homogeneous essential boundary conditions, i.e.

$$\mathrm{F}_{\mathrm{h}}^0(\Omega) = \{f \in \mathrm{L}^2(\Omega); \nabla f \in \mathbf{L}^2(\Omega);\ f|_\Gamma = 0\}, \tag{2.25}$$

$$\mathrm{F}_{\mathrm{h}}^1(\Omega) = \{\mathbf{f} \in \mathbf{L}^2(\Omega); \nabla \times \mathbf{f} \in \mathbf{L}^2(\Omega);\ \mathbf{n} \times \mathbf{f}|_\Gamma = \mathbf{0}\}, \tag{2.26}$$

$$\mathrm{F}_{\mathrm{h}}^2(\Omega) = \{\mathbf{f} \in \mathbf{L}^2(\Omega); \nabla \cdot \mathbf{f} \in \mathrm{L}^2(\Omega);\ \mathbf{n} \cdot \mathbf{f}|_\Gamma = 0\}. \tag{2.27}$$

At this point, one can choose either h-conform or b-conform formulations, which determine which fields are approximated in the numerical scheme, while the remaining ones are accessible by means of the constitutive laws, although the functional spaces are not adapted to their rigorous description. In h-conform formulations, the fields **H** and **J** are approximated, while **B** and **E** are estimated with the constitutive laws. The core property of the h-conform formulations is to enforce the continuity of the tangential components of **H**. In b-conform formulations, **B** and **E** are approximated, while **H** and **J** follow from the constitutive laws. This time, it is the continuity of the normal component of **B** that is ensured. The h-conform formulations are more adapted to the modelling of magnetic field inside superconductors, because they involve the electrical resistivity, which is well behaved in the power-law model. By contrast, the b-conform formulations involve the electrical conductivity, which diverges at low electric fields, so that convergence may sometimes be compromised [177]. In h-conform formulations, $\phi \in \mathrm{F}^0_\mathrm{h}(\Omega)$, $\mathbf{h} \in \mathrm{F}^1_\mathrm{h}(\Omega)$ and $\mathbf{J} \in \mathrm{F}^2_\mathrm{h}(\Omega)$.

2.2.5 Weak form of the general eddy-current problem in isotropic superconductor in the mixed state

Now that adequate function spaces for the different fields have been defined, the generic weak form of a **H**-ϕ formulation is derived. For this purpose, Faraday's law is first multiplied by a vector test function, $\mathbf{\Psi}$. Here, the Galerkin method is carried out, and the test functions coincide with the basis functions that approximate the magnetic field. Consequently, $\mathbf{\Psi} \in \mathrm{F}^1_\mathrm{h}(\Omega)$. The resulting equation is then integrated over Ω, so that one gets

$$\int_\Omega \dot{\mathbf{B}} \cdot \mathbf{\Psi}\, \mathrm{d}\Omega + \int_\Omega (\nabla \times \mathbf{E}) \cdot \mathbf{\Psi}\, \mathrm{d}\Omega = 0. \tag{2.28}$$

Using the vectorial identity $\nabla \cdot (\mathbf{a} \times \mathbf{b}) = (\nabla \times \mathbf{a}) \cdot \mathbf{b} - \mathbf{a} \cdot (\nabla \times \mathbf{b})$, Equation 2.28 rewrites as

$$\int_\Omega \dot{\mathbf{B}} \cdot \mathbf{\Psi}\, \mathrm{d}\Omega + \int_\Omega \nabla \cdot (\mathbf{E} \times \mathbf{\Psi})\, \mathrm{d}\Omega + \int_\Omega \mathbf{E} \cdot (\nabla \times \mathbf{\Psi})\, \mathrm{d}\Omega = 0. \tag{2.29}$$

Using the divergence theorem on the second term of the left-hand side of Equation 2.29, one has

$$\int_\Omega \dot{\mathbf{B}} \cdot \mathbf{\Psi}\, \mathrm{d}\Omega + \int_\Gamma (\mathbf{E} \times \mathbf{\Psi}) \cdot \mathbf{n}\, \mathrm{d}\Gamma + \int_\Omega \mathbf{E} \cdot (\nabla \times \mathbf{\Psi})\, \mathrm{d}\Omega = 0. \tag{2.30}$$

Since $\Omega \setminus \Omega_c$ is simply connected and current-free, $\nabla \times \mathbf{\Psi} = \mathbf{0}$ in $\Omega \setminus \Omega_c$, and one can find a scalar test function, Φ, such that $\mathbf{\Psi} = -\nabla\Phi$, with $\Phi \in \mathrm{F}^0_\mathrm{h}(\Omega \setminus \Omega_c)$. As a result, the third integral term of Equation 2.30 can be restricted to Ω_c. Besides, the second integral of Equation 2.30 is zero. In fact, with the help of the vectorial identity $\mathbf{a} \times (\nabla b) = b(\nabla \times \mathbf{a}) - \nabla \times (b\mathbf{a})$, this surface integral can be transformed as follows

$$\begin{aligned} \int_\Gamma (\mathbf{E} \times \mathbf{\Psi}) \cdot \mathbf{n}\, \mathrm{d}\Gamma &= -\int_\Gamma (\mathbf{E} \times (\nabla\Phi)) \cdot \mathbf{n}\, \mathrm{d}\Gamma \\ &= \int_\Gamma (\nabla \times (\Phi\mathbf{E})) \cdot \mathbf{n}\, \mathrm{d}\Gamma - \int_\Gamma \Phi\, (\nabla \times \mathbf{E}) \cdot \mathbf{n}\, \mathrm{d}\Gamma. \end{aligned} \tag{2.31}$$

Yet, Stokes theorem applied on Γ, which is deprived of any boundary, implies that the first integral in Equation 2.31 is identically zero, while $\Phi|_\Gamma = 0$, so that the second integral in Equation 2.31 vanishes as well.

Furthermore, one can make use of Equation 2.12, with $\mathbf{H}_a \in \mathbf{L}^2(\Omega)$, which is uniform in Ω_c, and $\mathbf{h} \in \mathrm{F}^1_{\mathrm{h}}(\Omega)$ to recast Equation 2.30. Ultimately, using Equation 2.17, Equation 2.18, and $\nabla \times \mathbf{H}_a = \mathbf{0}$ in Ω_c, one obtains the weak formulation of Faraday's law for an isotropic superconductor in the mixed state

$$\int_\Omega \mu_0 \dot{\mathbf{H}}_a \cdot \mathbf{\Psi} \,\mathrm{d}\Omega + \int_\Omega \mu_0 \dot{\mathbf{h}} \cdot \mathbf{\Psi} \,\mathrm{d}\Omega + \int_{\Omega_c} \rho\left(|\nabla \times \mathbf{h}|\right)(\nabla \times \mathbf{h}) \cdot (\nabla \times \mathbf{\Psi}) \,\mathrm{d}\Omega = 0. \quad (2.32)$$

It is worth mentioning that Equation 2.32 solves Faraday's law in the weak sense only. Ampere's law, and consequently current conservation, is solved in the strong sense, while the current-free condition in $\Omega \setminus \Omega_c$ and the cancelling of the tangential components of $\mathbf{h}$ on Γ are enforced through the definition of the test functions. Also, this formulation is valid for any square-integrable $\mathbf{H}_a$ which is curl-free in Ω_c, and can be extended to other constitutive laws than Equation 2.18. Since Gauss's law results from Faraday's law, and since Faraday's law is solved in the weak sense only, Gauss's law is therefore solved in the weak sense at every time step if and only if the initial solution obeys Gauss's law.

2.2.6 The finite-element approximation in the framework of the H-ϕ formulation

Most of the time, finding an analytical expression that verifies the strong form of the **H**-formulation, see for instance Equation 2.8, Equation 2.9, Equation 2.10, Equation 2.12 and Equation 2.15, is impossible. The only way to gather enough insight about $\mathbf{h}$ is to make use of numerical methods, among which the finite-element (FE) method. It consists in a twofold discretization [196]. First, a geometric discretization is carried out and consists in systematically dividing Ω in the union of smaller entities of predicted shape, called elements. Such a geometrical partition, $\mathcal{M}$, is called a mesh of Ω, and any arbitrary element of $\mathcal{M}$ will be denoted by $\mathcal{K}$. In this work, three-dimensional geometries are considered, and the element shapes are limited to hexahedra, prisms, tetrahedra or pyramids. An illustration of each kind of element is sketched in Figure 2.2. Hexahedra result from the extrusion along the third dimension of two-dimensional quadrangular meshes. Prismatic elements are three-dimensional elements that are structured along one dimension and are used in the extrusion of unstructured two-dimensional meshes. Tetrahedra are used in fully three-dimensional unstructured meshes. Finally, pyramids allow for the junction between three-dimensional structured and unstructured meshes. In the thin-film geometry, because of the high aspect ratio L/d of the film, where L is the planar extension of the film and d is its thickness, meshing Ω_c with tetrahedra leads to very flat elements of poor quality. Structured meshes based on hexaedra and prisms were used instead. In $\Omega \setminus \Omega_c$, the mesh can either be progressively relaxed to an unstructured mesh, with the help of pyramidal elements in a transition layer, or remain structured.

The second discretization occurs in function spaces which are constructed in such a way that basis functions are defined piecewise on the geometric entity of every element of the mesh, i.e. the nodes, the edges, the facets and on the volume of each element. Restricting the support of given basis function to a given element and the neighbouring ones is a crucial attribute of the FE method, because the resulting matrix becomes sparse.

The nodes of $\mathcal{M}$ can be gathered in one set, $\mathcal{N}(\Omega)$, and are labelled n_i, with $i \in$

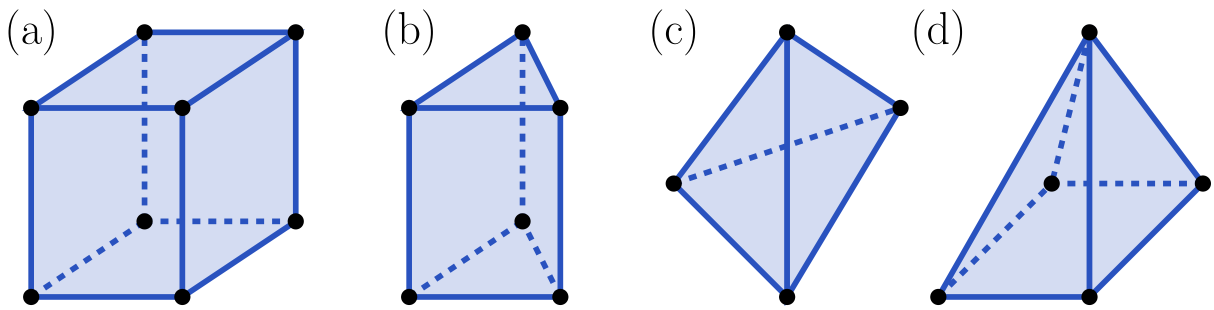

Figure 2.2: Sketch of different first-order elements, $\mathcal{K}$, which take the shape of (a) a hexahedron, (b) a prism, (c) a tetrahedron, and (d) a pyramid. Vertices are sketched as plain dark circles, edges are shown in cerulean, and the facets are coloured in light cerulean. Dashed cerulean lines are added for three-dimensional perspective.

$\{1, \cdots, \text{card}\,[\mathcal{N}(\Omega)]\}$. The set of all edges in $\mathcal{M}$ is denoted by $\mathcal{E}(\Omega)$ and each edge is given a unique label, e_{ij}, which corresponds to the edge linking the node n_i to the node n_j. In the context of the **H**-formulation, the reaction field $\mathbf{h} \in \mathrm{F}^1_\mathrm{h}(\Omega)$ in Equation 2.32 can thus be expressed as a linear combination of basis functions $\mathbf{s}_{ij} \in \mathrm{F}^1_\mathrm{h}(\Omega)$,

$$\mathbf{h} = \sum_{e_{ij} \in \mathcal{E}(\Omega)} h_{ij}\, \mathbf{s}_{ij}, \tag{2.33}$$

where the h_{ij} are the unknowns of the FE approximation. h_{ij} can be identified as the circulation of $\mathbf{h}$ along the edge e_{ij}

$$h_{ij} = \int_{e_{ij}} \mathbf{h} \cdot \mathbf{dl}. \tag{2.34}$$

However, the current-free property in $\Omega \setminus \Omega_c$ implies that the circulation on any closed path is zero, and global constraints between the coefficients h_{ij} in $\Omega\setminus\Omega_c$ must exist. These constraints can be resolved thanks to the magnetic scalar potential from which $\mathbf{h}$ derives in such a case, i.e. $\mathbf{h} = -\nabla\phi$, where $\phi \in \mathrm{F}^0_\mathrm{h}(\Omega \setminus \Omega_c)$. The circulation of $\mathbf{h}$ on any edge e_{ij} of $\Omega \setminus \Omega_c$ can in this case be written as

$$h_{ij} = \int_{e_{ij}} \mathbf{h} \cdot \mathbf{dl} = \phi_i - \phi_j, \tag{2.35}$$

where ϕ_i is the scalar magnetic potential at the node n_i. Accounting for Equation 2.35 and grouping all ϕ_{n_i} together, Equation 2.33 can be rewritten accordingly as

$$\mathbf{h} = \sum_{e_{ij} \in \mathcal{E}(\Omega_c)} h_{ij}\, \mathbf{s}_{ij} + \sum_{n_k \in \mathcal{N}(\Omega\setminus\Omega_c)} \phi_k\, \nabla s_k, \tag{2.36}$$

where the edges belonging to Γ_c are excluded from $\mathcal{E}(\Omega_c)$, while the nodes of Γ_c are included in $\mathcal{N}(\Omega \setminus \Omega_c)$, and the $s_k \in \mathrm{F}^0_\mathrm{h}(\Omega \setminus \Omega_c)$.

Furthermore, the essential boundary conditions are enforced through the degrees of freedom. For instance, in Equation 2.36, $\phi_k = 0$ for all nodes in Γ. Equation 2.36 corresponds to the FE approximation in the **H**-ϕ formulation. In comparison to the original

H-formulation, see Equation **2.33**, less degrees of freedom are allocated to the description of the magnetic field in $\Omega \setminus \Omega_c$ due to the scalar nature of ϕ, by contrast to the vectorial nature of $\mathbf{h}$ in the **H**-formulation [176, 177], which is advantageous.

Finally, one should keep in mind that if $\Omega \setminus \Omega_c$ is multiply connected, then $\nabla \times \mathbf{f} = \mathbf{0}$ does not systematically imply that $\mathbf{f}$ is equivalent to the gradient of a scalar potential. Nevertheless, a multiply connected domain can be transformed into a simply connected one by removing from the multiply connected space domain a set of N_h non-intersecting two-dimensional cuts, where N_h is the number of holes in the multiply connected domain [196, 198]. Equation **2.36** can be generalized to multiply connected geometries, by introducing additional basis functions that are associated to the cuts [199].

2.2.7 Basis functions

This subsection elaborates on the mathematical expression of the basis functions s_k and $\mathbf{s}_{ij}$ that appear explicitly in Equation **2.36**.

Nodal basis functions

The piecewise basis functions, which belong to $\mathrm{F}_\mathrm{h}^0(\Omega)$, are defined on each node n_i of every element $\mathcal{K}$ of the mesh of Ω, $\mathcal{M}$. To each node n_i is associated a nodal basis function, s_i, so that $n_i \in \mathcal{K}$. These nodal basis functions are defined in such a way that they equal 1 on the node n_i, and vary continuously across the element to reach 0 on all the other nodes $n_j \in \mathcal{K}$, $i \neq j$. This can be achieved with linear combinations of polynomials that depend linearly on the Cartesian coordinates. The element is then said to be of the first order. Similarly, it is possible to define higher-order elements, which will extend the polynomial basis to higher-order multi-variable polynomials.

Edge basis functions

Given an arbitrary domain Ω, $\mathbf{h}$ belongs to the function space $\mathrm{F}_\mathrm{h}^1(\Omega)$. The piecewise basis functions that are used on each element $\mathcal{K} \in \mathcal{M}$ also belong to the same functional space, $\mathrm{F}_\mathrm{h}^1(\Omega)$. They are defined on each edge of a given element, hence the name of edge basis function. The edge basis function that corresponds to the edge e_{ij} that is a part of a given element $\mathcal{K}$ is denoted by $\mathbf{s}_{ij}$ and is defined as [200]

$$\mathbf{s}_{ij} = s_i \operatorname{grad}\left\{\sum_{n_k \in \mathcal{N}_{i\bar{j}}} s_k\right\} - s_j \operatorname{grad}\left\{\sum_{n_k \in \mathcal{N}_{j\bar{i}}} s_k\right\}. \tag{2.37}$$

Edge functions thus involve nodal basis functions in such a way that the circulation along the edge e_{ij} in the element $\mathcal{K}$ equals ± 1 on the selected edge and 0 along all the other edges of $\mathcal{K}$, i.e.

$$\int_{e_{ab}} \mathbf{s}_{ij} \cdot \mathbf{dl} = \delta_{ab,ij}, \tag{2.38}$$

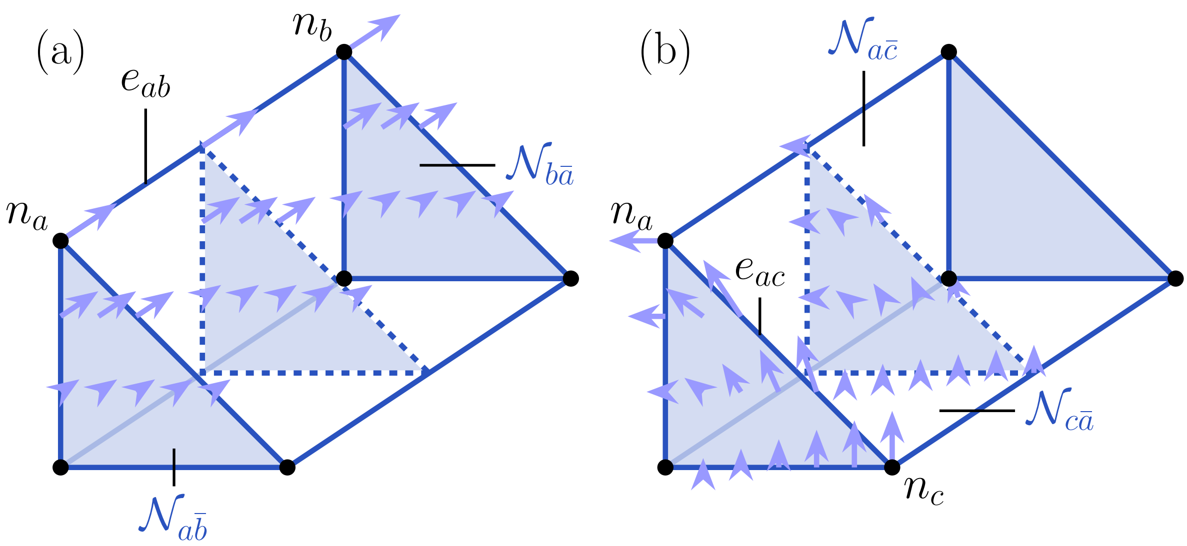

Figure 2.3: (a) Illustration of an edge basis function in a reference prismatic element. The shape of the edge function is drawn on three planes: the facets enclosed by the nodes in the sets $\mathcal{N}_{a\bar{b}}$ and $\mathcal{N}_{b\bar{a}}$, and an intermediate plane parallel to the triangular facets, which is outlined by the dashed line. $\mathcal{N}_{a\bar{b}}$ is the set of nodes that forms the facet containing the node n_a but not n_b. (b) Illustration of the edge basis function related to the edge e_{ac}.

with $\delta_{ab,ij}$ being the generalized Kronecker function that equals 1 if $a = i$ and $b = j$, -1 if $a = j$ and $b = i$, and 0 otherwise. The elementary vectorial field associated to a basis edge function that results from Equation 2.37 is shown in a prismatic element for two different edges in Figure 2.3.

2.2.8 Time discretization

Function spaces have been elaborated for $\mathbf{h}$ in Subsection 2.2.4 and the corresponding FE approximations have been introduced in Subsection 2.2.7. However, the second integrand in Equation 2.32 involves the time derivative of the reaction field, $\dot{\mathbf{h}}$, which must be discretized with respect to time. In terms of u, which is a linear form of $\mathbf{h}$, the weak form of Faraday's law takes the generic form $\dot{u} = F(u)$, which integration over time can be approximated as

$$\frac{u_{k+1} - u_k}{\Delta t} = rF(u_{k+1}) + (1-r)F(u_k), \tag{2.39}$$

where u_k is the evaluation of u at the current time, t, u_{k+1} is the evaluation of u at the next time, $t + \Delta t$, Δt is the time step, and r is a parameter between 0 and 1.

If $r = 0$, the right-hand side of Equation 2.39 only depends on u_k, and therefore only on the reaction field at the current time, $\mathbf{h}_k$. The time discretization is then said to be explicit. This approach is the most straightforward one, since it involves a direct evaluation of the non-linear electrical resistivity in Equation 2.32. However, explicit time discretization schemes are conditionally stable and Δt must be adapted to the mesh size. In the context of a diffusion problem, refining the mesh forces the time step to become prohibitively small, which is detrimental to the time efficiency of the FE method.

On the other hand, if $r > 0$, the right-hand side of Equation 2.39 also depends on u_{k+1}, and equivalently on the unknown, $\mathbf{h}_{k+1}$. In this case, the time discretization scheme is said to be implicit. In particular, if $r = 1$, the resulting method is better known as the Euler backward method, and if $r = 1/2$, Equation 2.39 yields the Crank-Nicolson implicit scheme. These two implicit methods possess an intrinsic advantage over explicit methods, due to their unconditional stability. However, a non-linear equation in $\mathbf{h}_{k+1}$ must be solved for each time level. Moreover, despite the absolute stability of the implicit scheme, the time-step value can still affect the quality of the numerical solution. In all results presented in this thesis, r is set to 1, which corresponds to the Euler backward method. Equation 2.32 then becomes

$$\begin{aligned}&\int_\Omega \frac{\mu_0}{\Delta t}\mathbf{h}_{k+1}\cdot\mathbf{\Psi}\,\mathrm{d}\Omega + \int_{\Omega_c} \rho\left(|\nabla\times\mathbf{h}_{k+1}|\right)(\nabla\times\mathbf{h}_{k+1})\cdot(\nabla\times\mathbf{\Psi})\,\mathrm{d}\Omega\\ &= \int_\Omega \frac{\mu_0}{\Delta t}\mathbf{h}_{k}\cdot\mathbf{\Psi}\,\mathrm{d}\Omega - \int_\Omega \mu_0\dot{\mathbf{H}}_a\cdot\mathbf{\Psi}\,\mathrm{d}\Omega. \end{aligned}\tag{2.40}$$

The well-posedness and the convergence of the FE method with a power law $\mathbf{E}(\mathbf{J})$ constitutive law and the backward Euler method is ensured [201, 202]. Implementing the Crank-Nicolson method might be an interesting idea to improve the accuracy of the solution for a given time step Δt, since the error is expected to scale as $\mathcal{O}(\Delta t^2)$, while the accuracy of the solution of backward Euler method scales as $\mathcal{O}(\Delta t)$ [201, 202, 203]. A more rigorous comparison between both methods could be investigated in further works.

2.2.9 Non-linear $\mathbf{E}(|\mathbf{J}|)$ and linearization with the Newton-Raphson algorithm

In order to use a fully implicit time discretization scheme as indicated in Equation 2.40, a non-linear equation must be evaluated at each time step to find $\mathbf{h}_{k+1}$. For this purpose, an iterative method is used to determine $\mathbf{J}_{k+1}$. The Picard's method is one possible way to cope with this. Here, ρ is evaluated for $\mathbf{J}^m_{k+1}$, so that

$$\mathbf{E}_{k+1} = \rho\left(\left|\mathbf{J}^{m+1}_{k+1}\right|\right)\mathbf{J}^{m+1}_{k+1} \approx \rho\left(\left|\mathbf{J}^{m}_{k+1}\right|\right)\mathbf{J}^{m+1}_{k+1},\tag{2.41}$$

where $\mathbf{J}^m_{k+1}$ is the result of the m-th iteration of the Picard's iterative loop that approximates $\mathbf{J}$ at $t+\Delta t$. Another method that can be used is the Newton-Raphson method, where $\mathbf{E}_{k+1}$ is estimated as a first-order Taylor expansion in $\mathbf{J}^m_{k+1}$ as

$$\mathbf{E}_{k+1} \approx \rho\left(\left|\mathbf{J}^{m}_{k+1}\right|\right)\mathbf{J}^{m}_{k+1} + \left.\frac{\partial\mathbf{E}}{\partial\mathbf{J}}\right|_{\mathbf{J}^m_{k+1}}\left(\mathbf{J}^{m+1}_{k+1} - \mathbf{J}^{m}_{k+1}\right).\tag{2.42}$$

Because of the vectorial nature of both $\mathbf{E}$ and $\mathbf{J}$, $\partial\mathbf{E}/\partial\mathbf{J}$ is a tensor, which expression for isotropic superconductors is given in Appendix A.

At each time step, whatever the selected iterative algorithm, the first guess $\mathbf{J}^0_{k+1}$ is estimated to be equal to $\mathbf{J}_k$. At each iterative step, $\mathbf{h}_{k+1}$ is replaced by $\mathbf{h}^{m+1}_{k+1}$ in Equation 2.40, and the difference between the right-hand side and the left-hand side of Equation 2.40 is then evaluated for every single test function. The Euclidean norm of the vector that gathers all these evaluations is then computed, and the result is called the residual of the iterative step. The iterative loop is repeated until the residual becomes less than an absolute criterion, ϵ_{abs}, or, when compared to the residual of the first iterative step, becomes less than a relative criterion, ϵ_{rel}.

It has been shown that the Picard's method is more efficient with concave constitutive laws, $\mathbf{J}(\mathbf{E})$, and the Newton-Raphson method is more adapted to convex constitutive laws, $\mathbf{E}(\mathbf{J})$, such as in Equation 2.18 [177]. Hence, Newton-Raphson is chosen to tackle the linearization process. Note that, despite the backward Euler method being unconditionally stable, the Newton-Raphson method still might converge slowly or even diverge if the estimate is too far from the expected solution, which might occur if Δt is too large. As a result, the choice of Δt and $\mathbf{J}^0_{k+1}$ still play an important role depending on the magnetodynamic problem [177]. A similar analysis to [177] for thin films subjected to a transverse field could be the topic of a further work.

2.3 Shell-transformation techniques

2.3.1 Influence of the proximity of Γ to Ω_c on the penetration of magnetic field in superconducting films

In Section 2.2, a general mathematical and formal overview of the FE method in the context of the $\mathbf{H}$-ϕ formulation has been detailed. The simulated domain, Ω, is of finite size and can take an arbitrary shape. In what follows, Ω consists in a large cubic box of side $2L_{ph}$. This configuration is referred to as the truncated geometry, because the scalar magnetic potential, ϕ, which is set to 0 on the nodes of Γ, cannot be imposed at an infinite distance from Ω_c, as it should theoretically be the case. Instead, $\phi|_\Gamma = 0$ at a finite distance L_{ph} of Ω_c because of the finite extension of Ω. This raises the question of the influence of the proximity of Γ on the eddy currents generated in Ω_c. The truncated geometry is illustrated on panel (d) of Figure 2.5.

In order to demonstrate the influence of the domain truncation, let us consider the penetration of magnetic field in a thin superconducting disk of radius $R = 141$ μm and thickness $d = 100$ nm that is submitted to a uniform out-of-plane applied field, $\mathbf{H}_a = H_a\hat{\mathbf{z}}$. In the simulations in the truncated geometry, the applied field is uniform in the whole domain Ω, and the applied field is ramped up from 0 at a constant rate $\dot{H}_a$ for a duration t_a. This configuration is referred to as the TD case. The geometrical and physical parameters of the simulations in the TD geometry can be found in the first column (TD) of Table 2.2, with the exception of L_{ph} that is allowed to vary in this subsection. In order to evaluate the accuracy of the truncated-box approach, we compare the FE simulations to the analytical distribution of the out-of-plane magnetic field, H_z, and the norm of the current density, $|\mathbf{J}|$, under the assumptions of the critical state model (CSM) in the thin-film approximation [113], as reminded by Equation 1.36 and Equation 1.37. In the TD geometry, the eddy currents flow azimuthally along circular paths and the current density and magnetic field distributions are independent on the azimuthal angle. The fields only vary as a function of the distance from the center of the film. Probing the profiles of H_z and $|\mathbf{J}|$ along a random radius and comparing the numerical results to the CSM is then enough to assess the validity of the numerical scheme in the TD case. In order to quantify how well the numerics replicate the expected analytical solution, the average absolute errors of H_z and $|\mathbf{J}|$ with respect to the CSM over the radius are computed, i.e.

$$\mathrm{MAE_H} = \frac{1}{N_R}\sum_{i=1}^{N_R}\left|\left[H_z\left(\frac{R}{N_R}i\right)\right]_{\mathrm{CSM}} - \left[H_z\left(\frac{R}{N_R}i\right)\right]_{\mathrm{FE}}\right|, \tag{2.43}$$

$$\mathrm{MAE_J} = \frac{1}{N_R}\sum_{i=1}^{N_R}\left|\left[|\mathbf{J}|\left(\frac{R}{N_R}i\right)\right]_{\mathrm{CSM}} - \left[|\mathbf{J}|\left(\frac{R}{N_R}i\right)\right]_{\mathrm{FE}}\right|, \tag{2.44}$$

where the radius of the disk is divided in N_R equidistant points. These absolute errors of $|\mathbf{J}|$ (resp. H_z) are then normalized with respect to J_c (resp. $J_c d$). It is also worth noting that $|\mathbf{J}|$ and H_z are evaluated from the linear curl-conforming test functions. This explains the continuous variations of H_z along the radius, while $|\mathbf{J}|$ varies discontinuously, as it will be shown below.

The H_z and $|\mathbf{J}|$ profiles along a radius of the disk are shown for L_{ph} as large as R, $2R$ and $10R$ in Figure 2.4. The geometric and physical parameters are summarized in the TD column of Table 2.2, with the exception of L_{ph} that varies. The mean absolute error on H_z decreases as L_{ph} increases, and is 2.4%, 1% and 0.8% of $J_c d$ when L_{ph} is R, $2R$ and $10R$, respectively. Similarly, the mean absolute error on $|\mathbf{J}|$ is 7%, 1.6% and 0.9% when L_{ph} is $R/2$, R, $2R$ and $10R$ respectively. In the light of the above results, it is clear that imposing the boundary conditions too close to Ω_c is detrimental to the quality of the FE solution. To overcome this issue, one can either consider a large value of L_{ph}, or consider shell transformations [195], which are investigated in the following subsections.

2.3.2 Parameters of the shell transformations

A shell transformation consists in a one-to-one map $\varphi : \mathbb{R}^3 \to \mathbb{R}^3$ of the points of a physical region, Ω_{ph}, onto a smaller one, Ω_{sh}, that is embedded in the simulated domain, Ω. Furthermore, a shell transformation not only maps the points of Ω_{ph} onto those of Ω_{sh}, it also maps the test functions that are used in the shell region, which usually are polynomials, into other functions that might be more suitable to interpolate the behaviour of the field. Shell transformations come in various shapes of Ω_{ph}, such as spherical shells, truncated pyramidal shells, or prismatic shells [195]. In what follows, these will be referred as spherical, trapezoidal and unidirectional shell transformations, respectively. These three kinds of shell transformations are sketched in two dimensions in Figure 2.5. From panel (a) to (c), the shape of Ω_{ph} and the corresponding Ω_{sh} onto which Ω_{ph} is mapped are illustrated for the three shell transformations. For each of them, φ transforms each of the coordinates X, Y, Z of $P' \in \Omega_{ph}$ into the coordinates x, y, z of $P \in \Omega_{sh}$. In the case of spherical and trapezoidal shell transformations, the change of coordinates, φ, follows the generic relations [195]

$$\begin{cases} X - X_O = F_\varphi(x,y,z)\ (x - X_O)\,, \\ Y - Y_O = F_\varphi(x,y,z)\ (y - Y_O)\,, \\ Z - Z_O = F_\varphi(x,y,z)\ (z - Z_O)\,, \end{cases} \tag{2.45}$$

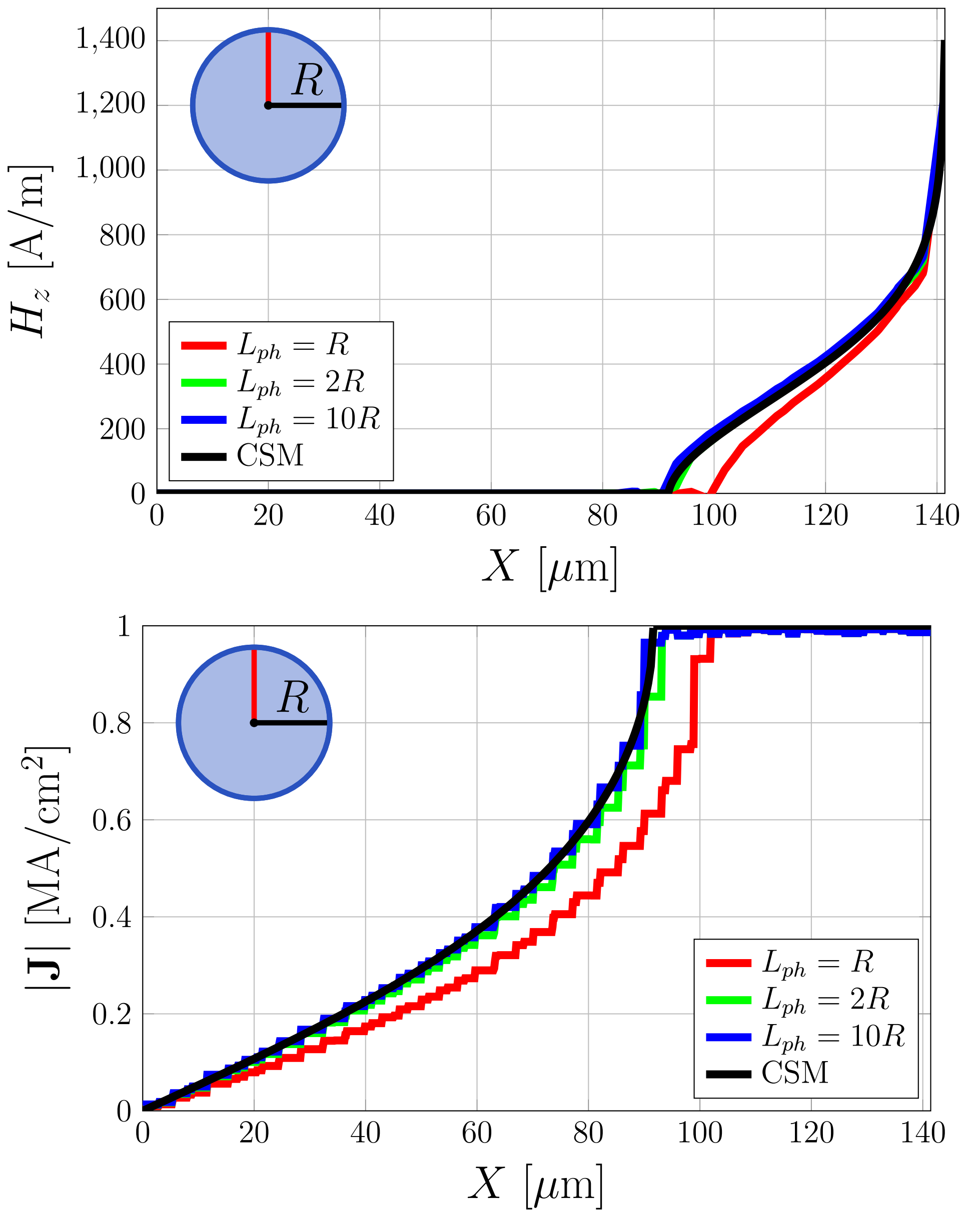

Figure 2.4: Out-of-plane magnetic field, H_z, and norm of the current density, $|\mathbf{J}|$, in a thin superconducting disk of radius $R = 141$ μm and thickness $d = 100$ nm in the case of a truncated geometry. The simulated domain corresponds to a cube of varying side $2L_{ph}$. The boundary conditions are thus applied at a finite distance from the film. The numerical results are taken along a radius of the disk and along the mid-plane cross section along the thickness. All the results are compared to the critical state model (CSM) analytical result within the thin-film approximation (in black).

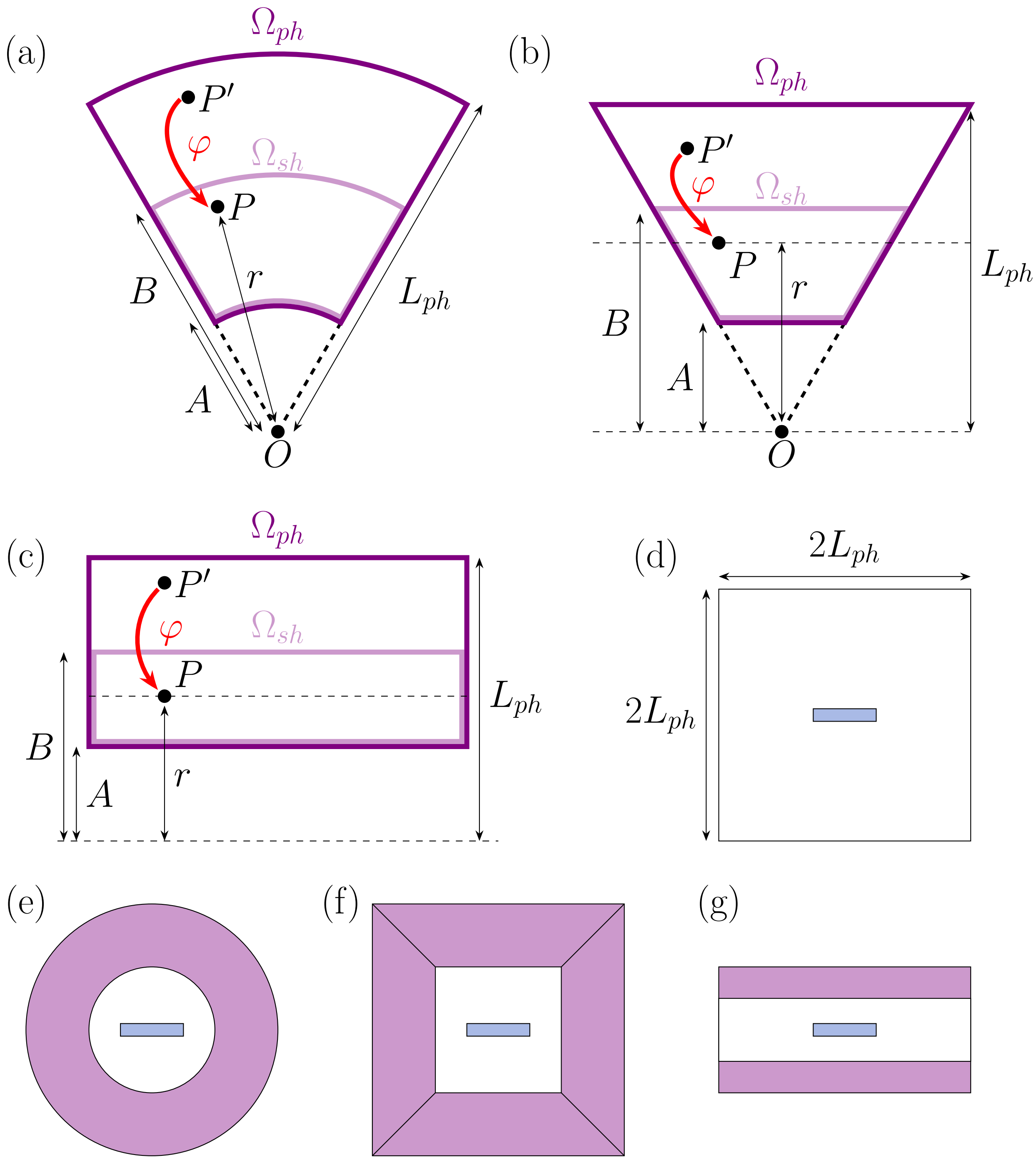

Figure 2.5: Drawing of (a) a spherical shell transformation, (b) a trapezoidal shell transformation, and (c) a unidirectional shell transformation. For the sake of clarity, all geometries have been sketched in two dimensions. A point P' in the physical region Ω_{ph}, which extends over a typical length $L_{ph} - A$, is mapped onto the point P in a shell region, $\Omega_{sh} \subset \Omega$, which characteristic length is given by $B - A$. The change of coordinates from Ω_{ph} to Ω_{sh} is characterized by the function φ. $r \in [A, B]$ is a parameter that is used to describe the mapping φ and is indicated for each shell shape. An illustration of a truncated geometry is also shown in panel (d). The location of Ω_{sh} in Ω is depicted for (e) a spherical shell, (f) a trapezoidal shell, and (g) a unidirectional shell. In panels (d) to (g), the light cerulean regions represent the conducting region, Ω_c, while the light violet regions represent Ω_{sh}. The boundary conditions are applied on the outermost boundary of Ω, and thus on the outermost boundary of Ω_{sh}.

where X_O, Y_O and Z_O are the coordinates of the fixed point of the shell transformation, see panels (a) and (b) in Figure 2.5, and where F_φ is equal to

$$F_\varphi(A,B,p,r) = \left(\frac{A(B'-A)}{r(B'-r)}\right)^p, \tag{2.46}$$

$$B' = \frac{L_0 B^2 - A^2}{L_0 B - A}, \tag{2.47}$$

$$L_0 = \left(\frac{L_{ph}}{B}\right)^{1/p}, \tag{2.48}$$

Whatever the shell configuration, the one-to-one mapping sends the shell Ω_{ph} of extension $L_{ph} - A$ to the shell of similar shape Ω_{sh} that extends over a distance $B - A$, with $B < L_{ph}$. The parameter r characterizes the distance from a point $P \in \Omega_{sh}$ to the fixed point O of the transformation, and its mathematical expression depends on the shape of the shell. For instance, in the case of spherical shell transformations, one has

$$r = \sqrt{(x - X_O)^2 + (y - Y_O)^2 + (z - Z_O)^2}, \tag{2.49}$$

while for trapezoidal shell transformations in the z direction, one has (it can be easily extended to the other principal directions x and y)

$$r = z - Z_O. \tag{2.50}$$

It is straightforward to see that A (resp. B) is the lower (resp. upper) bound of r. The parameter B' is a numerical parameter that takes into account the finite extension of Ω_{ph}. In particular, B' converges to B when $L_{ph} \to \infty$. Finally, the parameter $p > 0$ modifies the spatial dependence of the approximation space. Such a change is numerically implemented by the means of the Jacobian that results from Equation 2.45, $J_\varphi = \partial X_i / \partial x_j(x,y,z)$, with $X_i \in \{X, Y, Z\}$ and $x_j \in \{x, y, z\}$. It is also worth noting that in order to ensure the continuity of the metrics between the two coordinate systems, one must ensure that

$$\left.\frac{\partial X}{\partial x}\right|_{r=A} = \left.\frac{\partial Y}{\partial y}\right|_{r=A} = \left.\frac{\partial Z}{\partial z}\right|_{r=A} = 1 \tag{2.51}$$

which automatically holds when $B' = 2A$ [195].

As suggested by Equation 2.46, shell transformations interpolate fields that decay as Z^{-m} in Ω_{ph} with test functions that vary as $r^{m(p-1)}(B'-r)^{pm}$ in Ω_{sh}. Yet, far enough from the conducting region, the scalar magnetic potential is expected to decrease as Z^{-2}. Setting $p = 1$ in Equation 2.46 means that the far-field Z^{-2} of ϕ is mapped onto a parabolic function in Ω_{sh}. Since linear nodal test functions are used, this means that the parabola is approximated by piecewise linear test functions, which is a decent estimation, provided there are enough elements in Ω_{sh}.

In the case of a unidirectional shell transformation, which is illustrated in panel (c) of Figure 2.5, the one-to-one mapping remains the same as detailed previously for spherical and trapezoidal shells. For example, the mapping of a unidirectional shell transformation along the z direction is given as

$$\left\{\begin{array}{l} X = x, \\ Y = y, \\ Z - Z_O = F_\varphi(x,y,z)\ (z - Z_O), \end{array}\right. \tag{2.52}$$

with $F_\varphi(x, y, z)$ described by Equation 2.46, Equation 2.47, and Equation 2.48. However, there is no fixed point O in the unidirectional shell transformation. Instead, a reference plane is set at $z = Z_O$. This expression can be easily modified to consider unidirectional shell transformations along other directions, if needed. The previous remark about the continuity of the metrics, which is equivalent to $\partial Z/\partial z|_{z=A} = 1$, still holds, so that $B' = 2A$ and $p = 1$, and linear test functions can reasonably approximate the Z^{-2} dependence of the magnetic potential far from Ω_c.

2.3.3 Applying a uniform H_a in a domain of infinite extension

In the scope of this thesis, it is sought to simulate the response of thin superconducting films submitted to a uniform field, $\mathbf{H}_a$, which is directed in the out-of-plane direction to the cross section of the film, i.e. $\mathbf{H}_a = H_a\hat{\mathbf{z}}$, with H_a assumed uniform. In practice, such an $\mathbf{H}_a$ can be generated with a spherical assembly of coils with a current intensity varying as the sine of the elevation angle with respect to the plane perpendicular to the direction of the applied field [204]. In this case, the generated $\mathbf{H}_a$ is uniform across the sample under scrutiny, decays as a dipolar field outside this region of uniform field, and is divergence-free in Ω. Helmoltz coils could also be used to apply a uniform field in a restricted region of the three-dimensional space, before it decays far from the conducting regions. $\mathbf{H}_a \in \mathbf{L}^2(\Omega)$, and thus $\dot{\mathbf{H}}_a \in \mathbf{L}^2(\Omega)$ is also a prerequisite to the use of the weak form in Equation 2.32. Hence, if Ω extends to infinity along one direction, a uniform $\mathbf{H}_a$ over Ω is non-physical, since it does not take into account the inevitable decay of the magnetic field generated by a source. Even for finite Ω, forcing a uniform $\mathbf{H_a}$ everywhere in Ω is merely a convenient numerical approximation of an actual source delivering the applied field. A way to overcome the issue would consist in actually modelling the field source, at the cost of an increase of the number of unknowns of the problem. In what follows, another way to generate a uniform field, while ensuring that $\mathbf{H}_a \in \mathbf{L}^2(\Omega)$, is proposed.

In fact, one can rely on the divergence-free property of $\mu_0\mathbf{H}_a$ in $\Omega \setminus \Omega_c$ to recast the first term of Equation 2.32. To this aim, let us define an auxiliary closed domain, Ω_b, of arbitrary shape and which encloses Ω_c, as depicted in Figure 2.1. Its boundary is denoted by Γ_b and $\mathbf{n}_b$ is the outer unitary normal to Γ_b. Ω_b delineates the region where H_a is expected to be uniform. On the contrary, in $\Omega \setminus \Omega_b$, H_a is allowed to decrease at far distances from Ω_c. The first term of Equation 2.32 rewrites as

$$\int_\Omega \mu_0\dot{\mathbf{H}}_a \cdot \mathbf{\Psi}\, \mathrm{d}\Omega = \int_{\Omega_b} \mu_0\dot{\mathbf{H}}_a \cdot \mathbf{\Psi}\, \mathrm{d}\Omega + \int_{\Omega\setminus\Omega_b} \mu_0\dot{\mathbf{H}}_a \cdot \mathbf{\Psi}\, \mathrm{d}\Omega. \tag{2.53}$$

Given the current-free relation in $\Omega\setminus\Omega_c$, the properties of the function spaces $\mathrm{F}^0_\mathrm{h}(\Omega\setminus\Omega_c)$ and $\mathrm{F}^1_\mathrm{h}(\Omega\setminus\Omega_c)$, resulting to $\mathbf{\Psi} = -\nabla\Phi$, and the vectorial identity $(\nabla a)\cdot\mathbf{b} = \nabla\cdot(a\mathbf{b}) - a\,(\nabla\cdot\mathbf{b})$, the second integral of Equation 2.53 can be further modified

$$\begin{aligned}\int_{\Omega\setminus\Omega_b} \mu_0\dot{\mathbf{H}}_a \cdot \mathbf{\Psi}\, \mathrm{d}\Omega &= -\int_{\Omega\setminus\Omega_b} \mu_0\dot{\mathbf{H}}_a \cdot (\nabla\Phi)\, \mathrm{d}\Omega \\ &= \int_{\Omega\setminus\Omega_b} \Big(\nabla\cdot(\mu_0\dot{\mathbf{H}}_a)\Big)\, \Phi\, \mathrm{d}\Omega - \int_{\Omega\setminus\Omega_b} \nabla\cdot(\mu_0\dot{\mathbf{H}}_a\Phi)\, \mathrm{d}\Omega. \end{aligned}\tag{2.54}$$

The first integral cancels out because of the time derivative of Gauss's law, $\nabla\cdot(\mu_0\dot{\mathbf{H}}_a) = 0$. The divergence theorem can be applied to the second integral in such a way it becomes

$$\int_{\Omega\backslash\Omega_b} \nabla\cdot(\mu_0\dot{\mathbf{H}}_a\Phi)\,\mathrm{d}\Omega = \int_{\Gamma}\mu_0(\dot{\mathbf{H}}_a\cdot\mathbf{n})\Phi\,\mathrm{d}\Gamma - \int_{\Gamma_b}\mu_0(\dot{\mathbf{H}}_a\cdot\mathbf{n}_b)\Phi\,\mathrm{d}\Gamma. \tag{2.55}$$

The first integral of Equation 2.55 is zero because $\Phi|_\Gamma = 0$, and it immediately follows that Equation 2.54 is equivalent to

$$\int_{\Omega\backslash\Omega_b}\mu_0\dot{\mathbf{H}}_\mathbf{a}\cdot\mathbf{\Psi}\,\mathrm{d}\Omega = \int_{\Gamma_b}\mu_0(\dot{\mathbf{H}}_a\cdot\mathbf{n}_b)\Phi\,\mathrm{d}\Gamma. \tag{2.56}$$

Finally, substituting Equation 2.56 in Equation 2.53, one gets

$$\int_{\Omega}\mu_0\dot{\mathbf{H}}_a\cdot\mathbf{\Psi}\,\mathrm{d}\Omega = \int_{\Omega_b}\mu_0\dot{\mathbf{H}}_a\cdot\mathbf{\Psi}\,\mathrm{d}\Omega + \int_{\Gamma_b}\mu_0(\dot{\mathbf{H}}_a\cdot\mathbf{n}_b)\Phi\,\mathrm{d}\Gamma. \tag{2.57}$$

The first term of Equation 2.57 corresponds to the generation of a uniform field in the a restricted volume, while the second term ensures, through a surface integral, that $\mathbf{H}_a$ is square-integrable outside the box Ω_b. The most interesting feature that Equation 2.57 highlights is that the exact description of $\mathbf{H}_a$ is not needed outside Ω_b, where the field is non-uniform. This approach can be generalized to any $\mathbf{H}_a \in \mathbf{L}^2(\Omega)$ that is divergence-free and to any shape of Ω_b. Ultimately, using Equation 2.57, Equation 2.32 can be reformulated as

$$\begin{aligned}&\int_{\Omega_b}\mu_0\dot{\mathbf{H}}_a\cdot\mathbf{\Psi}\,\mathrm{d}\Omega + \int_{\Gamma_b}\mu_0(\dot{\mathbf{H}}_a\cdot\mathbf{n}_b)\Phi\,\mathrm{d}\Gamma\\ &+\int_{\Omega}\mu_0\dot{\mathbf{h}}\cdot\mathbf{\Psi}\,\mathrm{d}\Omega\\ &+\int_{\Omega_c}\rho\left(|\nabla\times\mathbf{h}|\right)(\nabla\times\mathbf{h})\cdot(\nabla\times\mathbf{\Psi})\,\mathrm{d}\Omega = 0.\end{aligned} \tag{2.58}$$

2.4 Analysis of the numerical performance of the shell transformations

2.4.1 Mesh for each shell transformation and truncated geometry

Now, let us evaluate the efficiency in terms of time performance and accuracy of the different shell transformations in comparison to the approach of truncating the physical domain. To this aim, the simulated response of a superconducting film to a uniform out-of-plane applied field will be investigated for the different shell geometries and for two types of thin films: a thin disk of radius R (TD) and a thin strip of width W and length L (TS). The results of the unidirectional shell transformation in a square film of side L (SF) will also be investigated later on, even though they will not be compared to the other shell geometries or to the truncation method. In each case, the thickness of the film is denoted by d. As mentioned in Subsection 2.3.1, the applied field is ramped from

0 for a duration t_a at a constant rate $\dot{H}_a$, so that the strength of the applied field reaches the value H_a. Panels (d) to (g) of Figure 2.5 show how the different regions of Ω are organized around Ω_c, which consists in the superconducting film with the desired cross section. Ω_c corresponds to the cerulean region on each of these panels. In panels (e), (f) and (g), Ω_{sh}, shown in light violet, is located at the periphery of $\Omega \setminus \Omega_c$ and is meant to be mapped onto a region of infinite extension in Ω_{ph}, i.e. $L_{ph} \to \infty$. The white regions match the subdomain in $\Omega \setminus \Omega_c$ where no jacobian shell transformation is applied to the elements contained in its interior. In the truncated geometry, L_{ph} is finite and the whole simulated domain extends over distances that are $50\sqrt{2}$ times larger than R in the TD configuration and 100 times larger than L in the TS configuration. In the TD geometry, the value of A is set to $2R$ for both the spherical and trapezoidal shell transformations, while A is set to $\sqrt{2}L$ in the TS geometry for the same two shell transformations. These values ensure that Γ is much closer to Ω_c than in the truncated geometry. In the case of the unidirectional shell transformation, the choice for A will be explained in Subsection **2.4.2**.

Because of the thin-film geometry, the mesh in Ω_c must be made of prisms or hexahedra to avoid very flat tetrahedra in Ω_c. Pursuing the same mesh quality requirements, the film cross section is also extruded above and below the film over a distance L_a, which is made of N_a layers. For all shell geometries and the truncated geometry, L_a is equivalent to the value of A for the unidirectional shell transformation. The in-plane extension of this box is set to 1.8 times R or $L/2$, depending on whether the TD or the TS case is considered. For the sake of comparison, this box is the same for the spherical shell, the trapezoidal shell, and the truncated geometry. By contrast, as far as the unidirectional shell geometry is concerned, since the shell transformation is only applied in the out-of-plane direction, the in-plane extension of Ω is limited to $5\sqrt{2}R$ and $5L$ in the TD and TS geometry, respectively. This is justified by the fact that ϕ mainly varies in the out-of-plane direction, so that a truncation along the in-plane direction does not influence much the solution in Ω_c.

The out-of-plane extension above and below the film in the interior of this structured box is thus the same in every shell configuration, the unidirectional one included. This structured-meshed box delimits Ω_b, where the applied field is assumed to be uniform when shell transformations are used, according to the developments of Subsection **2.3.3**. In the case of the truncated geometry, the applied field is uniform in the whole domain Ω. Yet, the structured-meshed box still exists and will still be referred to as Ω_b. The mesh and the geometry of $\Omega \setminus \Omega_c$ only differ outside Ω_b. As far as the spherical or trapezoidal shell transformations and the truncated geometry are concerned, whose meshes become unstructured outside Ω_b, the transition between the structured and the unstructured meshes is carried out by means of pyramidal elements. In the case of an out-of-plane unidirectional shell transformation, the mesh is fully structured in Ω, and Ω_{sh} starts directly after the N_a layers that lie above and below Ω_c. Ω_{sh} is then made of an extrusion of the same planar two-dimensional geometry over N_{sh} layers. The main geometrical, physical, and mesh parameters in each case are summarized in the TD, TS and SF columns of Table 2.2. The mesh is generated with Gmsh [205] and results from the Delaunay algorithm. The $\mathbf{H}$-ϕ formulation is implemented in the context of the FE method and solved in GetDP [191] on a CPU with an Intel Core i7 (3.6 GHz and 16 Gb RAM).

Parameter	TD	TS	SF
d (nm)	100	100	100
R (μm)	141	/	/
L (μm)	/	1200	200
W (μm)	/	400	/
Spherical: A (μm)	282	1700	/
Trapezoidal: A (μm)	282	1700	/
Unidirectional: A (μm)	32	80	25
Truncated: L_{ph} (cm)	1	1.2	/
N_a	3	3	3
N_{sh}	3	3	3
n	1000	1000	Var.
J_c (MA/cm^2)	1	1	1
$\dot{H}_a$ (kA/m.s)	1	1	1
t_a (s)	0.5	0.5	Var.

Table 2.2: Physical and numerical parameters for the simulation of magnetic field penetration in a thin superconducting disk (TD), thin superconducting strip (TS), and thin square film (SF). If a parameter is not relevant to the shape of the film under consideration, the entry is filled in with a slash. The abbreviation "Var." means that the parameters varies.

2.4.2 Determining the value of A in unidirectional shell transformations

First, let us focus on determining reasonable choices for the parameters that influence the quality of the FE approximation with a unidirectional shell transformation, namely, A, N_a, and N_{sh}. To this aim, the profiles of the out-of-plane component of the magnetic field, H_z, and the norm of the current density, $|\mathbf{J}|$, are compared to the analytical result of the critical state model (CSM), assuming the thin-film approximation, in a thin superconducting disk [113] (TD geometry). Because of the finite thickness of the simulated film and the finite value of n in Equation 2.18, one should expect some differences, even for very small mesh size and time steps. Nevertheless, n can be chosen to be very large, $n = 1000$, so that the deviations from the CSM results are expected to be small everywhere in the film. Given the large aspect ratio $R/d \sim 1000$, deviations in the magnetic field are expected close to the border, as H_z is expected to diverge in the thin-film approximation, whereas it should be cut off with a factor $\sim \log(R/d)$ for films of finite thickness [115, 116]. The mean absolute errors on H_z and $|\mathbf{J}|$ are inspected along a random radius of the disk, as already stipulated in Subsection 2.3.1.

Figure 2.6 shows H_z and $|\mathbf{J}|$ for different values of A in the TD configuration, when N_a and N_{sh} are both set to 3. While these values might appear rather small, the motivation behind such a choice will be given in Subsection 2.4.3. The mean absolute deviations of H_z and $|\mathbf{J}|$ from their CSM values are summarized in Table 2.3 and range from 0.6% of J_cd and 1.1% of J_c when $A = 40$ μm to 5.2% of J_cd and 2.3% of J_c when $A = 200$ μm. The former A-value is the optimal choice among the restricted number of investigated values of A. Too large or too small a value of A for given values of N_a and N_{sh} leads to a substantial underestimation of the magnitude of H_z and $|\mathbf{J}|$ in the film with respect to the CSM predictions, more specifically in the non-penetrated regions. In particular, the position of the flux front is sensibly underestimated. However, it appears that the value of A can still be chosen in a fairly large range, since the results from $A = 40$ to $A = 80$ μm are qualitatively very close to each other, as indicated by the mean absolute errors on H_z and $|\mathbf{J}|$, which remain nearly the same. It is also worth reminding that these observations are valid for the given values of $N_a = 3$ and $N_{sh} = 3$. The quality of the approximations is expected to improve as N_a and N_{sh} increase.

In order to motivate the selection of a reasonable value of A, one can for instance turn to the analysis of the out-of-plane dependence of the magnetic scalar potential in the TD geometry. Such dependence is shown on a logarithmic-scale plot in Figure 2.7, and stems from the analytical resolution of Biot-Savart law applied to the azimuthal current distribution that is established in a fully penetrated thin superconducting disk within the CSM formalism. The calculations on which this graph relies are detailed in Section B.1 in Appendix B. As one gets further from the film, ϕ varies in $\Omega \setminus \Omega_c$ from a finite value on the surface of the film, which is ϕ_0, to zero at an infinite distance from the conducting domain. The current loops that circulate in Ω_c affect the behaviour of ϕ in a region that is restricted to the immediate neighbourhood of the film. The region of space where the shape of the induced current loops in the superconducting film dictates the variations of ϕ is called the near-field region. At far distances, ϕ decreases as $\phi \sim Z^{-2}$, independent of the shape of the film. This is reminiscent of how the magnetic field and the associated scalar potential decay around a magnetic dipole, and this region will be referred to as the far-field region.

Given that one wishes to keep N_a and N_{sh} a small as possible, understanding why the choice of A is crucial to the quality of the solution becomes now clearer. In Equation 2.46, the value $p = 1$ enables a good approximation of the Z^{-2} decay of ϕ in the far-field region. On the one hand, if A is too small, the scalar potential that is evaluated in the shell region does not strictly vary as Z^{-2}, as a part of the near-field region is included in Ω_{ph}. A sufficiently large number of test functions is then required in the shell region to correctly estimate the variations of ϕ, which means increasing N_{sh}. On the other hand, if A is too large, part of the far-field region is contained in $(\Omega \setminus \Omega_c) \setminus \Omega_{sh}$, where the test functions are linear, and thus do not approximate well the Z^{-2} decay. A solution in Ω_c of good quality then requires to increase the number of layers N_a. Opting for an intermediate value of A allows one to delimit a region where ϕ varies smoothly when $Z < A$, which can be faithfully approximated by a few linear test functions, while approximating the Z^{-2} behaviour with the mapped test functions for $Z > A$ with only a few layers in Ω_{sh}. Of course, it is also possible to increase either N_a or N_{sh}, at the cost of an increase of the number of DOF. A pragmatic, but arbitrary, choice consists in choosing A such that ϕ is divided by a factor 2 with respect to the value of the scalar potential on the surface of the superconductor, ϕ_0, as illustrated in Figure 2.7.

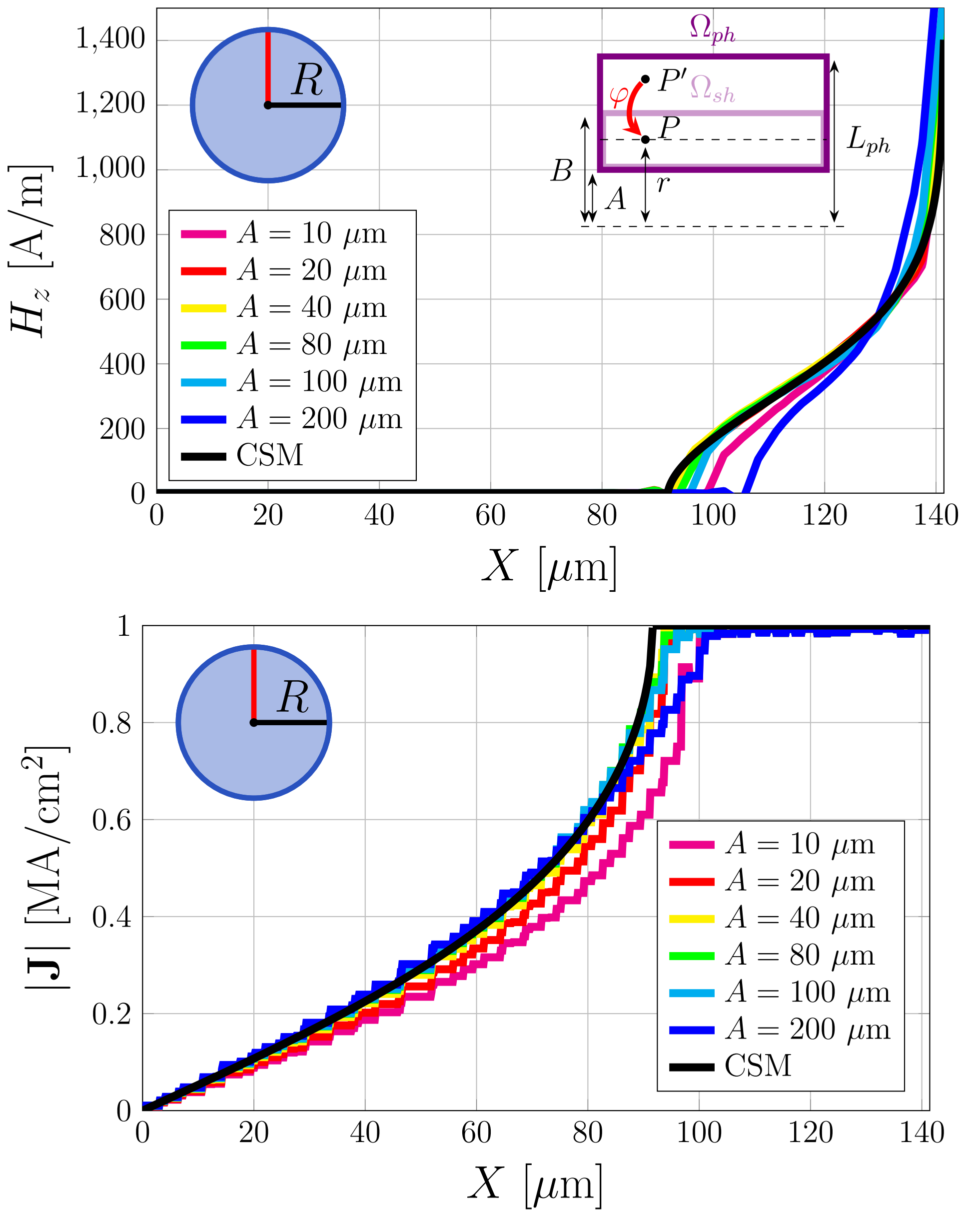

Figure 2.6: Out-of-plane component of the magnetic field, H_z, and norm of the current density, $|\mathbf{J}|$, in a thin superconducting disk of radius $R = 141$ μm and thickness $d = 100$ nm for different values of A. The numerical results are taken along the radius of the disk, and along the mid-plane cross section along the thickness, as depicted in the inset. All results are compared to the analytical result of the critical state model in the thin-film approximation (in black).

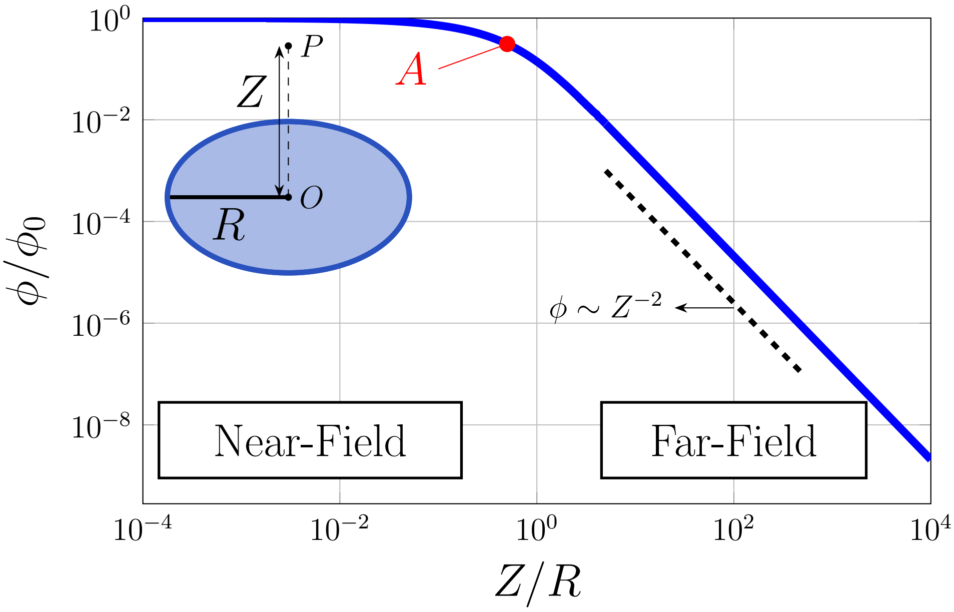

Figure 2.7: ϕ/ϕ_0 as a function of Z/R, the out-of-plane distance from a fully penetrated thin superconducting disk of radius R and thickness d, on a logarithmic-scale plot. ϕ_0 is the scalar magnetic potential on the surface of the film. The red circle indicates the value of A for which $\phi/\phi_0 = 1/2$. One finds $A \approx 0.23\,R$. The near-field and the far-field regions are also roughly indicated. The dashed line is a guide for the eye which emphasizes a Z^{-2} dependence to which the far-field ϕ corresponds. O is the origin of an orthonormal basis that is used in the analytical developments of Section **B.1** in Appendix **B**.

A (μm)	N_a	N_{sh}	DOF	Wall time (min)	Error $\|\mathbf{J}\|$	Error H_z
10	3	3	104825	168	5.8%	1.7%
20	3	3	104825	167	2.8%	0.6%
40	2	3	88220	124	1.4%	1.2%
40	3	1	71603	84	3.4%	1.1%
40	3	2	88220	124	1.9%	0.7%
40	3	3	104825	168	1.1%	0.8%
40	3	4	121456	225	0.9%	0.9%
40	3	5	138704	299	0.8%	0.9%
40	3	10	221164	948	0.8%	1%
40	4	3	121456	224	1.1%	0.7%
40	5	3	138704	297	1.1%	0.7%
40	10	3	221164	947	1.1%	0.7%
80	3	3	104825	167	1%	1.2%
100	3	3	104825	168	1.2%	1.6%
200	3	3	104825	169	2.3%	5.2%

Table 2.3: Accuracy and time performance of the unidirectional shell transformation for different values of A, N_a and N_{sh} in the thin disk geometry.

2.4.3 Determining the values of N_a and N_{sh} in unidirectional shell transformations

In the light of the results of Subsection 2.4.2, the value of A has been set to an intermediate value that lies between the near-field and the far-field region. However, as it has already been discussed, this means that ϕ does not exactly evolves as Z^{-2} in Ω_{ph} and several layers in Ω_{sh} might be necessary to obtain an accurate approximation of ϕ hence a correct evaluation of the magnetic field in Ω_{sh}. Since the structured nature of the mesh implies that the in-plane mesh in Ω_{sh} is the exact replication of the in-plane mesh in Ω_c, increasing the number of layers N_{sh} might rapidly increase the number of elements in the non-conducting regions to levels that are prohibitive in practice. One may seek to determine the minimal value N_{sh}, so that the quality of the solution in Ω_c is preserved. To this aim, the profiles of H_z and $|\mathbf{J}|$ in the TD situation are plotted along the radius for various N_{sh}. A is set to 40 μm. The results of the FE method are shown in Figure 2.8 and are compared to the CSM. Details about the mean absolute errors, the number of DOF and the duration of the simulations are mentioned in Table 2.3. As N_{sh} increases, the profiles of H_z and $|\mathbf{J}|$ are closer to the predictions of the CSM. The mean absolute errors vary from 1.1% of J_cd and 3.4% of J_c when $N_{sh} = 1$ to 0.7% of J_cd for $N_{sh} = 2$ and 0.8% of J_c for $N_{sh} = 10$. Meanwhile, the number of DOF increases, which manifests as an increase of the duration of the simulations, expressed in minutes. However, once $N_{sh} \geq 3$, the results for both H_z and $|\mathbf{J}|$ do not significantly vary. The mean absolute error on H_z is less than 1% of J_cd, while the mean absolute error on $|\mathbf{J}|$ becomes less than 1% of J_c as well. Taking $N_{sh} = 3$ appears to be a reasonable choice of N_{sh}, when $N_a = 3$, which simultaneously limits the number of DOF in $\Omega \setminus \Omega_c$, while ensuring that the approximation error on $|\mathbf{J}|$ remains around 1%.

Similarly, let us investigate the impact of the value of N_a while keeping $N_{sh} = 3$. The associated H_z and $|\mathbf{J}|$ profiles are compared to the results of the CSM and shown in Figure 2.9. The mean absolute errors on H_z and $|\mathbf{J}|$ and the duration of the simulations are gathered in Table 2.3. Similarly to Figure 2.8, increasing the value of N_a enhances the quality of the FE approximation. This is assessed by the mean absolute errors on $|\mathbf{J}|$ and H_z, which range from 1.4% of J_c and 1.2% of J_cd respectively for $N_a = 2$ to 1.1% of J_c and 0.7% of J_cd respectively when $N_a = 10$. Increasing either N_{sh} or N_a has the merit of improving the FE approximation close to the flux front mostly. Increasing the value of N_a also seems to reduce the level of H_z close to the boundary of the sample, while changing N_{sh} leaves this value nearly unaffected. Refining the mesh close to the film is responsible for a better approximation of ϕ in this region, so that it is not surprising that N_a influences more H_z in the vicinity of the thin-disk circumference. Once again, referring to the results gathered in Table 2.3, for $N_{sh} = 3$ and $N_a \geq 3$, the mean absolute errors on $|\mathbf{J}|$ and H_z does not vary, so that choosing $N_a = 3$ and $N_{sh} = 3$ simultaneously seems to be the best compromise that ensures a good quality of the FE simulations, while keeping the number of DOF as low as possible.

Also, note that increasing N_{sh} while keeping N_a fixed does not lead to a monotonic reduction of the mean error on H_z, see Table 2.3. The solution to which the FE scheme converges might differ from the analytical result of the CSM, because ϕ in Ω_b is only approximated by $N_a = 3$ layers. Similarly, if N_a (resp. N_{sh}) increases while $N_{sh} = 3$ (resp. $N_a = 3$) is kept constant, the errors do not tend to zero. Several factors may

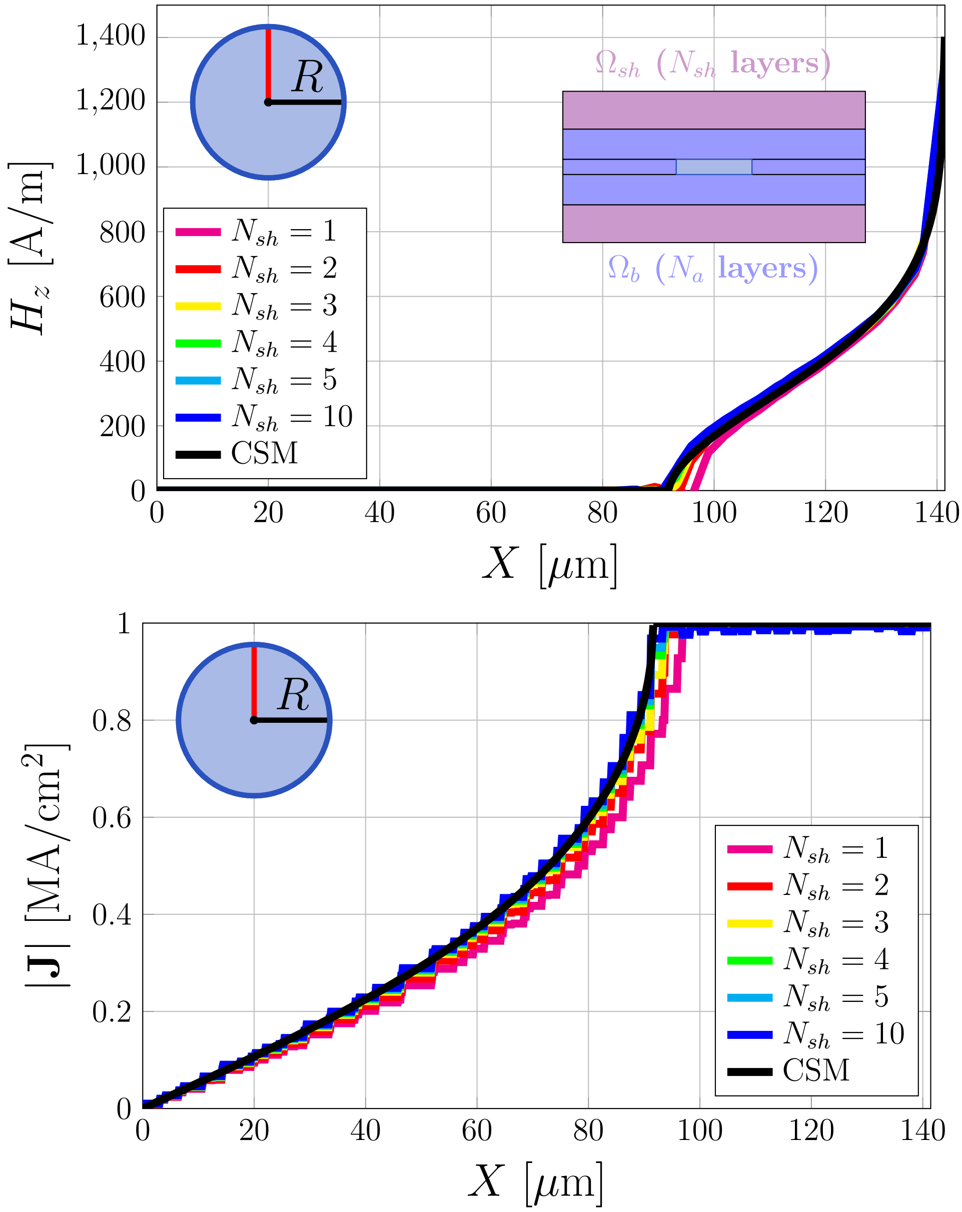

Figure 2.8: Out-of-plane magnetic field, H_z, and norm of the current density, $|\mathbf{J}|$, in a thin superconducting disk of radius $R = 141$ μm and thickness $d = 100$ nm for different values of N_{sh}, the number of layers in the shell domain, Ω_{sh}, for $N_a = 3$. The numerical results are taken along the radius of the disk, and along the mid-plane cross section along the thickness, as depicted in the inset. All results are compared to the analytical result of the critical state model in the thin-film approximation (in black).

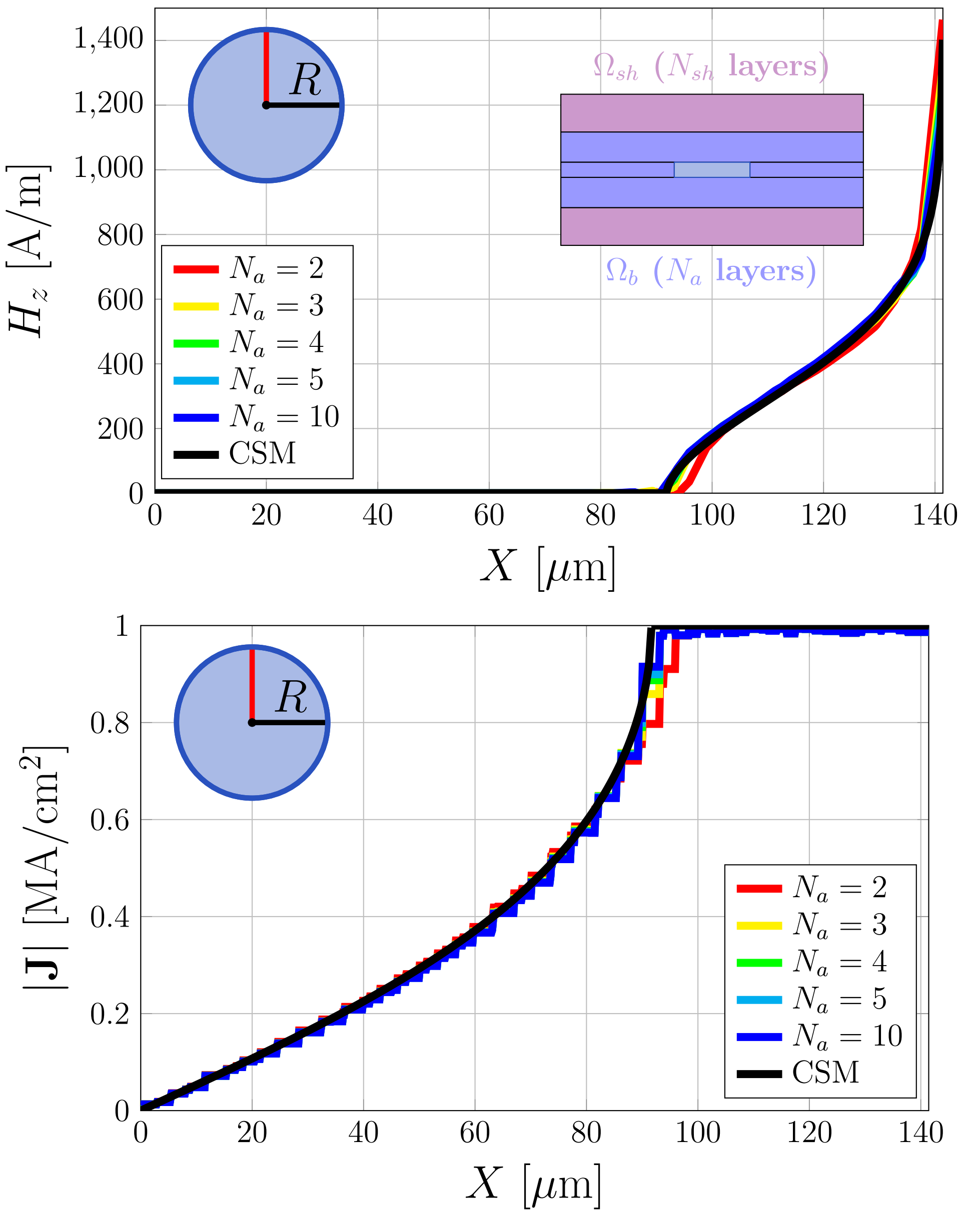

Figure 2.9: Out-of-plane magnetic field, H_z, and norm of the current density, $|\mathbf{J}|$, in a thin superconducting disk of radius $R = 141$ μm and thickness $d = 100$ nm for different values of N_a, the number of layers in Ω_b above and below the superconducting film, for $N_{sh} = 3$. The numerical results are taken along the radius of the disk, and along the mid-plane cross section along the thickness, as depicted in the inset. All results are compared to the analytical result of the critical state model in the thin film approximation (in black).

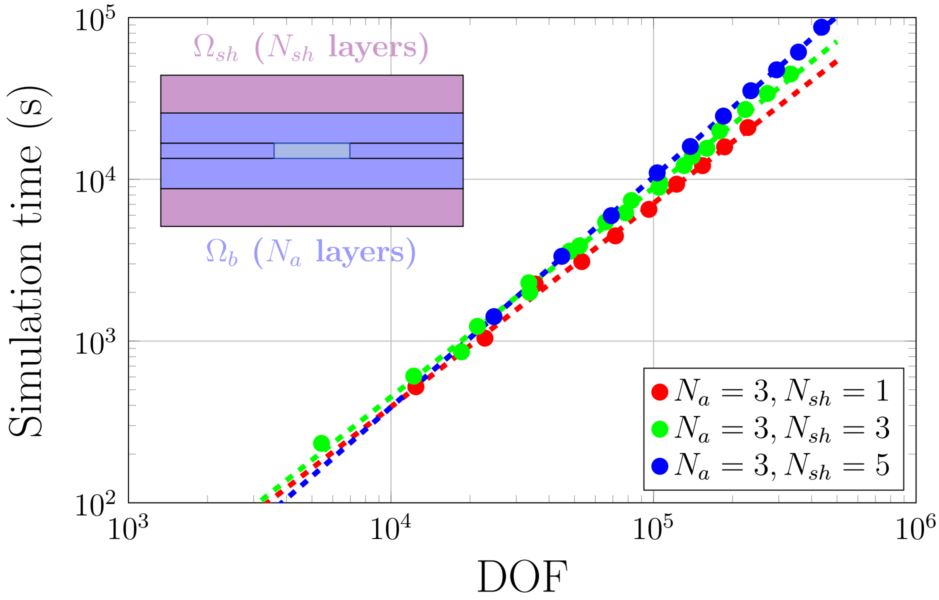

Figure 2.10: Logarithmic-scale plot of the simulation time as a function of the number of DOF, N, in a thin disk of radius $R = 141$ μm and thickness $d = 100$ nm. Results are shown for $N_{sh} = 1$ (in red), $N_{sh} = 3$ (in green) and $N_{sh} = 5$ (in blue), while $N_a = 3$ in every configuration. The curves remain unchanged if the values of N_a and N_{sh} are swapped. The time complexity of the unidirectional shell transformation is $\mathcal{O}(N^{1.26})$, $\mathcal{O}(N^{1.29})$ and $\mathcal{O}(N^{1.42})$ for $N_{sh} = 1$, $N_{sh} = 3$ and $N_{sh} = 5$, respectively, as highlighted by the slope of the dotted lines, which serve as a guide to the eye.

explain this. Although the aspect ratio $R/d > 1400$ is very large, the finite thickness of the film has the effect of cutting off the divergence arising at the edge of the film, which implies deviations of the FE scheme from the CSM. Similarly, despite $n = 1000$ being very large, it is not infinite. As a result of this, $|\mathbf{J}|$ is not strictly equal to J_c in the penetrated region, which also influences the profiles of H_z as well.

2.4.4 Time complexity of the unidirectional shell transformations

Finally, now that the number of layers, N_a and N_{sh}, and the value of A have been optimized, the scaling of the unidirectional shell transformation with respect to the quality of the in-plane mesh in the TD layout is investigated. The mesh inside the thin disk is progressively refined, which in turn increases the number of degrees of freedom of the simulation. The mesh size of the disk ranges from 2 to 20 μm. The simulation time as a function of the number of degrees of freedom in Ω are represented on a logarithmic-scale plot in Figure 2.10 for $N_{sh} = 1$, $N_{sh} = 3$ and $N_{sh} = 5$, with $N_a = 3$. For each value of N_{sh}, the logarithmic plot shows a linear trend, which is equivalent to say that the time complexity scales as N^α, where N is the number of DOF and α is a real parameter. A linear regression on the log-log plot of these curves directly gives the order of the monomial, hence the time complexity of the FE scheme with the unidirectional shell transformation. These linear regressions are indicated by dashed lines in Figure 2.10. One can see that the time complexity is enhanced when the number of layers in the non-conducting region

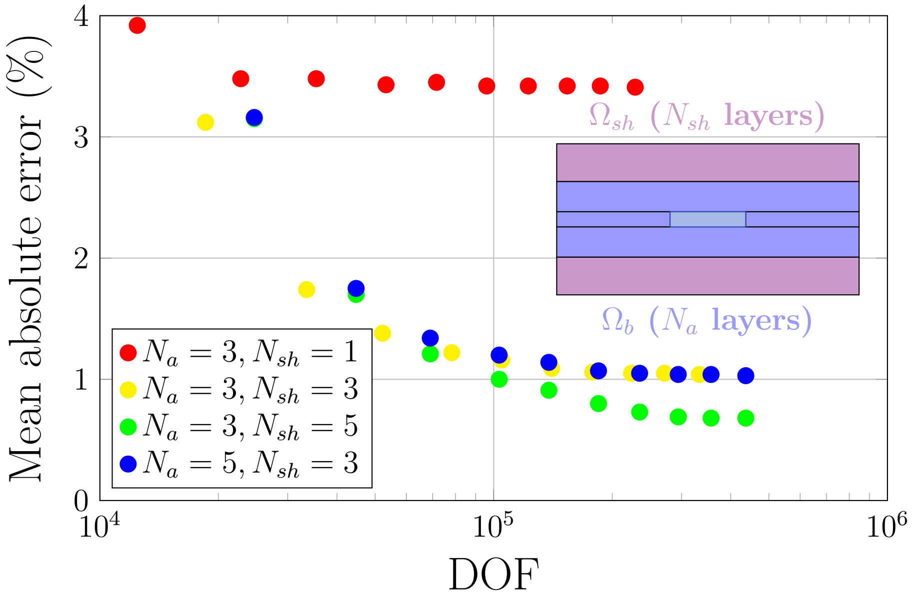

Figure 2.11: Convergence of the **H**-ϕ formulation with a unidirectional shell transformation in the TD geometry. The convergence of the FE scheme is evaluated by means of the mean absolute error of $|\mathbf{J}|$ as a function of the number of DOF for different combinations of N_a and N_{sh}. The number of DOF varies by changing the typical mesh size in the superconducting disk.

is lowered, since it is found that it scales as $\mathcal{O}(N^{1.26})$, $\mathcal{O}(N^{1.29})$ and $\mathcal{O}(N^{1.42})$ for $N_{sh} = 1$, $N_{sh} = 3$ and $N_{sh} = 5$, respectively (or equivalently, for $N_a = 1$, $N_a = 3$ and $N_a = 5$, respectively, with $N_{sh} = 3$). The increase of the computational complexity as the number of extruded layers increases might come in part from the increase of the time allocated for assembling the matrices at each time step, which is a mandatory process given the non-linear nature of the simulations.

The mean absolute error of $|\mathbf{J}|$ is also plotted against the number of DOF in Figure 2.11 for different combinations of N_a and N_{sh}. Independent of the combination, the mean absolute error made on $|\mathbf{J}|$ decreases with the number of DOF and reaches a lower threshold which depends on the value of N_a and N_{sh}. For a given value of N_a (resp. N_{sh}), increasing N_{sh} (resp. N_a) reduces the error. Besides, increasing the number of layers N_{sh} seems to be more beneficial to the quality of the FE approximation than increasing N_a, as proved by the comparison between the case $N_a = 3$ and $N_{sh} = 5$ and the case $N_a = 5$ and $N_{sh} = 3$, which both require the same computing time. Combining the results of Figure 2.10 to those of Figure 2.11, one understands that refining the mesh in the non-conducting region with the unidirectional-shell-transformation technique soon loses its interest, as the increase of the duration of the simulation is not compensated by a significant improvement of the FE approximation. In conclusion, $N_a = 3$ and $N_{sh} = 3$ appears to be a reasonable choice of values that achieves good numerical accuracy, while sparing DOF and keeping a reasonable simulation time.

2.4.5 Comparison of the shell transformations with the truncated geometry in thin disks

The implications of Subsection 2.4.2 and Subsection 2.4.3 are combined so that the unidirectional shell transformations can be compared to the other shell transformations and the truncated geometry. All cases are compared to the analytical results of the CSM. The numerically simulated profiles of H_z and $|\mathbf{J}|$ across a radius in the TD configurations are shown in Figure 2.12. All cases seem to reproduce the expected analytical solution of the CSM fairly well. This is corroborated by the mean absolute errors of both fields, which are indicated in Table 2.4. The typical mesh size in the superconducting disk is more or less equal to 4 μm. The error on H_z and $|\mathbf{J}|$ are rather low. For instance, the mean absolute error is the lowest in the case of the unidirectional shell transformation, with a mean absolute error of 0.6% $J_c d$. In the other shell configurations, the error on H_z is still limited to 0.7% $J_c d$. As far as $|\mathbf{J}|$ is concerned, the errors are $\sim$ 1% J_c in every case, but seem to be the lowest for the trapezoidal and spherical shell transformations, with 0.8% J_c, and the largest for the unidirectional shell transformation, with 1.1% J_c. The number of DOF however varies quite a lot depending on the shell geometry. The spherical shell transformation appears to spare the most DOF among all shell transformations and is also the most time-efficient one, reducing the duration of the simulation by $\sim$ 35% with respect to the truncated geometry. Besides, although it remains more time-consuming than trapezoidal or spherical shell transformations, the unidirectional shell transformation proves to be more efficient than the truncated geometry, dropping the simulation duration by $\sim$ 8%, while proving to be slightly more accurate. In the particular case of the TD geometry, the use of shell transformations appears to be beneficial to the user, by reducing significantly the duration of the simulations, while being slightly more accurate than the truncated-geometry approach.

The fact that spherical and trapezoidal shell transformations systematically require less DOF than the unidirectional shell transformation stems from the unstructured nature of the mesh in Ω_{sh}, which allows to relax the mesh along the three principal directions, therefore sparing a substantial amount of DOF. In fact, the structured mesh implies the extrusion of the in-plane mesh over several layers in Ω_{sh}. More specifically, the extrusion of the film mesh in the out-of-plane direction generates an unnecessary fine in-plane mesh in Ω_{sh}, increasing the number of elements there. The larger extension of the in-plane cross section in the case of the unidirectional shell might also explain the excess of DOF that is observed regarding the unidirectional shell.

2.4.6 Comparison of the shell transformations with the truncated geometry in thin rectangular strips

Let us turn now to the case of thin rectangular strip of length L and width W (TS geometry). This verification is of importance, since most of the films that are used in experiments and in the subsequent simulations are either square or rectangular. In the TS geometry, the current lines form closed contours that become parallel to the longer sides of the strip once the current is probed sufficiently far from the smaller sides of the rectangle. In comparison to the TD case, the value of A must change, because the

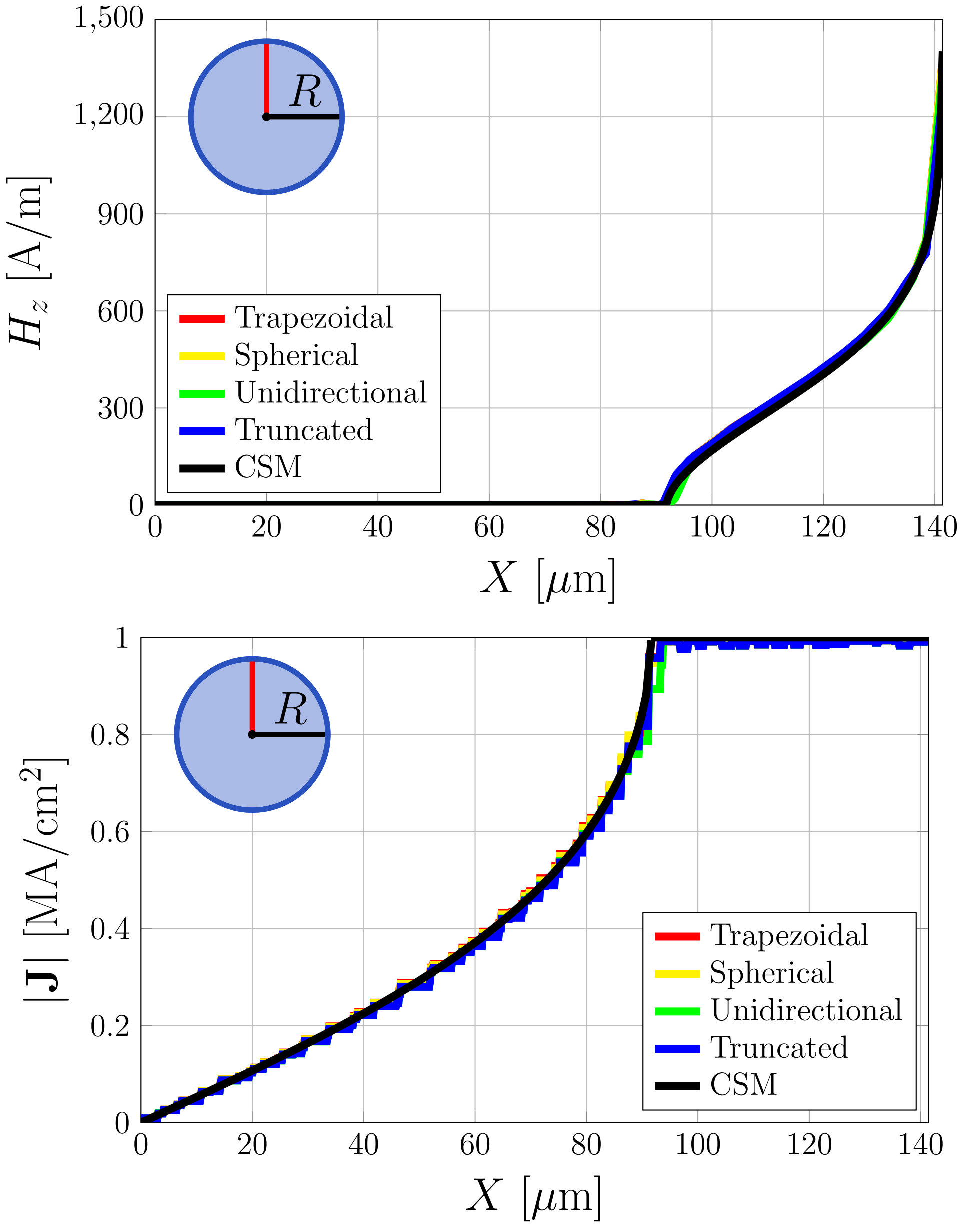

Figure 2.12: Out-of-plane magnetic field, H_z, and norm of the current density, $|\mathbf{J}|$, in a superconducting thin disk of radius $R = 141$ μm and thickness $d = 100$ nm for a trapezoidal (in red), a spherical (in yellow), a unidirectional (in green) shell transformation, and for the truncated geometry (in blue). The numerical results are taken along the radius of the disk, and along the mid-plane cross section along the thickness. All results are compared to the analytical result of the critical state model (CSM) in the thin-film approximation (in black).

Planar geometry	Shell geometry	DOF	Wall time (min)	Error $\|\mathbf{J}\|$	Error H_z
TD	Truncated	93542	182	1%	0.7%
	Trapezoidal	73338	128	0.8%	0.7%
	Spherical	68181	118	0.8%	0.7%
	Unidirectional	104825	168	1.1%	0.6%
TS	Truncated	191939	489	0.9%	1.9%
	Trapezoidal	186617	478	0.9%	1.9%
	Spherical	186800	467	0.9%	1.9%
	Unidirectional	225280	538	1.2%	2.4%

Table 2.4: Accuracy and time performance of the different shell transformations in the thin-disk and thin-strip geometries. The accuracy is computed as the mean absolute error of the evaluated physical quantity. The time performance is assessed with the time needed to perform the whole simulation. As a matter of comparison, the number of DOF is given for each case.

current loops have changed from circular to roughly rectangular shapes. To this aim, let us consider the TS geometry and let us determine the value of A for various aspect ratio L/W, sticking to the criterion that was used in the TD case, $\phi/\phi_0 = 1/2$. The evolution of ϕ as a function of Z is once again evaluated along the lines of the calculations in Section **B.2** in Appendix **B**, in the case of a fully penetrated thin strip of width W and length L. The evolution of A/W as a function of L/W is shown in Figure **2.13** for aspect ratios ranging from 1 to 10. This curve serves as a rule of thumb to select the value of A for rectangular strips. For example, in the TS case, one gets $A \approx 0.20 \times W \approx 80$ μm, while in the SF configuration, $A \approx 0.13 \times L \approx 25$ μm, as indicated in Table **2.2**. In the context of this thesis, the cross sections of the films will be either squares or rectangles, so that the predictions of Figure **2.13** can be safely used throughout the manuscript. Nevertheless, one could still use the results of Figure **2.13** as a first guess for a thin film with arbitrary cross section by roughly approximating the cross section as the smallest rectangle that circumscribes the actual film. The length and the width of the rectangle can then be used to determine the value of A. For the sake of illustration, in the TD geometry, one would obtain $A \approx 0.13 \times 2R \approx 37$ μm. The factor 0.13 corresponds to the value of A/W for a square ($L/W = 1$), which corresponds to the fact that the smallest rectangle containing a circle of radius R is a square of side $2R$. In fact, it can be shown analytically that $A \approx 0.23 \times R \approx 32$ μm, as shown in Table **2.2**, which is close to the prediction for a thin square film. Note that rounding the value of A, as it was done in Table **2.2**, is not detrimental to the quality of the solution, since the value of A can be chosen in a large range of values, as discussed in Subsection **2.4.2**.

In order to assess the validity of the shell-transformation methods in this geometry, the profiles of the out-of-plane component of the magnetic field, H_z, and the norm of the current density, $|\mathbf{J}|$, are once again compared to the analytical results of the CSM, assuming the thin-film approximation for an infinitely thin superconducting strip [114], see also Equation **1.38** and Equation **1.39**. Given the parameters of the TS column in Table **2.2**, one has $L/W = 3$. The mesh in the strip is non-regular, as the mesh size goes from 20 μm in the vicinity of the small lateral borders of the strip to 2 μm along the smallest median. Due to the finite aspect ratio of the strip, a direct comparison to the results of the infinitely long and thin strip is valid only at a sufficiently far distance from the

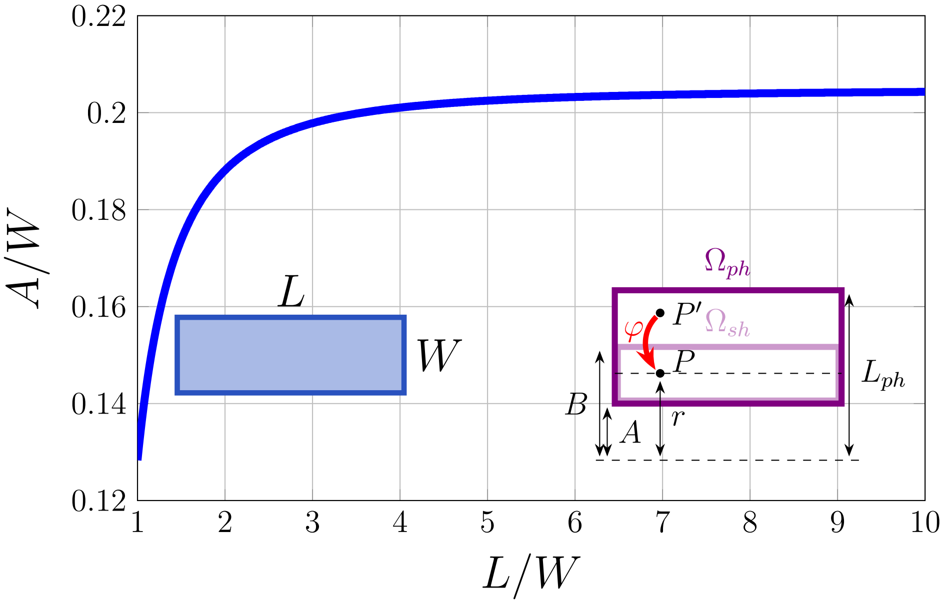

Figure 2.13: Size of the layer, A/W, as a function of the aspect ratio of a thin rectangular film, L/W, where L and W are the length and the width of the rectangular film, respectively. These results were obtained in the framework of the mathematical developments of Section B.2 in Appendix B.

corners of the rectangular cross section. The border effects are thus the smallest along the smallest median of the strip, which is where the numerical results are collected and compared to the CSM in the TS case. The average absolute errors of H_z and $|\mathbf{J}|$ along the smallest median are calculated to estimate how well the simulations interpolate the analytical profiles of the CSM.

The profiles along the smallest median of the rectangular cross section of the out-of-plane component of the magnetic field, H_z, and the norm of the current density, $|\mathbf{J}|$, for the different shapes of Ω_{sh} are summarized in Figure 2.14. The accuracy and the time performance for every shell-transformation shape and the truncated geometry are reported in Table 2.4. The number of degrees of freedom are also indicated, for the sake of comparison. Note that for all geometries $N_a = 3$ and $N_{sh} = 3$ in the unidirectional shell transformation, in a direct application of the observations of Subsection 2.4.3. It can be immediately observed that the numerical results fit the analytical ones for an infinitely long strip very well for each shape of Ω_{ph}, except close to the border and at the flux front, where the main differences with respect to the CSM are found. The error on H_z and $|\mathbf{J}|$ are higher for the TS case than in the TD case, independent of the shell geometry. The mean absolute error on H_z are multiplied by a factor 3 to 4, and the mean absolute errors on $|\mathbf{J}|$ increase slightly as well. The number of DOF remains pretty much the same for the truncated geometry, the spherical and the trapezoidal shell transformations. The simulation times are then roughly the same, even if an improvement of 5% is observed with the spherical shell transformation with respect to the truncated geometry. The mean absolute error on $|\mathbf{J}|$ and H_z are equal to 0.9% of J_c and 1.9% of $J_c d$ respectively, in all cases. The unidirectional shell transformation, however, appears to use more DOF and, as a result of this, the simulation also lasts 10% longer than for the truncated-geometry case. The error on $|\mathbf{J}|$ and H_z are also larger than in the previous cases, reaching 1.2%

of J_c and 2.4% of $J_c d$ respectively. The larger error on H_z associated to the FE method mainly comes from the estimation of H_z close to the borders and at the flux front. In fact, in an infinitely thin film, H_z diverges at the border of the film. This divergence is absent in the simulations, since the thickness of the films is finite. The value of H_z at the border of the strip varies with the shell transformation and is partly responsible for the significant differences in the mean absolute error on H_z. The quality of the FE approximation at the flux front could be enhanced by increasing the values of N_a and N_{sh}, as discussed in Subsection **2.4.3**.

Nevertheless, in the scope of the simulations carried out for this particular cross section, it appears that the shell transformations do not contribute much to improving the accuracy of the numerical solutions with respect to the truncated geometry, and do not significantly improve the time performance either. As far as the unidirectional shell transformation is concerned, the numerical evaluation of H_z also appears to be slightly worse, while increasing the number of DOF and thus the duration of the simulation.

2.4.7 Magnetic field penetration in thin superconducting square films

Until now, the exponent n has been set to a very large value so that the numerical results could be compared to the analytical expressions of the CSM. In practice, the value of n is much less than 1000. Besides, the choice for the value of A relies on analytical developments in fully penetrated samples. In order to test the validity of the shell-transformation approach in partially penetrated thin films and for more practical values of n, a unidirectional shell transformation is used in a film with square cross section (SF geometry), with a more realistic value of $n = 20$. Because of the square geometry and the limited value of n, it becomes impossible to compare the FE simulations to existing CSM or other analytical solutions. Instead, they will be tested against the results of the Brandt's method [206], that serves as a reference. All numerical and physical parameters can once again be found in Table 2.2, in the SF column. The mesh in the Brandt's method consists in a uniform grid of 103 elements along half a side of the square, using symmetry boundary conditions along the median the square to account for the square symmetry. In the FE simulations, the square is meshed with triangular elements, according to the Delaunay algorithm, and the side of the square is subdivided in 200 points, giving rise to a mesh size of 1 μm.

The numerical profiles of H_z and $|\mathbf{J}|$ along one of the median of the square are then compared to the results of the Brandt method in Figure 2.15, for different durations of the applied field ramp, t_a, or equivalently, different values of H_a. One can see that for each value of H_a, the FE simulations are very much on par with the Brandt method. The main differences arise at the flux front, where $|\mathbf{J}|$ starts to decrease and where H_z reaches 0. The FE method seems to deliver H_z and $|\mathbf{J}|$ profiles that penetrate less inside the sample than the numerical results of Brandt's method. Far enough from the flux front, the profiles in the penetrated region are in excellent agreement with each other.

Similarly, if one sets t_a to 0.5 s, so that $H_a = 500$ A/m, the profiles of H_z and $|\mathbf{J}|$ for diverse values of n are shown in Figure 2.16. The FE results are once again compared

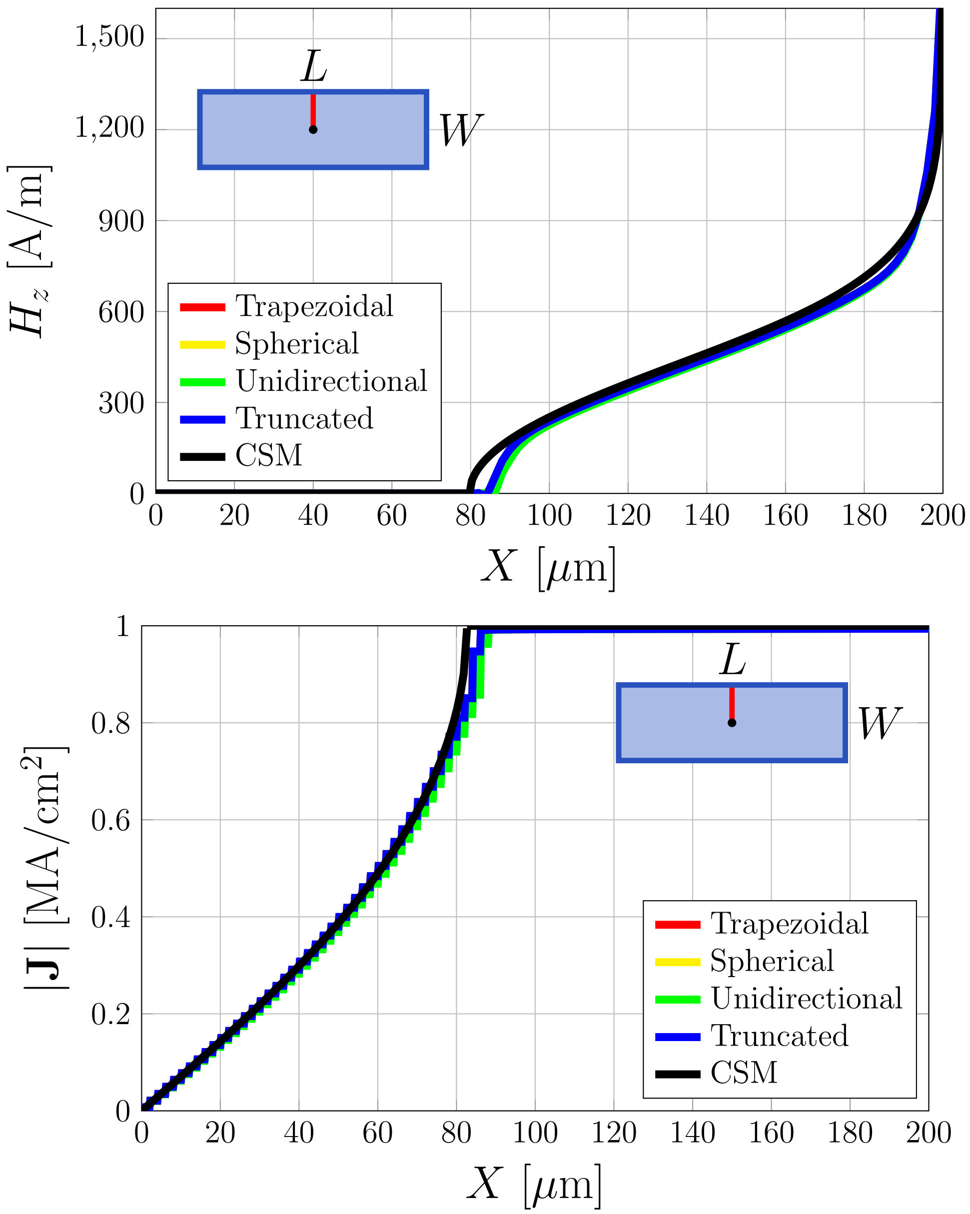

Figure 2.14: Out-of-plane magnetic field, H_z, and norm of the current density, $|\mathbf{J}|$, in a thin superconducting strip of length L = 1.2 mm, width W = 400 μm and thickness d = 100 nm for a trapezoidal (in red), a spherical (in yellow) and a unidirectional (in green) shell transformation, and for the truncated geometry (in blue). The numerical results are taken along the smallest median of the strip, and along the mid-plane cross section along the thickness. All results are compared to the analytical result of the critical state model (CSM) in the thin-film approximation (in black).

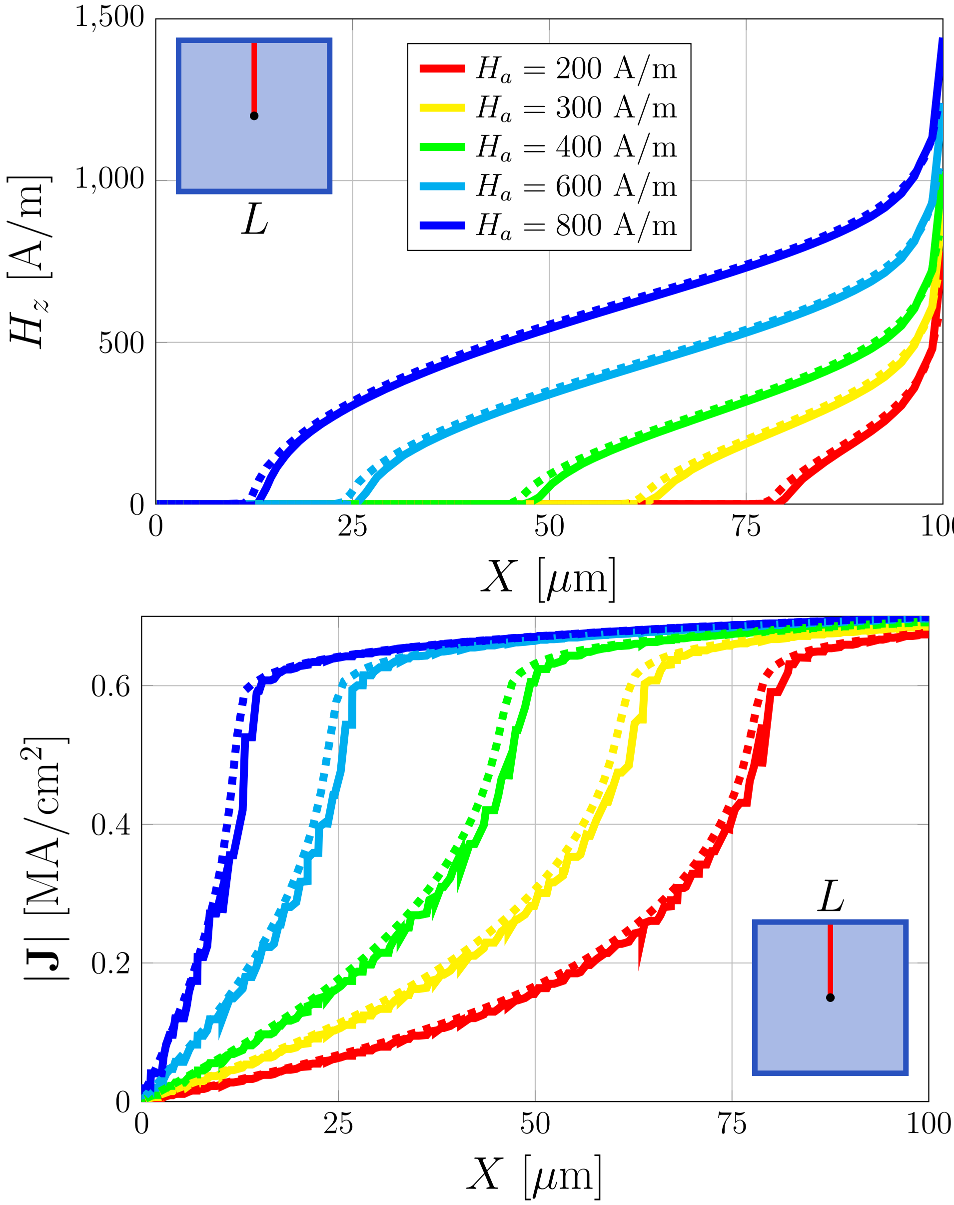

Figure 2.15: Out-of-plane magnetic field, H_z, and norm of the current density, $|\mathbf{J}|$, in a thin superconducting square film of side length $L = 200$ μm and thickness $d = 100$ nm for various values of H_a and $n = 20$. The numerical results are taken along one of the median of the square, and along the mid-plane cross section along the thickness. The FE results are indicated by the plain lines, and are compared to the numerical results of the Brandt method [206], shown in dashed lines.

to those of Brandt's method. The results are in close agreement. When compared to Brandt's method, the FE method seems again to systematically underestimate the location of the magnetic flux front. Such effect does not seem more pronounced for higher values of n, even though it is significantly reduced for $n = 10$. This could be attributed to inevitable differences that arise between the two-dimensional thin-film approximation, which is assumed in Brandt's method, with respect to the fully three-dimensional modelling of the thin-film geometry in the FE method. Besides, since $N_a = 3$ and $N_{sh} = 3$, the mesh in the close proximity of the film might be too coarse and introduce numerical errors that manifest close of the flux front. Finally, one should also bear in mind that although Brandt's method is considered as a reference scheme, its results are numerically evaluated and are thus accurate within an error bar that is inherent to the method. Despite all of this, the qualitative and quantitative agreement between both methods remain very good, and the validity of the unidirectional shell transformation is corroborated.

2.5 Conclusion

In this chapter, the mathematical formalism of the FE method in the context of a $\mathbf{H}$-ϕ formulation has been introduced. This approach is the main numerical tool on which the numerical results of the next chapters rely. The shell-transformation technique, where infinitely large physical domains are mapped onto meshed shell domains of finite extension, has also been introduced as a way to prevent the truncation error arising in the truncated-geometry approach. This technique has been applied to diverse shapes of the shell region, Ω_{sh}, such as spherical, trapezoidal and unidirectional shells. The validity, accuracy and time performance of the shell-transformation approach were tested against the truncated-geometry approach for thin disks (TD), thin rectangular strips (TS), and thin square films (SF). In the TS geometry, shell transformations and the truncated geometry yield profiles of H_z and $|\mathbf{J}|$ of equivalent accuracy and equivalent simulation times. In the TD case, shell transformations slightly improve the accuracy of the results and reduce the duration of the simulations up to 35% with respect to the truncated case, when a spherical shell transformation is used. In the SF geometry, the results of the unidirectional shell transformation were found to be similar to those of the Brandt method for different applied fields and n exponents. The time efficiency and the quality of the shell-transformation approach is thus corroborated for specific cross sections, and their use may be encouraged in comparison with the usual truncated-geometry approach.

In the TD geometry, emphasis was put on the mesh parameters of the unidirectional shell transformation. Based on the analytical developments of Appendix **B**, a suggestion for choosing the size of the shell domain, Ω_{sh}, was proposed. This approach was extended to thin films with rectangular cross section. Then, attention has been drawn to the value of N_a and N_{sh} in the TD geometry, which both control the mesh quality in the non-conducting region. It was found that the values $N_a = 3$ and $N_{sh} = 3$ ensure a good balance between mesh quality and reasonable simulation durations.

For the unidirectional shell transformation, a proper choice of the size of the shell region, A, is paramount to obtain reliable numerical approximations of the magnetic field and the current density inside the film. However, the value of A can still be chosen in a rather

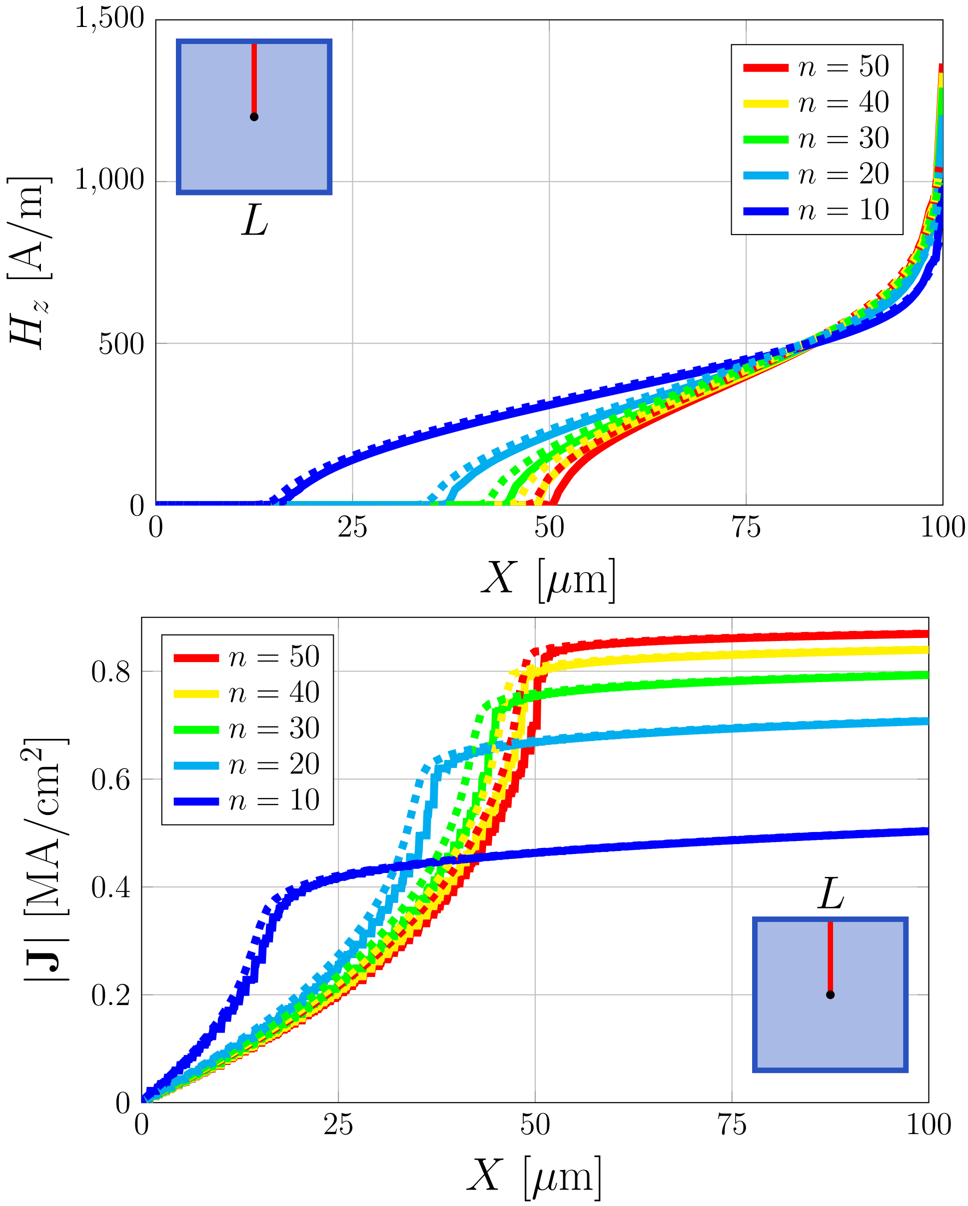

Figure 2.16: Out-of-plane magnetic field, H_z, and norm of the current density, $|\mathbf{J}|$, in a thin superconducting square film of side length $L = 200$ μm and thickness $d = 100$ nm for various values of the exponent n, at a constant applied field, $H_a = 500$ A/m. The numerical results are taken along one of the median of the square, and along the mid-plane cross section along the thickness. The FE results are indicated by the plain lines, and are compared to the numerical results of the Brandt method [206], shown in dashed lines.

large set of possible values without significantly impacting the quality or the simulation duration. Although the suggestion for A is formally guided by the decay of the scalar magnetic potential for fully penetrated thin disks and thin strips, one should not be worried about adapting the value of A to the exact shape of the film or to partially penetrated thin films, as suggested by the numerical results in the SF case of Subsection **2.4.7** and Appendix **B**. In addition, the criterion that determines A is arbitrary and was chosen in this work as a reduction of ϕ by a factor of 2 with respect to its value at the surface of the film. Other valid criteria could be considered as well.

From a formal standpoint, it is important to recognize that the values of A calculated in Appendix **B** are limited to single fully penetrated thin disks or rectangles. Besides, the critical current density is assumed to be constant and magnetic-field-independent. The question therefore arises of whether these calculations are rigorously adapted to the description of more elaborated constitutive laws or more complex geometries, such as indented films or three-dimensional assemblies of films with different cross sections, that will oftentimes be investigated in the following chapters. For this reason, in the next chapters, the truncated geometry with a very large value of L_{ph} will be preferred over shell transformations, in such a way to avoid any ambiguity about the validity of the results that might be related to the choice of A. Nonetheless, an empirical validation of the unidirectional shell transformation in these contexts will also be carried out in some instances.

Chapter 3

Surface barrier effects near an edge indentation

3.1 Introduction

Consider a superconducting film with an indentation along one of its borders. The indentation perturbs the distribution of eddy currents generated by an out-of-plane magnetic field. In accordance with current conservation, the current lines must bend around the indentation. As explained in Section **1.3.2**, these sharp turns result in the formation of discontinuity lines, or d-lines, which can be clearly identified in the thin-film geometry if one uses magneto-optical imaging (MOI) of the sample. As shown in panel (a) of Figure **3.1**, in the context of the Bean critical state model (CSM), the d-lines that develop around an indentation of depth h follow, sufficiently far from the indentation, a parabolic trajectory of equation

$$\mathcal{P} \equiv y = \frac{x^2}{2h} + \frac{h}{2} \sim ax^2, \tag{3.1}$$

where $a = 1/(2h)$ is the concavity parameter of the parabola. Therefore, a solely depends on the depth of the indentation. In particular, the larger h, the larger the opening of the parabola, $\mathcal{P}$. Furthermore, according to the Bean model, the presence of the indentation induces a magnetic field excess penetration depth, $\Delta_p = h$, that is not bound to the vicinity of the indentation, but is instead visible at the flux front of the penetrated region, which might be much larger than the indentation size. Note that Δ_p is formally defined as the distance between the flux front originating from the indentation tip and that originating from the sample border, as shown in red in panel (a) of Figure **3.1**.

Since the parameters a and Δ_p depend only on h in the CSM, it is legitimate to ask whether the size of an indentation can be directly inferred from the measurement of the concavity parameter of the parabolic d-lines. Brisbois et al. investigated this possibility for thin niobium films in [41]. To this aim, they recorded the penetration of magnetic field around lithographically defined edge indentation of known geometrical characteristics by means of MOI, and fitted the observed d-lines with a parabolic function $\mathcal{P} \equiv ax^2 + c$. Relying on the predictions of the Bean model to assess the depth of the indentations, they found that the values of h were systematically overestimated, and that the discrepancy

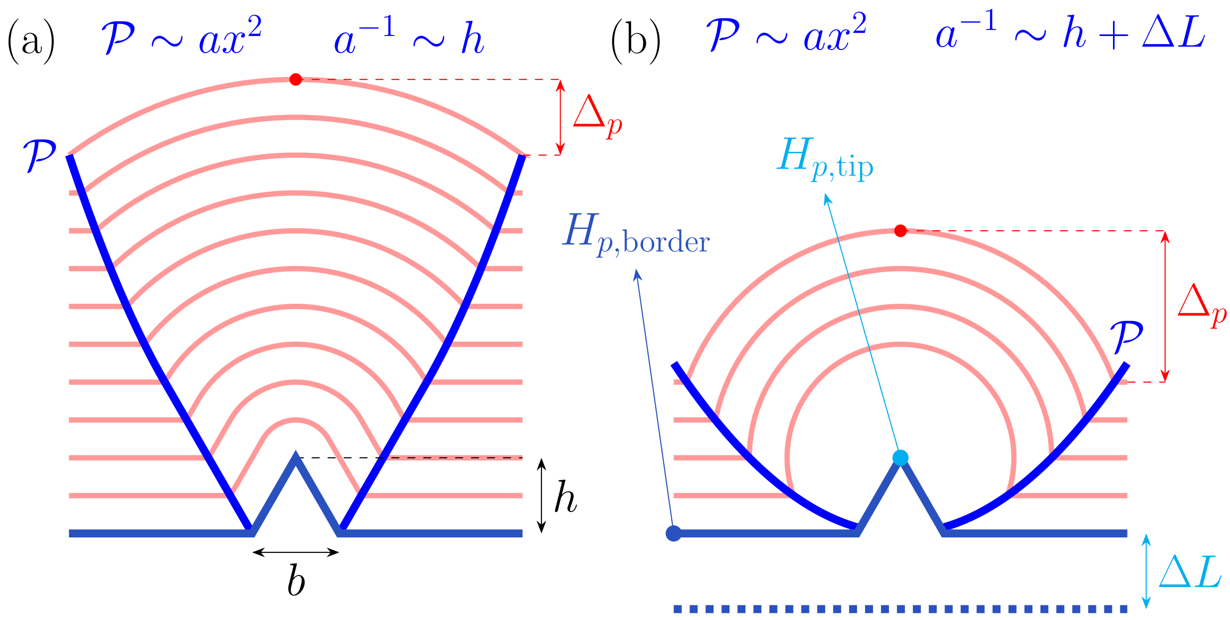

Figure 3.1: Discontinuity lines around a triangular indentation of basis length b and height h when (a) surface barriers are neglected, i.e. $H_{p,\mathrm{border}} = H_{p,\mathrm{tip}} = 0$, and (b) surface barriers are accounted for, with a depleted barrier height at the indentation tip, i.e. $H_{p,\mathrm{border}} > H_{p,\mathrm{tip}} > 0$. Current lines are represented in light red, the last of which corresponds to the location of the flux front in the longitudinal geometry. The thick blue lines correspond to the d-lines that develop around the triangular indentation. In the Bean model, the d-lines take the shape of a parabola at a large enough distance from the indentation, $\mathcal{P} \sim ax^2$, where a is the concavity parameter of the parabola and can be evaluated by the relations (a) $a^{-1} \sim h$, and (b) $a^{-1} \sim h + \Delta L$, where $\Delta L \sim (H_{p,\mathrm{border}} - H_{p,\mathrm{tip}})/J_c$, is the excess path length and J_c is the critical current density in the superconductor. The excess penetration depth, Δ_p, is also shown in red in both cases.

with the theoretical prediction was exacerbated as the sample temperature, T_0, increased. For the sake of illustration, for triangular indentations of height $h = 10$ μm and basis length $b = 20$ μm, they estimated that $2h = 1/a$ was respectively equal to 12.5 μm and 28 μm for $T_0/T_c \approx 0.45$ and 0.89, with $T_c = 9$ K. In other terms, although the data show some scatter influencing the fitting of the parameter a, there appears to be a consistent widening of the parabolic d-line as temperature increases, which is not predicted by the Bean model. Besides, magneto-optical measurements also revealed that the maximal value of Δ_p monotonically increases when the temperature is raised.

In superconductors, several parameters are temperature-dependent, such as the parameter n and the critical current density, J_c, that both appear in the **E-J** power law of Equation 1.33. In [41], it is shown that the observed parabola widening cannot be reproduced by a continuous electrodynamics model that includes the **E-J** power law and takes into account the temperature dependence of the n value. Reducing the n value leads to a smearing of the flux distribution, but the location of the d-lines remains very close to those prescribed by the results of the Bean model. Accounting for the temperature dependence of J_c does not modify the d-lines with respect to the patterns predicted by the Bean model, which are governed by geometrical considerations, i.e. the equidistance of intersecting flux fronts that originate from the sample boundary or the sharp corners of the indentation. Numerical simulations have shown that temperature does not have any influence on this criterion. Moreover, in regard with the low applied field rates that induce insignificant spatial variations of heat dissipation, negligible temperature gradients are generated in the system.

In [207], Vestgaarden et al. studied the excess penetration induced by the presence of a circular indentation of radius R, by means of an electrodynamic model for thin films that uses the usual **E-J** power law. It was shown that Δ_p is an n-dependent and non-monotonous function of the applied field, H_a, reaching a maximal value $\Delta_{p,\max}$ at a field $H_a = H_{\max}$, where $\Delta_{p,\max} > h$. These numerical observations were validated experimentally in the case of thin YBCO films [207], and the experimental excess penetrations in niobium films also follow this trend [41]. However, according to [207], if T increases, n decreases and so do $\Delta_{p,\max}$ and $H_{\max}$. This contradicts what was observed experimentally in [41] for niobium films, as $H_{\max}$ indeed decreases with T, whereas $\Delta_{p,\max}$ increases with T.

In [41], it was suggested that the opening of the d-lines could be explained in terms of a depletion of the first penetration field in the vicinity of the tip of the triangular indentation. Moreover, in a first approximation, one can rely on the Bean model in the longitudinal geometry to estimate the additional excess penetration depth, $\Delta_p - h$, that is induced by the difference of surface barriers. If one denotes the first penetration field at the border and at the tip of the indentation by $H_{p,\text{border}}$ and $H_{p,\text{tip}}$ respectively, then

$$\Delta_p - h \sim \frac{H_{p,\text{border}} - H_{p,\text{tip}}}{J_c} = \frac{\Delta H_p}{J_c}, \tag{3.2}$$

where $\Delta H_p \equiv H_{p,\text{border}} - H_{p,\text{tip}}$. By raising the temperature, if the reduction of the first penetration field difference is slower than the decrease of J_c, then one can expect that Δ_p increases with T.

In this chapter, we would like to further scrutinize the hypothesis that the surface barrier variations are responsible for both the d-line and Δ_p dependences on T. The remaining of the chapter is organized as follows. Section **3.2** investigates from a theoretical perspective the effect of inhomogeneous surface barriers on the curvature of the parabolic d-lines that surround triangular indentations. The case of the longitudinal geometry is first considered by means of the Bean model, which leads to a rough estimation of the expected widening of the parabolas. Then, the main differences between surface barriers in longitudinal and thin-film geometries are highlighted and their relevance is discussed. Section **3.3** is devoted to the description of the surface barrier modelling in superconducting thin films and bulks, in the framework of the finite-element (FE) method. In Section **3.4**, a numerical study addressing the influence of the inhomogeneous surface barriers on the excess penetration depth and the curvature of the parabolic d-lines emerging from a triangular border indentation is carried out for a slab of infinite height and then extended to the thin-film geometry. Finally, Section **3.5** summarizes the main findings of the chapter.

3.2 Influence of inhomogeneous surface barriers on the curvature of the parabolic d-lines around an edge indentation

In this section, it will be discussed how the argument of [41] based on the indentation-induced inhomogeneity of the surface barrier can also explain the widening of the parabolic d-lines. To this aim, the case of the longitudinal geometry will be first considered, and the relevance of extending the conclusions to the thin-film geometry will then be discussed.

Longitudinal geometry

In the longitudinal geometry, i.e. a superconducting sample with infinite height that is subjected to an applied magnetic field parallel to the infinite height, the surface barrier that vortices must overcome to enter the sample is the Bean-Livingston barrier. As explained in Subsection **1.2.5**, this barrier results from the balance between two opposing forces acting on a vortex, namely (1) the Lorentz force that drives the vortex in the superconductor, because of the interaction between the vortex and the Meissner currents, and (2) a force that pulls the vortex back outside and which is generated by the mirror image of the vortex. When $H_{c,1} < H_a < H_{BL}$, where H_{BL} is the penetration field, this balance gives birth to an energy barrier that extends over distance that are of the order of λ to ξ. When $H_a > H_{BL}$, the barrier vanishes, and the vortex enters the sample. The Bean-Livingston barrier is of the order of magnitude of the thermodynamic field, so that $\mu_0 H_{BL} \sim \mu_0 H_c \sim \phi_0/2\sqrt{2}\pi\lambda\xi$, see Equation **1.12**. The magnetic field variation at the interface between the superconductor and the non-conducting region implies the existence of a surface current $J_{c,\mathrm{surf}} \sim H_s/\lambda$ which is of the order of magnitude of the depairing current density, $J_{dep} \sim \phi_0/3\sqrt{3}\mu_0\lambda^2\xi$.

The presence of defects may locally reduce the surface barrier and lead to local flux entrance, as it is shown in Figure **3.2** [208], which is known as the flux gate mechanism. It was shown in [209] that the penetration field is reduced in the vicinity of the tip of a triangular indentation. The explanation for the lower penetration field is the consequence of two distinct effects that weakens the Bean-Livingston barrier. First, current crowding occurs near the tip of the indentation, which increases the Lorentz force pushing the vortices inside the sample. Second, the indentation perturbs the vortex currents, so that the attractive force that is exerted by the mirror image of the vortex is reduced. Therefore, for a given applied field, the Bean-Livingston barrier is reduced and H_{BL} is reduced with respect to the situation of a flat border.

Now, let us analyse the effect of a depletion of the surface barrier at the tip of a triangular indentation on the parabolic d-lines. Consider a triangular indentation of basis length b and height h that lies on the border of an infinitely long superconducting slab. The slab is subjected to a uniform applied field of magnitude H_a parallel to the slab, so that $\mathbf{H}_a = H_a\mathbf{e_z}$. The critical current density inside the superconductor is assumed to be uniform and its value is denoted by J_c. In the longitudinal geometry, the magnetic field is always parallel to the slab, i.e. $\mathbf{H} = H_z\mathbf{e_z}$, while the current density only has in-plane components, i.e. $J_z = 0$. A close-up view of the cross section of the slab in the vicinity of

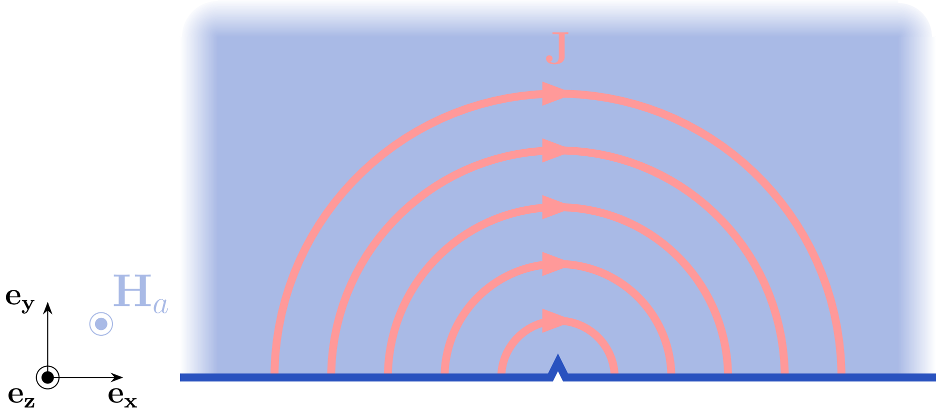

Figure 3.2: Schematic illustration of the flux-gate mechanism, where the reduction of the surface barrier around an edge defect facilitates the entrance of magnetic flux through the defect. The current density is assumed uniform in the superconductor, which is coloured in light cerulean. The current lines are drawn in light red, and describe a circular trajectory around the indentation, before following the boundary of the sample, so that the surface current density exceeds that in the bulk of the sample.

the indentation is represented in Figure 3.1.

We suppose that a constant Bean-Livingston barrier exists everywhere along the border of the superconductor, but is depleted at the tip of the triangular indentation. The penetration fields along the smooth border of the film and at the indentation are again denoted by $H_{p,\text{border}}$ and $H_{p,\text{tip}}$ respectively. As discussed in the previous paragraph, $H_{p,\text{tip}} < H_{p,\text{border}}$. Following the model of Clem [210], the surface barrier can be modelled as a constant drop of the magnetic field at the boundary of the slab, so that $H_z = H_a - H_p$ on the surface of the superconductor if $H_a > H_p$, and $H_z = 0$ if $H_a < H_p$. Meissner currents shield the external magnetic field over a layer that lies in the vicinity of the boundary of the superconductor, and is typically as large as a few times λ. Given that $h \gg \lambda$, the detailed behaviour of the induced currents in this layer are ignored and the layer is considered infinitely thin.

The sample remains flux-free as long as $H_a \leq H_{p,\text{tip}}$ ($H_z = 0$). For $H_{p,\text{tip}} < H_a < H_{p,\text{border}}$, magnetic flux penetrates inside the slab through the tip of the indentation, and the current lines follow circular patterns that are centred around the tip of the indentation itself [208]. For $H_a > H_{p,\text{border}}$, the magnetic field is now able to penetrate the sample through the straight borders. The current lines that emerge parallel to the straight borders, and the circular ones that are centred around the tip of the indentation intersect to form d-lines. Hence, the d-lines correspond to the locus of equidistance of diffusion between the horizontal straight border and the tip of the indentation, which is a parabola. The situation is similar to what was derived in panel (a) of Figure 3.1, where no surface barrier along the whole boundary was considered, but now an additional path length difference must be accounted for to emulate the difference of surface barrier heights between the tip and the border. One has

$$\Delta L = \frac{H_a - H_{p,\text{tip}}}{J_c} - \frac{H_a - H_{p,\text{border}}}{J_c} = \frac{H_{p,\text{border}} - H_{p,\text{tip}}}{J_c} = \frac{\Delta H_p}{J_c} > 0. \qquad (3.3)$$

The resulting d-lines are therefore identical to those found in a situation where no surface barrier is accounted for, provided the border is shifted downwards by a distance ΔL, as shown in panel (b) Figure 3.1. Hence, far enough from the indentation, it is expected that the opening of the parabola corresponds to that of a sample with no surface barrier and for an indentation of length $h+\Delta L$. The curvature of the parabola is therefore given by $a \sim 1/(h+\Delta L)$, which implies that the parabola opens up by increasing ΔL. Note that Equation 3.2, related to the excess penetration depth, Δ_p, and Equation 3.3, related to the parabola widening, share the same expression. The simple line of reasoning that was used to explain the increase of the excess penetration in thin niobium films in [41] is therefore also able to explain the wider parabolas that are observed in experiments.

An order of magnitude of ΔL for bulk niobium can be estimated from the above considerations. The reduction of the surface barrier $H_{p,\text{border}} - H_{p,\text{tip}}$ can be estimated as a fraction of H_c. The current density induced at the surface of the superconductor is of the order of J_{dep}, so that ΔL is of the order of

$$\Delta L \lesssim \frac{H_c}{J_c} \sim \frac{J_{dep}}{J_c}\lambda. \tag{3.4}$$

Interestingly, the excess path length, which is a consequence of the spatial inhomogeneity of the surface barrier, can thus be interpreted as the consequence of the mismatch between the current densities that are found at the surface and in the bulk of the superconductor. From [41], one has $\lambda \sim 50$ nm and $\xi \sim 16$ nm for $T/T_c = 0.65$, while one can roughly estimate $J_c \sim 1$ MA/cm^2. Then, $J_{dep} \sim 8$ MA/mm^2. Finally, one finds $\Delta L \sim 25$ μm. This calculation shows that the variations of the barrier height might be responsible for parabola openings that are wider than the size of the defect, which is in this case $h = 10$ μm. The widening of the parabolic d-lines when the temperature is increased might thus be explained by surface barrier effects, if it is possible to show that ΔL increases with temperature.

Thin-film geometry

Up to this point, the arguments that were developed apply to the longitudinal geometry. However, several differences may arise when considering real geometries. The Bean-Livingston barrier is still present in thin superconducting films, although it is now associated with the Pearl length, $\Lambda = 2\lambda^2/d$, if $d < \lambda$ where d is the thickness of the film, instead of the London penetration depth, λ. Besides, a geometrical barrier that depends on the geometric shape of the edges is also present. As it was mentioned in Subsection 1.2.5, this barrier results from the balance between the driving Lorentz force, which stems from the interaction between the vortex and the Meissner currents, and a restraining force that is associated with the deformation of the vortex, as it moves from the edge into the interior of the superconductor. The deformation of the vortex is thus responsible for a potential barrier that must be overcome before the vortex can enter the superconductor. The irreversible entrance of vortex occurs when the applied magnetic field exceeds a value H_{GB}. Therefore, in superconducting films, both the Bean-Livingston and the geometrical barriers contribute to the surface barrier, especially for thick samples, $d \gg \lambda$ [211, 212]. For films of thickness $d < \lambda$, the geometric barrier can however be neglected [212].

Due to the demagnetizing effect of the thin-film geometry, both types of barriers take the generic form

$$H_s \simeq \sqrt{\frac{d}{W}}\, H_p\,, \tag{3.5}$$

where W and d are the characteristic lateral length and the thickness of the film, respectively. For a perfect Bean-Livingston barrier, $H_p = H_c$, while $H_p \simeq H_{c,1}$ for a perfect geometrical barrier [212]. In practice, in the former case, $H_{c,1} \leq H_p < H_c$, since the presence of imperfections or edge indentations reduces the surface barrier, as explained earlier.

Another difference between bulk samples and thin films manifests itself in the magnetic-field distribution. In the thin-film geometry, a vortex-free region can form near the edges of the superconductor [89]. The presence of surface overcritical Meissner currents drive the vortices that have just overcome the surface barrier to the centre of the film, until the pinning force becomes large enough to balance the driving Lorentz force. Subsequently, the vortices pile up in the center, and a magnetic-flux dome is formed, which extends progressively towards the edge as the applied field is increased [89, 213, 214, 215]. In principle, a model where surface barriers are accounted for should also take into account the extension of the vortex-free region. Indeed, the contribution of the vortex-free region may vary with the local value of the magnetic field, which is larger at the indentation than far from it. This would alter further the value of ΔL. However, vortex-free regions are more easily observed in weak-pinning samples [215] and were not observed in the strong-pinning niobium samples in [41]. It is therefore expected that the contributions of such regions can be neglected, as it will be assumed so in what follows.

Besides, since the thickness of the samples in [41] is $d = 100$ nm and the Pearl length is estimated as $\Lambda \sim 50$ nm, we have $d \sim \Lambda$, so that the surface barriers are presumably dominated by the Bean-Livingston barrier. Therefore, it is reasonable to assume that the argument of Daumens and Buzdin from [209] still holds for thin films, so that one can assume that the surface barrier and the value of H_s are reduced near the tip of the indentation.

The previous arguments point to the relevance of surface barriers in the magnetic-flux pattern. We argue that the d-lines are influenced by differences in the surface barrier heights between the tip of a triangular indentation and the straight borders of the film that surround it. Even though the d-lines are observed for fields that can be much larger than the penetration fields, their shape is determined by the surface barrier difference at the first stage of magnetic-flux penetration.

3.3 Inhomogeneous surface barriers in thin superconducting films

This section is devoted to the modelling of inhomogeneous surface barriers that arise in the presence of a triangular indentation in thin superconducting films. In fact, the modelling of surface barriers in infinitely thin strips has already been addressed by means of a semi-analytical approach [90]. Nevertheless, the problem is rather complex for three-dimensional geometries, such as thick films, and when dynamical aspects must be accounted for. Following a suggestion of [88], the main phenomenology of the problem will be instead captured by mimicking the surface barrier height with regions of surface pinning that lie in the vicinity of the border. The height of the surface barrier is then adjusted by adapting locally the strength of the surface pinning and hence the magnitude of the corresponding critical current density.

A few remarks about the choice of the parameters are in order. First, the region where surface currents are generated is expected to be much smaller than the lateral dimension of the film, L. It will also be supposed that its depth is constant along the edge of the sample. Besides, based on the remarks of Section **3.2**, the effect of the vortex-free regions and the geometrical barrier will be neglected. Therefore, based on the orders of magnitude that were estimated previously, a perfect Bean-Livingston barrier should give rise to surface current densities of the order of the depairing current density, which is estimated to surpass by two orders of magnitude the value of the critical current density in the rest of the film. Near the tip of the indentation, the value of the surface critical current density is reduced, in such a way to emulate the reduction of the surface barrier height around the sharp edge of indentations.

For the sake of illustration, Figure **3.3** shows the different regions within a superconductor of square cross section and where a triangular indentation is introduced along one of its edges. The length of the square is denoted by L, while the basis length and the height of the triangle are denoted by b and h respectively. The sample is subjected to an out-of-plane magnetic field that is ramped up from 0 to a maximal value, H_a, at a constant rate $\dot{H}_a$. A band of constant depth h_{surf} parallel to the boundary of the superconductor corresponds to the region where the surface currents flow. This region is itself divided in two parts, which are coloured in dark cerulean and cyan in Figure **3.3**. In the dark cerulean (resp. cyan) region, the critical current density is set to a value $J_{c,\text{border}}$ (resp. $J_{c,\text{tip}}$), while it is equal to J_c elsewhere (in the light cerulean region). From the previous remark about the surface barrier height and the surface current intensity, the relation $J_c < J_{c,\text{tip}} < J_{c,\text{border}}$ holds.

The penetration of magnetic field inside the superconductor is addressed numerically by means of the FE method which was detailed in Chapter **2**. The **E**-**J** constitutive law consists in a power-law. Moreover, it is assumed that $\mathbf{B} = \mu_0 \mathbf{H}$, although non-linear $\mathbf{B}(\mathbf{H})$ relations have also been used to address the modelling of surface barriers [90, 91]. The effect of the vortex-free regions are also neglected, given that they do not appear at all in the MO images.

3.4 Excess penetration depth and the curvature of the d-lines around an edge indentation

In order to validate the model, consider first the case of an infinitely long slab, which cross section is the same as described in Figure **3.3**. The values of Δ_p and a obtained numerically will then be compared with the theoretical predictions of the Bean model, see for instance Equation **3.2** and Equation **3.3**. In the context of this simulation, one has $L = 200$ μm, $b = 10$ μm and $h = 10$ μm, while $H_a = 0.8$ MA/m and $\dot{H}_a = 1$ kA/m.s. In

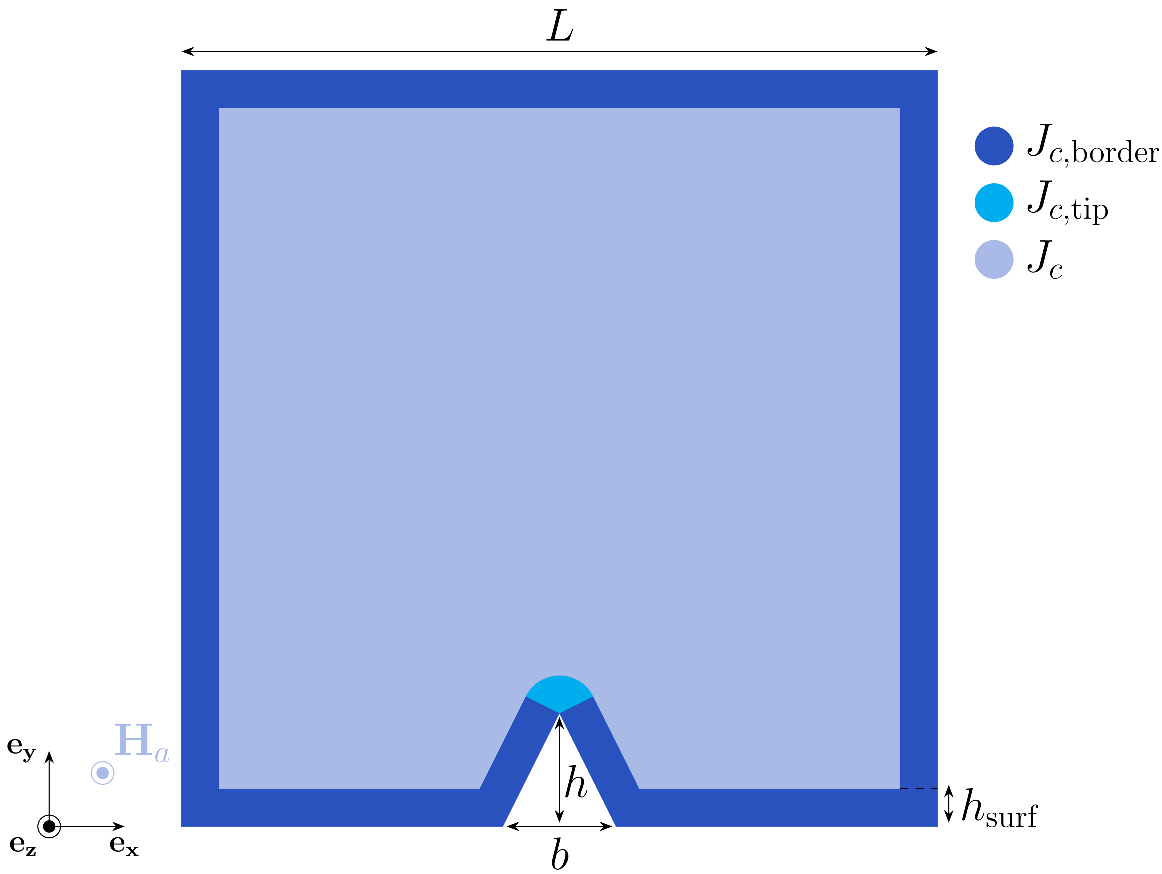

Figure 3.3: Distribution of the critical current density, J_c, in the surface barrier model, for a square film of length L with a triangular indentation at the bottom edge. The width and the height of the isosceles triangle are denoted by b and h respectively. The critical current density takes the value $J_{c,\text{border}}$ in the peripheral region, in dark cerulean, $J_{c,\text{tip}}$ in the cyan region, which lies in the vicinity of the indentation, and J_c in the light cerulean region, which corresponds to bulk pinning. The depth of the peripheral region, i.e. the union of the dark cerulean and cyan areas, is kept constant with respect to the border of the superconductor. This spatial extension of the barrier is denoted by h_{surf}. We assume $J_c < J_{c,\text{tip}} < J_{c,\text{border}}$.

the absence of demagnetizing effects, the magnetic field along the boundary of the slab is equal to the applied field. In the peripheral region, i.e. the deep dark cerulean region in Figure 3.3, we have $J_{c,\text{border}} = 10$ MA/cm^2 over a distance h_{surf}. Note that $J_{c,\text{border}} < J_{dep}$ for numerical reasons. Since the value of the penetration field can be estimated as $\mu_0 H_p = \mu_0 J_{c,\text{border}} h_{\text{surf}}$, one can chose $h_{\text{surf}} = 1.4$ μm, so that $\mu_0 H_p \approx \mu_0 H_c = 175$ mT, which is an acceptable order of magnitude for a perfect Bean-Livingston barrier for niobium [68, 216]. Bearing in mind a proper comparison with the Bean-model, n is set to a very large value, i.e. $n = 1000$.

Figure 3.4 shows the distribution of the out-of-plane magnetic field in the indented slab for four distinct sets of parameters. Panel (a) serves as the reference case and consists in the situation where surface barrier are not absent, i.e. $J_{c,\text{border}} = J_{c,\text{tip}} = J_c = 1$ MA/cm^2. In panel (b), surface barriers are accounted for, but it is supposed uniform in the entire peripheral band, so that $J_{c,\text{border}} = J_{c,\text{tip}} = 10$ MA/cm^2. The last two panels show the

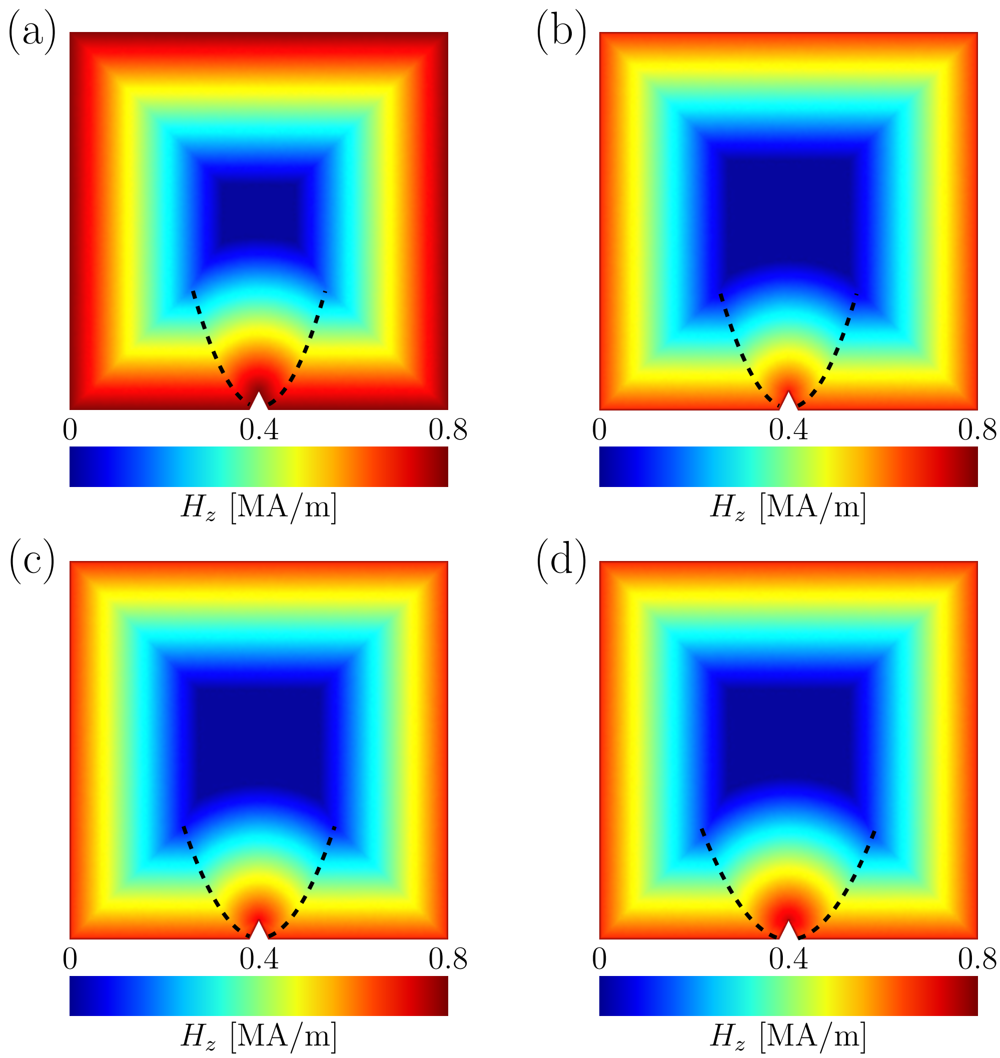

Figure 3.4: Distribution of the out-of-plane magnetic field, H_z, in an infinitely long slab of square cross section of length $L = 200$ μm. A triangular indentation of basis length $b = 10$ μm and height $h = 10$ μm is cut along one of the edge. The surface barriers and their spatial variations are modelled by means of inhomogenous surface pinning, as described in Figure 3.3. In panel (a), surface barriers are absent, so that $J_{c,\text{border}} = J_{c,\text{tip}} = 1$ MA/cm^2. In the other panels, surface barriers are accounted for, and $J_{c,\text{border}} = 10$ MA/cm^2. $J_{c,\text{tip}}$ is set to (b) 10, (c) 8 and (d) 5 MA/cm^2. In all cases, the bulk critical current density, J_c, is equal to 1 MA/cm^2. The d-lines are highlighted by the black dashed lines.

$\mu_0 \Delta H_p$ (mT)	Δ_p (μm)	a (1/mm)	ΔL (μm)
No surface barrier (Bean model)	10	50	0
No surface barrier (FEM)	10	50	0
0	11	47	0.7
35	14	37	3.5
88	18	28	8

Table 3.1: Simulated values of the excess penetration depth, Δ_p, the concavity of the parabola around the triangular indentation, a, and the excess path length, ΔL, as a function of the surface barrier difference, $\mu_0 \Delta H_p = \mu_0 \left(H_{p,\text{border}} - H_{p,\text{tip}}\right)$, in the longitudinal geometry. The analytical predictions within of the Bean model, neglecting surface barrier effects, are indicated for the sake of comparison. The size of the triangular indentation is $h = 10$ μm. The corresponding magnetic field distributions are shown in Figure 3.4.

distribution of the magnetic field when it is assumed that the indentation suppresses the surface barrier in its vicinity, so that $J_{c,\text{border}} = 10$ MA/cm^2 and (c) $J_{c,\text{tip}} = 8$ MA/cm^2, or (d) $J_{c,\text{tip}} = 5$ MA/cm^2. It can be seen that the smaller $J_{c,\text{tip}}$, the larger the excess penetration depth and the wider the parabola. In terms of the d-line shape, little to no difference is visible between panel (a) and (b), which points to the fact that the spatial variations of the surface barrier are indeed crucial to observe deviations of Δ_p and the concavity of the parabolic d-lines, a, from the predictions of the Bean model. However, since the surface barrier delays the entrance of the magnetic field until the first penetration field is reached, the magnetic field logically penetrates less when surface barriers are considered.

The excess penetration depths and the curvatures of the parabolic d-lines that characterize the presence of the triangular indentation, when surface barriers are modelled, are now compared quantitatively with the help of FE simulations. On the one hand, the excess penetration depths are obtained through a mere subtraction of the positions of the flux front that stems from the indentation and from the opposite side. On the other hand, the radius of curvature of the parabola is obtained from the magnetic field contour lines. The global shape of the simulated d-lines is extracted by determining the position where the orientation the contour lines changes abruptly. A parabolic fitting on the resulting set of points is carried out afterwards, yielding the value of a. Equation 1.42 can then be used to correlate the value of a to an equivalent indentation size, $h_{eq} = h + \Delta L$, where $h_{eq} = 1/(2a)$.

The obtained values of Δ_p, a and ΔL are summarized in Table 3.1 . When the surface barriers are not included in the model, the values of Δ_p, a and ΔL are close to what is expected within the Bean model, i.e. $\Delta_p = h = 10$ μm, $a = 1/(2h) = 50$ mm^{-1} and $\Delta L = 0$. The small differences with respect to the Bean model can be attributed to the mesh quality, which leads to errors in the determination of the location of the flux fronts. When surface barriers are accounted for, while ignoring the reduction of the surface barrier at the indentation, the simulated Δ_p, a and ΔL are close to what is predicted within the Bean model. These values are nearly the same as in the case of a sample without surface barrier. As soon as the suppression of the surface barriers around the tip of the triangular indentation is considered, the numerical results start to deviate from the Bean model. More specifically, Δ_p and ΔL both increase as $\mu_0 \Delta H_p$ increases, while a decreases, which confirms the main conclusions that were inferred from Figure 3.4.

Finally, it is interesting to compare the results of the numerical simulations to the first-order theoretical evaluation of Δ_p and ΔL that were derived in the context of the Bean model. According to Equation 3.2 and Equation 3.4, $\Delta_p - h$ and ΔL are both ~ 2.8 and $7\ \mu$m for $\mu_0 \Delta H_p = 35$ and 88 mT respectively. In fact, the numerical simulations agree fairly well with these analytical estimations. This advocates for the relevance of modelling surface barriers by means of strong surface pinning, mimicking the large surface currents that come in pair with it.

Let us turn now to the case of a thin superconducting film of thickness $d = 100$ nm, and which cross section is identical to that of the bulk sample, i.e. $L = 200\ \mu$m, $b = 10\ \mu$m and $h = 10\ \mu$m. The applied perpendicular field is ramped from 0 to $H_a = 500$ A/m at a rate $\dot{H}_a = 1$ kA/m.s. h_{surf} is set to $2\ \mu$m, while $J_c = 1$ MA/cm^2, $J_{c,\text{border}} = 10$ MA/cm^2. In the **E**-**J** constitutive law, we take $n = 19$. The magnetic field penetration in the indented film is numerically solved by means of the FE **H**-ϕ formulation that was described in Chapter 2. The boundary condition $\phi|_\Gamma = 0$ is set at an infinite distance from the superconducting film with the help of a unidirectional shell transformation, following the conclusions of the analysis from Chapter 2. The surface barriers are still emulated by the presence of peripheral regions of enhanced pinning, as depicted in Figure 3.3. It is therefore assumed that the ratio $(J_{c,\text{border}} - J_{c,\text{tip}})/J_c$ is representative of the surface barrier difference that is introduced by the presence of the indentation.

Figure 3.5 shows the distribution of the out-of-plane component of the magnetic field, H_z, for the same combinations of the critical current densities ($J_{c,\text{border}}$, $J_{c,\text{tip}}$ and J_c) as in Figure 3.4. When the effect of surface barriers is taken into account, unphysical negative values of H_z appear near the boundary of the bulk region, which corresponds to the dark cerulean area in Figure 3.3. Since the peripheral region is merely introduced to model the surface barrier in the film, only the positive values of H_z in the bulk region are represented in panel (b), (c) and (d) of Figure 3.5. The remaining part of the film, which is limited to the periphery of the film, is filled in dark blue. First, one can note that the smaller $J_{c,\text{tip}}$, the larger the maximal value of H_z. The maximum of H_z is always located around the indentation tip, and is the largest when the surface barriers are neglected, the situation that is depicted in panel (a) of Figure 3.5. Such an observation is coherent with the fact that larger surface barrier heights should accentuate the reduction of the magnetic field level in the bulk region. Similarly to the longitudinal case, it can be seen that magnetic flux that enters from the indentation tip penetrates further inside the film as $J_{c,\text{tip}}$ decreases, while the flux front does not change when it originates from the top edge. In conclusion, Δ_p and $1/a$ are found to increase with the ratio $(J_{c,\text{border}} - J_{c,\text{tip}})/J_c$. Comparing the distributions of $|\mathbf{J}|$ in panel (a) and (b), the flux penetration is still more advanced when no surface barrier is considered than in the case of a uniform barrier.

The general observations of Figure 3.5 are quantitatively corroborated in Figure 3.6, which shows the value of Δ_p and a obtained numerically as a function of the ratio $(J_{c,\text{border}} - J_{c,\text{tip}})/J_c$. This time, the d-lines around the triangular indentation are defined as the set of the local minima of magnetic field along horizontal lines that are completely circumscribed to the penetrated region in the bottom quarter of the square. The concavity is then defined as the coefficient that corresponds to the quadratic term of a parabolic fit to the obtained d-lines.

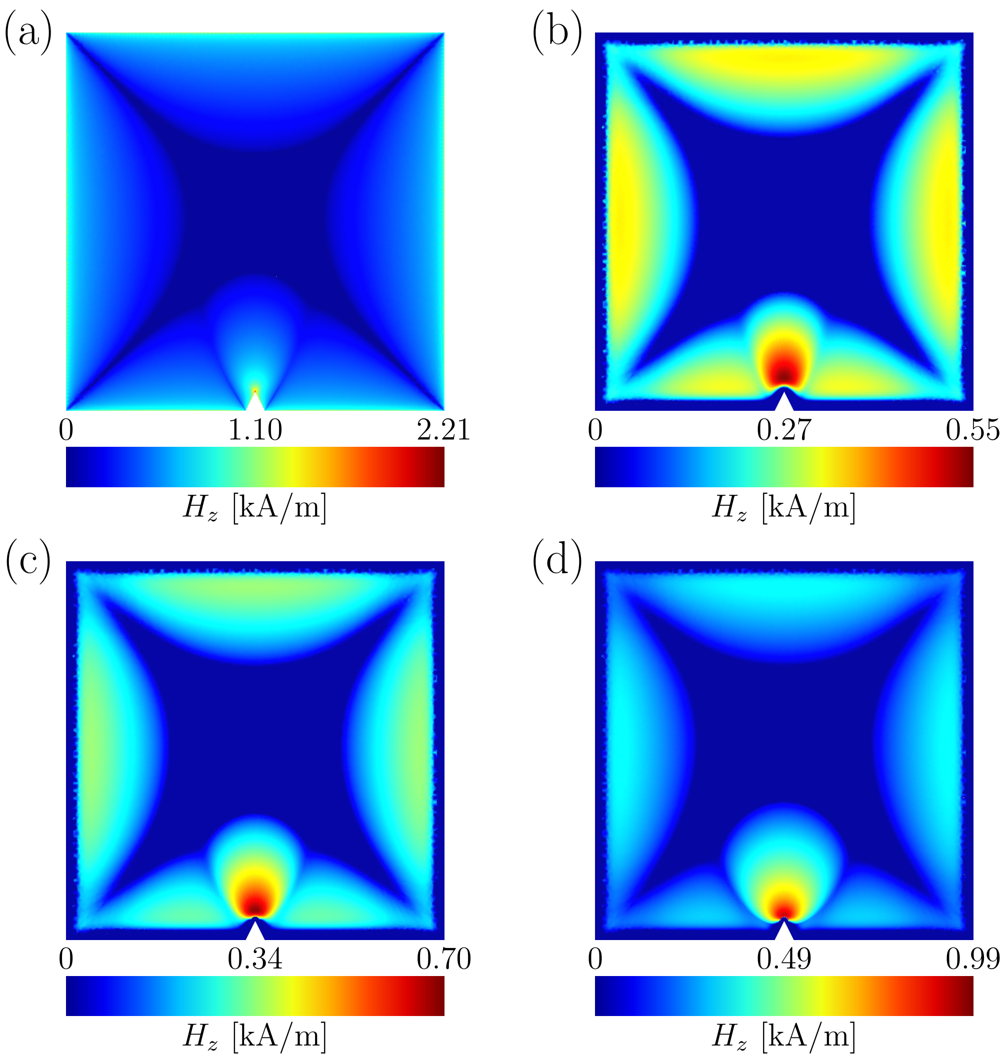

Figure 3.5: Distribution of the out-of-plane component of the magnetic field, H_z, in a thin film in the form of a square of length $L = 200$ μm. A triangular indentation of basis length $b = 10$ μm and height $h = 10$ μm is also cut along one of the edges. The surface barriers and their spatial variations are modelled by means of inhomogenous surface pinning, as described in Figure 3.3. In panel (a), surface barriers are neglected, so that $J_{c,\mathrm{border}} = J_{c,\mathrm{tip}} = J_c = 1$ MA/cm^2. In the other panels, surface barriers are accounted for, and $J_{c,\mathrm{border}} = 10$ MA/cm^2. $J_{c,\mathrm{tip}}$ is set to (b) 10, (c) 8 and (d) 5 MA/cm^2. In all cases, the bulk critical current density, J_c, is set to 1 MA/cm^2. The distributions of $|\mathbf{J}|$ are only shown in the bulk pinning region, which appears in light cerulean in Figure 3.3.

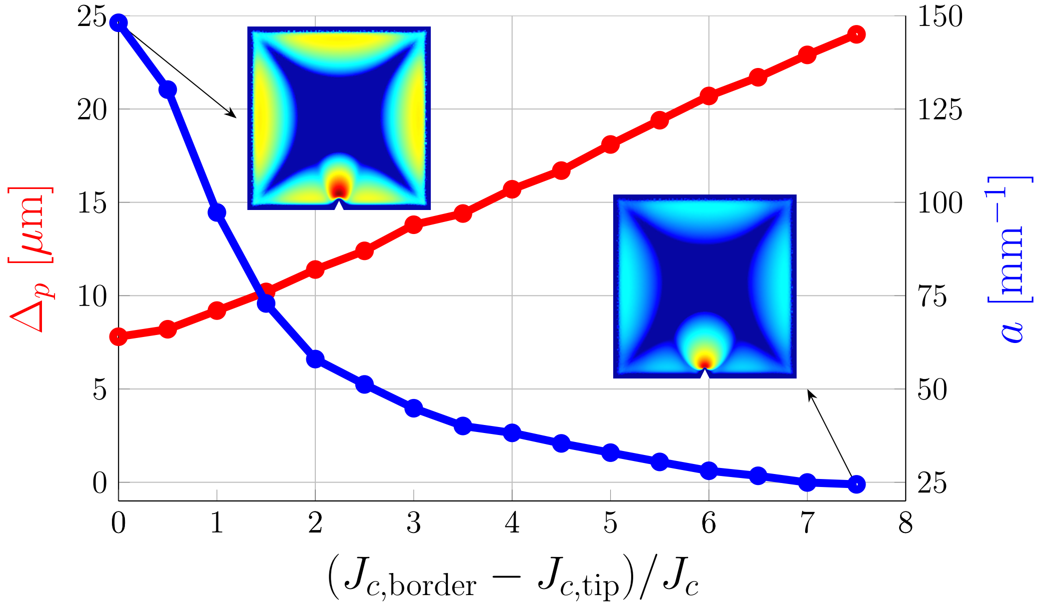

Figure 3.6: Excess penetration depth, Δ_p, and the concavity of the d-lines around the triangular indentation, a, as a function of $(J_{c,\text{border}} - J_{c,\text{tip}})/J_c$ in a thin film of length $L = 200$ μm and thickness $d = 100$ nm, with a triangular indentation of basis length $b = 10$ μm and height $h = 10$ μm. The surface barriers are modelled by means of the critical current density model, with bulk pinning and surface pinning that are set to $J_c = 1$ MA/cm^2 and $J_{c,\text{border}} = 10$ MA/cm^2 respectively, see Figure 3.3 for a description of the different pinning regions.

The value of Δ_p appears to increase linearly with $(J_{c,\text{border}} - J_{c,\text{tip}})/J_c$, i.e. as the surface barrier mismatch becomes larger. By contrast, a is inversely proportional with $(J_{c,\text{border}} - J_{c,\text{tip}})/J_c$. This is coherent with what was obtained numerically in the longitudinal geometry and theoretically predicted with the simplified analysis in the beginning of the chapter. However, for the smaller values of the critical current density ratio, one has $\Delta_p < 10$ μm and $a > 50$ mm^{-1}, i.e. results that deviate from the predictions of the Bean model. When the surface barriers are omitted from the modelling, it was found that $\Delta_p = 9$ μm and $a = 66$ mm^{-1}, which still differs from what is expected in the Bean model.

This actually points to different difficulties concerning the definition of a that go beyond the uncertainty due to the mesh quality. First, the d-lines around an indentation are parabolic only far enough from the indentation. Closer to the indentation, this is not the case, as for instance illustrated in the context of the Bean model without surface barrier effects, where the d-lines first form straight lines which are dependent on the geometry of the indentation [41]. Since the location of the transition between the non-parabolic and the parabolic parts of the d-lines is difficult to assess, the parabolic fitting of the magnetic field minima may be influenced. Second, the nature of the criterion that is chosen to locate the d-lines can also lead to a large uncertainty on the value of a for the lowest ratios $(J_{c,\text{border}} - J_{c,\text{tip}})/J_c$. Finally, one should be aware that the values of Δ_p might change with H_a and n [207], even though it was verified that a remains insensitive to these parameters. However, these imperfections do not question the clear variations of Δ_p and a with changing $(J_{c,\text{border}} - J_{c,\text{tip}})/J_c$.

Finally, let us discuss how the influence of the temperature can be related to the opening of the parabolic d-lines when surface barriers are considered. First, one expects J_c, $H_{c,1}$, and H_c to scale as $1 - T/T_c$ near T_c. For no indentation and a perfect barrier along the edge, $H_p \sim H_c$ and one does not expect substantial variations of the ratio H_p/J_c. One possible mechanism arises when $H_p(T)$ experimentally exhibits a non-linear variation with T, as shown in [87, 217] for untwinned YBCO crystals. In the presence of a small surface defect, $H_p(T)$ exhibits two temperature regimes. Near T_c, the vortices have radii much larger than the defect size and their nucleation is unaffected, yielding $H_p \sim H_c \propto 1 - T/T_c$. For lower temperatures, the defect effectively acts as a flux gate and $H_p(T)$ exhibits a smaller temperature variation. In such a scenario, the ratio H_p/J_c would increase with T in the first regime and level off as T approaches T_c. Other mechanisms leading to non-linear variations may also arise from thermal activation over the barriers [218]. In such a case, one would expect the penetration of magnetic flux to be increasingly easier near the tip as T is increased, since the height of the surface barrier is lower in this region.

Eventually, the temperature dependence of the excess path length $\Delta L = (\Delta H_{p,\text{border}} - \Delta H_{p,\text{tip}})/J_c$ will depend on the temperature variations of the surface barrier both near the tip and along the border, so that it is difficult to conclude without further experimental observations of the magnetic flux penetration as a function of temperature. Furthermore, this phenomenon might be absent in some samples, such as in twinned YBCO [87]. In fact, the influence of temperature on the shape of the d-lines that surround rectangular and quadrilateral edge indentations has been studied in YBCO films, which were grown on a $LaAlO_3$ substrate by chemical solution deposition [130]. Photolithography masks were made by direct-writing on a photoresist reproducing the indented film shape, with the help of a micro-writer system endowed with laser-assisted technology. Wider d-lines were not reported as the temperature was increased, since the trajectories of the d-lines matched the prediction of the Bean model. The difference between YBCO and Nb films might stem from the difference in surface barriers between both materials [130]. For a given temperature, the coherence length and the lower critical field are typically lower in YBCO than in Nb, which points towards higher surface barriers in niobium films. The absence of surface barrier effects in YBCO thin disks has been reported in [219].

3.5 Conclusion

The aim of this chapter was to investigate the influence of surface barriers on the excess penetration depth and the shape of the d-lines that are induced by the presence of an edge indentation of microscopic size. In particular, it was sought to clarify whether variations of the surface barrier height in the presence of the indentation could be at the root of the opening of the parabolic d-lines, as experimentally observed in niobium films by Brisbois et al [41].

First, a preliminary study on the surface barriers in the longitudinal geometry was carried out. Relying on the results of the Bean model where edge barriers were accounted for, it was shown analytically that the suppression of the Bean-Livingston barrier in the vicinity of the sharp tip of a triangular indentation could indeed induce wider parabolic d-lines around an indentation with respect to the case where surface barriers were neglected.

A quantitative estimation of the resulting d-line opening evidenced that the amplitude of the surface barrier inhomogeneity is significant enough to induce visible changes in the curvature of the surrounding d-lines. Finally, the case of the thin-film geometry was discussed. The predominance of the Bean-Livingston barrier over geometrical barrier was justified.

Thereafter, based on a model that emulate the large peripheral Meissner currents that shield the applied field and prevent its entrance inside the superconductor, the distributions of magnetic field in the longitudinal and in the thin-film geometry were numerically investigated in the case where surface barriers are taken into account. In the longitudinal geometry, this approach appeared to correctly emulate the effect of surface barriers. The values of the excess penetration depth, the concavities of the parabolic d-lines, and the corresponding excess path length were in good agreement with the predictions of the Bean model. Using a three-dimensional FE $\mathbf{H}$-ϕ formulation, it was shown that surface barrier differences between the flat borders and the indentation tip could be held responsible for the increase of the excess penetration depth and the widening of the d-lines around the indentation in thin superconducting films. Ultimately, combined with results from the literature that highlight different temperature dependences of the first penetration field and the critical current density in YBCO when the temperature is far enough from T_c, the previously obtained numerical results advocate for the possibility of temperature-dependent widened parabola in superconducting thin films with edge indentations.

Nonetheless, the correlation between spatial inhomogeneities of the surface barriers and the temperature-dependent geometry of the d-lines should be consolidated with further experimental evidence. The temperature dependence of the penetration field in niobium films should for instance be experimentally measured, in a similar fashion to what was carried out for YBCO crystals in [217]. One could also observe the temperature dependence of the shape of the d-line patterns in other superconductors, such as MgB_2 or NbN, which surface barrier height is expected to be between that of Nb and YBCO [130]. Artificial and external interventions could also be considered to modulate the value of the first penetration field. For example, the effect of surface barriers can be reduced by evaporating a conducting layer on top of a superconducting layer [220]. Similarly, the surface barriers can be suppressed by tilting the applied magnetic field, by polishing the sample into a prismatic shape, or by directly cutting gaps or cracks in the sample [213].

The interest of surface barriers is not limited to fundamental physics, as they play a key role in many technological devices as well. For instance, superconducting bridges can have their critical current dominated by surface barrier. In this case, most of the current is concentrated along the periphery of the bridge in the form of the surface current that are generated by the surface barriers [89]. Surface barriers can also be a crucial factor in SQUIDs or single-photon detectors, as the motion of trapped vortices induce noise that affects the sensitivity of the device [221, 222]. Surface barriers also play a crucial role for the flux-flow instability mechanism by enhancing the heat dissipation close to the boundary of the superconducting film, because of the larger surface current that edge barriers generate [222, 223]. Finally, surface barriers have also been suspected to influence the onset of flux avalanches at edge indentations [41]. Indeed, it was suggested that the indentations might act as tiny flux faucets where the diffusion of magnetic flux is smoothed, as a consequence of the lowered surface barrier height in the vicinity of the indentation tip. Making progress in understanding the physics of surface barriers and developing numerical models that allow to emulate and evaluate their impact on the distribution of magnetic field in three-dimensional geometries is therefore also important from a practical standpoint.

Chapter 4

Selective triggering of magnetic flux avalanches by an edge indentation

4.1 Introduction

Thermomagnetic avalanches are sudden bursts of magnetic flux that mostly occur in superconductors in the thin-film geometry [41, 224, 225]. They are triggered because of the inability of the medium to efficiently remove the heat that is dissipated as magnetic flux progresses into the sample. The resulting local increase of temperature degrades the superconducting properties, and this in turn favours further penetration of magnetic flux. Additional heat is dissipated, and a positive feedback loop is activated that leads to the generation of flux avalanches. From a technological viewpoint, these flux avalanches often limit the accuracy, range of application, or properties of superconducting devices. The sudden bursts of magnetic flux that characterize thermomagnetic events generate noise in superconducting devices, such as SQUID magnetometers [226]. Moreover, during these flux avalanches, the temperature can locally exceed the critical temperature in a very short lapse of time, leading to the quenching of the superconducting material, or sometimes even degrading the sample irreversibly as a consequence of the local melting of the material [227, 228]. The nucleation of hotspots also implies a reduction of the critical current density in the vicinity of the avalanche, and causes the degradation of the transport abilities of the superconducting sample [229, 230].

Flux avalanches are extremely complex and erratic phenomena, showing a clear stochastic nature [46]. The morphology of magnetic flux avalanches depends on several parameters such as the thermal conductivity, the specific heat, and the normal state diffusivity, but also depends on the substrate temperature and the applied field [46]. Besides, predicting the location of flux avalanches is most of the time impossible, since they may occur anywhere along the border of a film with uniform superconducting properties. Nonetheless, the nucleation of flux avalanches can sometimes be provoked, prevented or guided by means of an external intervention [231, 232, 233], or by changing the microstructure of the sample [234].

In particular, the onset of avalanches is believed to be facilitated by the presence of indentations or around sharp concave turns [149, 227, 234]. In the vicinity of micro-scaled indentations, the pattern of the current-density lines is perturbed, in accordance with current conservation. These changes of orientations also imply a concentration of current lines in the close proximity of the sharp vertices of the indentations, which is known as *current crowding* [235]. Due to the accumulation of current lines, the electric field, $\mathbf{E}$, locally increases [103, 207, 236], which is the signature of a more intense magnetic flux line motion activity in the region, in accordance to Faraday's law [149, 236]. Both the increase of $\mathbf{J}$ and $\mathbf{E}$ leads to the increase of the Joule heat dissipation per unit volume, $\mathbf{E} \cdot \mathbf{J}$. Given the fact that current theories of avalanches relate their onset with a threshold electric field, E_{th} [123, 125], it can be easily understood that indentations are usually considered to act as preferred spots for triggering magnetic flux avalanches [227].

However, quite surprisingly, it has been observed experimentally that flux avalanches sometimes seem to avoid sharp indentations and are preferentially triggered along smooth borders [41]. This counter-intuitive observation was observed in niobium samples and are in clear contrast with what is commonly reported in the literature. In [41], it was argued that indentations could possibly act as tiny flux faucets that actually help in releasing magnetic flux as a result of a reduction of the surface barrier at these locations. However, to the best of my knowledge, this hypothesis has not yet been corroborated in the literature by complementary theoretical or numerical works.

Another element for the avoidance of the sharp indentations as preferred spots for triggering thermomagnetic events has been proposed recently, in a work to which I collaborated [237]. It is suggested that the magnetic field dependence of the critical current density, $J_c(|\mathbf{B}|)$, plays a role in determining whether the first magnetic flux avalanche nucleates somewhere along the smooth borders, at the indentation, or does not nucleate at all. As will be shown below, a magnetic-field-dependent critical current density leads to a few modifications in the actual distributions of the current lines and the electric field. Hence, the standard arguments based on current crowding, which were historically elaborated for constant J_c, need to be reanalysed. The purpose of this chapter is to revisit the notion of current crowding in the presence of magnetic-field-dependent critical current density, in relationship with the conditions for triggering magnetic flux avalanches. The chapter is organized as follows.

Section **4.2** revisits the notion of current crowding in the most common case where the critical current density is considered constant and uniform. It is assessed how an internal hole inside a superconducting slab deviates the current density flow with respect to the situation of a plain sample within which a given amount of current is fed, leading to the concentration of current lines in the vicinity of the hole. The results are studied with respect to the exponent n of the non-linear isotropic $\mathbf{E}(\mathbf{J})$ law.

In Section **4.3**, I consider the profiles of current density in a superconducting square film with a triangular indentation cut on one of its edges. The profiles are analysed to determine the location of highest electric field in the film, given that the critical current density is magnetic-field-dependent and follows Kim's law [84]. In the same time, by contrast with the case of a constant critical current density, it is shown that current lines become less dense in the vicinity of the tip of the indentation than along a non-indented border.

In Section 4.4, I explain from a more theoretical and conceptual standpoint how the $J_c(|\mathbf{B}|)$ dependence plays a role in determining whether the first flux avalanche nucleates along the smooth edges or at the sharp indentation. Based on $\mu_0 H_a$-J_c diagrams and the arguments of Section 4.3, the value of the threshold applied field, $\mu_0 H_{th}$, is estimated at both locations, which allows one to deduce the location of nucleation of the first magnetic flux avalanche. Finally, Section 4.5 concludes the chapter.

4.2 Current crowding around a circular hole in an infinitely long slab with constant J_c

Consider the theoretical case of an infinitely long superconducting slab, which extends laterally to infinity. A single circular columnar defect of radius R is pierced at some location in the sample, and an in-plane current is forced through the infinite slab along $\mathbf{e_y}$, as shown in Figure 4.1. In a defect-free sample, the trajectory of the current lines would correspond to straight lines, with a current density denoted by J_0. However, due to the presence of the circular hole, which is a current-free region, the current lines are deflected from their straight trajectory, as illustrated in Figure 4.1. From this drawing, it is immediately understood that current conservation leads to a concentration of the current lines in the vicinity of the defect, while they are nearly unaffected far enough from it. The purpose of this Section is to introduce the notion of current crowding, as it is usually understood, and to discuss its global characteristics depending on the value of the n exponent that appears in the $\mathbf{E}(\mathbf{J})$ power-law of Equation 2.18, when the critical current density, J_c, is assumed to be uniform and constant. The results of this analysis will serve as a basis of comparison with the $J_c(|\mathbf{B}|)$ case that will be investigated later on.

To this aim, the weak formulation of Faraday's law is adapted to the problem at hand. Starting from Equation 2.30 of Chapter 2 and rewriting the surface integral, one gets

$$\int_\Omega \dot{\mathbf{B}} \cdot \mathbf{\Psi} \, \mathrm{d}\Omega + \int_\Omega \mathbf{E} \cdot (\nabla \times \mathbf{\Psi}) \, \mathrm{d}\Omega - \int_\Gamma (\mathbf{E} \times \mathbf{n}) \cdot \mathbf{\Psi} \, \mathrm{d}\Gamma = 0, \tag{4.1}$$

where $\mathbf{n}$ is the normal to the boundary of Ω that points outwards. Using the constitutive laws of Equation 2.17 and Equation 2.7, one has

$$\int_\Omega \mu_0 \dot{\mathbf{H}} \cdot \mathbf{\Psi} \, \mathrm{d}\Omega + \int_\Omega \rho\left(|\nabla \times \mathbf{H}|\right)(\nabla \times \mathbf{H}) \cdot (\nabla \times \mathbf{\Psi}) \, \mathrm{d}\Omega - \int_\Gamma (\mathbf{E} \times \mathbf{n}) \cdot \mathbf{\Psi} \, \mathrm{d}\Gamma = 0, \tag{4.2}$$

where $\rho(|\nabla \times \mathbf{H}|)$ is given by Equation 2.18. The basis functions, Ψ, are still included in the function space $\mathrm{F}_1^{\mathrm{h}}(\Omega)$. However, the slab geometry allows for some simplifications. The absence of demagnetizing effects allows one to reduce the three-dimensional problem to a two-dimensional one, with $\mathbf{H} = H_z(x, y)\, \mathbf{e}_z$, and $\mathbf{J}$ being oriented in-plane. Moreover, the boundary conditions can be directly applied on the border of the slab, so that the non-conducting region does not have to be meshed and thereby $\Omega \equiv \Omega_c$.

The boundary conditions of the system are imposed as follows. The origin of the coordinate system is taken as the centre of the circular hole and denoted by O. The magnetic field is set to $H_z = H_a = J_c L$ on the left edge of the square domain, $H_z = -H_a = -J_c L$ on its right edge, and $H_z = 0$ on the circumference of the cavity. By Ampere's law, these

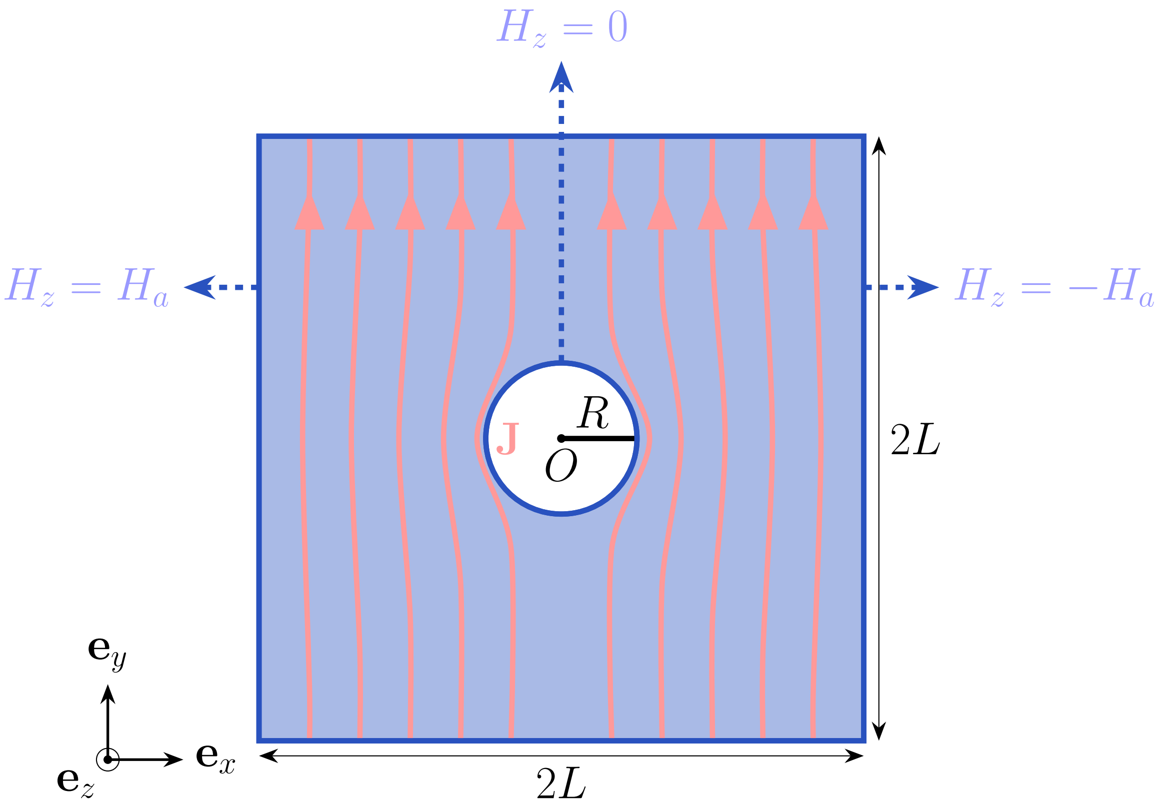

Figure 4.1: Illustration of a square domain of length $2L$ that is centred around O, the centre of a columnar defect of radius R, which is pierced into an infinitely long slab of infinite planar extension. O coincides with the origin of the Cartesian orthonormal coordinate system. The current lines, $\mathbf{J}$, are schematically represented in pink. The boundary condition $H_z = -H_a$ is imposed on the right side and $H_z = H_a$ on the left side of the square cross section that encloses Ω. $H_z = 0$ on the circumference of the hole. The indicated boundary conditions force a net current density across the upper and lower edges of the domain, which is directed in the $\mathbf{e}_y$ direction and which intensity is $J_0 = H_a/L$.

conditions impose a net current $2J_cL$ per unit height inside the superconductor, while no current flows through the cavity. Furthermore, the symmetry of the geometry and the boundary conditions imply that the surface integral in Equation 4.2 vanishes over Γ. These specific boundary conditions and the geometry of Ω are summarized in Figure 4.1. In the context of the simulations of this section, $L = 50\sqrt{2}R$, $J_c = 1$ MA/cm^2. The mesh size varies from $R/(50\sqrt{2})$ on the boundary of the defect to $L/50$ on the boundary of the square.

Figure 4.2 shows the amplitude of the perturbation of the current density around the hole, δJ, on the line that is aligned with $\mathbf{e}_x$ axis and passes through the center of the circular hole, as shown by the red line in the inset. X is the distance of a point on this line from the centre of the defect. The excess current density, δJ, is defined as

$$\delta J = |\mathbf{J}| - J_0, \tag{4.3}$$

where $\mathbf{J}$ is the current density that is numerically evaluated in the case of the pierced slab. The profiles of δJ are numerically evaluated for different values of the exponent n,

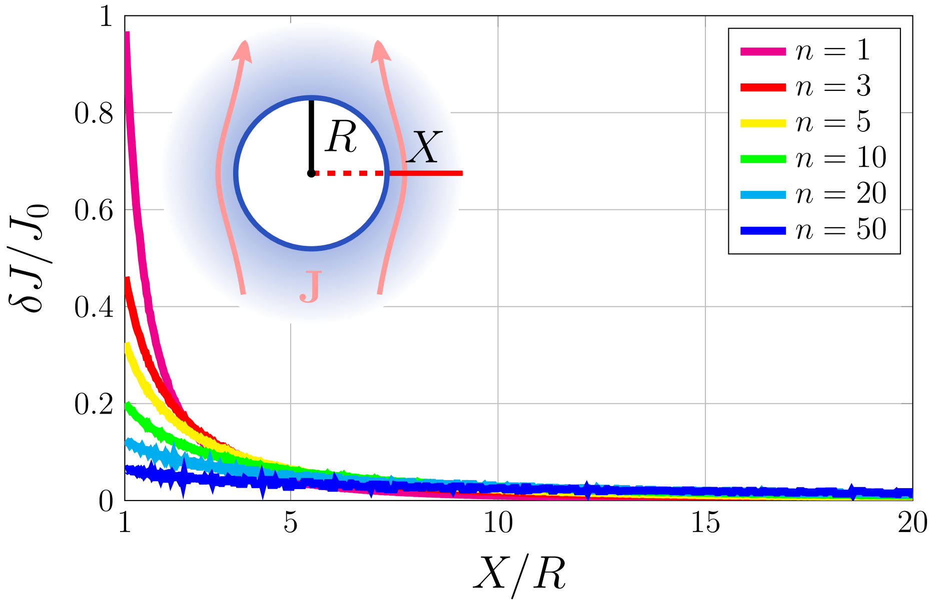

Figure 4.2: Excess current density, $\delta J/J_0$, around a circular hole of radius R as a function of the distance from the center of the disk, X/R, along a horizontal line that passes through the center, in red in the inset. J_0 is the current density that would flow in a sample without the hole. The perturbation $\delta J/J_0$ is represented for various values of the exponent n that describes the non-linear $\mathbf{E}(\mathbf{J})$ law.

and J_0 is set to 1 MA/cm^2 for all values of n. For each n, the monotonic decay of $\delta J/J_0$ with X/R is obvious. Besides, two main observations can be inferred from these graphs. On the one hand, one can observe that the higher n, the smaller δJ in the vicinity of the hole. This is equivalent to say that current crowding around the hole is reduced with n. On the other hand, the smaller n, the steeper the decay of the perturbation. This last effect is a consequence of current conservation, which prescribes that the integral of δJ from $X/R = 1$ to $X/R \to \infty$ is equal to $J_0 R$ for any value of n, since $\mathbf{J}$ is directed towards $\mathbf{e}_y$ along this line for symmetry reasons.

It is possible to give an estimate of the steepness of the monotonic decrease of $\delta J/J_0$ as a function of X/R by assuming that $\delta J/J_0$ decays as $C.(X/R)^p$, where C and p are a parameters that depend on n. In particular, p describes the steepness of the decay of $\delta J/J_0$. A least-square fit of the $\delta J/J_0$ profiles for different values of $1 \leq n \leq 50$ yields the n-dependence of the index p shown in Figure 4.3. As n increases, p increases monotonically, which corroborates the smoother variations of $\delta J/J_0$ observed in Figure 4.2. Thus, the distribution of $|\mathbf{J}|$ becomes more uniform as n increases, and the perturbation of the current density around the hole extends over larger spatial scales.

It is interesting to compare the extreme cases $n = 1$ and $n \to \infty$ with each other. The case $n = 1$ corresponds to an ohmic material. It can be theoretically demonstrated that the perturbation behaves as $(X/R)^{-2}$, while current conservation dictates that the current density at the boundary of the hole is twice its value at an infinite distance from it, i.e. $\delta J/J_0 = 1$ when $X/R = 1$. The current deviations are therefore rapidly smeared out, so that the current lines are significantly deviated in the close proximity of the defect only. This was indeed numerically validated in Figure 4.2 and Figure 4.3. By contrast, in the

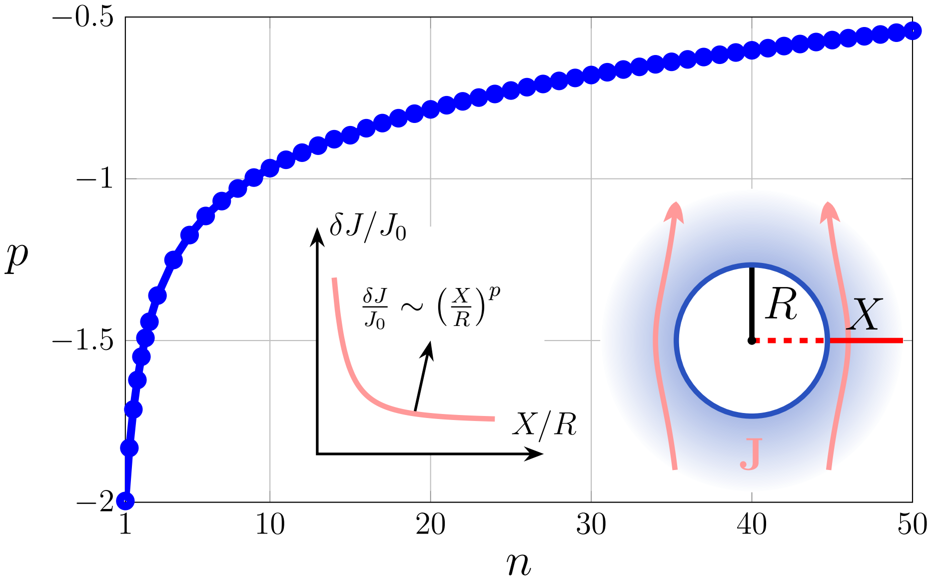

Figure 4.3: Value of the exponent p as a function of the exponent n in the non-linear $\mathbf{E}(\mathbf{J})$ constitutive law. The exponent p characterizes the decrease of the excess current density, $\delta J/J_0$, that results from current crowding around a circular hole of radius R, provided it takes the form $C.(X/R)^p$, with X being the distance from the centre of the disk along a horizontal line that passes through the center, in red in the inset, and C is a constant. J_0 is the current density that would flow in the same sample without the hole.

other limiting case $n \to \infty$, one should expect $\delta J/J_0$ to tend to 0, while the perturbation extends over an infinite distance, i.e. $p = 0$. This situation corresponds to the critical state model, according to which a defect modifies the distribution of the current density in the whole material. Interestingly, this last situation is similar to the perturbation of alignment that stems from a book placed under a wall of bricks. The bricks being very rigid, they cannot align in the vicinity of the book. The misalignment propagates over the whole wall, since the position of a given brick depends on the layout of the other bricks on top of which it is placed. From this analogy, increasing n can thus be interpreted as a stiffening of the medium from an electromagnetic point of view.

While the current density is enhanced along the $\mathbf{e}_x$ axis, this is not the case everywhere in the whole surroundings of the hole. This is illustrated in Figure 4.4 which represents the two-dimensional maps of $\delta J/J_0$ for the same values of n as in Figure 4.2. The color scales confirm the enhancement of the current density along $\mathbf{e}_x$, especially in the vicinity of the hole, while they also indicate that the current density is depressed close to the apexes of the circular hole. In any case, the value of $\delta J/J_0$ wanes with the distance from the hole and therefore asymptotically tends to zero. The regions of enhanced and depressed current density are delimited from each other by a geometrical structure that becomes more salient as n increases. These structures take a parabolic shape and are reminiscent of discontinuity lines that emerge around a circular defect in superconductors [41].

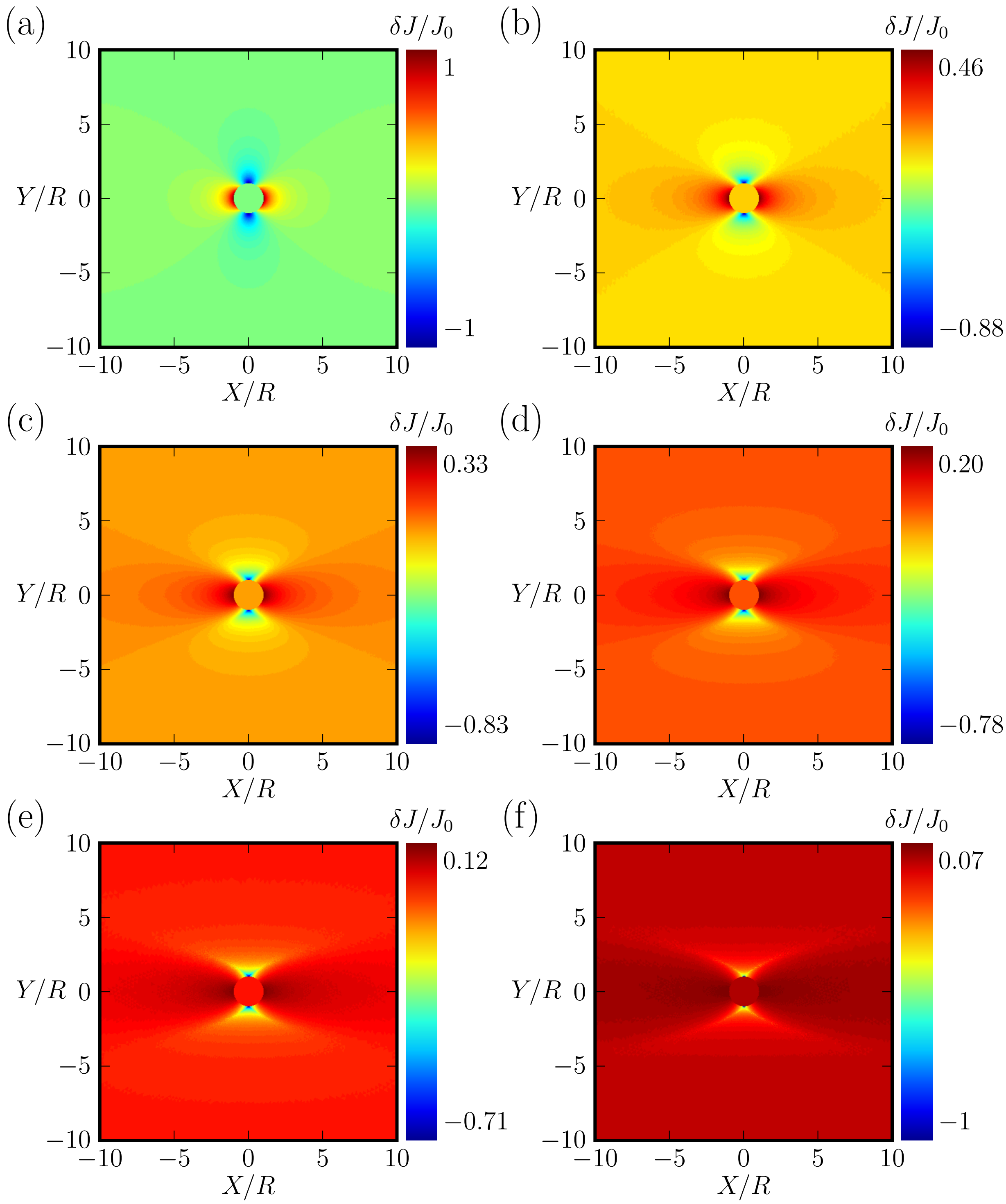

Figure 4.4: Two-dimensional maps of the current density perturbations around a circular hole of radius R in a superconducting slab of infinite extension for various values of the exponent n of the non-linear $\mathbf{E}(\mathbf{J})$ constitutive law. One has (a) $n = 1$, (b) $n = 3$, (c) $n = 5$, (d) $n = 10$, (e) $n = 20$ and (f) $n = 50$. A constant current density of magnitude $J_0 = 1$ MA/cm^2 is forced from the bottom edge to the top edge. The current-crowding effect is assessed through the normalized perturbation of the norm of the current density with respect to J_0, which is denoted by $\delta J/J_0$.

4.3 Influence of $J_c(|\mathbf{B}|)$ on the distribution of H_z, $|\mathbf{J}|$ and $|\mathbf{E}|$ in thin films with an edge indentation

In the previous section, a general investigation of the deviation of the current lines around a circular defect, in the slab geometry, and considering a constant current density, has been carried out. In particular, it was shown that the presence of the defect induces an accumulation of current lines around the hole, in the regions where the current has to bypass it. This is known as the current-crowding effect. This analysis is now extended to the more realistic case of a thin square film of length L and thickness d, where a triangular indentation of height h and basis b is cut in the middle of one of its edges. The film is subjected to an out-of-plane magnetic field of intensity H_a, which is ramped up from 0 at a constant rate $\dot{H}_a$. The critical current density is also assumed to be magnetic-field-dependent and to follow Kim's law.

Two objectives are pursued in this section. First, it sought to determine how the triangular indentation affects the distribution of the out-of-plane component of the magnetic field, H_z, the norm of the current density, $|\mathbf{J}|$, and the norm of the electric field, $|\mathbf{E}|$, with respect to non-indented edges, when a magnetic field dependence of the critical current density is accounted for. Second, it will be analysed if the behaviour of these fields is sensitive to changing parameters, such as the temperature of the substrate, the applied field rate, or the detailed magnetic field dependence.

To this aim, the finite-element $\mathbf{H}$-ϕ formulation that was developed in Chapter 2 is used. The simulated domain, Ω, consists in a cubic box of extension $2L_{ph}$, with $L_{ph} = 0.1$ m, with the Dirichlet boundary conditions applied on its boundary, Γ. The conducting region, Ω_c, consists in the indented superconducting film, with $L = 2$ mm, $d = 100$ nm, $h = 62$ μm, and $b = 124$ μm. The applied field rate is set to $\mu_0 \dot{H}_a = 3$ T/s. The critical current density and the exponent n that appears in Equation 1.33 are assumed to vary as [237]

$$J_c(T, B) = J_c(0,0) \left(1 - \frac{T}{T_c}\right) \frac{B_0}{B_0 + |\mathbf{B}|}, \tag{4.4}$$

$$n(T) = n(0)\, \frac{T_c}{T}, \tag{4.5}$$

with $J_c(0,0) = 12$ MA/cm^2 and $n_0 = 20$. The magnetic field dependence of Equation 4.4 follows Kim's law with $\alpha = 1$, see Equation 1.25. Note that all geometric and physical parameters correspond to those in [237]. The substrate temperature is in a first time set to $T_0 = 2.5$ K, and the critical temperature is $T_c = 9.2$ K. Although the heat equation should be coupled to Maxwell's equations to model flux avalanches, as it was done in [237], in practice, the heat equation oftentimes has little effect on the variations of the electromagnetic properties of the superconductor when $H_a < H_{th}$, where H_{th} is the threshold field at which the first avalanche is recorded. This is for instance illustrated in panel (b) of Figure 9 in [237], which indicates that the temperature is nearly uniform and equal to T_0 before the first avalanche is triggered. In what follows, Maxwell's equations will be solved assuming a constant temperature $T = T_0$ until the conditions for triggering a magnetic flux avalanche are met.

In what follows, it is sought to evaluate how the value of B_0 influences the distributions

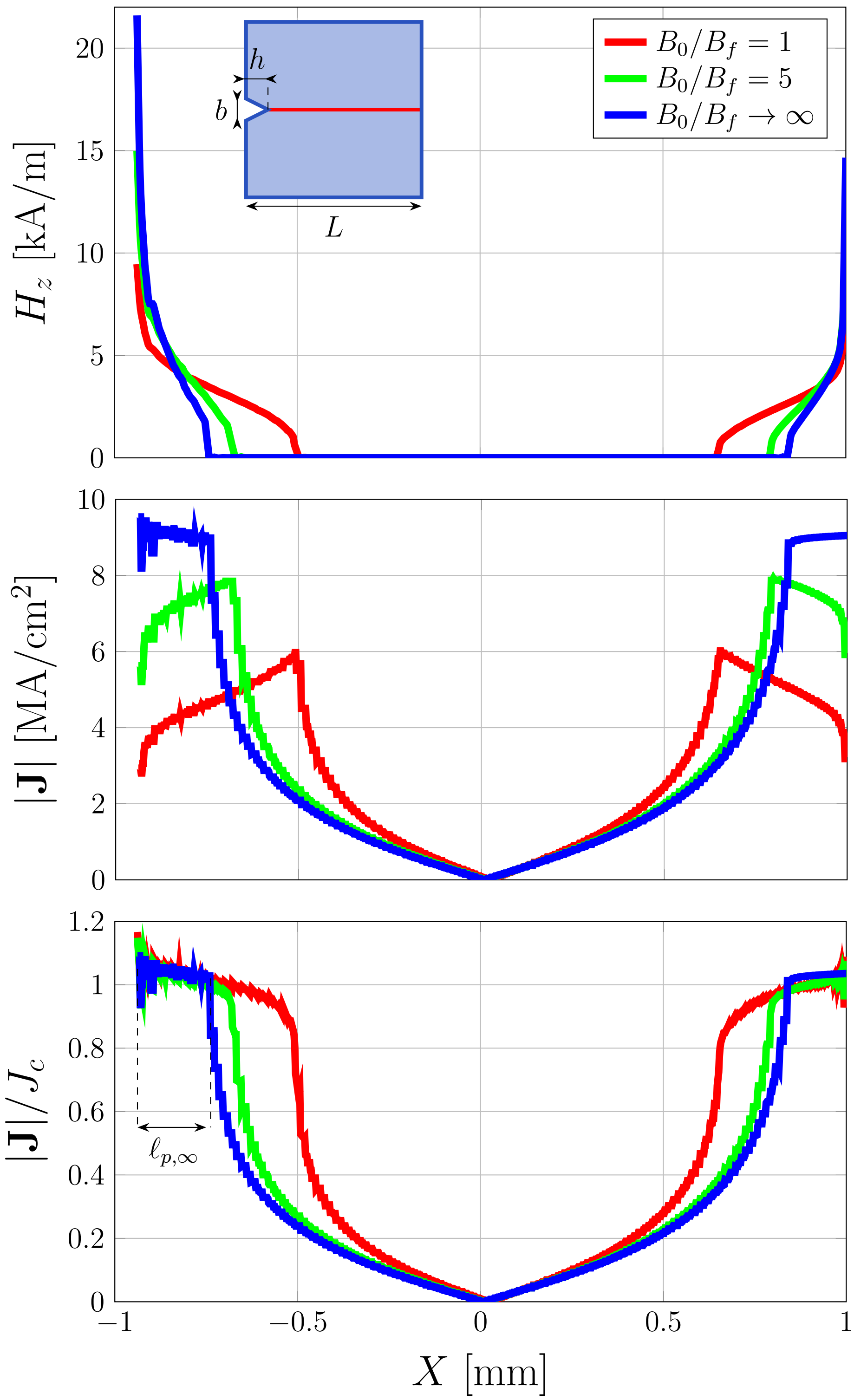

Figure 4.5: Profiles of H_z (top panel), $|\mathbf{J}|$ (middle panel), and the ratio $|\mathbf{J}|/J_c$ (bottom panel) in an indented film of length $L = 2$ mm and thickness $d = 100$ nm, for $B_0/B_f = 1$ (in red), $B_0/B_f = 5$ (in green), and $B_0/B_f \to \infty$ (in blue), where B_0 describes the magnetic field dependence of J_c, according to Kim's law, see Equation 4.4, and $B_f = \mu_0 J_c(0,0)d/\pi$. The indentation is a triangle of basis $b = 124$ μm and height $h = 62$ μm,. The shown profiles are taken along the red line depicted in the inset of the upper panel. The penetration depth when $B_0 \to \infty$, $\ell_{p,\infty}$, is also indicated in the lowest panel. $T_0 = 2.5$ K, $T_c = 9.2$ K, $J_c(0,0) = 12$ MA/cm^2, $n_0 = 20$, $\mu_0 \dot{H}_a = 3$ T/s and $\mu_0 H_a = 3$ mT.

of H_z, $|\mathbf{J}|$ and $|\mathbf{E}|$, and how their levels close to the tip of the triangular indentation and in the vicinity of the middle of one of the smooth edges compare to each other. In what follows, the magnitude of $|\mathbf{J}|/J_c \sim |\mathbf{E}|^{1/n}$ will be represented instead of $|\mathbf{E}|$. Figure 4.5 shows the profiles of H_z, $|\mathbf{J}|$ and $|\mathbf{J}|/J_c$ along the median of the square that passes through the tip of the indentation for $B_0/B_f = 1$, $B_0/B_f = 5$ and $B_0/B_f \to \infty$, with $B_f = \mu_0 J_c(0,0)d/\pi$ being a characteristic field amplitude in the film geometry [238, 239], and for an applied field $\mu_0 H_a = 3$ mT. The magnetic field dependence of the critical current density therefore plays a major role when $B_0/B_f = 1$, even at an early stage of flux penetration, while it is rather limited until the applied field reaches large values in the case $B_0/B_f = 5$, or even non-existent when $B_0/B_f \to \infty$. First, let us focus on the profiles of H_z, as depicted in the top panel of Figure 4.5. Magnetic field decreases monotonically as one progresses deeper inside the sample and approaches the center. The presence of the indentation implies two main characteristics, which are an excess of field penetration at the indentation, and higher levels of H_z around the indentation in comparison to those observed at the smooth border. These observations hold independent of B_0. Finally, if one defines $f_{H,\triangle}$ as

$$f_{H,\triangle} = \frac{H_z(h)}{H_z(L)}, \tag{4.6}$$

with $H_z(x)$ being the value of H_z at a distance x from the left border of the film, as indicated in the inset of panel (a) of Figure 4.5, one obtains the ratios $f_{H,\triangle} = 1.25$, $f_{H,\triangle} = 1.34$ and $f_{H,\triangle} = 1.47$ for $B_0/B_f = 1$, $B_0/B_f = 5$ and $B_0/B_f \to \infty$, which quantify the enhancement of the magnetic field at the indentation. Increasing the value of B_0 thus seems to increase the enhancement of the magnetic field around the indentation with respect to its value along the smooth borders.

The corresponding $|\mathbf{J}|$ profiles are shown in the middle panel of Figure 4.5. In the case $B_0 \to \infty$, which is the case of a magnetic field independent critical current density, the current density decreases monotonically from the edges towards the centre of the film. Despite the presence of numerical fluctuations in the vicinity of the indentation, a slight increasing trend is observed as one approaches the tip of the indentation. The level of the current density is higher around the tip of the indentation than on the smooth border, which reflects the current-crowding effect around the tip of the indentation. According to Equation 4.5, the large value $n = 73.6$ explains why current crowding only influences marginally the value of $|\mathbf{J}|$, as it is enhanced by 5.4% with respect to the value of $|\mathbf{J}|$ at the smooth border.

When $B_0/B_f = 1$ or $B_0/B_f = 5$, $|\mathbf{J}|$ increases in the penetrated regions, as one gets closer to the magnetic flux front and is the lowest close to the boundary of the film. In the Meissner current region, the current density decreases as one progresses towards the centre. Moreover, the extension of the penetrated region increases as B_0 decreases. These features are signatures of Kim's model [238, 239] and were also analytically derived in the slab geometry, see for instance Equation 1.27, Equation 1.28 and Figure 1.6. Besides, the magnitude of $|\mathbf{J}|$ in the penetrated area increases as B_0 is increased. Let us define the enhancement of the current density $f_{J,\triangle}$ as

$$f_{J,\triangle} = \frac{|\mathbf{J}|(h) - |\mathbf{J}|(L)}{|\mathbf{J}|(L)}, \tag{4.7}$$

where $|\mathbf{J}|(x)$ represents the value of $|\mathbf{J}|$ at a distance x from the left border of the film. The levels of $|\mathbf{J}|$ appear to be slightly depleted at the indentation in comparison to their level at the middle of a non-indented border, as corroborated by the values $f_{J,\triangle} = -7.9\%$ and $f_{J,\triangle} = -5.1\%$ for $B_0/B_f = 1$ or $B_0/B_f = 5$, respectively. The indentation thus exacerbates the natural depletion of $|\mathbf{J}|$ that results from Kim's law. This observation contrasts with the case of a magnetic field independent J_c, i.e. $B_0/B_f \to \infty$, where the current density is the largest at the vertex of the indentation.

Let us finally turn to the bottom panel of Figure 4.5. As it can be seen from the comparison with the top panel, when $B_0 \to \infty$, the profiles of $|\mathbf{J}|/J_c$ and $|\mathbf{J}|$ coincide. This is unsurprising, since J_c is constant. However, once B_0 is finite, the profiles of $|\mathbf{J}|/J_c$ differ with those of $|\mathbf{J}|$. For any B_0, the ratio $|\mathbf{J}|/J_c$ barely changes over the distance $\ell_{p,\infty}$, which is the penetration length in the case $B_0 \to \infty$. $\ell_{p,\infty}$ is the minimal extension of the penetrated region for a given $\mu_0 H_a$ and variable B_0. For any value of B_0, the profiles of $|\mathbf{J}|/J_c$ are monotonically decreasing when approaching the centre of the film, and the highest values are reached at the boundary of the film. In particular, the highest value of the ratio $|\mathbf{J}|/J_c$ is located around the tip of the indentation, while $|\mathbf{J}|$ reaches its lowest value there. The numerical fluctuations are one more time detrimental to the direct comparison of all these curves close to the borders or the triangular indentation. However, based on the simulations, it seems that the levels $|\mathbf{J}|/J_c$ are slightly enhanced at the indentation with respect to the levels at the smooth borders. Therefore, the indentation always coincides with the location where the ratio $|\mathbf{J}|/J_c$ is the largest, whether a $J_c(|\mathbf{B}|)$ dependence is used or not.

From the inspection of Figure 4.5, three important implications can be established. First, since the ratio $|\mathbf{J}|/J_c$ remains higher at the tip of the triangular indentation than on the smooth border in all cases, the magnitude of the electric field $|\mathbf{E}| = E_c|\mathbf{J}/J_c|^n$ is the highest at the tip of the indentation. As usually reported in the literature, indentations enhance the intensity of the electric field. Second, contrarily to what is commonly assumed, current crowding does not necessarily mean that current lines are concentrated around the tip of the triangular indentation as a result of the deformation of the current lines close to it. On the contrary, considering a magnetic-field-dependent J_c implies that current density is the lowest at the sharp tip, so that the magnetic field gradients are lower at the indentation tip than along the straight edges of the film. Finally, the indentation always enhances the magnetic field intensity with respect to what it is along the smooth borders.

Up to this point, the role played by the indentation on the distributions of H_z, $|\mathbf{J}|$ and $|\mathbf{J}|/J_c$ when a magnetic-field-dependent $J_c(|\mathbf{B}|)$ is accounted for has been highlighted. The above observations were obtained for an invariant set of values of the parameters $\mu_0 H_a$, $\mu\dot{H}_a$ and T_0, which all influence the distributions of the aforementioned fields. Therefore, it is legitimate to ask if variations of these parameters change anything to the way the indentation modifies the magnitude of the electromagnetic fields, when a $J_c(|\mathbf{B}|)$ dependence comes into play.

The results of Figure 4.6, Figure 4.7 and Figure 4.8 show the distributions of H_z, $|\mathbf{J}|$ and $|\mathbf{J}|/J_c$ when $\mu_0 H_a$, $\mu_0\dot{H}_a$ and T_0 vary, respectively, while the other parameters are kept constant. In all three figures, $J_c(|\mathbf{B}|)$ follows Kim's law, with $B_0/B_f = 1$. The sets of parameters that are used in each simulation are mentioned in the captions of each figure. From Figure 4.6, it can be noted that magnetic field penetrates further in the film when H_a is increased, as expected, while its level globally increases with H_a. Meanwhile, the profiles of $|\mathbf{J}|/J_c$ progressively rise as H_a is ramped up.

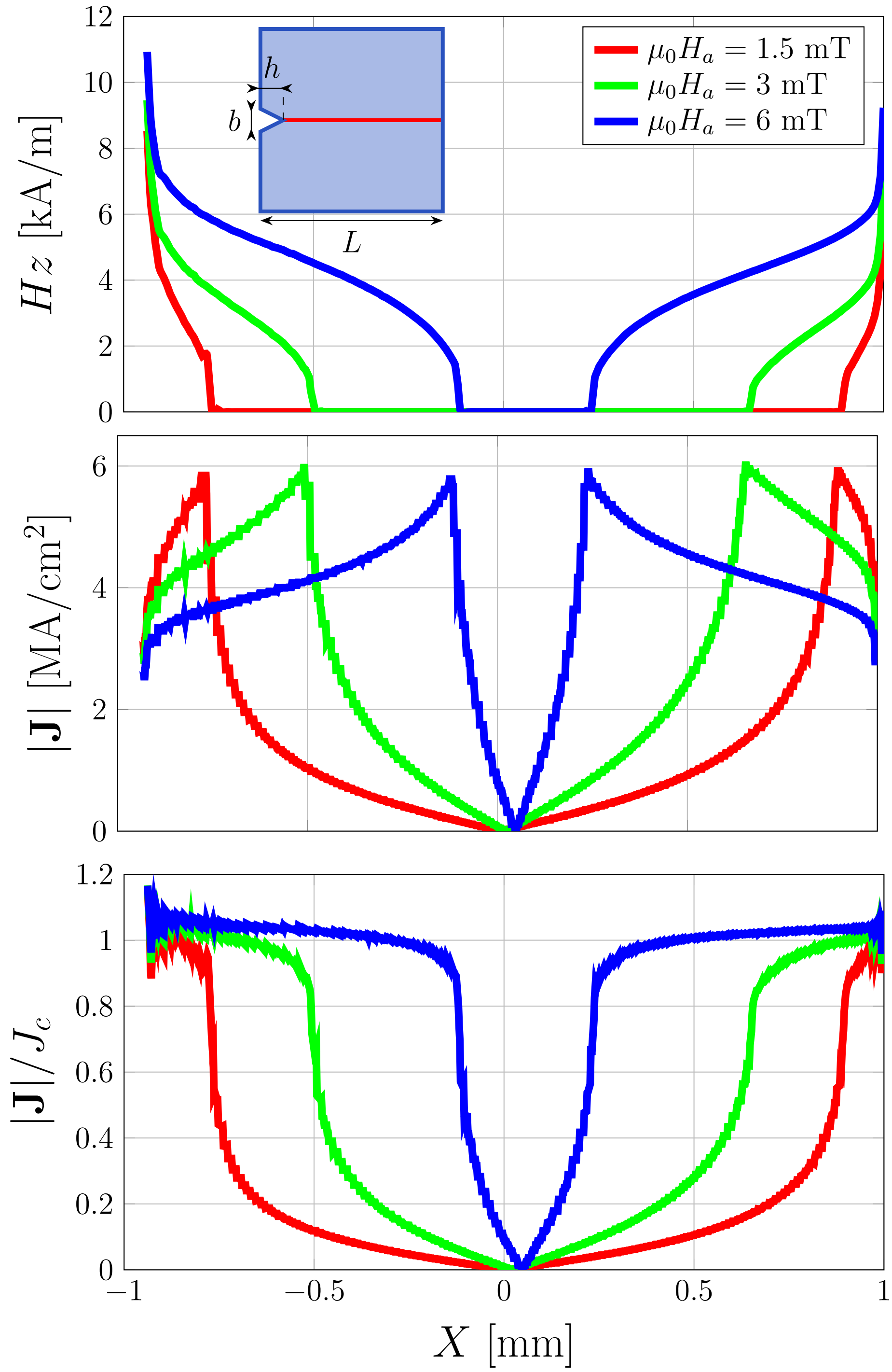

Figure 4.6: Profiles of H_z (top panel), $|\mathbf{J}|$ (middle panel), and the ratio $\mathbf{J}/J_c$ (bottom panel) in an indented film of length $L = 2$ mm and thickness $d = 100$ nm, for an applied field equal to $\mu_0 H_a = 1.5$ mT (in red), $\mu_0 H_a = 3$ mT (in green), and $\mu_0 H_a = 6$ mT (in blue). The indentation is a triangle of basis $b = 124$ μm and height $h = 62$ μm, and the shown profiles are taken along the red line depicted in the inset of the upper panel. The critical current density follows Kim's law, see Equation 4.4. $T_0 = 2.5$ K, $T_c = 9.2$ K, $J_c(0, 0) = 12$ MA/cm^2, $B_0 = B_f = 4.8$ mT, $n_0 = 20$, and $\mu_0 \dot{H}_a = 3$ T/s.

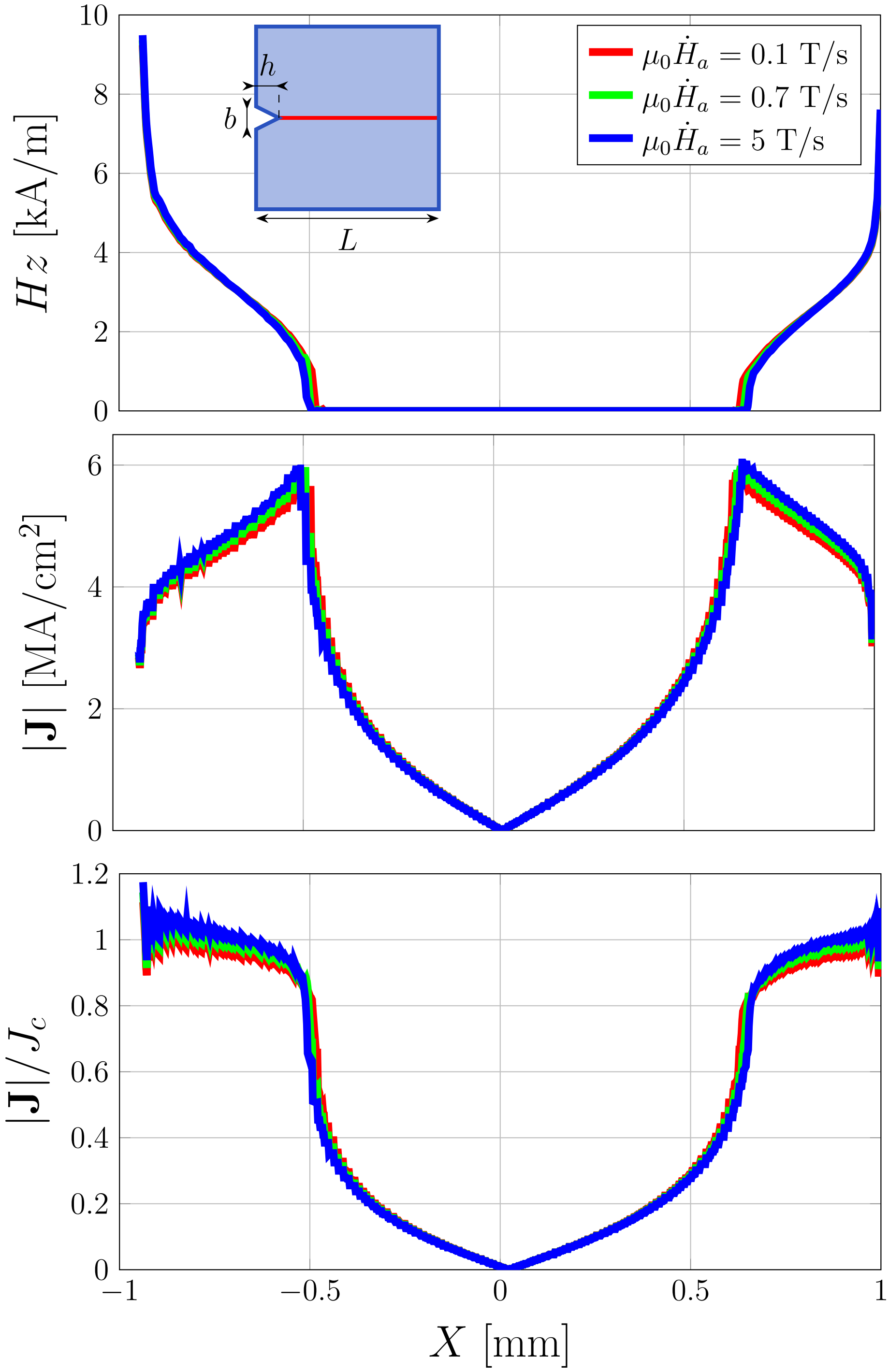

Figure 4.7: Profiles of H_z (top panel), $|\mathbf{J}|$ (middle panel), and the ratio $|\mathbf{J}|/J_c$ (bottom panel) in an indented film of length $L = 2$ mm and thickness $d = 100$ nm, for an applied field rate equal to $\mu_0\dot{H}_a = 0.1$ T/s (in red), $\mu_0\dot{H}_a = 0.7$ T/s (in green), and $\mu_0\dot{H}_a = 5$ T/s (in blue). The indentation is a triangle of basis $b = 124$ μm and height $h = 62$ μm, and the shown profiles are taken along the red line depicted in the inset of the upper panel. The critical current density follows Kim's law, see Equation 4.4. $T_0 = 2.5$ K, $T_c = 9.2$ K, $J_c(0,0) = 12$ MA/cm^2, $B_0 = 4.8$ mT, $n_0 = 20$ and $\mu_0 H_a = 3$ mT.

B_0 (mT)	$\mu_0 H_a$ (mT)	$\mu_0 \dot{H}_a$ (T/s)	T_0 (K)	$f_{H,\triangle}$	$f_{J,\triangle}$
4.8	3	3	2.5	1.25	−7.9%
24	3	3	2.5	1.34	−5.1%
∞	3	3	2.5	1.47	5.4%
4.8	1.5	3	2.5	1.30	−10.3%
4.8	6	3	2.5	1.18	−5.3%
4.8	3	0.1	2.5	1.25	−7.7%
4.8	3	0.7	2.5	1.25	−7.9%
4.8	3	5	2.5	1.25	−8%
4.8	3	3	3.5	1.25	−5.3%
4.8	3	3	5	1.25	−1.5%

Table 4.1: Summary of the values of $f_{H,\triangle}$ and $f_{J,\triangle}$ for the different combinations of the parameters B_0, $\mu_0 H_a$, $\mu_0 \dot{H}_a$ and T_0 that are used in Figure 4.5, Figure 4.6, Figure 4.7 and Figure 4.8.

Increasing $\mu_0 \dot{H}_a$ implies an increase of the electric field, as commanded by Faraday's law. Equivalently, this has the effect of increasing the ratio $|\mathbf{J}|/J_c$, which can be observed in the bottom panel of Figure 4.7, where the curves are clearly trending upwards as $\mu_0 \dot{H}_a$ increases. By contrast, the profiles of H_z and $|\mathbf{J}|$, which are depicted in the top and middle panels of Figure 4.7 respectively, barely change, since $\mu_0 H_a$ is set to a given value.

Last, increasing T_0 simultaneously lowers J_c and n, as indicated by Equation 4.4 and Equation 4.5. For this particular value of $\dot{H}_a$, and as T_0 increases, magnetic flux enters further into the sample, the amplitude of $|\mathbf{J}|$ globally decreases, while the profiles of $|\mathbf{J}|/J_c$, and thus the profiles of the electric field, increase. This is evidenced with the middle and bottom panels of Figure 4.8. The magnetic field levels at the periphery of the film also appear to be lowered as T_0 increases, which is seen in the top panel of the same figure.

Furthermore, it is possible to compare the levels of the electromagnetic fields at the indentation with those at the middle of the opposite border by computing the ratios $f_{H,\triangle}$ and $f_{J,\triangle}$ for each set of parameters. The obtained values are summarized in Table 4.1. Similarly to what was inferred from Figure 4.5, it can be concluded that, in the investigated range of parameters, whatever the parameter that varies, the indentation simultaneously induces an enhancement of both $|\mathbf{E}|$ and H_z, and a reduction of $|\mathbf{J}|$ with respect to their respective levels along the smooth borders. When a $J_c(|\mathbf{B}|)$ dependence is assumed, the indentation therefore acts as spot of enhanced electric field and magnetic field, but cannot be considered as the location where current crowding occurs, as usually assumed in the literature.

4.4 Influence of $J_c(|\mathbf{B}|)$ on the location where magnetic flux avalanches trigger

The above analysis focuses on a general argument about the mechanism at the core of triggering magnetic flux avalanches, i.e. heat dissipation caused by Joule effect. However,

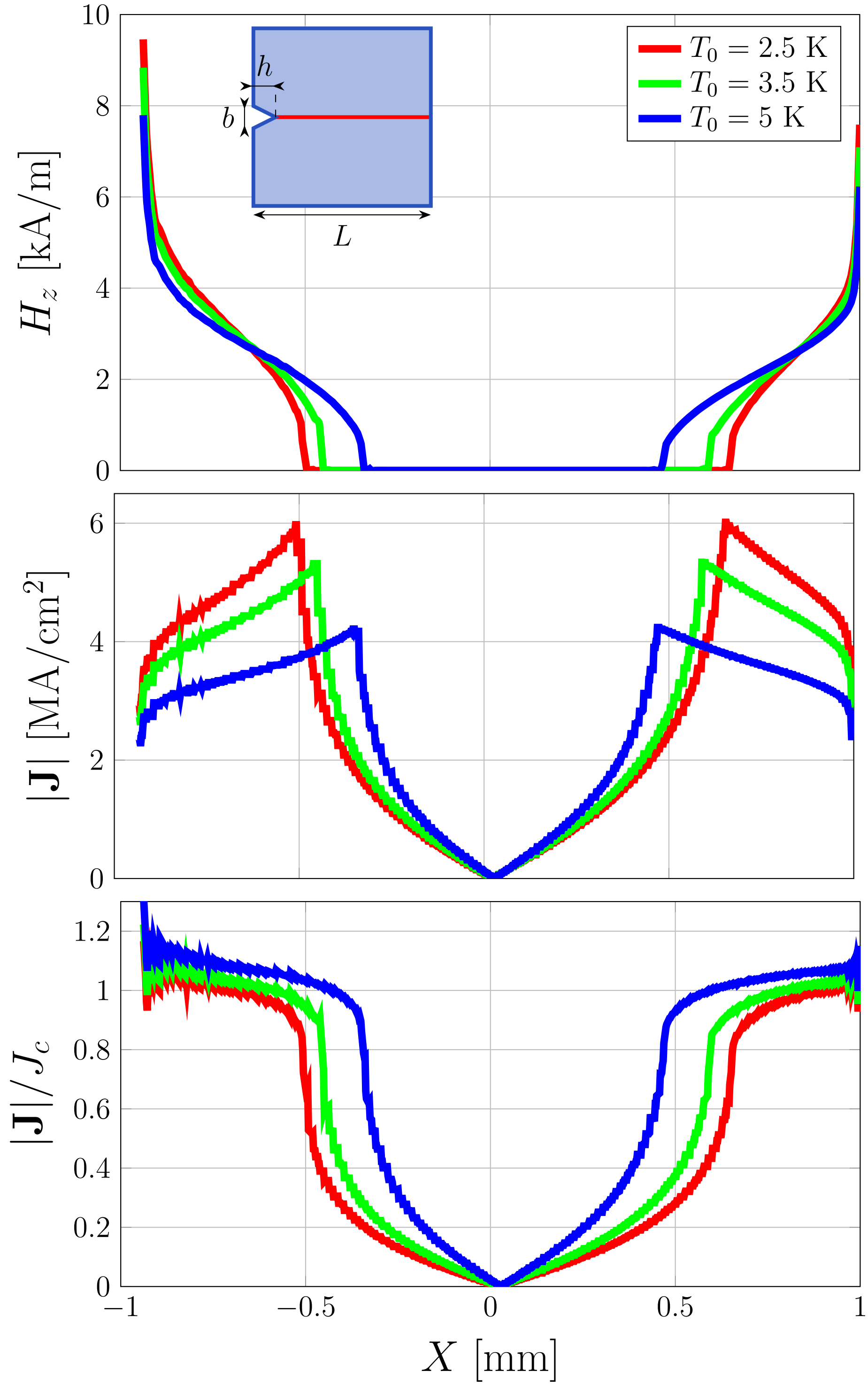

Figure 4.8: Profiles of H_z (top panel), $|\mathbf{J}|$ (middle panel), and the ratio $|\mathbf{J}|/J_c$ (bottom panel) in an indented film of length $L = 2$ mm and thickness $d = 100$ nm, when the temperature of the film is equal to the substrate temperature $T_0 = 2.5$ K (in red), $T_0 = 3.5$ K (in green), and $T_0 = 5$ K (in blue). The indentation is a triangle of basis $b = 124$ μm and height $h = 62$ μm, and the shown profiles are taken along the red line depicted in the inset of the upper panel. The critical current density follows Kim's law, see Equation 4.4. $T_c = 9.2$ K, $J_c(0, 0) = 12$ MA/cm^2, $B_0 = B_f = 4.8$ mT, $n_0 = 20$, $\mu_0 \dot{H}_a = 3$ T/s and $\mu_0 H_a = 3$ mT.

it does not really come with a definitive explanation for the onset of flux avalanches along smooth borders. To this aim, let us instead proceed with an alternative approach, which is based on the theoretical results of [126], which provides a mathematical expression for H_{th}, the onset applied field for triggering the first magnetic flux avalanche in an infinitely long thin superconducting strip of thickness d and width W, as a function of its critical current density J_c. This expression is given by the following equation, which depends on the electrical and thermal properties of the superconducting material

$$H_{th} = \frac{J_c d}{\pi} \operatorname{arccosh}\left(\frac{1}{1 - 2\ell_{th}/W}\right), \tag{4.8}$$

where

$$\ell_{th} = \frac{\pi}{2}\left(\sqrt{\frac{|\mathbf{E}|J_c}{\kappa_t T_{th}}} - \sqrt{\frac{2h_0}{nd\kappa_t}}\right)^{-1}, \tag{4.9}$$

where κ_t and h_0 are the heat conductivity and the thermal heat exchange coefficient respectively.

For a given location, the threshold field at which the first avalanche is triggered can be obtained as the intersection between the theoretical $\mu_0 H_{th}$ curve and the $\mu_0 H_a(J_c)$ curve that is evaluated at the location of interest. If the curves do not meet, no avalanche forms. Evaluating $\mu_0 H_{th}$ curves as a function of J_c requires the estimation of several thermal parameters, but also an estimate of the value of the electric field at the location where the avalanches are expected. What is sought here is to draw qualitative curves of $\mu_0 H_{th}$ that confirm the phenomenology and respect the orders of magnitude reported in the thermomagnetic simulations of [237], while keeping the explanation as simple as possible.

Starting from the main conclusions of Section **4.3**, two elements are considered. On the one hand, the magnetic field enhancement that occurs at the indentation implies different $\mu_0 H_a(J_c)$ curves at the indentation and along the smooth borders. Evaluating $\mu_0 H_a(J_c)$ can be carried out accurately by means of the FE simulations. In the present case, for $B_0/B_f = 1$, $B_0/B_f = 5$, and $B_0/Bf \to \infty$, the inverse curves $J_c(\mu_0 H_a)$ are computed numerically from 0 to $\mu_0 H_a = 6$ mT, at the indentation and at the middle of the opposite border. On the other hand, since the electric field is larger at the indentation, the values of $\mu_0 H_{th}$ are always smaller at the tip of the triangular indentation than along the smooth borders. Note that in [237], it was instead suggested that the reduction of $\mu_0 H_{th}$ at the indentation stems from the enhancement of magnetic field that occurs there. In either case, the values of $\mu_0 H_{th}$ are lowered at the indentation with respect to those along the smooth edges.

The $\mu_0 H_{th}$ and $\mu_0 H_a(J_c)$ curves for the various values of B_0/B_f at both locations are represented in Figure 4.9. The values of $\mu_0 H_{th}$ close to the triangular indentation correspond to the plain orange curve, while the dashed orange curve depicts $\mu_0 H_{th}$ around a smooth edge. Following the previous remarks, the plain orange curve systematically lies under the dashed orange one. The temperature-dependent thermal and electrical parameters are those of [237], i.e. $L = 2$ mm, $d = 100$ nm, $T_c = 9.2$ K, $T_0 = 2.5$ K, $J_c(0,0) = 12$ MA/cm^2, $n_0 = 20$, $\kappa_t = 20$ W/K.m and $h_0 = 10$ W/K.m^2. The J_c curves for $B_0/B_f = 1$, $B_0/B_f = 5$ and $B_0/B_f \to \infty$ are drawn in red, green and blue respectively. The plain curves correspond to the J_c that were numerically evaluated at the indentation, while the dashed ones were evaluated on the opposite non-indented border. The values of the electric field at the indentation and at the middle of the opposite border are set to 20 mV/m and 18.7 mV/m, respectively. Note that these orders of magnitude are coherent with those computed by means of thermomagnetic simulations in [237]. One should however keep in mind that Equation 1.49 and Equation 1.50 are in principle valid for infinitely long strips with perfectly smooth borders, although they have been assumed to hold true for finite geometries and indented samples.

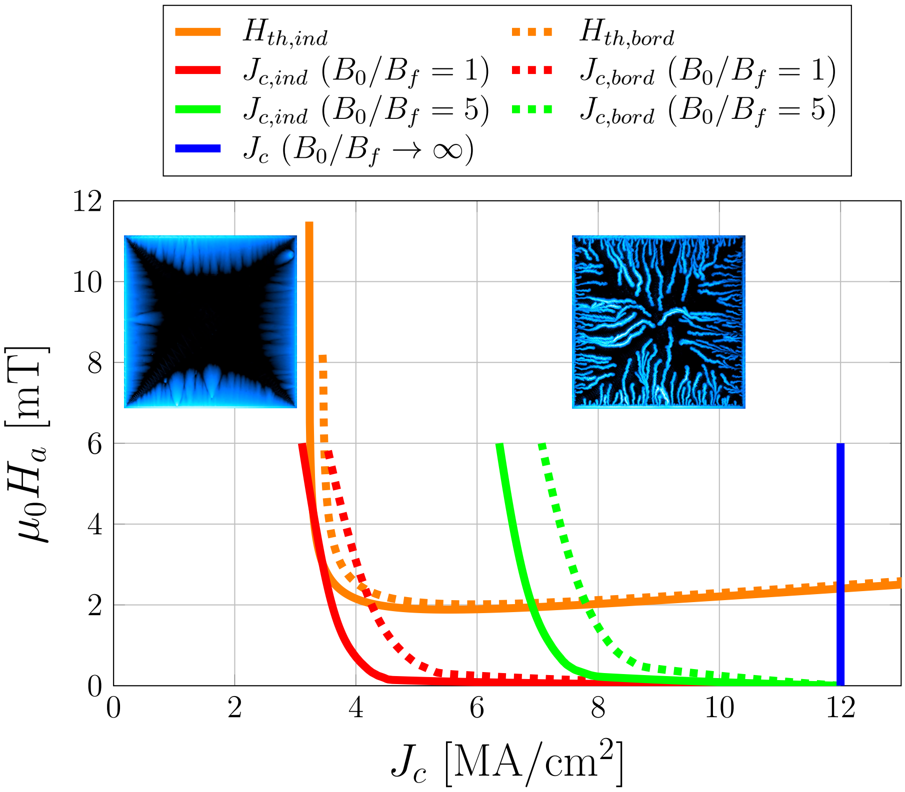

Figure 4.9: Threshold magnetic field, $\mu_0 H_a$, in mT, as a function of J_c, in MA/cm^2 in a thin film of length $L = 2$ mm and thickness $d = 100$ nm. The threshold fields (in orange) are evaluated accounting for the following physical parameters [126, 237]: $T_c = 9.2$ K, $T_0 = 2.5$ K, $J_c(0,0) = 12$ MA/cm^2, $n_0 = 20$, $\kappa_t = 20$ W/K.m and $h_0 = 10$ kW/K.m^2. The current densities are evaluated at the indentation (plain lines) and along a smooth border (dashed lines) for $B_0/B_f = 1$ (in red), $B_0/B_f = 5$ (in green) and $B_0/B_f \to \infty$ (in blue), with $B_f = \mu_0 J_c(0,0) d/\pi = 4.8$ mT, based on the results of the finite-element numerical simulations for a triangular indentation of basis $b = 124$ μm and height $h = 62$ μm.

When $B_0/B_f \to \infty$, the J_c curve (in blue) is vertical. Therefore, the avalanche, when it occurs, can only be triggered at the tip of the indentation, since the $\mu_0 H_a(J_c)$ will always meet the plain orange curve first. The situation differs once a magnetic field dependence is accounted for. When $B_0/B_f = 5$ (in green), the plain and the dashed J_c curves differ, because of the magnetic field enhancement at the indentation tip. The plain orange and green curves intersect at a value of $\mu_0 H_{th} = 1.94$ mT that remains lower than the $\mu_0 H_{th} = 2.10$ mT, which results from the intersection of the dashed curves. Therefore, an avalanche still prefers to develop around the triangular indentation. By contrast, if $B_0/B_f = 1$, the intersection of the plain red and orange curves results in a higher $\mu_0 H_{th} = 3.04$ mT than the one that corresponds to the intersection of the dashed curves, which is $\mu_0 H_{th} = 2.39$ mT. In this case, the avalanche is triggered along the smooth border rather than at the tip of the indentation, despite the electric field being larger there. If the plain red curve was slightly shifted to the left of the graph, it would even be possible to observe that avalanches only trigger along the smooth borders. These conclusions corroborate what is numerically observed in [237].

Interestingly, Figure 4.9 shows that the intensity of $|\mathbf{E}|$ does not single-handedly determine the location where avalanches trigger. The indentation is also responsible for the local enhancement of the magnetic field, which reduces the magnitude of the critical current density, and consequently the current density, in the vicinity of the indentation. Therefore, the $\mu_0 H_a(J_c)$ curve at the indentation differs from that along the border. Smaller J_c means smaller flux gradients, so that the magnetic field is less concentrated around the indentation than elsewhere, which might displace the value of the threshold field in favour of triggering avalanches along the smooth edges. The location of the avalanche nucleation thus results from the balance between the excess heat dissipation and the release of magnetic pressure that occur at the indentation.

4.5 Conclusion

This chapter was mainly devoted to explaining why magnetic flux avalanches might preferentially trigger along smooth edges rather than at the tip of an edge indentation. In a first time, current crowding has been quantified in the theoretical geometry of a circular hole in a superconducting slab that laterally extends to infinity and with constant critical current density. In order to circumvent the defect, the applied current density distribution is non uniform. An excess current density concentrates in the vicinity of the hole, and progressively relaxes back as one gets further from the hole. This relaxation back to the current density that is expected in the absence of the hole has been quantified as a function of the exponent n of the $\mathbf{E}(\mathbf{J})$ power-law. It appears that n characterizes the index of electrical rigidity of the superconducting medium. Indeed, larger values of n come with long-range perturbations of the current density profiles, which can be infinitely long in the context of the critical state model ($n \to \infty$), although the effect of current crowding is reduced, but always present.

Then, focus was put on the analysis of current crowding and the levels of magnetic field, current density, and electric field around a triangular indentation in a thin square film, considering the critical current density to be magnetic-field-dependent. It has been shown how the parameters such as the substrate temperature, B_0, a parameter that dictates the typical magnetic field dependence of the critical current density, or the applied field rate could influence the levels of the electromagnetic fields in the film. Besides, contrary to what is usually assumed, it was shown that introducing a magnetic field dependence of the critical current density implies a less dense repartition of current lines at the triangular indentation, although the location of maximal electric field still coincides with the tip of the indentation. The magnetic field was also shown to be enhanced at the triangular tip.

Finally, the previous finite-element analysis was used to explain how magnetic flux avalanches can preferentially nucleate along the smooth borders rather than at the indentation. Firstly, the enhancement of the electric field at the indentation does not only mean that more power is dissipated there, but is also equivalent to a reduction of the onset field, $\mu_0 H_{th}$, with respect to its value along the smooth borders. Secondly, the enhancement of the magnetic field at the indentation implies smoother flux gradients at the indentation, which prevents the onset of avalanches, provided that a magnetic-field-dependent critical current density is accounted for. Flux avalanches will first nucleate at the indentation only if the threshold applied magnetic field is lower there than in the close vicinity of the tip of the indentation. This was shown to happen only for sufficiently large ratios B_0/B_f, while for the smaller ratios, the avalanches develop along the smooth edges or does not occur at all.

The influence of the magnetic field dependence of the critical current density is a plausible explanation for the triggering of avalanches at locations that do not coincide with the places where power dissipation is the most intense. A balance between the enhanced dissipated power and the reduced current density occurring around the indentation is thus at the core of the determining the location of flux avalanches. This balance is intricately related to the physical properties of the film and the value of external parameters. It is however worth insisting on the fact that the results of this chapter do not exclude the possibility that a depletion of the surface barrier in the vicinity of an indentation can also prevent avalanches from nucleating at the tip of sharp indentations, as suggested in [41], and further work should be carried out to evaluate the soundness of this suggestion.

Chapter 5

Metamorphosis of discontinuity lines in thin superconducting films perforated with a regular array of triangular holes

5.1 Introduction

Ratchets consist in systems where the notion of some physical entities which motion is facilitated in a given direction, but is hindered in the opposite direction. In particular, a ratchet effect can be found in molecular motors [240], particle separation [241], rectification of self-propelled swimmers [242, 243, 244] or directional cell migration [245]. Similarly, the rectification of the motion of the flux quanta inside a superconducting sample is a ratchet phenomenon. Superconducting systems have drawn a lot of attention since one can easily vary the density of the interacting vortices, by adjusting the applied field to the right intensity, or the landscape of the vortex potential, for instance by etching arrays of antidots or defects in the superconducting sample. Not only superconducting films make for a perfect playground to study and illustrate the ratchet effect, but it has also been suggested to use them to prevent stray magnetic flux from entering in some areas in SQUID detectors [246]. Ratchet effect and networks of antidots can also be used to control the dynamics of vortices or the sudden burst of magnetic flux that occurs when thermomagentic flux avalanches are triggered [47].

Although the ratchet motion of magnetic flux is well understood at the micro-scale [247, 248], little progress has been done about the impact of non-symmetric pinning landscapes on the subsequent penetration of magnetic flux in such systems. A possible way to form a non-symmetric pinning landscape consists in etching the surface of the film with a regular lattice of single identical steps with an uneven height across the step. This was for instance done for MgB_2 films [249]. From the observation of the magnetic flux penetration patterns in the remanent state, one can infer the existence of anisotropy that does not exceed a few percent between the critical current densities associated with a current flow either along or perpendicular to the steps. It was also shown that when magnetic flux propagates in the form of sudden thermomagnetic flux avalanches, its penetration is favoured along the direction that is perpendicular to the substrate surface steps.

Another way of obtaining a non-symmetric pinning landscape consists in etching, inside the superconducting film, a square array which unit cell is made of two square antidots of different sizes. For instance, this was made in Pb films with antidot sizes larger than the coherence length and the penetration depth [250]. The directionality of the flux penetration depends on the size of the holes and the temperature of the superconductor. At low temperature, dendritic flux avalanches burst into the Pb film and propagate in the direction that frontally faces the larger hole, which coincides with the easy direction of the asymmetric pinning potential. At intermediate temperature, magnetic field diffuses smoothly inside the film and its penetration is found to be isotropic. Finally, at high temperature, magnetic field enters in the form of finger-like patterns forming along the hard direction of the pinning potential.

This chapter addresses the penetration of magnetic field in thin films that are perforated with an array of regularly spaced triangular antidots, which is yet another way to etch a ratchet potential in a superconducting film. The film is made of niobium and is subjected to a uniform out-of-plane magnetic field. The antidots are all similar and consist in equilateral triangles with side of length b and a centre-to-centre spacing $s_{\triangle}$. One of the vertices of the triangular antidots is oriented towards the $\mathbf{e_y}$ direction, as schematically depicted in Figure 5.1. Such a sample contains several different geometrical symmetries. On the one hand, to the film, being a square of length L, is associated a C_4 symmetry. The regular layout of the antidots also displays a C_4 symmetry. On the other hand, the triangles being equilateral, the holes themselves introduce a C_3 symmetry in the system. In particular, the potential landscape through which the vortices move as the applied field is increased is non-symmetric along the $\mathbf{e}_y$ direction. This particular lack of symmetry is thus expected to generate a ratchet effect for the penetration of magnetic field inside the superconducting sample [247, 248]. The principal aim of the chapter is to determine how these different symmetries combine with each other and how they affect the penetration of magnetic field and the current density distribution at the macro-scale, in response to a uniform magnetic field that is applied perpendicular to the cross section of the film.

The chapter is structured as follows. Section **5.2** contains a brief overview of the experimental details of the studied sample. The experimental evidence of the effect of the array of antidots on the penetration of the magnetic field in the sample is then also provided. Section **5.3** is devoted to the characterization and quantification of the critical current density along the four different principal directions of the square based on the results of time-dependent Ginzburg-Landau (tdGL) simulations. The signature of the ratchet effect that is suggested by the non-symmetric shape of the antidots is highlighted. Section **5.4** capitalizes on the main conclusions of Section **5.3** to devise a macroscopic model that can reproduce the most salient characteristics of the penetration of magnetic field in the sample etched with the antidot array that were observed in the experiments of Section **5.2**. A critical state model is also proposed to help in understanding the experimental results.

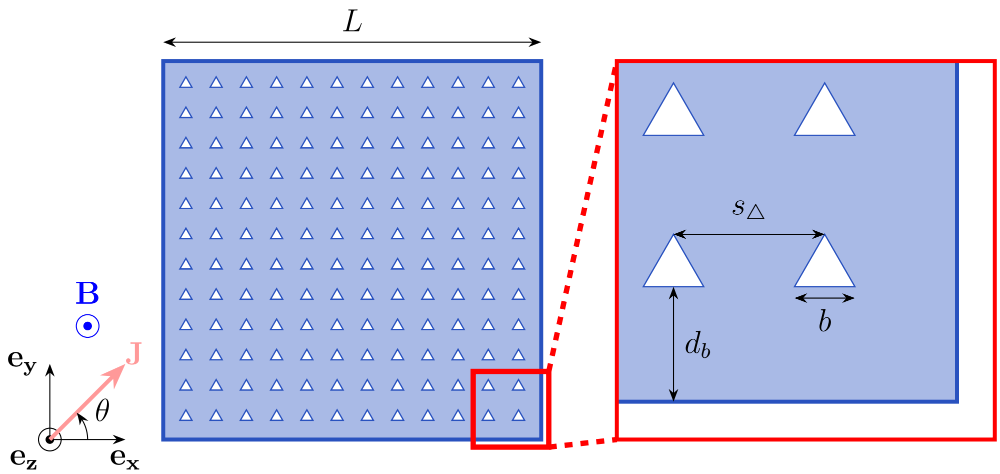

Figure 5.1: Schematic representation of the thin square superconducting film of length $L = 5$ mm, and wherein a square array of triangular antidots is etched. A close-up view over a square region containing a few triangular antidots around the lower right corner of the sample is also shown on the right part of the figure. The array is made of identical equilateral triangles, whose edges are $b = 1.5$ μm long, and which are all separated by the same center-to-center distance $s_\triangle = 4$ μm. The rows and columns of triangles start at a distance $d_b = 1$ μm from the borders.

5.2 Magnetic-field-dependent critical states in a square film with a regular array of non-symmetric antidots

The investigated samples consist in lithographically defined niobium films deposited on Si/SiO_2 substrates by ultra-high vacuum direct current magnetron sputtering. The deposited thickness of niobium is 45 μm and the length of the side of the film is $L = 5$ mm. The patterns of antidots are etched by lift-off processing, and the critical temperature of the films is 6.8 K. A small portion of the film is schematically depicted in Figure 5.1 to illustrate the array of identical antidots. They consist in equilateral triangles of length $b = 1.5$ μm, and are organized as a square array across the whole 5×5 mm^2 film. The unit-cell size of the array, which corresponds to centre-to-centre spacing between two consecutive triangles, $s_\triangle$, is hence constant and equals 4 μm. Moreover, the distance between the borders of the square film and the closest row of triangles is 1 μm along each edge of the film, in order to avoid any asymmetric surface barrier that could interfere with the results [251]. From the temperature derivative of the upper critical field near T_c and the temperature-dependent dirty-limit expressions of $\xi(T)$ and $\lambda(T)$, one can estimate that $\xi(0) = 8$ nm and $\lambda(0) = 132$ nm. As a result, ξ and λ are much lower than the size of the antidots over the whole probed temperature range.

The distribution of the magnetic field in the films with the array of non-symmetric antidots are shown in Figure 5.2. They were obtained by means of magneto-optical imaging. The measurements have been carried out by A.V. Silhanek and M. Motta, and the images of Figure 5.2 are shown with their courtesy. The Faraday-active indicators that were used in the setup are bismuth-substituted yttrium iron garnet films (Bi:YIG) with in-plane

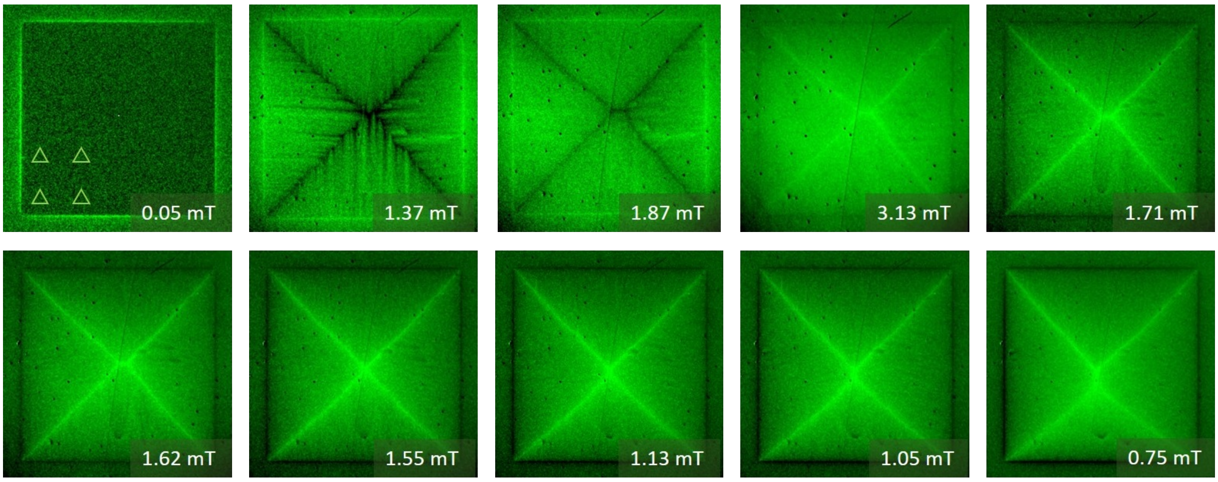

Figure 5.2: Magneto-optical imaging of the penetration of magnetic field in a thin square superconducting film within which a symmetric array of equilateral triangular antidots is etched. The applied field is perpendicular to the film and is first ramped up to 5 mT before being progressively decreased back to 0. The first three images are taken when the field is ramped up, while the other snapshots are taken during the field decrease. When the field is increased, the d-lines appear in black, while they stand out in light green when the field is decreased back to zero.

magnetization that is used to suppress the parasitic visual artefacts that correspond to the magnetic domains of the film [252]. Upon a field increase, it appears that the magnetic field fills the sample. At $\mu_0 H_a = 1.37$ mT, the d-lines seem to coincide with the diagonals of the square, as it would be expected in a square sample without antidots and with uniform J_c. However, when the applied field is large enough, a clear horizontal line arises at the centre of the sample, for $\mu_0 H_a = 1.87$ mT. This d-line stabilizes as the field is progressively increased and even when the applied field is progressively reversed, see for instance the distribution of magnetic field at $\mu_0 H_a = 3.13$ mT. However, the central d-line is progressively shifted to the left and to the bottom half of the film as the field is further decreased. In addition to this change of location, the horizontal d-line shrinks. This is visible from the magneto-optical images by comparing the magnetic flux distributions at $\mu_0 H_a = 1.71$ mT and $\mu_0 H_a = 1.62$ mT. The reduction of the length of the d-line continues until it degenerates in a single point for $\mu_0 H_a = 1.55$ mT. The transformation of the central critical structure keeps going, as the d-line becomes vertical, as observed at $\mu_0 H_a = 1.13$ mT. This new vertical d-line extends further as the applied field decreases further, as illustrated when $\mu_0 H_a = 1.05$ mT and $\mu_0 H_a = 0.75$ mT.

The results of Figure **5.2** illustrate how much an array of antidots can influence the diffusion of magnetic field inside a superconducting film. The d-line patterns deviate from the diagonals of the square, which is normally expected, and a d-line emerges at the centre of the sample. Moreover, the arising d-line patterns do not remain frozen as the applied field strength varies. Their shape visibly changes with the applied field. In what follows, an explanation for the shape of these critical structures is sought.

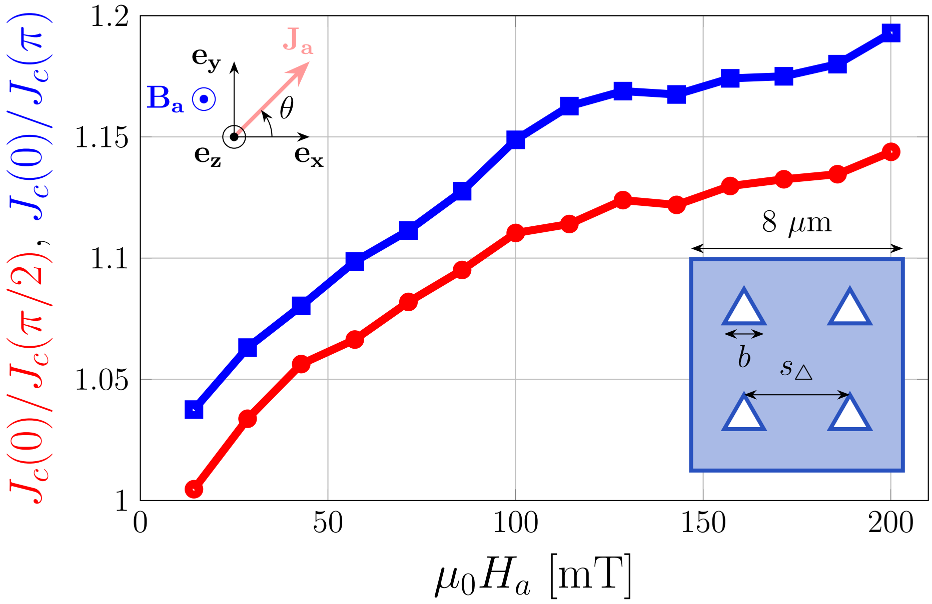

Figure 5.3: $J_c(0)/J_c(\theta)$ curves as a function of $\mu_0 H_a$, with H_a being the applied field strength, for $\theta = \pi/2$ and π. The angle θ, which is the orientation of the applied current $\mathbf{J}_a$, is defined as in the drawing on the upper left corner of the figure. The geometry of a reduced cell of antidots, that is used for the time-dependent Ginzburg-Landau simulations, is shown in the inset drawing. Four identical triangular antidots are contained within the cell, which extends over a 8×8 μm^2 region. The cell is chosen in such a way that the geometry is symmetric with respect to the vertical median of the square. Each antidot is separated from the next antidot by a distance $s_\triangle$, and each of them consists in a equilateral triangle of length b.

5.3 Assessment of the anisotropy of the critical current density with time-dependent Ginzburg-Landau simulations

In order to understand the magneto-optical measurements, one can first look at how the vortices are distributed around the antidots, opting for a micro-scale approach. To this aim, time-dependent Ginzubrg-Landau (tdGL) simulations were carried out by Ž. L. Jelić, J. D. González Acosta, and M. V. Miloševic at the University of Antwerp. The data that appear in these section are on their credit and are reproduced here for argumentation purposes, since the conclusions of these tdGL simulations will be used in Section 5.4. The tdGL simulations are based on Equation 1.8 and Equation 1.9. Furthermore, these simulations were carried out in the effective type-II limit, which states $\Lambda/\xi \gg 1$, with Λ being the Pearl length and ξ is the coherence length, while the thin-film limit, $d \ll \lambda$, is assumed, where λ is the London penetration length. The order parameter, ψ, is numerically computed over a square region that covers a 8×8 μm^2-area, which includes 4 triangular antidots of side $b = 1.5$ μm and separated by a 4 μm distance, as shown in the bottom inset of Figure 5.3.

An out-of-plane field, $\mathbf{B}_a = \mu_0 H_a \mathbf{e}_z$ is first applied to the whole system. Then, an in-plane current density, $\mathbf{J}_a$, is injected in a given direction, θ, and its intensity is progressively increased. The definition of θ and the direction of both $\mathbf{B}_a$ and $\mathbf{J}_a$ are shown in the drawing in the upper left corner of Figure 5.3. In practice, the norm of the current density is forced to be equal to J_a, while the current density is forced to be normal to the superconductor-normal (SN) interface, which corresponds to the sides of the simulated domain that are perpendicular to the current flow. Besides, superconductor-vacuum (SV) boundaries coincide with the sides of the square domain that are parallel to the direction of the applied current. The SV boundary conditions encompass both zero normal current density and zero supercurrent density conditions. The voltage V can then be defined as the mean of the electrical potential difference between two lines that are parallel to the SN interface, at a distance of $40\,\xi$ from both of them. As J_a increases, V changes, which leads to $V(J_a)$ curves from which the critical current densities, $J_c(\theta, B_a)$, can be extracted. These values correspond to the detection of a 20 μV voltage across the control lines and correspond to the onset of the vortices dynamics. The numerical details of the simulations can be found in [48].

The ratios $J_c(0)/J_c(\pi/2)$ and $J_c(0)/J_c(\pi)$ as a function of $\mu_0 H_a$ are shown Figure 5.3. In the range of the investigated values of $\mu_0 H_a$, the results show that $J_c(\pi) < J_c(\pi/2) < J_c(0)$. Furthermore, the ratios $J_c(0)/J_c(\pi/2)$ and $J_c(0)/J_c(\pi)$ increase with $\mu_0 H_a$. The non-symmetric anisotropy of the current density and its magnetic field dependence that are revealed by the tdGL simulations are of a particular importance and will be retained for the macroscopic simulations to come. The orientation-dependent current density can be understood from a microscopic viewpoint as the manifestation of the non-symmetric potential landscape that is induced by the shape of the antidots. The triangular shape of the antidots implies that the cross section through which an applied current flows in the vertical direction [$J_c(\pi/2)$] is larger than the cross section through which the same applied current goes when the current density move in the horizontal direction [$J_c(0)$ and $J_c(\pi)$], which might explain the differences between the value of $J_c(\pi/2)$ and those of $J_c(0)$ and $J_c(\pi)$.

Besides, the vortices face an non-symmetric landscape while moving in the vertical direction. This defines easy and hard magnetic field penetration axes, which results in a rectification phenomenon [248, 253]. The vortices that stem from the upper edge and move towards the center of the sample face the sharp tip of the triangular indentations, while those that enter from the bottom edge meet the flat bases of the triangular antidots. Around the vertices of the triangles, the supercurrent density lines are denser because of the current-crowding effect [235], so that the vortices are more easily depinned from the hole within which they were trapped. The motion of vortices is thus facilitated when vortices move while facing the basis of the triangle and made harder in the opposite direction, while facing the vertices. As a result, $J_c(0)$, which is associated with a downward motion of vortices when the applied field points along $\mathbf{e}_z$, is larger than $J_c(\pi)$, which is related to vortices that move in the opposite direction. The C_3 symmetry of the triangular holes is thus responsible for the observed ratchet effect by breaking the C_4 symmetry that comes from the regular square layout of the antidots and the global square shape of the sample. Furthermore, the C_3 symmetry does not introduce any asymmetry of the potential landscape for vortices that penetrate from the left or the right border, since the vortices face the same tilted edges. Their motion is thus not fundamentally different if one forces the current to flow in the direction of $\mathbf{e}_y$ or in the opposite direction, so that one can reasonably assert that $J_c(\pi/2) = J_c(3\pi/2)$.

It is worth noticing that the ratio $J_c(0)/J_c(\pi)$ does not necessarily vary as shown in Figure 5.3 for all materials and might greatly depend on the size of the antidots [248]. In what follows, the present tdGL results are used, as the results are adapted to niobium parameters and to the size of the antidots in the experimental sample.

5.4 Macroscopic modelling of the discontinuity line reversal with the finite-element method

At the microscopic scale, the tdGL simulations have highlighted the anisotropic feature of the critical current density, $J_c(\theta, \mathbf{B})$, that results from the non-symmetric potential landscape. In this section, the most salient results of the tdGL simulations are implemented in a macroscopic model, and the critical states that are formed in the superconducting film are then investigated. The aim of such an approach is to prove that the anisotropic $J_c(\theta, \mathbf{B})$ law can explain the reversal of the central d-line that is observed experimentally, while keeping a minimal amount of key parameters.

Before going into the description of the numerical model, let us explain how the anisotropy in the critical current density can lead to the different critical states observed in MOI. For the sake of the simplicity of the argument, the magnetic field dependence of J_c is knowingly omitted, so that the $\mathbf{B}$ variable of $J_c(\theta, \mathbf{B})$ will be momentarily dropped in the following developments. Based on the observations that were inferred from the tdGL simulations, one can assume that $J_c(0) > J_c(\pi/2) > J_c(\pi)$ and $J_c(\pi/2) = J_c(3\pi/2)$. Assuming, without loss of generality, that the induced currents circulate in the clockwise direction as a consequence of an upward applied magnetic field, the square film can be divided into four sectors, where the amplitude of the critical current density varies with the direction of the eddy currents. For instance, the current density is parallel to the borders and forms rectangular patterns within which the current density flows in a given direction. The current density J_c is equal to $J_c(0)$, $J_c(\pi/2)$, $J_c(\pi)$ and $J_c(3\pi/2)$ in the upper, left, bottom and right quarter, respectively. The shape of the quarters are uneven, and are delimited by the oblique d-lines, which inclination is determined from current conservation.

In the context of the Bean model, the conditions $J_c(0) > J_c(\pi/2) > J_c(\pi)$ and $J_c(\pi/2) = J_c(3\pi/2)$ then yield three different possible sets of d-lines that can arise in a fully penetrated sample after zero-field cooling, which are depicted in Figure 5.4, depending on the values of $J_c(0)$, $J_c(\pi)$, $J_c(\pi/2)$ and $J_c(3\pi/2)$. Panel (a) corresponds to the case where a central vertical line arises. Since $J_c(\pi/2) = J_c(3\pi/2)$, the vertical line is centred. Consequently, in accordance to current conservation across the leftmost oblique d-lines, one can write

$$\left(\frac{L}{2} - \delta_{w,1}\right) J_c(0) = \frac{L}{2} J_c(\pi/2) = \left(\frac{L}{2} + \delta_{w,2}\right) J_c(\pi), \tag{5.1}$$

and one can express the length of the vertical line, ℓ_v, as $\ell_v = \delta_{w,1} - \delta_{w,2} > 0$. Similarly, in panel (b), given that $J_c(\pi/2) = J_c(3\pi/2)$, one can write

$$\left(\frac{L}{2} - \delta_w\right) J_c(0) = \frac{L}{2} J_c(\pi/2) = \left(\frac{L}{2} + \delta_w\right) J_c(\pi), \tag{5.2}$$

while in panel (c), it can be easily deduced that

$$\left(\frac{L}{2}-\delta_w\right) J_c(0) = \left(\frac{L}{2}-\frac{\ell_h}{2}\right) J_c(\pi/2) = \left(\frac{L}{2}+\delta_w\right) J_c(\pi), \tag{5.3}$$

where the condition $\ell_h < 2\delta_w$ holds, to agree with the hierarchy of the critical current densities magnitude $J_c(0) > J_c(\pi/2) > J_c(\pi)$. Equation 5.1, Equation 5.2 and Equation 5.3 can be recast as a function of the following sum of current density ratios,

$$R_J \equiv \frac{J_c(\pi/2)}{J_c(0)} + \frac{J_c(\pi/2)}{J_c(\pi)}, \tag{5.4}$$

and a simple but strong relation can be inferred from this set of equations and related to each of the d-line layouts, i.e.

$$R_J = \begin{cases} 2\frac{\ell_v}{L} < 2 & \text{for panel (a),} \\ 2 & \text{for panel (b),} \\ 2\frac{L}{L-\ell_h} > 2 & \text{for panel (c).} \end{cases} \tag{5.5}$$

It is worth stressing out that the magnetic-field-independent Bean model cannot reproduce the reversal of the central d-line, since definite values of $J_c(0)$, $J_c(\pi/2)$ and $J_c(\pi)$ determine the critical states once and for all, even as the applied magnetic field is decreased back to zero. An additional mechanism is thus required to justify the change from an horizontal d-line to a vertical one, in other words, to explain why the value of R_J drops from a value that is greater than 2 when the applied field is ramped up to a value that goes below 2 when approaching the remanent state.

The most natural way to account for the magnetic field dependence of the critical states is to include a magnetic field dependence of the critical current density, $J_c(\theta, \mathbf{B})$. Such upgrade is justified since the tdGL simulations clearly indicate magnetic-field-dependent ratios $J_c(\pi/2)/J_c(0)$ and $J_c(\pi)/J_c(0)$. A magnetic field dependence of $J_c(\pi)/J_c(0)$ has also been experimentally evidenced in YBCO films [248]. Such modifications of these ratios lead to variations of R_J as a function of $\mathbf{B}$, and the central d-line is then expected to vary as the applied field changes. In order to illustrate the $J_c(\theta, \mathbf{B})$ in a more graphical way, the values of $J_c(\theta)$ are represented on a polar plot for different values of the applied field, $\mu_0 H_a = 14.3$ mT, 57.2 mT and 200.6 mT, see Figure 5.5. The results are normalized with respect to the value of $J_c(0)$. The continuous lines are guides to the eye that evidence the global shape of the critical surface, which boundary is $J_c(\theta)$. Note that only the upper half of the $J_c(\theta)$ curve is shown for symmetry reasons, i.e. $J_c(\theta, |\mathbf{B}|) = J_c(2\pi-\theta, |\mathbf{B}|)$ for $\theta \in [0, \pi]$, generalizing the relation $J_c(\pi/2, |\mathbf{B}|) = J_c(3\pi/2, |\mathbf{B}|)$. It can be immediately seen that, as $\mu_0 H_a$ is increased, the ratio $J_c(\pi/2)/J_c(0)$ and $J_c(\pi)/J_c(0)$ become smaller and the ovoid-shaped $J_c(\theta, \mathbf{B})$ appears to cover a smaller area. The critical surface that outlines $J_c(\theta, \mathbf{B})$ is thus progressively deformed as the applied field changes, the ovoid-like shape being accentuated at larger fields.

The numerical method that is used to model the penetration of magnetic field in the film relies on the FE $\mathbf{H}$-ϕ formulation that was developed in Chapter 2. The truncated-geometry approach is used to apply the boundary conditions. The length of the cubic non-conducting domain is $L_{ph} = 200\,L = 1$ m. The mesh is also non-uniform, the unstructured mesh size being on average equal to 0.1 m in the non-conducting region, while the planar

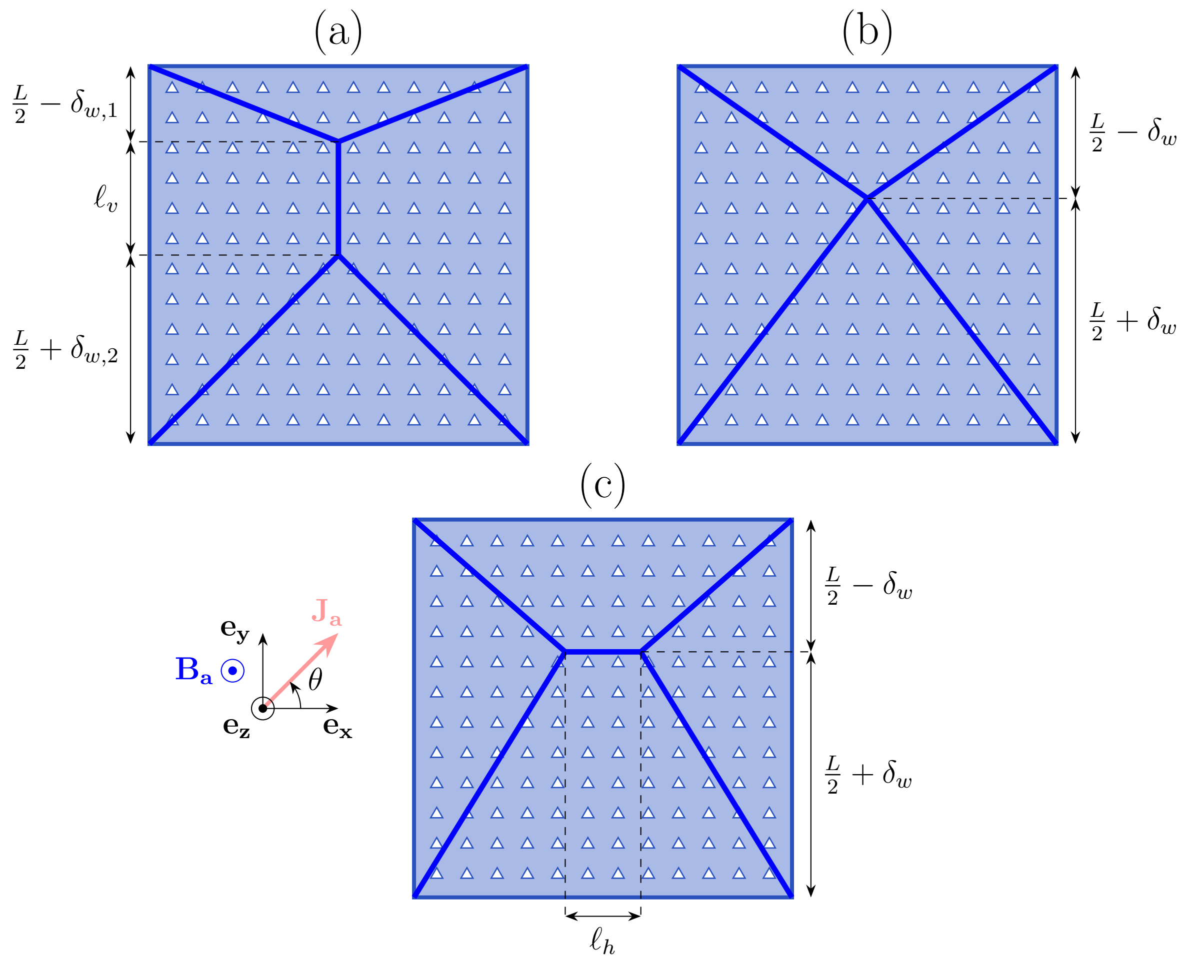

Figure 5.4: Schematic representation of the different possible networks of discontinuity lines, as predicted by the critical state model. The eddy currents in the film form rectangular loops that circulate clockwise, so that $J_c = J_c(0, |\mathbf{B}|)$. In particular, depending on the values of $J_c(0, |\mathbf{B}|) > J_c(\pi/2, |\mathbf{B}|) > J_c(\pi, |\mathbf{B}|)$ and $J_c(\pi/2, |\mathbf{B}|) = J_c(3\pi/2, |\mathbf{B}|)$, the oblique d-lines that stem from each corner of the square sample (a) give rise to a central vertical d-line of length ℓ_v, (b) meet at a single point, and (c) delimit a central horizontal d-line of length ℓ_h. The exact condition that determines the shape of the d-line set is given by Equation 5.4 and Equation 5.5.

size of the structured mesh in the conducting region is on average equal 50 μm on the boundary of the film and is progressively reduced to 10 μm in the central region of the film, allowing for a finer grid in the region where the central d-lines are expected. The main challenge resides in finding a way to model the anisotropic current density at the macroscopic scale by using Maxwell's equations and appropriate constitutive laws, which can faithfully capture the physics of the problem in a range that goes from a few microns to a few mm.

The anisotropic magnetic response of the superconductor is modelled following a previous work from Badia et al. [140, 108]. This method is based on a thermodynamic approach which describes the behaviour of hard superconductors once they are driven out of equilibrium by overcritical currents. When the system is in the critical state, the superconductor is characterized by a critical current density $\mathbf{J_c}$ that can be represented in the

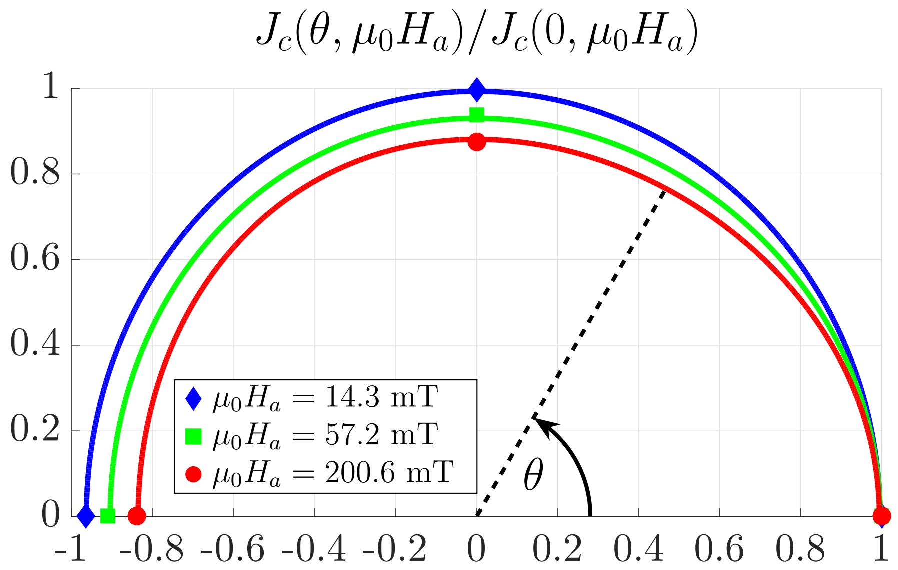

Figure 5.5: Polar plot of the critical current density, $J_c(\theta, \mu_0 H_a)/J_c(0, \mu_0 H_a)$, for $\mu_0 H_a =$ 14.3 mT, $\mu_0 H_a$ = 57.2 mT, and $\mu_0 H_a$ = 200.6 mT, in blue, green, and red, respectively. The orientation of the current density is denoted by θ and the circles, squares, and diamonds represent the values of $J_c(\theta, \mu_0 H_a)$ that were obtained in the framework of the time-dependent Ginzburg-Landau simulations. The plain curves act as a guide to the eye and take the shape of half ovoids, which highlight in an ideal way the asymmetry of the anisotropic characteristics of the critical current density along the principal axes. Only half the curve is shown for symmetry reasons, since the relation $J_c(\theta, |\mathbf{B}|) = J_c(2\pi - \theta, |\mathbf{B}|)$ with $\theta \in [0, \pi]$ holds true for an ovoid, which is inspired from the relation $J_c(\pi/2, \mu_0 H_a) = J_c(3\pi/2, \mu_0 H_a)$.

(J_x,J_y) plane, delineating a closed curve in this plane, that will be labelled as the critical surface. If external excitations force the displacement of vortices, an out-of-equilibrium state is reached, while the current density, $\mathbf{J}$, lies outside the region that is enclosed by the critical surface. The system then relaxes back to equilibrium by dissipating energy at a rate $\mathbf{E} \cdot \mathbf{J}$, which is estimated by means of a dissipative function, $\mathcal{F}(\mathbf{J})$. It was shown in [140] that the electric field can be derived from this dissipation function as $\mathbf{E} = \nabla_{\mathbf{J}} \mathcal{F}$. In such a case, one defines an electrodynamically consistent **E**-**J** constitutive law which can be adapted to the problem under scrutiny.

According to [108], the dissipative function $\mathcal{F}$ can be expressed in the following practically manageable generic form

$$\mathcal{F} = \mathcal{F}_0 \left(\mathcal{E}(\mathbf{J})\right)^M , \tag{5.6}$$

where $\mathcal{E}$ is a functional of the current density that accounts for all the relevant symmetries of the pinning sites, while the dimensionless exponent M typically depends on the pinning characteristics and the magnetic relaxation properties of the sample. It is worth noticing that M is reminiscent of the exponent n of the usual isotropic **E**-**J** constitutive law. The level set $\mathcal{F} = \mathcal{F}_c$ delimits the critical surface that encloses the critical region, which must be convex. Similarly to how the value of the critical electric field, E_c, can be chosen arbitrarily in the isotropic **E**-**J** law, $\mathcal{F}_c$ can also be chosen arbitrarily.

The major remaining challenge consists in finding an appropriate mathematical expression for $\mathcal{E}$ that encodes all the crucial conclusions unveiled by the tdGL simulations. Once such $\mathcal{E}$ is established, one can infer an expression of $\mathbf{E}(\mathbf{J})$, which can in turn be used in the weak form of Faraday's law, see Equation 2.32. For instance, one wishes to enforce the condition $J_c(0,|\mathbf{B}|) > J_c(\pi/2,|\mathbf{B}|) > J_c(\pi,|\mathbf{B}|)$, while adopting a continuous transition for intermediate angles. Besides, it is sought that the ratio $J_c(0,|\mathbf{B}|)/J_c(\pi,|\mathbf{B}|)$ increases as $|\mathbf{B}|$ becomes larger, which reflects the enhancement of the ratchet effect as $|\mathbf{B}|$ increases, as demonstrated in Figure 5.3. The ovoid-shaped J_c curves that are depicted in Figure 5.5 for several values of $\mu_0 H_a$ are for instance a reasonable contender that can correctly encode the kind of anisotropic feature that characterizes the system under investigation. Keeping a minimal number of powers of $\mathbf{J}$ and its components in the modelling, one can write the ansatz

$$\mathcal{E} = \mathcal{E}_s + \mathcal{E}_a, \tag{5.7}$$

$$\mathcal{E}_s = \left(\frac{J_x}{J_{c,x}}\right)^2 + \left(\frac{J_y}{J_{c,y}}\right)^2, \tag{5.8}$$

$$\mathcal{E}_a = -\frac{C_x}{\sqrt{\mathcal{E}_s}}\left(\frac{J_x}{J_{c,x}}\right)^3, \tag{5.9}$$

where $J_{c,x}$, $J_{c,y}$ and C_x are parameters that control the amplitude of the critical current density along the principal axes of the square (x and y directions) and the asymmetry of the critical current density along the x direction. $\mathcal{E}(\mathbf{J})$ is an homogeneous functional of degree two, which ensures that the shape of the ovoid does not vary with the value of $\mathcal{F}_c$, and that the shape of the critical surface is independent on the choice of $\mathcal{F}_c$. In particular, if one considers the case $\mathcal{F}_c = \mathcal{F}_0$ with Equation 5.7, Equation 5.8, and Equation 5.9, one can obtain convenient expressions for $J_c(0,|\mathbf{B}|)$, $J_c(\pi/2,|\mathbf{B}|)$ and $J_c(\pi,|\mathbf{B}|)$ that can be used to ponder the balance between these critical current densities. One can easily derive that

$$J_c(0,|\mathbf{B}|) = \frac{J_{c,x}}{\sqrt{1-C_x}}, \tag{5.10}$$

$$J_c(\pi/2,|\mathbf{B}|) = J_{c,y}, \tag{5.11}$$

$$J_c(\pi,|\mathbf{B}|) = \frac{J_{c,x}}{\sqrt{1+C_x}}. \tag{5.12}$$

Do not forget that $\mathbf{E}$ is a non-linear function of $\mathbf{J}$. Since the linearisation of $\mathbf{E}$ is carried out by means of the Newton-Raphson scheme, Equation 5.6 must actually be derived with respect to the components of $\mathbf{J}$ twice. This yields a tensor $\partial\mathbf{E}/\partial\mathbf{J}$ which mathematical expression is more complex than what was derived in Appendix A.1. This is a consequence of the anisotropic shape of the critical surface, which, according to [108], allows $\mathbf{E}$ and $\mathbf{J}$ to be oriented along different directions. The formal expression of the $\partial\mathbf{E}/\partial\mathbf{J}$ tensor that accounts for an anisotropic $\mathbf{E}$-$\mathbf{J}$ constitutive law can be found in Appendix A.2.

In order to clarify the role played by the parameters C_x, $J_{c,x}$ and $J_{c,y}$, it is interesting to consider some particular choices. If $C_x = 0$ and $J_{c,x} = J_{c,y} = J_c$, one recovers the isotropic flux-creep law, given $\mathcal{F}_0 = E_c J_c/2M$ and $n = 2M - 1$. If $C_x = 0$ but $J_{c,x} \neq J_{c,y}$, the critical surface takes the form of an ellipse which translates an intrinsic anisotropy feature of the superconducting sample along the principal directions x and y, without accounting for the ratchet effect.

In the latter case, the model can be validated by considering the case of a thin superconducting disk submitted to an out-of-plane magnetic field, with a magnetic-field-independent $J_c(\theta)$, a case which was studied in the critical state limit ($M \to \infty$) in [142]. To this aim, let us consider a thin disk of radius $R = 200$ μm and of thickness $d = 100$ nm. The applied field is ramped up from 0 to H_a at a constant rate $\dot{H}_a = 1$ kA/m.s, and H_a/H_c is set to either arccosh(2) or arccosh(50), with $H_c = J_{c,x}d/2$. The exponent M that is involved in Equation 5.6 is set to a large value of $n = 200$ and $n = 2M - 1$, in such a way that one can compare the numerical results to those of the critical state model. Taking $C_x = 0$ and $J_{c,y} = 2J_{c,x} = 2$ MA/cm^2, one obtains the results of Figure 5.6.

For both partial and complete penetrations, the penetration depth in the x and y directions, the iso-lines of magnetic field and the corresponding shape of the current density lines are in good qualitative agreement with what was found in [142, 254], which validates the way the anisotropic critical current density is modelled. One can also observe that in a similar fashion to [142], despite having the relation $J_{c,y} = 2J_{c,x}$, the numerically computed ratio between the penetration lengths in the horizontal and vertical direction, $\ell_{p,x}$ and $\ell_{p,y}$, respectively, is indeed more or less equal to 4 when $H_a/H_c = \text{arccosh}(2)$. When the magnetic field penetration is complete ($H_a/H_c = \text{arccosh}(50)$), a discontinuity line forms at the centre of the disk, which extension is measured to be equal to $1.46\,R$, close to the value predicted in [142], i.e. $1.43\,R$. The magnitude of the current density that moves strictly upwards or downwards ($\theta = \pi/2$ or $\theta = 3\pi/2$) is equal to twice the value of $\mathbf{J}$ that moves to the left or to the right ($\theta = 0$ or $\theta = \pi$), as expected.

Returning to the discussion of the parameters of the **E**-**J** law, consider now $C_x > 0$ and $J_{c,x} \neq J_{c,y}$. The symmetry along the x-axis is now broken, and the shape of the critical surface can comply with the results of Figure 5.3 if the parameters are wisely selected. The shape of the ovoid changes with respect to the applied field, so that the parameters $J_{c,x}$, $J_{c,y}$ and C_x must include a magnetic field dependence that reliably reproduces the metamorphosis of the central d-line, going from a horizontal position, when the magnetic field is ramped up, to a vertical one, close to the remanent state. Put in a different way, the ratio $R_J < 2$ if $|\mathbf{B}|$ is low, while $R_J > 2$ when the levels of $|\mathbf{B}|$ become sufficiently large. The parameters $J_{c,x}$, $J_{c,y}$ are assumed to follow Kim's law [84], while the magnetic field dependence of C_x is chosen to be continuous, strictly increasing and a bounded function of $|\mathbf{B}|$. More explicitly, the following dependences are used

$$J_{c,x} = \frac{J_{c,x,0}}{1 + |\mathbf{B}|/B_x}, \tag{5.13}$$

$$J_{c,y} = \frac{J_{c,y,0}}{1 + |\mathbf{B}|/B_y}, \tag{5.14}$$

$$C_x = C_{x,0}\frac{|\mathbf{B}| + B_1}{|\mathbf{B}| + B_2}, \tag{5.15}$$

where $J_{c,x,0}$, $J_{c,y,0}$, B_x, B_y, B_1, B_2 and $C_{x,0}$ are the parameters that need to be adapted to the phenomenology and the observations that were evidenced by the MOI and the microscopic study of the sample. Therefore, one is looking for a set of parameters that verifies $J_c(0, |\mathbf{B}|) > J_c(\pi/2, |\mathbf{B}|) > J_c(\pi, |\mathbf{B}|)$, while giving an increasing $J_c(0, |\mathbf{B}|)/J_c(\pi, |\mathbf{B}|)$ ratio as a function of $|\mathbf{B}|$. In addition, the values of the parameters are chosen in such a way that the levels of the applied magnetic field at which the different critical state shapes

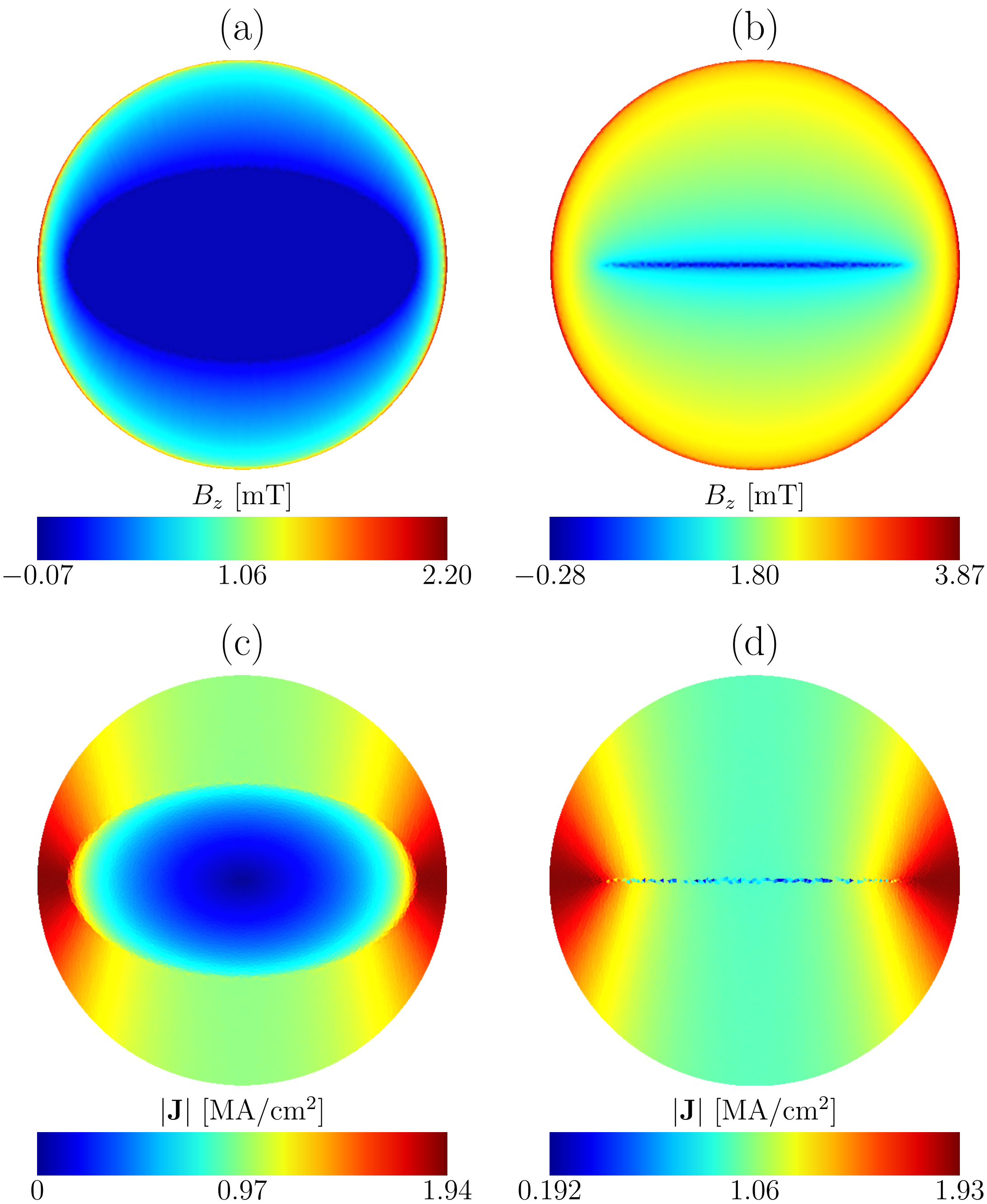

Figure 5.6: Out-of-plane magnetic field (panels (a) and (b)) and norm of the critical current density (panels (c) and (d)) in a thin superconducting disk with an anisotropic critical current density. The radius of the disk is $R = 200$ μm and its thickness is $d = 100$ nm. The disk is subjected to an out-of-plane magnetic field that is raised from 0 to $H_a/H_c = \text{arccosh}(2)$ (panel (a) and (c)) or $H_a/H_c = \text{arccosh}(50)$ (panel (b) and (d)), with $H_c = J_{c,x}d/2$, at the constant rate $\dot{H}_a = 1$ kA/m.s. The critical current density is anisotropic, so that, according to the thermodynamic dissipation-function approach, the critical surface is an ellipse with principal axes lengths equal to $J_{c,y} = 2J_{c,x} = 2$ MA/cm^2.

Parameter	Units	Value
$J_{c,x,0}$	$\mathrm{MA/cm^2}$	1
$J_{c,y,0}$	$\mathrm{MA/cm^2}$	0.95
B_x	mT	1.4
B_y	mT	1.58
B_1	mT	1
B_2	mT	1.1
$C_{x,0}$	-	0.15

Table 5.1: Numerical parameters of the anisotropic **E-J** constitutive law that allow to reproduce the change of critical states observed in the magneto-optical images of the penetration of magnetic field in the square film with the regular array of triangular antidots, see Figure 5.7.

occur match the experimental ones. The chosen set of parameters is reported in Table 5.1. The resulting critical states for different values of the applied field are depicted in Figure 5.7. One starts from a virgin state and apply a maximal field of 5 mT. One can observe first a horizontal d-line when $\mu_0 H_a = 3.11$ mT, when the applied field is progressively increased. When the external field is ramped back down to zero, the horizontal line shrinks to a single point at $\mu_0 H_a = 1$ mT, and at $\mu_0 H_a = 0.75$ mT, a small vertical line is obtained. This vertical line further extends as the remanent state is reached. This succession of events is therefore very similar to what is observed experimentally.

Interestingly, if one uses the shell-transformation method, taking $N_a = N_{sh} = 3$ and $A \approx 0.13\,L = 0.65$ mm, in agreement with the discussions of Chapter 2, the obtained magnetic field levels in the numerical results do not differ by more than a few percent from those yielded by the truncated approach. The difference is maximal during the first numerical iterations and quickly vanishes afterwards. The lengths of the numerically simulated sets of d-lines are also exactly the same, independently of the selected method. This empirically corroborates the validity of the unidirectional shell-transformation model combined with this kind of anisotropic constitutive law, as the results are nearly identical to those of the truncated method.

Several remarks are worth mentioning. First, from the inspection of the values of the ratios $J_c(\pi/2)/J_c(0)$ and $J_c(\pi)/J_c(0)$ obtained in the tdGL calculations, see Figure 5.3, it appears that the value of R_J is always less than 2 and does not seem to ever cross that threshold. This can be attributed to the fact that the tdGL simulations themselves have their own limitations, especially regarding the size of the investigated domain, and the corresponding boundary conditions, which do not correspond to those of the very dense array of antidots that fills the superconducting film. Assuming the phenomenological shape suggested by Equation 5.13, Equation 5.14, and Equation 5.15, a parametrization based on a least-square fit of the tdGL data that shows an R_J parameter crossing the threshold level of 2 can be derived. However, the obtained parameters yield a reversal of the d-line patterns in the wrong direction, i.e. the central d-line is first vertical as the applied field increases, before it becomes horizontal as the field is decreased back to zero. The correct order of events can however be achieved by making small adjustments to the fitting parameters. Nonetheless, the order of magnitude of the magnetic field dependence of the tdGL results is not consistent with those of the experimental data. Therefore, the parametrization of Figure 5.7 has been purposely scaled with respect to the typical range of magnetic field amplitude over which the metamorphosis of the d-lines is experimentally observed. Although the reversal of the central d-line can be reproduced with the magnetic field dependence of the parameters, this comes with the identification of an appropriate set of parameters. This highlights that, despite revealing rather small pinning-induced asymmetries (typically, the J_c anisotropy does not exceed a few percent), the observed critical states result from a delicate balance between the critical current densities along each principal direction, which are very sensitive to the model parameters.

Second, it is worth highlighting that the anisotropy is assumed to be an homogeneous property in the whole sample. This assumption of course ignores the complete symmetry of the system, since the C_4 symmetry of the array is not accounted for, neither is the possibility that the interstitial pinning in between the holes may create channels of magnetic field penetration along the principal axis. The present convex $\mathcal{F}$ model should therefore be adapted to include these additional effects.

Finally, one should bear in mind that the anisotropy, as it is modelled here, does not reflect all peculiarities of the critical states that are shown in the experimental images. The numerically computed lengths of the vertical and the horizontal d-lines are underestimated with respect to the ones that are measured experimentally. The agreement with experiments is thus only qualitative, by highlighting the correct metamorphosis of the central d-line. Moreover, in experiments, the d-lines appear to be slightly off-centred to the right when the field is increased, and to the left as the applied field is decreased. This contrasts with the numerical simulations, where the structure is always centred with respect to the vertical median of the square, because of the C_3 symmetry of the equilateral holes, i.e. $J_c(\pi/2, |\mathbf{B}|) = J_c(3\pi/2, |\mathbf{B}|)$. Also, the oblique parts of the d-line patterns feature several disruptions, which could be attributed to the presence of defects that perturb the smooth penetration of magnetic field, and could also introduce some array-unrelated horizontal asymmetries that are not included in the model. From a conceptual standpoint, it is possible to model this horizontal offset by introducing a non-symmetric term along the $\mathbf{e}_y$ axis in $\mathcal{E}_a$. This supplementary term would involve another cubic dependence, which importance would be controlled by an additional parameter C_y, similar to how the asymmetry along the $\mathbf{e}_x$ axis was modelled in Equation 5.9. However, the physical origin of the off-centred d-line remains unclear and is therefore difficult to justify, while the current model capture the most salient features of the observed physics.

5.5 Conclusion

In this chapter, the critical states were investigated in a thin square film which surface is etched by a very dense regular array of small triangular antidots and subjected to an out-of-plane magnetic field. The magneto-optical images revealed that the discontinuity lines that develop in the samples do not follow the diagonals of the square, but rather form more complex patterns that change with the applied field. A very distinctive feature of such critical states is a central horizontal d-line that forms when the applied magnetic field is progressively increased, and which transforms into a vertical d-line when decreasing the field and approaching the remanent state.

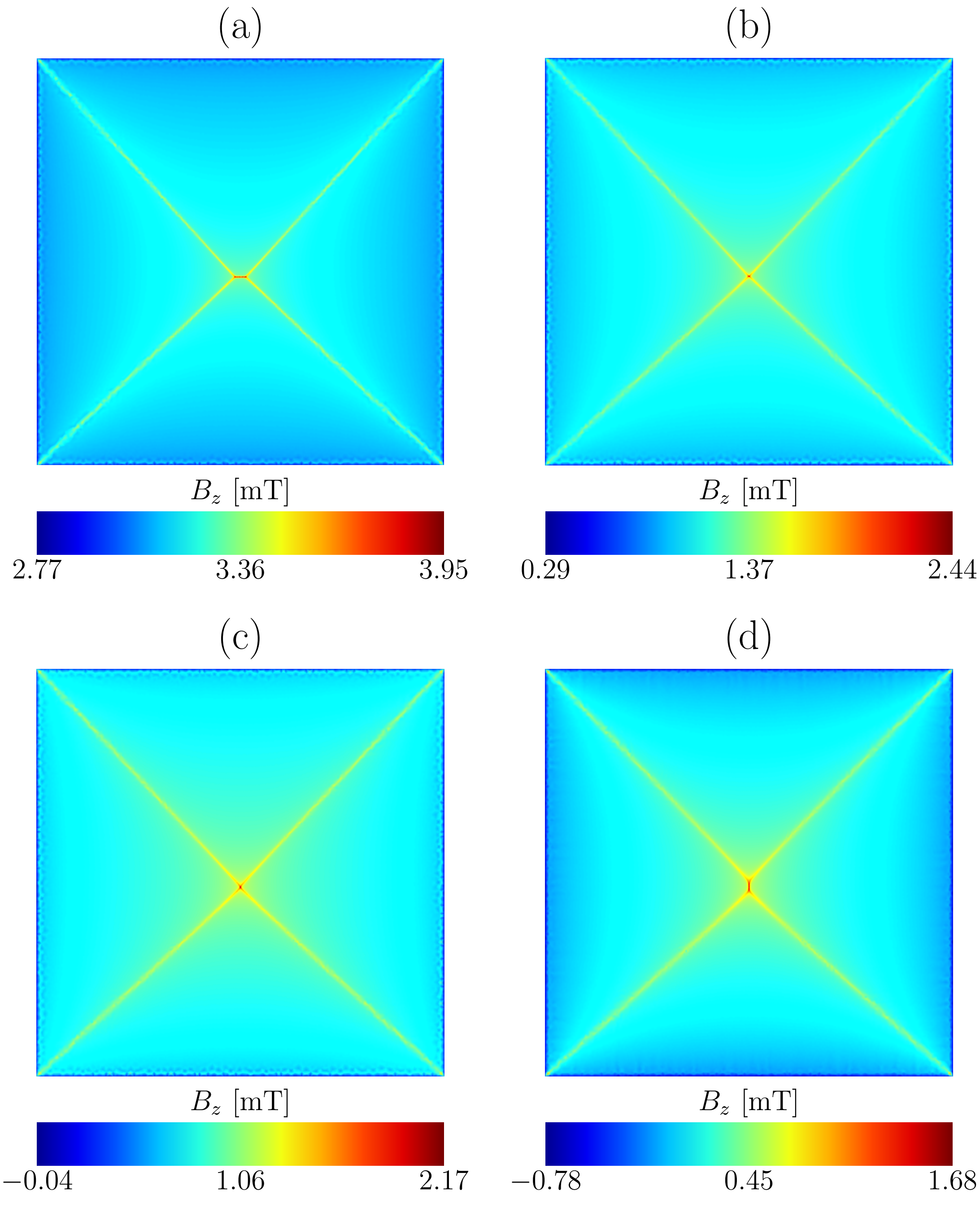

Figure 5.7: Out-of-plane magnetic field, B_z, in a thin square superconducting film which is characterized by a magnetic-field-dependent anisotropic **E**-**J** law. After a first magnetization up to $\mu_0 H_a = 5$ mT at the constant rate $\dot{H}_a = 1$ kA/m.s, the applied field is decreased at the same rate, and the distributions of B_z are shown at (a) $\mu_0 H_a = 3.13$ mT, (b) $\mu_0 H_a = 1$ mT, (c) $\mu_0 H_a = 0.75$ mT, and (d) in the remanent state. The simulations show the reversal of the central d-line from a horizontal position to a vertical one, which coincides with the experimental observations.

Time-dependent Ginzburg-Landau simulations were performed on a reduced area that include only four equilateral triangles and showed that the critical current density varies with the direction of the current flow. A reduction of the critical current density when the vortices exit the tips of the antidots occurs, as a consequence of the enhancement of the current crowding effect in the vicinity of the vertices. In comparison, the vortices that move towards the flat borders of the triangular antidots depin less easily, and the associated critical current density is larger than that associated to vortices moving towards the triangle tips. Most importantly, the ratio between these two critical current densities, which reflects the prominence of the ratchet effect, varies as a function of the applied field, in agreement with previous works.

Based on the main conclusions of the microscopic study of the critical current density, a macroscopic model was used to replicate the critical states that were observed in experiments. The widespread isotropic **E**-**J** law that models flux-creep was replaced by an anisotropic constitutive law based on a thermodynamic approach of the out-of-equilibrium critical states that relies on a functional of the dissipated energy to bring the system back to equilibrium. It allowed to formally address the anisotropic and non-symmetric features of the critical current density along the principal axes of the square film. A meticulous choice of the model parameters enabled the qualitative emulation of the critical state structures that are observed in practice. This thermodynamically motivated model encapsulates the most remarkable observations, based on the magneto-optical imaging of the system, while keeping a small number of model parameters.

Both the microscopic and macroscopic numerical simulations point to the fact that arrays of non-symmetric antidots induce a slight anisotropy of the critical current density, which turns out to be responsible for the unexpected sets of d-lines and their continuous metamorphosis. Besides, it is yet another evidence of a category of systems that illustrates the non-trivial influence of a magnetic-field-dependent critical current density on the distribution of magnetic field and the associated critical states in superconducting films. If the magnetic field dependence of the critical current density is not accounted for, the current density anisotropy alone does in fact not suffice to explain the reversal of the central critical structure.

Chapter 6

Critical states in superimposed superconducting films

6.1 Introduction

As discussed in Chapter 1, discontinuity lines, or d-lines, coincide with the locations where the current density make sharp turns, e.g. near a corner of the sample, in order to ensure current conservation. In the idealized case of the critical-state model, current flows along loops that are parallel with the boundaries of the film. Consequently, as was illustrated in Chapter 1, the d-lines form along symmetry lines of the film, and mostly depend on film geometry, as well as the local values of critical current density, in the case of anisotropic samples. To illustrate these principles, the d-lines in a thin square film with uniform current density are located along the diagonals of the square. Similarly, the d-lines in a thin rectangular strip form a 'double Y' shape, which originates from the corners and follows 45-degrees lines before merging into a central line lying along the longest median of the strip. Because of the logarithmic divergence of the magnetic-field levels in the close proximity of the d-lines, magneto-optical imaging (MOI) enables the in-situ visualization of the sets of d-lines for the two film geometries, as shown in panels (a) and (b) of Figure 6.1, for a square and a rectangular film, respectively. Note that in these images, the darker the contrast, the less intense the magnetic field, i.e. the rectangular strip is in the remanent state, while the square film is in a fully penetrated state.

To the best of my knowledge, while the critical states in single films are fairly well documented for various film shapes, critical states in multilayer assemblies of films have not been studied extensively. Tamegai et al. recently probed the magnetic-field distribution in an assembly made of a thin square film of side $L = 200$ μm on which a rectangular strip of width $W = L/2$ and length L is superimposed [44]. In this structure, proximity effects are suppressed by separating both films by a SiO_2 layer of thickness $t_{SiO_2} = 300$ nm, and the thickness of both films are equal to 300 nm. The longest median of the rectangular strip is aligned with respect to one of the medians of the square. A three-dimensional view of the assembly, which comprises the two films and the intermediate SiO_2 layer, is sketched in panel (d) of Figure 6.1. In the experiment of [44], the magnetic field in the remanent state of the assembly was imaged by magneto-optical techniques. Interestingly,

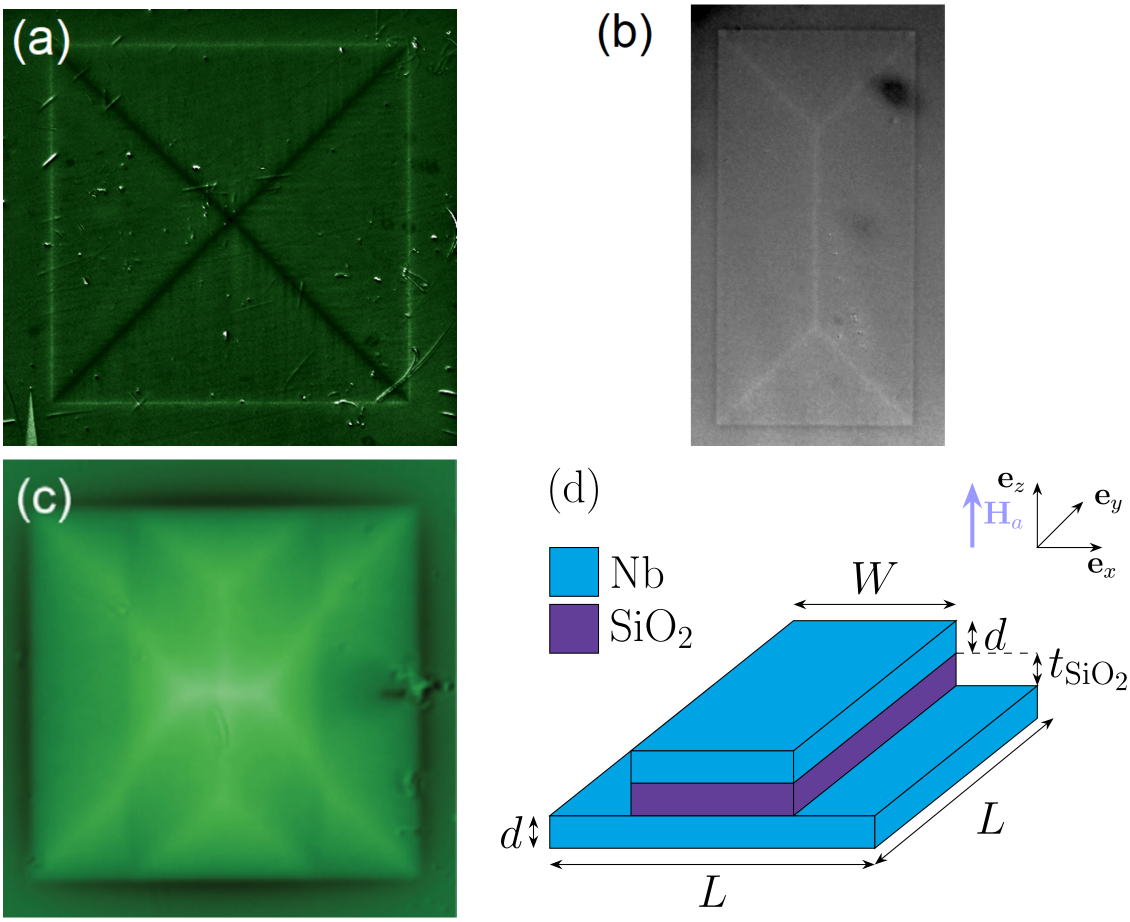

Figure 6.1: Magneto-optical images of the critical state (a) in a completely penetrated square superconducting film, (b) in a rectangular superconducting strip in the remanent state, and (c) in the superposition of a rectangular superconducting strip over a square superconducting film in the remanent state. The geometry of the assembly corresponding to the image in panel (c) is depicted in panel (d). In each magneto-optical image, the brighter the contrast, the higher the magnetic field.

instead of observing a simple superposition of the d-lines of the thin square film and those of the thin strip, the MOI of the assembly shows a richer network of d-lines, see panel (c) of Figure 6.1. In the overlap region, the 'double Y'-shaped d-lines of the thin strip are still clearly recognizable. In the region where the films are not superimposed, the d-lines remain aligned with the diagonals of the square film, as expected. However, in the overlap region, the d-lines deviate from the diagonals of the square film. They change their direction abruptly, in such a way that the d-lines originating from the left corners of the square film meet to the left of the assembly center, while the ones that start from the right corners of the square film intersect to its right. Moreover, an additional horizontal d-line arises at the center of the assembly, linking both intersections. Such a pattern differs from those usually observed in single thin films.

The presence of a central horizontal d-line in a thin square film is reminiscent of the critical-state patterns encountered in films with an anisotropic critical current density. Anisotropy is either induced by the microstructure of the material itself, in this case it is referred to as intrinsic anisotropy [95], or by an external in-plane applied field, in this case it is called an extrinsic anisotropy [97]. In the latter case, the anisotropy is induced in a direction perpendicular to the applied in-plane field. In [44], the pinning in the niobium films is homogeneous, so that anisotropy is not intrinsic. Furthermore, in order to induce extrinsic anisotropy in thin films, large in-plane magnetic fields must be applied. For instance, in a 300 nm thick niobium film, it is necessary to apply a background in-plane field of 300 Oe [97]. In the context of the experiment in [44], an in-plane film was in fact applied to suppress the magnetic domains in the magneto-optical indicator, which spoils the quality of the MO images. However, this applied field did not exceed 180 Oe, and thus could not induce an anisotropic behaviour in the film. Moreover, the in-plane field is applied parallel to the diagonals of the film, so that the anisotropy and the subsequent modification of the critical state are expected to develop perpendicular to the chosen diagonal. The physical origin of the patterns in Figure 6.1 thus remains to be elucidated.

In what follows, an explanation for these peculiar d-line patterns and the actual shape of the current loops in two-layer assemblies is proposed, based on the magnetic-field dependence of the critical current density. The chapter is organized as follows. In Section **6.2**, the magnetic response of an assembly of a thin rectangular film placed on top of a thin square film is numerically investigated. The numerical simulations are then confronted to MOI measurements, and the effect of the field dependency $J_c(|\mathbf{B}|)$ is clearly demonstrated. The basic mechanism is then illustrated with a simplified model based on the critical-state model. Then, the influence of geometrical parameters, such as the thickness of the insulating layer, t_{SiO_2}, the width of the thin rectangular strip, W, and the lateral offset of the rectangular strip, X_c, are investigated in Section **6.3**. The distribution of magnetic field is studied for various three-layer assemblies of square and rectangular films in Section **6.4**. Section **6.5** concludes this chapter.

6.2 Comparison of the numerically modelled magnetic response of the two-layer assembly to experimental measurements

6.2.1 Experimental details on the two-layer samples

The films were made in Tokyo University by I. Veschunov and T. Tamegai. The niobium films were grown on Si substrates by using magnetron sputtering, photolitography and SF_6 reactive ion etching. A clean and clear-cut superposition of the rectangular film on top of the square film is performed by means of caldera planarization [255]. Both films are separated with a 300 nm thick SiO_2 layer, which acts as an insulator to avoid proximity effects. The MOI is used to probe the critical states that result from the penetration of magnetic field inside the superimposed assembly, which relies on the Faraday effect in a ferromagnetic garnet film in direct contact with the sample [44, 256, 257]. The in-situ snapshots of the out-of-plane component of the magnetic field are recorded with a commercial optical microscope (Olympus BX30MF) and a cooled-CCD camera with 12-bit resolution (ORCA-ER, Hamamatsu). Samples are cooled down to 6 K according to a zero-field cooled (ZFC) procedure in a He-flow cryostat (Microstat HighRes II, Oxford Instruments). The critical temperature of the niobium films was measured to be $T_c = 9$ K, which is consistent with the onset of diamagnetism measured with a SQUID magnetometer. An out-of plane external field is applied to the sample, as a constant in-plane applied field, which magnitude is 180 Oe, is directed along one of the diagonals of the square to erase the otherwise visible reaction of the ferromagnetic magneto-optical indicator.

6.2.2 Details on the numerical method to emulate the penetration of magnetic field in superconducting two-layer assemblies

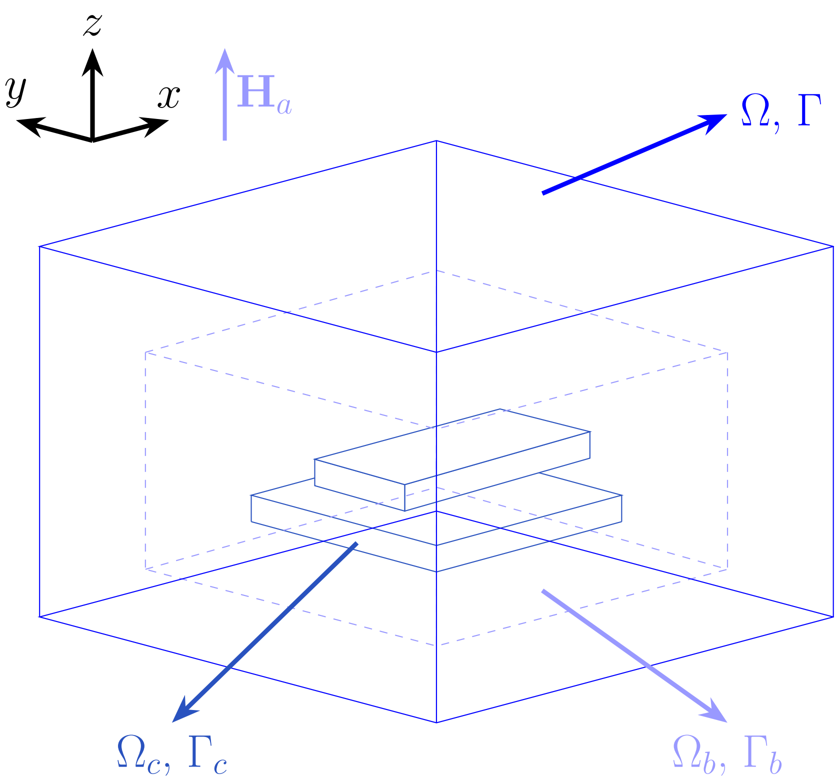

Figure 6.2: Domains considered in the **H**-ϕ formulation. Ω is the computational domain, Ω_c contains the superconducting materials, and Ω_b is an auxiliary box introduced for the application of the external field. The corresponding boundaries of the domains are Γ, Γ_c, and Γ_b respectively.

To simulate the assembly sketched in Figure 6.1 (d), we use the **H**-ϕ formulation introduced in Section 2.2. The applied field is ramped from 0 to 1000 Oe at a rate $H_a = 1$ kA/m.s, which is $\sim$ 12.5 Oe/s. A schematic representation of the simulated geometry is depicted in Figure 6.2. Both the rectangular strip and the square film, where eddy currents are induced, belong to Ω_c, which is shown in dark blue. The non-conducting domain, $\Omega \setminus \Omega_c$, includes the SiO_2 layer.

Throughout the chapter, the boundary conditions will be applied by means of either the truncated-geometry approach or the unidirectional shell transformation. In the case of the truncated-geometry approach, the films are included in a larger cubic box of size $2L_{ph}$, with $L_{ph} = 100\,L = 20$ mm, where L is the length of the square film. For the unidirectional shell transformation, Ω_c is embedded in an arbitrary box, Ω_b, which corresponds to the dashed light blue domain in Figure 6.2, where the applied field is set to be uniform, as described in Subsection 2.3.3. By default, the domain truncation will be used, so that it will be explicitly mentioned when the shell-transformation approach is used. The mesh used in the simulations is non-uniform. In particular, the typical planar mesh size in the assembly varies from 5 μm near the external borders of the square film to 1 μm in the overlap region. Refining the mesh in the overlap region allows a better visualization of the critical-state structures, where the central d-line develops. When the truncated-geometry technique is used, the mesh size on the boundary of Ω is typically set to a tenth of L_{ph}.

In the thin films, the non-linear constitutive law

$$\mathbf{E} = \frac{E_c}{J_c}\left(\frac{|\mathbf{J}|}{J_c}\right)^{n-1}\mathbf{J}, \tag{6.1}$$

is assumed, with $E_c = 1$ μV/cm and $n = 19$. J_c, the critical current density, is assumed to be magnetic-field dependent, and follows the generalized Kim law [83, 84], which is convenient to reach a satisfactory fit to experimental data while keeping as few parameters as possible,

$$J_c\left(|\mathbf{B}|\right) = \frac{J_c(0)}{(1+|\mathbf{B}|/B_0)^{\alpha}}. \tag{6.2}$$

Here, $J_c(0)$ is the critical current density at $\mathbf{B} = \mathbf{0}$, B_0 is a parameter that describes the characteristic scale of decay of J_c with $\mathbf{B}$, and α is a dimensionless parameter that tunes the asymptotic decay of J_c with $\mathbf{B}$. Neglecting surface barriers and the lower critical-field, $H_{c,1}$, the magnetic induction, $\mathbf{B}$, is given as

$$\mathbf{B} = \mu_0\mathbf{H}, \tag{6.3}$$

where $\mathbf{H}$ is the magnetic field.

The rectangular and the square films were not made out of the same niobium samples. Hence, the parameters $J_c(0)$, B_0 and α must be determined separately for each film. Their values were chosen to fit at best the experiments. For the thin square film, this procedure led to $J_c(0) = 3.4$ MA/cm^2, $B_0 = 1.25$ mT and $\alpha = 0.42$, while for the thin rectangular film, it led to $J_c(0) = 5.4$ MA/cm^2, $B_0 = 4.9$ mT and $\alpha = 0.51$.

6.2.3 Results of the numerical simulations and comparison with the MOI results

The numerical results are now compared to the MOI results when the applied field is ramped up from 0 to a fixed value, H_a, at the constant rate $\dot{H}_a = 12.5$ Oe/s. Figure 6.3 (a) to (f) show the magneto-optical distributions of the out-of-plane magnetic field, $\mu_0 H_z$, for $H_a = 50$, 100, 150, 200, 300 and 500 Oe. Figure 6.3 (A) to (F) display the corresponding numerical results. At the first stage of flux penetration, which is illustrated on panel (a) at $H_a = 50$ Oe, vortices preferentially enter from the edges of the square sample, along the portions that exclude the boundary delineating the film overlap region. Roughly, d-lines appear along the diagonals of the square. However, the magnetic flux barely penetrates the sample along the edges of the thin strip, where the flux front is

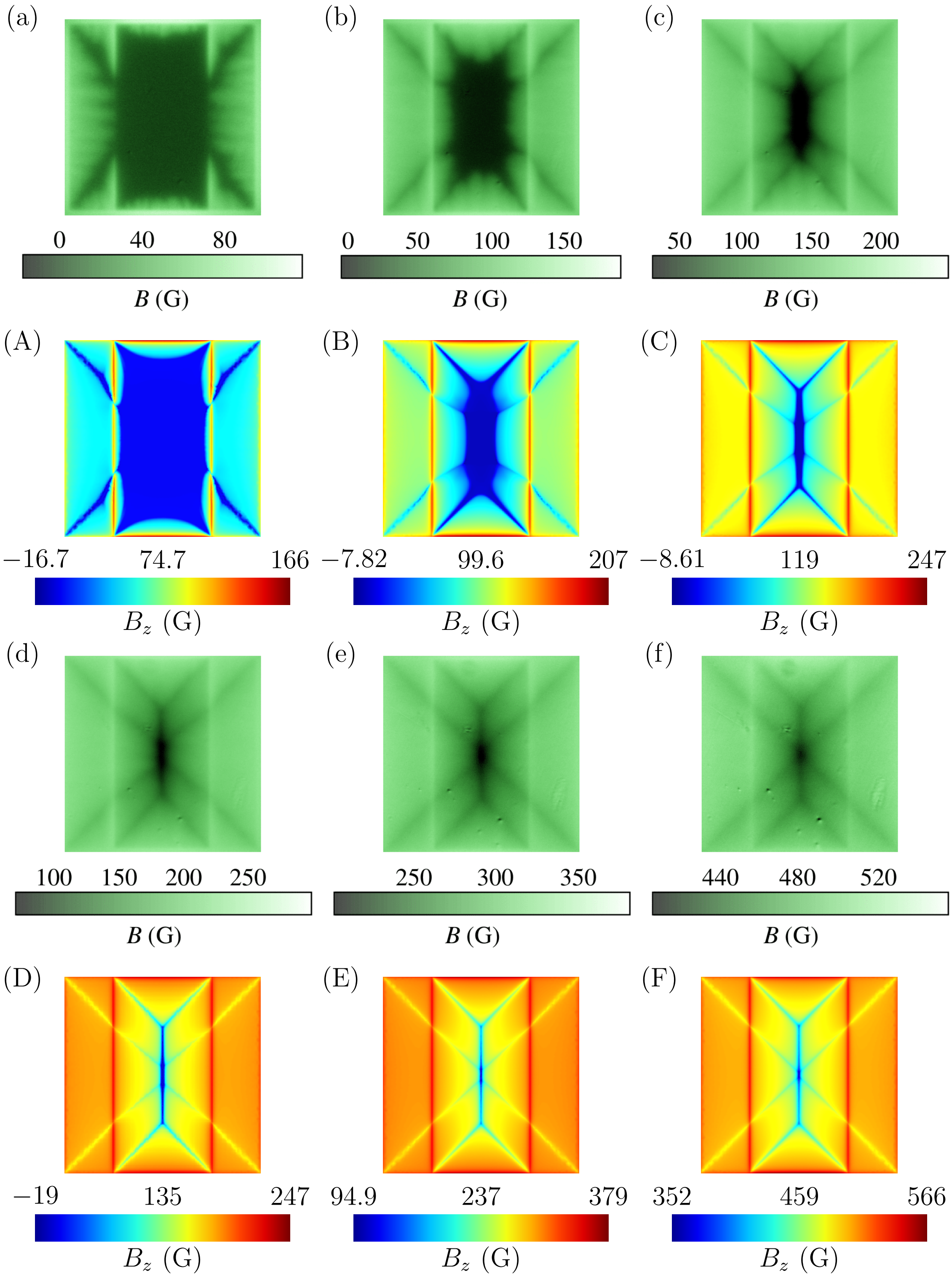

Figure 6.3: Distributions of magnetic field in the niobium two-layer assembly, $B_z = \mu_0 H_z$, where, after a zero-field cooling to 6 K, the applied field is ramped up to a fixed value H_a given as (a) 50, (b) 100, (c) 150, (d) 200, (e) 300, and (f) 500 Oe. The magneto-optical images showing the experimental distributions of B_z are expressed in Gauss (dark pixels correspond to low field strengths) and are shown in panels (a) to (f). Their numerical counter-parts, showing the simulated distributions of $\mu_0 H_z$ for the same applied fields as panels (a) to (f), are shown in panels (A) to (F).

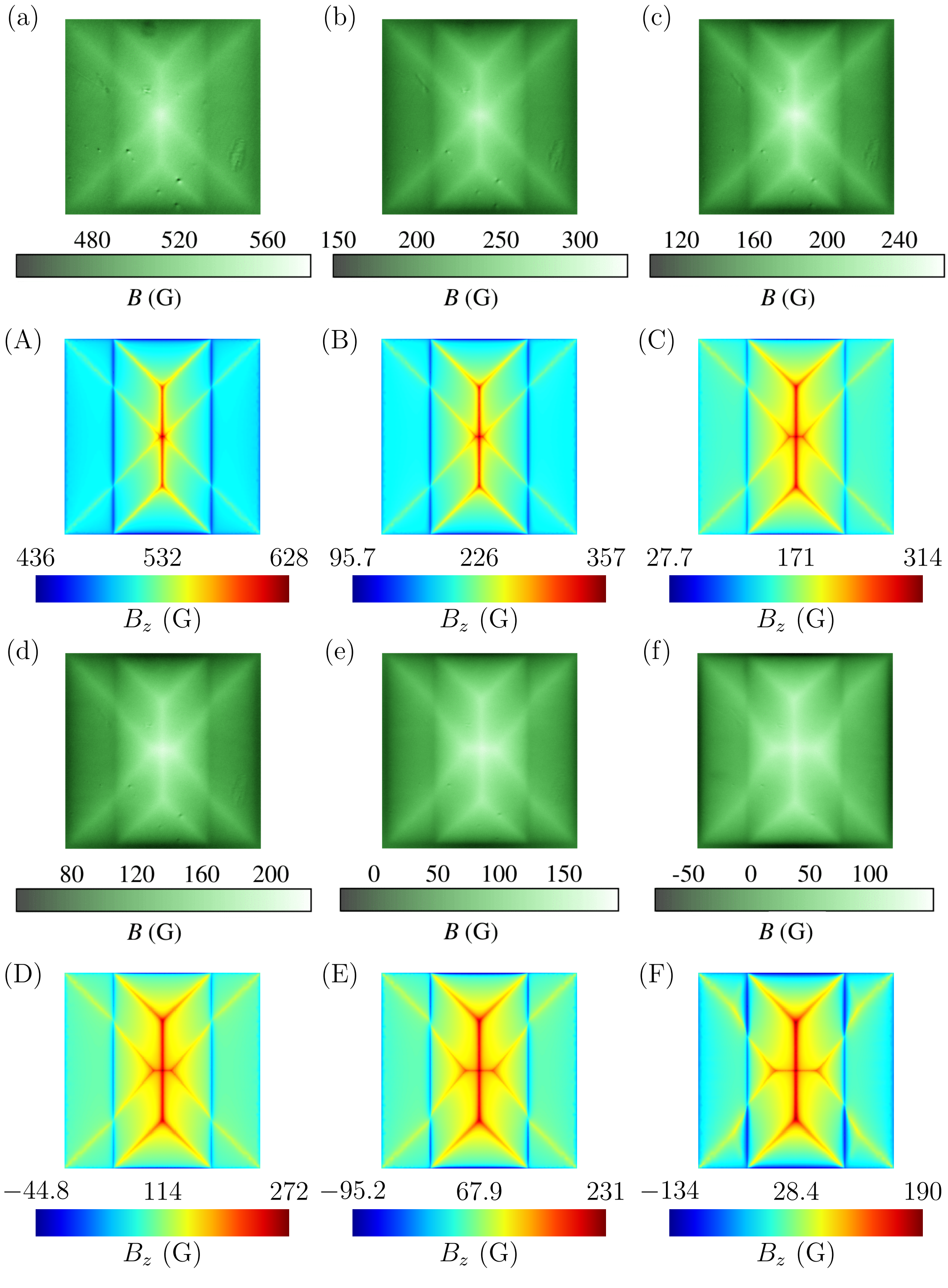

Figure 6.4: Distributions of the magnetic field in the niobium two-layer assembly, $B_z = \mu_0 H_z$, where, after a zero-field cooling to 6 K, the applied field is ramped up to 1000 Oe and decreased to a fixed value H_a given as (a) 500, (b) 200, (c) 150, (d) 100, (e) 50, and (f) 0 Oe. The magneto-optical images showing the experimental distributions of B_z (dark pixels correspond to low field strengths) correspond to panels (a) to (f). Their numerical counter-parts, showing the simulated distributions of $\mu_0 H_z$ for the same applied fields as panels (a) to (f), are shown in panels (A) to (F).

much less advanced in comparison. Upon further increasing the applied field to $H_a = 100$ Oe (panel (b)), the magnetic flux finally enters the central overlap region. The 'double Y' shape in the rectangular strip starts forming while the d-lines along the diagonals extend in the overlap region. However, their orientation seems to change abruptly at the limit between the overlap region and the rest of the square film. This trend is confirmed from $H_a = 150$ Oe and on, as is clearly illustrated in panels (c) to (f). A 'kink' in the d-lines appears when one goes from the region where the films do not overlap to the region where they do. Ultimately, this change of orientation means that the d-lines originating from the corners of the square film do not meet at the center of the film. Instead, the two d-lines that stem from the upper corners of the square meet above the center, while the two d-lines that originate from the bottom corners intersect below the center. This results in a central vertical line, which spans over a length ℓ_v.

Besides, from the inspection of panel (d), (e) and (f), one notices that ℓ_v decreases as H_a increases. At the same time, as the applied field is increased, the orientation of the d-lines in the overlap region seems to be progressively corrected. At 500 Oe (panel (f)), this kink can barely be observed with the naked eye. Even though it is not shown in Figure 6.3, ℓ_v still decreases and tends to 0 as H_a goes to 1000 Oe, in such a way that the kink completely fades away. The common vertical tail of the 'double Y'-shaped d-line, which is typical of thin rectangular strips, is also progressively recovered, as the applied field is ramped up from 200 to 500 Oe.

Similarly, Figure 6.4 (a) to (f) show the magneto-optical images of the magnetic-flux distributions in the assembly when the applied field is ramped down from 1000 Oe to H_a, at the same rate $\dot{H}_a = 12.5$ Oe/s, where $H_a = 500$, 200, 150, 100, 50, 0 Oe. The corresponding FE results are gathered in panels (A) to (F) in Figure 6.4. At 500 Oe (panel (a)), the d-lines are found to be the same as the superposition of the array of d-lines expected in separate square and a rectangular samples. No kink is apparent at the junction between the overlap region and the outer parts of the square film, as the d-lines seem to follow the diagonals of the square film and meet in its center. As the applied field is reduced and goes back to zero, as illustrated in panel (b) to panel (f), the d-line patterns change and differ from those observed in the increasing field stage. In particular, one does not recover the vertical d-line. The d-lines that stem from the corners of the square film still follow the diagonals, until they reach the overlap region, where they break and change their orientation. However, instead of meeting above and below the center of the projection of the assembly along the x-y plane, the d-lines originating from the left corners of the square sample now meet on the left side of the assembly and, reciprocally, the d-lines that started from the right corners intersect on the right half of the assembly. Both intersection points now delimit a central horizontal d-line, which extends over a length ℓ_h, that can be easily identified from 150 Oe and below (panels (c) to (f)). As H_a is lowered, ℓ_h steadily increases, and the d-lines further deviate from the diagonals of the square. Finally, at the remanent state (panel (f)), the horizontal d-line reaches its maximal extension and nearly crosses the whole width of the overlap region.

For both increasing and decreasing fields, the results computed numerically with the FE $\mathbf{H}$-ϕ formulation are in very good qualitative and quantitative agreement with the magneto-optical measurements. Nonetheless, when the applied field is ramped up, the numerical model seems to slightly overestimate the entrance of magnetic flux inside the sample. Diverse justifications to these qualitative differences can be given. First, values for the parameters of the generalized Kim law are difficult to assess for the two films. Second, the numerical model ignores the effect of surface barriers. Hence, this model assumption has the consequence of effectively favouring flux penetration. Finally, the resolution of the MO images might also limit the relevance of a strict comparison of the numerically computed flux-front extensions with the experimental ones.

Furthermore, these imperfections are also translated into systematic quantitative differences between the experimentally recorded levels of $\mu_0 H_z$ and those evaluated numerically. These differences appear to be more marked for the lowest values of H_a. Besides, the numerical snapshots of the $\mu_0 H_z$ distribution correspond to the levels of the magnetic field in the mid cross-sectional plane of the square film, while the magnetic-field levels that are evaluated by means of MOI correspond to flux penetrations at a finite distance of a few microns above the superimposed assembly, where the magnetic-field strength is slightly reduced with respect to what it is inside the films themselves.

Nevertheless, the salient phenomenological results, such as the global shape of the d-line networks, the smooth transition from an additional vertical d-line to an horizontal one, the field-dependent value of ℓ_v and ℓ_h, and the sudden breaking of the diagonal d-lines when they cross the border of the overlap region, are faithfully reproduced and modelled. The numerical estimations of ℓ_v and ℓ_h are in very good agreement with respect to what transpires in the magneto-optical snapshots. In summary, the $\mathbf{H}$-ϕ formulation, coupled with the constitutive laws described by Equation 6.1, Equation 6.2, and Equation 6.3, gives an appropriate description of the experimental observations in [44].

6.2.4 The critical role played by the magnetic-field dependence of the current density

The essential role played by the magnetic-field dependence of the critical current density is now demonstrated. From now on, in order to simplify the interpretation, it is assumed that both films share the same properties, i.e. $J_c(0)$, B_0 and α are the same in the square and rectangular films. Moreover, it is assumed that $\alpha = 1$, so that Equation 6.2 corresponds to Kim's law. In order to show the necessity of a magnetic-field dependence of the critical current density, let us compare the case of a uniform magnetic-field independent critical current density $J_c = 2$ MA/cm^2 in both films to the case of a magnetic-field dependent critical current density, which obeys Kim's law in Equation 6.2 with $J_c(0) = 4$ MA/cm^2, $B_0 = 20$ mT and $\alpha = 1$ in both films. The applied field is ramped up from 0 to 500 Oe at a rate $\dot{H}_a = 12.5$ Oe/s, before being ramped down to zero again at the same rate.

The resulting remanent-state critical states and the distributions of the out-of-plane magnetic field, $B_z = \mu_0 H_z$, are presented in Figure 6.5. The difference is striking. On the one hand, when J_c is constant, no central horizontal d-line is observed, as it can be seen in panels (a) and (c). The magnetic-field distribution then displays the combination of the footprints of the d-lines of each individual film, i.e. a 'X'-shaped pattern that stems from the square sample and the 'double Y' pattern of the rectangular sample. On the other hand, once a magnetic-field dependence of J_c is considered, the horizontal d-line arises in the centre of the assembly in the remanent state, which is imprinted in the out-of-plane component of the magnetic field of both films, as illustrated in panel (b) and (d).

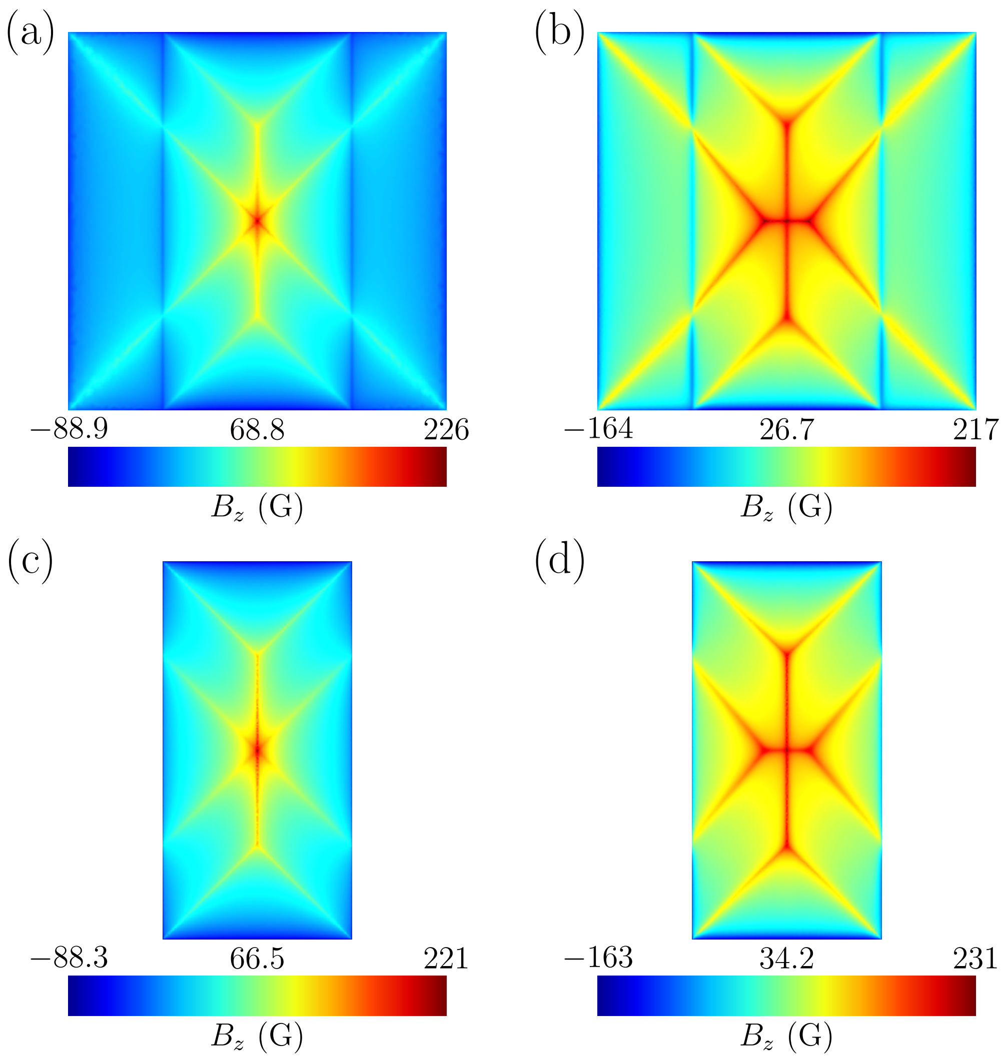

Figure 6.5: Simulated $B_z = \mu_0 H_z$ distributions in the square film (panels (a) and (b)) and the rectangular strip (panels (c) and (d)), when J_c is assumed constant with, $J_c = 2$ MA/cm^2 (panels (a) and (c)), and when J_c is assumed to depend on $|\mathbf{B}|$ according to Kim's law, with $J_c(0) = 4$ MA/cm^2, $B_0 = 20$ mT and $\alpha = 1$ (panel (b) and (d)). The films are in the remanent state (magnetization from a virgin sample to 500 Oe, see text).

This is fully coherent with the experimental and numerical results that were discussed in Subsection **6.2.3**, despite the simplified assumptions. This straightforward comparison directly shows the necessity of considering the contribution of $J_c(|\mathbf{B}|)$ for reproducing the distortion of the network of d-lines in the overlap region.

Further insight on the origin of the convoluted patterns unveiled by the $\mu_0 H_z$ mappings in both films can be acquired by analysing the current density inside the films. The circulation of $\mathbf{J}$ inside the films is represented through the normalized components of the current densities, $J_x/|\mathbf{J}|$ and $J_y/|\mathbf{J}|$, in the rectangular and square films. First they are depicted in the case of a constant critical current density $J_c = 2$ MA/cm^2. As it can be seen from panel (a) and (c), the square film is divided in four sectors that are identical according to a C_4 symmetry, where $J_x = 0$ in the left and right sectors, and $J_y = 0$ in the upper and lower sectors. In fact, the critical current density being constant and uniform in each individual film, $|\mathbf{J}|$ is the same in each sector, as shown in panel (e) of Figure

6.6. In short, in the square film, the current lines move in the counter-clockwise direction and describe square patterns. The inspection of panel (b), (d) and (f) leads to the same conclusion regarding the current paths in the rectangular film, although the patterns now consist in rectangular contours that are parallel to the borders of the film, and delimit four unequal sectors, delimited by the 'double Y' pattern.

The situation differs when the critical current density becomes magnetic-field dependent, as shown in Figure 6.7. In the rectangular strip, current density can be divided in four sectors that globally form the 'double Y' pattern. **J** remains roughly parallel to the edges of the strip, despite very slight deviations around the center of the strip, where the external 'X' pattern is observed, as shown in panels (b) and (d) of Figure 6.7. A slight $J_x/|\mathbf{J}|$ component can be observed, while $J_x/|\mathbf{J}| = 0$ inside the same region for a magnetic-field independent J_c. In that sense, the current loops are very similar to those of an uncoupled thin strip, and so are the d-line network that they generate.

This situation contrasts with what happens in the square film. The starkest difference with the current loops that are described in an isolated square film occurs around the center of the film, where currents curl around the central horizontal d-line, as it can be inferred from panel (a) and panel (c) in Figure 6.7. As assessed by the clear transition from blue to red along the horizontal median in panel (a), the current density sharply reverses its direction around the location of the central d-line. As it can be seen in panel(c), the current lines in the upper and lower regions are not strictly horizontal, but rather present a small but non-negligible inclination, which can be seen from the non-zero $J_y/|\mathbf{J}|$ at several locations in the upper and lower regions. These deviations are exacerbated around the central d-line. In the leftmost and rightmost sectors, the current density is strictly vertical. However, the sector delimitations no longer coincide with the square diagonals.

While the films share nearly the same distributions of $\mu_0 H_z$, see panels (b) and (d) of Figure 6.5, the distribution of **J** differ radically from one film to another, in the overlap region, as illustrated in Figure 6.7. In particular, the map of $|\mathbf{J}|$ in the square and the rectangular films indicate different levels from one film to another, as depicted in panels (e) and (f) of Figure 6.7. Also, note that the non-uniform distribution of $\mu_0 H_z$ implies the more evident variations of $|\mathbf{J}|$ in accordance to Kim's law, by contrast with the magnetic-field independent case, where the distribution was rather uniform.

6.2.5 A simplified model for explaining the distorted d-line patterns

In order to have a better grasp on the shape of the eddy-current loops inside the square film, where the additional d-line arises and evolves when the applied field varies, a simplified model based on the critical-state model (CSM) is proposed. The kinks that appear at the limits of the overlap region and the resulting critical states shown in Figure 6.3 and Figure 6.4 are reminiscent of what would happen in a square film with an inhomogeneous sheet critical current density, $J_{c,s}(x,y) = \int_{-d/2}^{d/2} J_c(x,y,z)\,\mathrm{d}z$. Eddy currents are generated in the square film in response to the superposition of the external applied field and the reaction field of the strip. From the perspective of the square film, the external

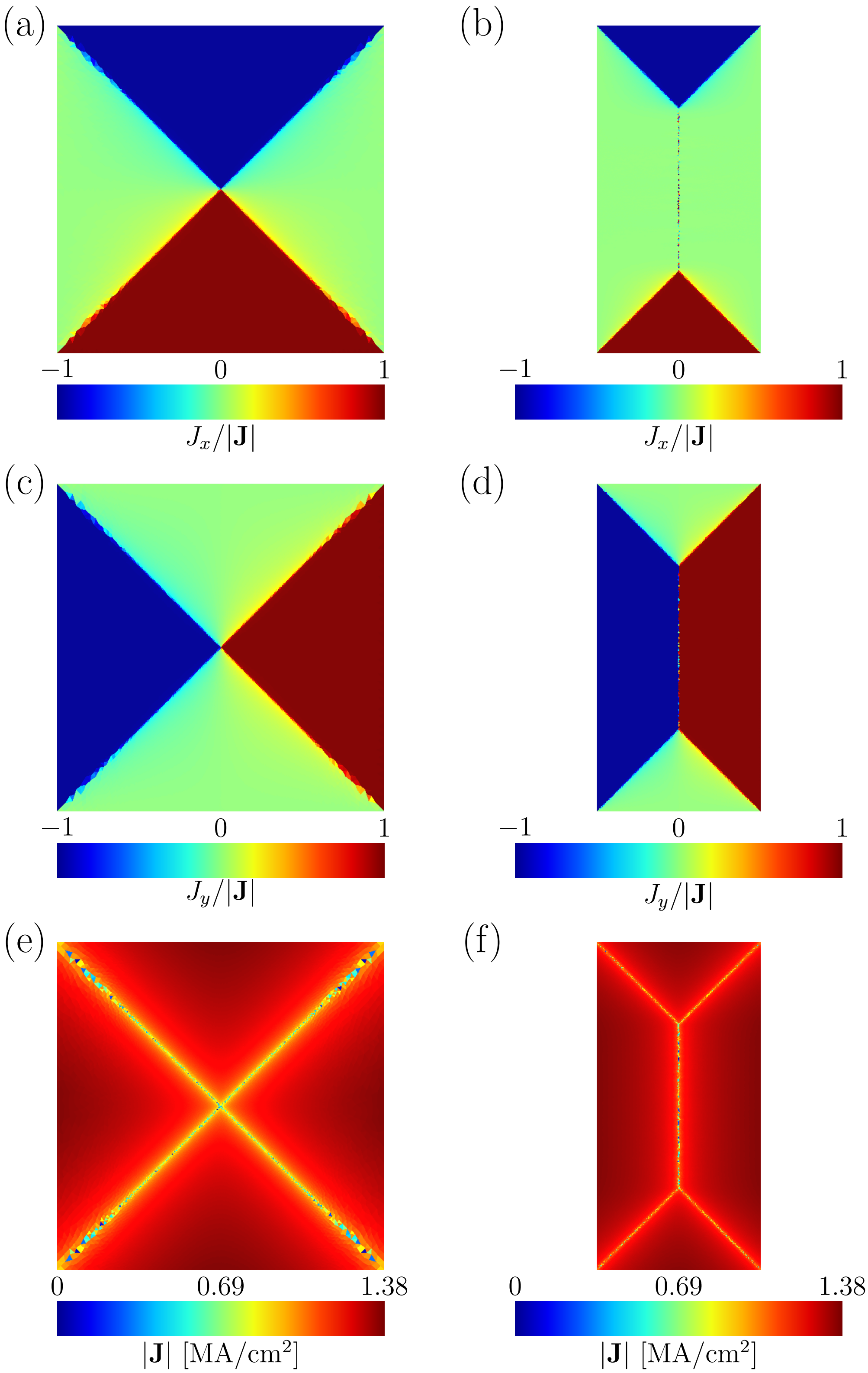

Figure 6.6: Distributions of J_x (panels (a) and (b)), J_y (panels (c) and (d)), and $|\mathbf{J}|$ (panels (e) and (f)) in the square film (panels (a), (c) and (e)) and in the rectangular strip (panels (b), (d) and (f)) for the case of a magnetic-field independent $J_c = 2$ MA/cm^2. The films are in the remanent state (magnetization from a virgin sample to 500 Oe, see text).

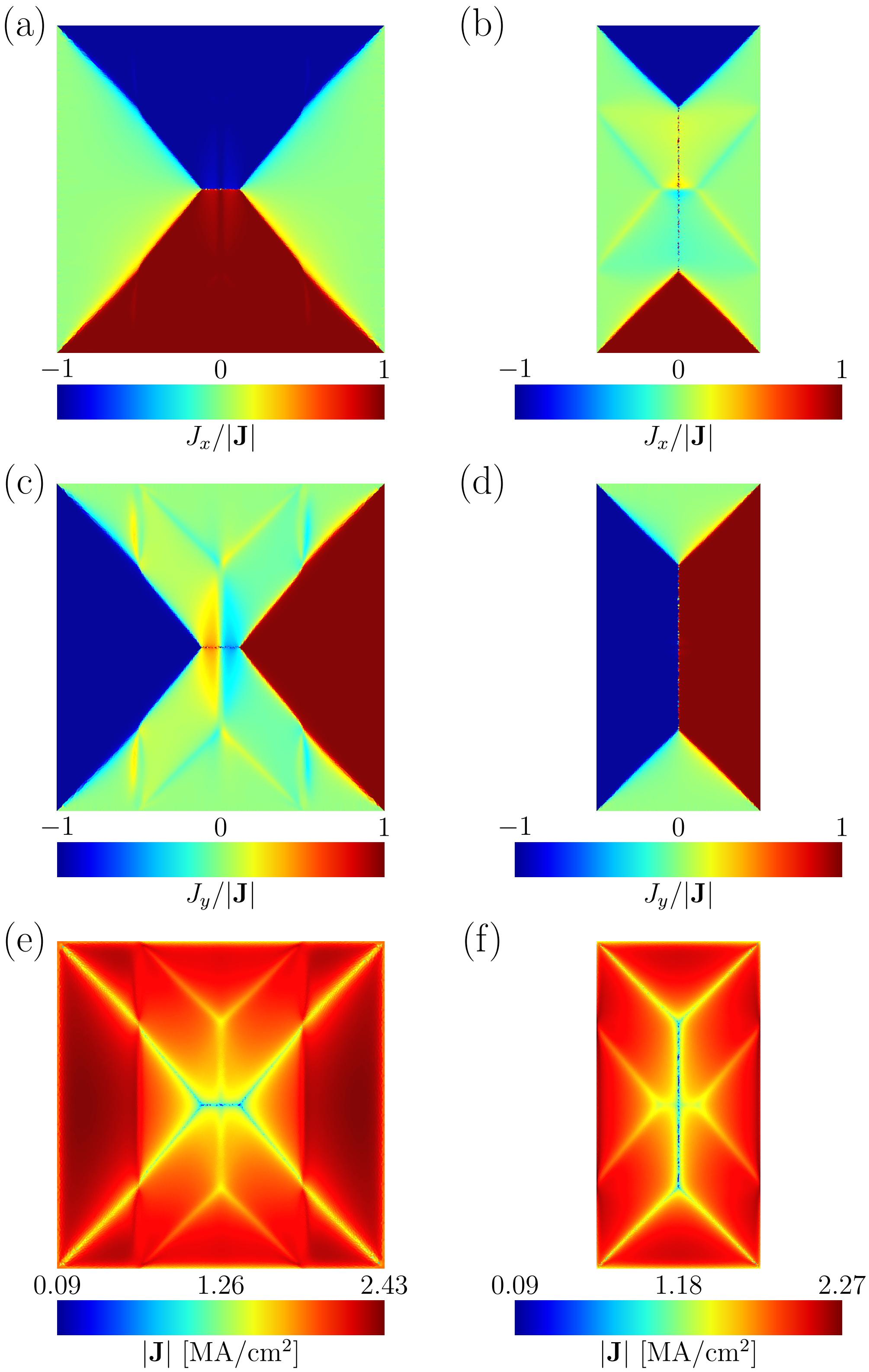

Figure 6.7: Distributions of J_x (panels (a) and (b)), J_y (panels (c) and (d)), and $|\mathbf{J}|$ (panels (e) and (f)) in the square film (panels (a), (c) and (e)) and in the rectangular strip (panels (b), (d) and (f)) for the case of a magnetic-field dependent $J_c(|\mathbf{B}|)$ following Kim's law, see Equation 6.2, with $J_c(0) = 4$ MA/cm^2, $B_0 = 20$ mT and $\alpha = 1$. The films are in the remanent state (magnetization from a virgin sample to 500 Oe, see text).

source magnetic field is therefore different in the overlap region, where the influence of the strip is the strongest, than in the rest of the film, where this influence is weak. The C_4 symmetry of the square film is broken, and the square film can be divided into three rectangular bands: the overlap area between the two films, and the two bands to the left and the right of the central band.

The crudest way to model the influence of the rectangular film on the critical current density in the square film consists in considering that $J_{c,s}$ is uniform within each region, whereas its value differs in the overlap and in the outer bands. In what follows, the values of $J_{c,s}$ in the overlap and lateral regions are denoted by $J_{c,s-\text{int}}$ and $J_{c,s-\text{ext}}$, respectively. Under such an assumption, one can use the Bean model in the longitudinal geometry to draw the current loops and infer the position of the d-lines in the square film. It is supposed that the sheet current density reaches its critical value everywhere, i.e. $|\mathbf{J_s}| = J_{c,s}$, which corresponds to the situation of completely penetrated films. The current loops in the thin-film geometry then coincide with those obtained in the longitudinal geometry. This assumption allows one to estimate the current distributions in the square film at large applied fields and in the subsequent remanent state.

Two cases can then be dissociated. Upon magnetization from a virgin state, the local magnetic field is less intense at the center of the assembly, because magnetic field first enters the sample through the edges of the square before it reaches the overlap region. Hence, according to Kim's law, $J_{c,s-\text{int}} > J_{c,s-\text{ext}}$. By contrast, upon a reduction of the applied-field intensity, magnetic field progressively evacuates the superconductors through its borders. The magnetic response of the film consists in a trapped flux that is globally more intense in the overlap region. From Kim's law, one can then safely assume that $J_{c,s-\text{int}} < J_{c,s-\text{ext}}$.

In order to illustrate the current-line patterns that are predicted by the simplified model, Figure 6.8 shows the current lines in the top right quarter of the square film upon a magnetization from a virgin state in the particular case of $J_{c,s-\text{int}} = 2J_{c,s-\text{ext}}$ and for a rectangular strip of width $W = L/2$. Similarly, Figure 6.9 depicts the current lines in the remanent state for the case $J_{c,s-\text{ext}} = \sqrt{3}/2J_{c,s-\text{int}}$ and $W = L/2$. There are similarities with the MO images and the numerical results in Figure 6.3 and Figure 6.4. In particular, one recovers the vertical d-line in Figure 6.8, while the horizontal d-line at the center of the sample is visible in Figure 6.9. The kinks that characterize the d-lines in the remanent state are also reproduced qualitatively, as it can be seen from the comparison between panel (F) of Figure 6.4 and Figure 6.9. In particular, the d-line that stems from point O changes direction two times, at points A and B. Similar deviations occur at points A and B in Figure 6.8. However, these deviations are difficult to pinpoint in panels (D), (E) and (F) of Figure 6.3, where the film has reached a fully penetrated state.

Besides being a two-dimensional model while the assembly is three-dimensional, the model is extremely simplified because it completely neglects the non-uniformity of the magnetic field within a given region. Instead, only differences between the outer and the overlap regions are considered. However, this model provides a first estimate of the expected critical-state architecture, from which a theoretical expression of the lengths ℓ_v and ℓ_h can be extracted. If one considers a centred thin strip of length L and width $W = L/2$,

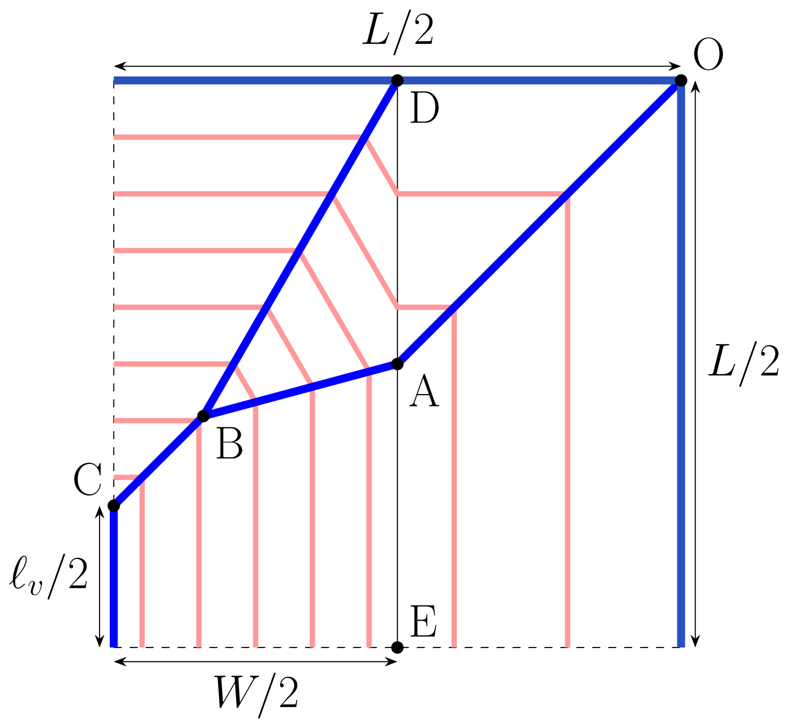

Figure 6.8: Critical state in the simplified model corresponding to a magnetization of the square + strip assembly, assuming $J_{c-\mathrm{int}} = 2J_{c-\mathrm{ext}}$ and $W = L/2$. Only the upper right part of the structure is shown. The other parts can be obtained by reflection symmetry, the axes of symmetry being highlighted with dashed lines. The dark blue lines correspond to the d-lines, while light red lines represent the current lines in the square film. The filled circles mark the locations where d-lines change their trajectory abruptly.

it can be shown that :

$$\ell_{v,h} = \frac{L}{2}\left|\frac{J_{c,s-ext}}{J_{c,s-int}} - 1\right|. \tag{6.4}$$

The detailed mathematical developments leading to this result are given in Appendix C for a centred strip with aspect ratio $W/L < 1$. One should however keep in mind how elementary and simplified the two-dimensional model is, so that the resulting ℓ_v and ℓ_h must be considered as first-order estimations.

Equation 6.4 can be expressed in a slightly different way, owing to the magnetic-field dependence of the critical current density described by Equation 6.2 with $\alpha = 1$, which is Kim's law. Assuming that the average strength of the magnetic induction over the overlap and outer regions is $\mathbf{B}_{int}$ and $\mathbf{B}_{ext}$, respectively, one can rewrite the length of the additional horizontal d-line as

$$\ell_h = \frac{L}{2}\frac{|\mathbf{B}_{int}| - |\mathbf{B}_{ext}|}{|\mathbf{B}_{ext}| + B_0}. \tag{6.5}$$

Because of the aforementioned limitations of the model, the result is however not expected to hold strictly and match exactly the simulated ℓ_h, as the distribution of the magnetic induction, and even more so the distribution of critical current density, are non-uniform within each region. Nevertheless, Equation 6.5 illustrates how the apparition of a central horizontal d-line is intimately related to the breaking of the square C_4 symmetry that

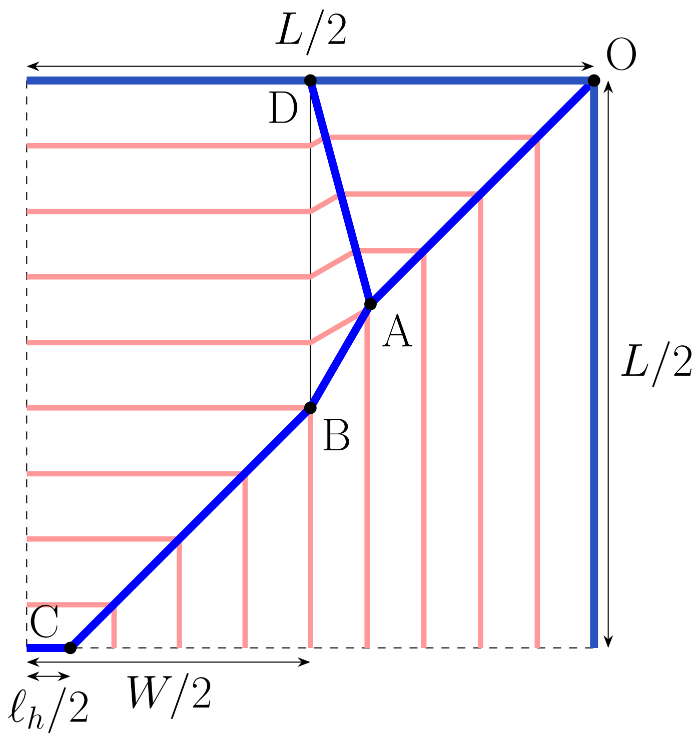

Figure 6.9: Critical state in the simplified model corresponding to a remanent state in the square + strip assembly, assuming $J_{c,s-\mathrm{int}} = \sqrt{3}/2 \times J_{c,s-\mathrm{ext}}$ and $W = L/2$. Only the upper right part of the structure is shown. The other parts can be obtained by reflection symmetry, the axis being highlighted by dashed lines. The dark blue lines correspond to the d-lines, while the light red lines show the current lines in the square film. The filled circles mark the locations where d-lines change their trajectory abruptly.

stems from the mutual magnetic interaction between the square and the rectangular films. The unequal levels of trapped field in the different delimited regions are then responsible for inhomogeneous critical-current-density distributions, because of Kim's law, which leads to the deformation of the d-line network.

Both parameters B_0 and $J_c(0)$ influence the distributions of magnetic field inside the superconducting film. In the remanent state, the trapped magnetic field depends on the entrance and exit of vortices, so that one can expect that ℓ_h vary with respect to both B_0 and $J_c(0)$. In order to assess the dependence of ℓ_h on these parameters, the magnetic response of the assembly in the remanent state is simulated for several values of B_0 and $J_c(0)$. The resulting values of the dimensionless quantity ℓ_h/L are shown as a function of $B_0/\mu_0 J_c(0)d$ in Figure 6.10, where $\mu_0 J_c(0)d$ has been chosen as the typical level of the local reaction field that is generated by the assembly. In these simulations, one still has $L = 200$ μm, $W = L/2$, and $d = 300$ nm. The out-of-plane magnetic field is ramped up from 0 to a maximal value H_a at the constant rate $\dot{H}_a \sim 12.5$ Oe/s, before being ramped back to zero at the same rate. For each set of parameters, the extreme value of H_a is chosen so as to ensure the complete penetration of the films. The mesh size in the superimposed region is set to 1 μm, while it is either 1 or 5 μm in the outer regions of the square film.

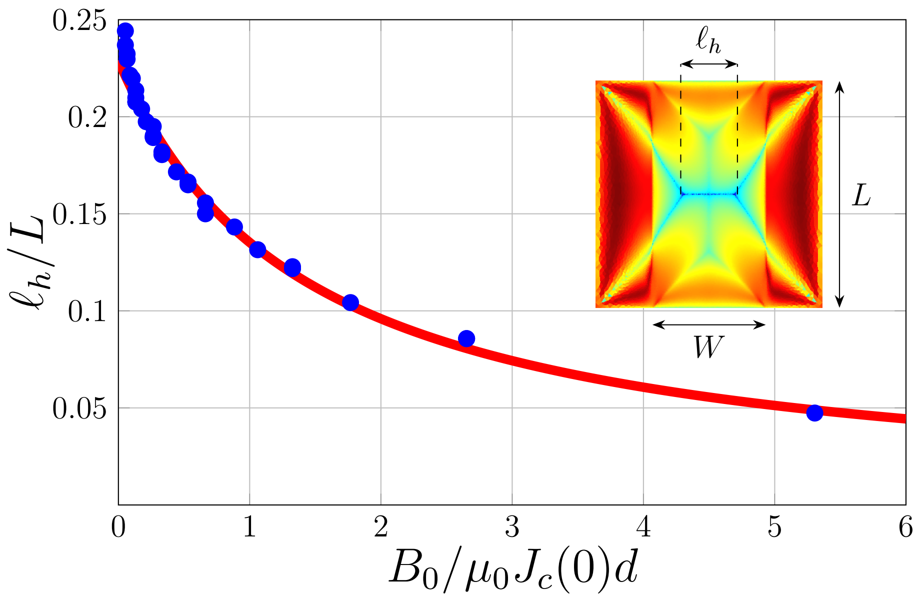

Figure 6.10: ℓ_h/L as a function of $B_0/\mu_0 J_c(0)d$. B_0 and $J_c(0)$ are parameters that describe the magnetic-field dependence of the critical current density. The plain red curve corresponds to the least-square fit on the data, based on the expression of Equation 6.6, which yields $C_1 = 0.33$ and $C_2 = 1.44$. The measured values of ℓ_h emerging from the numerical simulations are indicated by the blue circles. For each simulation, $L = 200$ μm, $W = L/2$ and $d = 300$ nm. The applied field is ramped at a constant rate $\dot{H}_a = 12.5$ Oe/s, from 0 to a maximal applied field that entails the complete penetration of the films, before being decreased back to the remanent state, where ℓ_h is probed.

A unidirectional shell transformation with $A = 75$ μm was used for all simulations. Note that the selected value of A lies in the interval of values that was prescribed in Chapter 2 for a single film. In the particular case $B_0 = 20$ mT and $J_c(0) = 4$ MA/cm^2, the obtained magnetic-field distribution was also compared to the results simulated with a truncated-geometry approach, and to those obtained with a unidirectional shell transformation with $A = 26$ μm, which is the recommended value of A for a thin square film of length $L = 200$ μm, see Figure 2.13. The mean absolute errors of the magnetic field in the square film did not exceed 2% of the field trapped at the center of the assembly, with most error occurring at the level of the d-line. Besides, the critical-state structures were found to be identical. In particular, the length ℓ_h remained the same in all tested simulations.

Remarkably, the values of ℓ_h appear to fall on a unique curve that decreases with increasing $B_0/\mu_0 J_c(0)d$. The magnetic induction $\mathbf{B}_{int}$ and $\mathbf{B}_{ext}$ in Equation 6.5 can be normalized with respect to $B_0/\mu_0 J_c(0)d$, in such a way that Equation 6.5 now reads as

$$\frac{\ell_h}{L} = \frac{C_1}{C_2 + \frac{B_0}{\mu_0 J_c(0)d}}. \tag{6.6}$$

Equation 6.5 thus suggests a first-order estimation of the variations of ℓ_h as a function of the physical parameters that are involved in Kim's law, which are B_0 and $J_c(0)$. The values of C_1 and C_2 can be estimated from the least-square fit of Equation 6.6 on the numerical results of Figure 6.10. One finds $C_1 = 0.33$ and $C_2 = 1.44$. The resulting fitting curve, indicated by the plain red line in Figure 6.10, is found to be in excellent agreement with the numerically estimated ℓ_h.

One can easily understand why ℓ_h decreases when B_0 increases, as inferred from Figure 6.10. For fixed $J_c(0)$ and a high value of B_0, $J_c(B)$ barely decreases with $|\mathbf{B}|$, in agreement with Kim's law. The magnetic-field variations induce small current-density changes, reducing the influence of the three-dimensional geometry and hence the value of ℓ_h. Moreover, it is interesting to note that the ratio $B_0/J_c(0)$ is also found in the CSM expression of the critical current density in the longitudinal geometry, which is

$$\frac{J_c(0)}{|J_y(x)|} = \sqrt{\left(1+\frac{\mu_0 H_a}{B_0}\right)^2 + \frac{2\mu_0 J_c(0)}{B_0}\left(|x| - \frac{W}{2}\right)}, \tag{6.7}$$

where x is the distance from the center of an infinitely long superconducting slab of width W. Equation 6.7 indicates that $B_0/J_c(0)$ controls the amplitude of the variations of the critical current density in bulk samples. Similarly, the ratio $B_0/\mu_0 J_c(0)d$ characterizes the distributions of the magnetic field and the current density in thin superconducting films [238]. Therefore, it sounds logical that this ratio is related to the distance ℓ_h, which is the distinctive trait of the two-layer assemblies.

At this stage, the influence of Kim's law on the critical states in the three-dimensional two-layer assemblies has been made very clear. Nevertheless, it is worth stressing out again that this mechanism is not the only one that can be held responsible for the apparition of unusual central d-lines. Applying an external in-plane magnetic field is for instance able to induce anisotropy of the critical current density and therefore modify the critical-state networks [97]. The in-plane components of the reaction field generated by one film could potentially lead to induced in-plane anisotropy in the other film. However, the numerical simulations confirm the absence of induced in-plane anisotropy. First, the numerical simulations present striking quantitative similarities with the experimental results, although no in-plane field was generated in the assembly. Second, the computed intensity of the in-plane components of the reaction field inside the films does not exceed 60 Oe, that is to say much less than the required 300 Oe.

6.3 Influence of the geometrical parameters of the two-layer assembly on ℓ_h

In Section 6.2, it was suggested that the additional central d-line arises in the two-layer assemblies for two reasons. First, the natural C_4 symmetry of the square film is broken as the consequence of the magnetic interaction with the closely placed rectangular film. Second, the magnetic-field dependence of the critical current density is paramount to the development of these additional d-lines. The influence of the $J_c(\mathbf{B})$ law was discussed thoroughly in Subsection 6.2.4 and Subsection 6.2.5. In this section, the focus is put on the role played by the magnetic interaction between the two films. Its effect is studied by varying the geometrical parameters of the two-layer assembly: the thickness of the insulating layer, $t_{\mathrm{SiO_2}}$, the width of the strip, W, and the lateral position of the rectangular film with respect to the center of the square film, X_c.

In what follows, the assembly will always be composed of a square film of side $L = 200$ μm, above which is superimposed a thin rectangular strip of length L and width $W < L$, in such a way that its longest median is aligned with the vertical median of the film. The thickness of both the square and the rectangular films are set to 300 nm. The assembly is still subjected to an out-of-plane magnetic field, $H_a\hat{z}$, which is raised from 0 to a maximal applied field, before being ramped back to the remanent state at the same constant rate, $\dot{H}_a \approx 12.5$ Oe/s. The parameters of Equation 6.2 are set to the given values $J_c(0) = 4$ MA/cm^2, $B_0 = 20$ mT, and $\alpha = 1$. Individual geometrical characteristics of the geometry, i.e. $t_{\mathrm{SiO_2}}$, W, and X_c, are now changed one by one, and their effect on ℓ_h and the d-line layout is numerically monitored and commented in the rest of the section.

6.3.1 Influence of $t_{\mathrm{SiO_2}}$ on ℓ_h

First, let us investigate the effect of the strength of the magnetic coupling between the square and the rectangular film. The intensity of the reaction field generated by one of the superconducting films decays as one gets further from the surface of the film. In the simulations, this can be done by changing the thickness of the insulating SiO_2 layer, $t_{\mathrm{SiO_2}}$, that separates the two superconducting films.

In these upcoming simulations, the maximal value of H_a was set to 25 kA/m $\approx$ 315 Oe, in order to reach full penetration during the raising stage of the applied field. A shell-transformation technique was used, with $A = 75$ μm. $t_{\mathrm{SiO_2}}$ ranges over several orders of magnitude, from 3 nm to 300 μm. Since the effect of the coupling between the films is investigated here, the insulating layer is subdivided in 10 layers in order to ensure a good interpolation of ϕ in between the films. To keep the duration of the simulations acceptable, the in-plane mesh of the extruded layers was reduced in consequence, so that the mean mesh size is uniform in the whole square and rectangular films and equal to 5 μm. The uncertainty on the reported values of ℓ_h is thus expected to be larger than in the previous simulations. Simulations with a finer mesh size ~ 1 μm in both films were also carried out for $t_{\mathrm{SiO_2}} = 3$ nm, 300 nm and 3 μm, yielding a more precise estimation of ℓ_h. Nonetheless, the obtained values were the same as those computed with the coarser mesh.

Whatever the thickness of the insulating layer, the d-line patterns are the same as that described in Subsection 6.2.3. The ℓ_h-values are collected for each value of $t_{\mathrm{SiO_2}}$ and the results are displayed in Figure 6.11 on a logarithmic-scaled plot. Up to $t_{\mathrm{SiO_2}} \sim 10$ μm, ℓ_h is almost constant. When $t_{\mathrm{SiO_2}} \gtrsim 10$ μm, ℓ_h decreases monotically with $t_{\mathrm{SiO_2}}$. For very large $t_{\mathrm{SiO_2}} \gg d$, for which $\ell_h \ll L$, alongside the shrinkage of ℓ_h, the kinks that affect the d-lines at the junction between the overlap region and the rest of the square film progressively vanish, and d-lines stemming from the corners of the film progressively align with the diagonals of the square.

The results of Figure 6.11 materialize the intricate relation between the intensity of the magnetic coupling between the films and the architecture of the critical states, in particular, the length ℓ_h. In fact, the closer the films, the stronger the coupling between the films, and the more the d-lines are distorted. By contrast, if the films are far from each other, the mutual influence of both films weakens, and the current distribution in the films

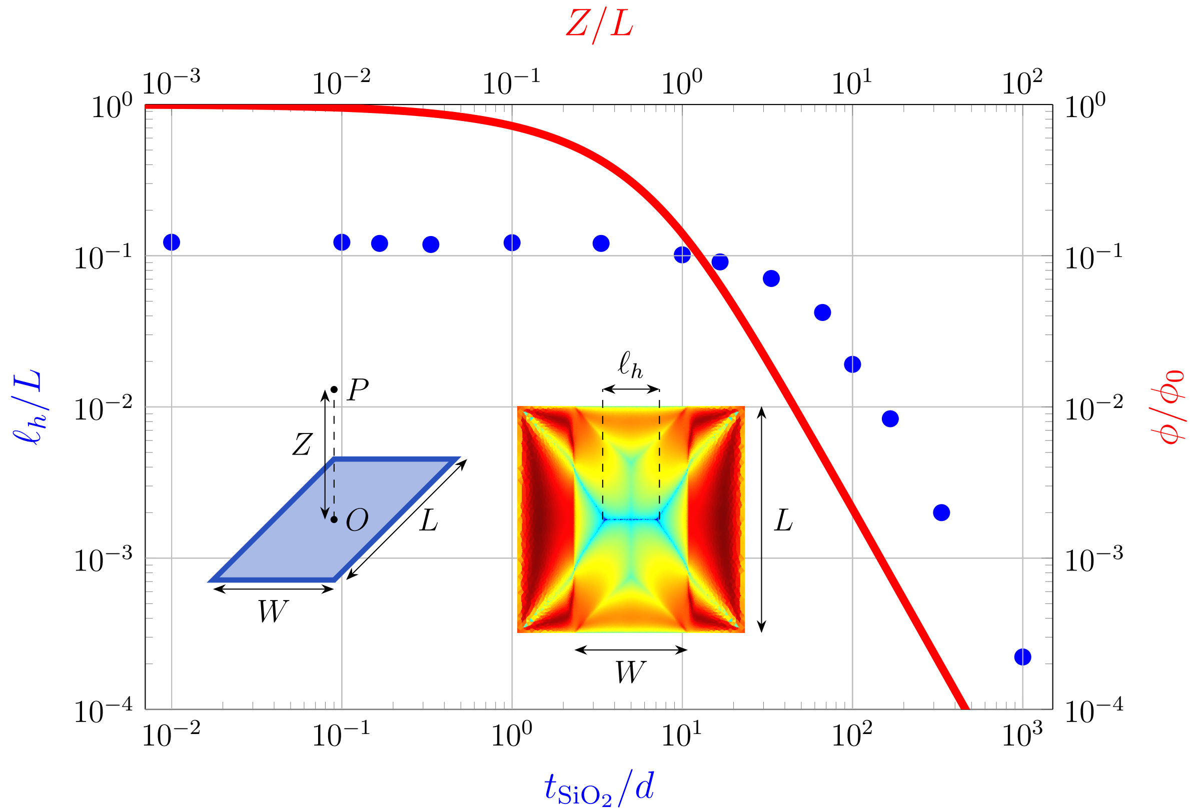

Figure 6.11: Dimensionless extension of the horizontal d-line, ℓ_h/L, as a function of normalized insulating thickness between both films, $t_{\mathrm{SiO_2}}/d$. In each simulation, the values of ℓ_h/L are measured when the two-layer assembly is in the remanent state, after an initial magnetization from a virgin state up to 315 Oe (50 kA/m). The values of ℓ_h/L correspond to the blue circles. The red curve depicts the evolution of the normalized scalar magnetic potential, ϕ/ϕ_0, as a function of the dimensionless distance from the square-film surface, Z/L. ϕ_0 is the magnetic potential on the upper surface of the film, evaluated at O, the center of the square film, and ϕ is evaluated at a distance Z from O, as shown in the left inset. $L = 200$ μm, $W = L/2$ and $d = 300$ nm. The parameters of the generalized Kim law are $J_c(0) = 4$ MA/cm^2, $B_0 = 20$ mT and $\alpha = 1$.

approaches the undisturbed distribution that is observed in isolated films. Interestingly, the decrease of ℓ_h/L as a function of $t_{\mathrm{SiO_2}}/d$ is reminiscent of the decay of the scalar magnetic potential, ϕ/ϕ_0, as a function of the distance from the top surface of the film. This is illustrated by the red curve in Figure 6.11, which corresponds to the value of ϕ/ϕ_0 derived in Appendix **B** for a fully penetrated square film.

6.3.2 Influence of W on ℓ_h

Now, let us consider variations of the rectangular strip width W. The motivation behind this analysis starts with Equation 6.5, which gives a theoretical estimate of ℓ_h as a function of the average trapped field in the overlap region and in the outer bands of the square film. When W is increased, the area of the overlap region increases, which implies the reduction of the area covered by the outer regions. This might influence the average amount of trapped magnetic field in each region, and consequently the values of ℓ_h. The aim of this subsection is therefore to evaluate the influence of W on ℓ_h. To this aim, $t_{\mathrm{SiO_2}}$ is set to 300 nm again, while W is allowed to vary.

Figure 6.12 shows the out-of-plane component of the magnetic field, $B_z = \mu_0 H_z$, in the square film for various widths (a) $W = L/12$, (b) $W = L/4$, (c) $W = L/2$ and (d) $W = 3L/4$, respectively, with $L = 200$ μm. The maximal applied field is now set to 500 Oe to ensure the full penetration of magnetic field in the assembly before decreasing H_a to zero. The d-line network is fairly similar to what was observed previously. The diagonal d-lines undergo several kinks and clear changes of directions that remind the ones obtained with the simplified model, see Figure 6.9. The length of the central horizontal line, ℓ_h, does not vary monotonously with W. For the smallest $W = L/12$, see panel (a), $\ell_h \sim W$. Then, as W increases, ℓ_h increases as well, as shown in panel (b), where $W = L/4$. It then increases slightly for $W = L/2$, see panel (c), and finally decreases when $W = 3L/4$, as shown in panel (d).

A more detailed picture of the evolution of ℓ_h as a function of W is shown in Figure 6.13. One can verify that ℓ_h first increases as $\sim W$ for the smallest W, before it reaches a maximum, which is close to $5W/12$ for this particular set of parameters. In the extreme configuration $W = L$, ℓ_h vanishes. This situation corresponds to a stack of two square films, a configuration where the out-of-plane symmetry of the assembly is recovered, so that the d-lines correspond to the diagonals of the square films.

One can also refer to the generalization of the simplified critical-state model of Subsection **6.2.5** to the case of a centred strip of arbitrary width $W \leq L$, whose mathematical developments are derived in Appendix **C.2**, see for instance Equation C.12, which is verified if the condition described by Equation C.14 holds. As $W \to L$, $|\mathbf{B}_{int}|$ decreases because the area of the overlap region increases and includes less intense magnetic field levels, as it can be inferred from panels (b), (c) and (d) of Figure 6.12. Therefore, $J_{c,s-int}$ is enhanced, leading to a reduction of the ratio $J_{c,s-ext}/J_{c,s-int}$ and ℓ_h, in agreement with Equation C.12. Note that, according to Equation C.12, this reduction is further exacerbated by the factor $1 - W/L$.

It is worth noting that the simplified model leading to Equation 6.5 is not valid for small W, as explained in Appendix **C.2**. Instead, it appears that ℓ_h is limited to the width of the strip, with clear kinks on the diagonal d-lines that arise in the regions where the films do not overlap. This trend is shown in Figure 6.13 by drawing the line $\ell_h = W$, which corresponds to the red dotted line. One can indeed see that the simulated results fall on this line until $W \approx L/10$. Put differently, Figure 6.13 exemplifies the non-trivial and non-linear impact of the magnetic interaction between the films on the geometrical characteristics of the d-lines, including the ℓ_h-values.

6.3.3 Influence of X_c on ℓ_h

Up to this point, the rectangular film was always centred with respect to the square film, i.e. the projection of the longest median of the rectangular film coincides with one of the

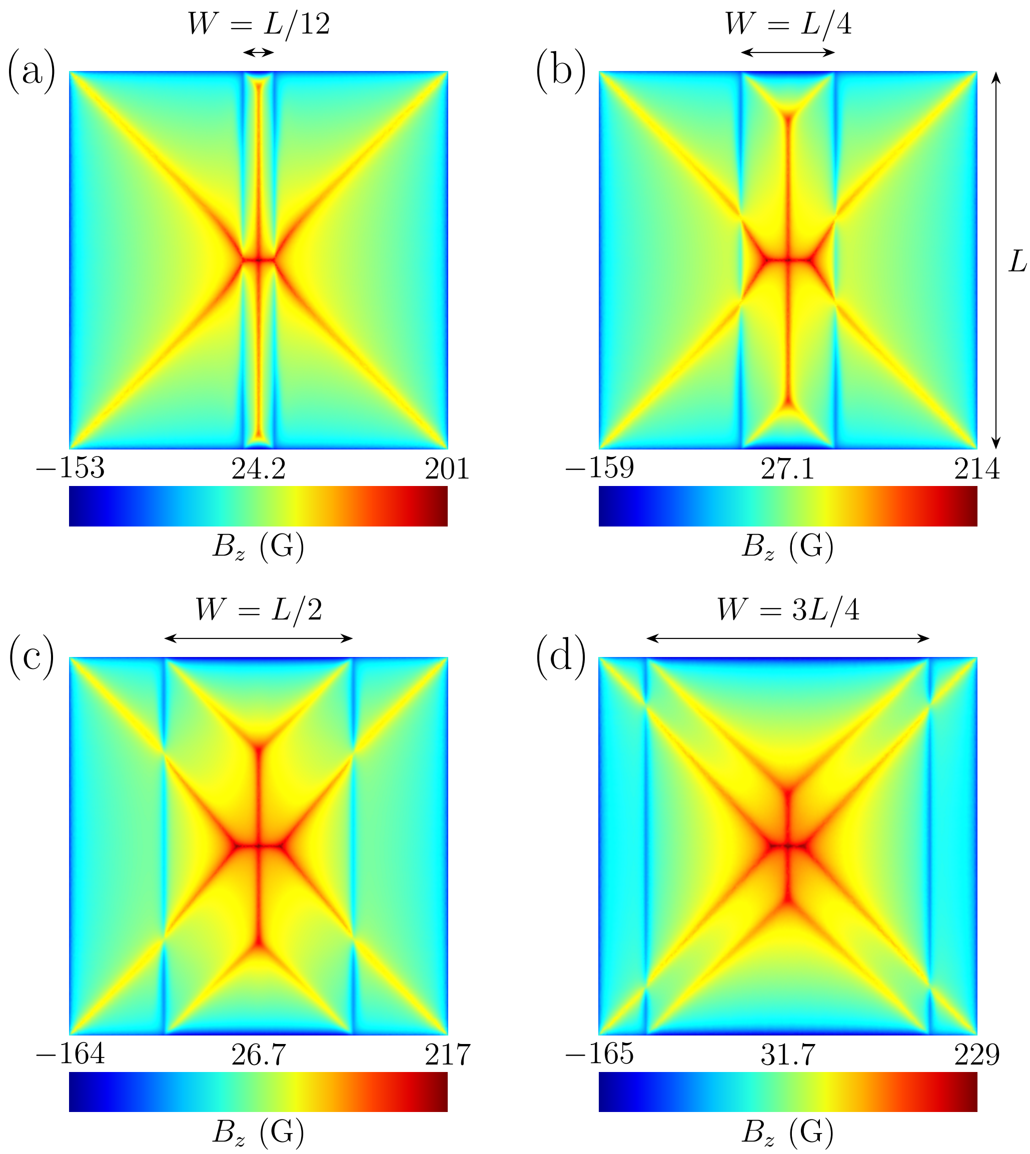

Figure 6.12: Distributions of $B_z = \mu_0 H_z$ in the square film of the two-layer assembly for different values of the strip width, W. The assembly is in the remanent state, after an initial magnetization from a virgin sample to 500 Oe. (a) $W = L/12$, (b) $W = L/4$, (c) $W = L/2$ and (d) $W = 3L/4$. In each simulation, $L = 200$ μm and $d = 300$ nm. The parameters of the generalized Kim law are $J_c(0) = 4$ MA/cm^2, $B_0 = 20$ mT and $\alpha = 1$.

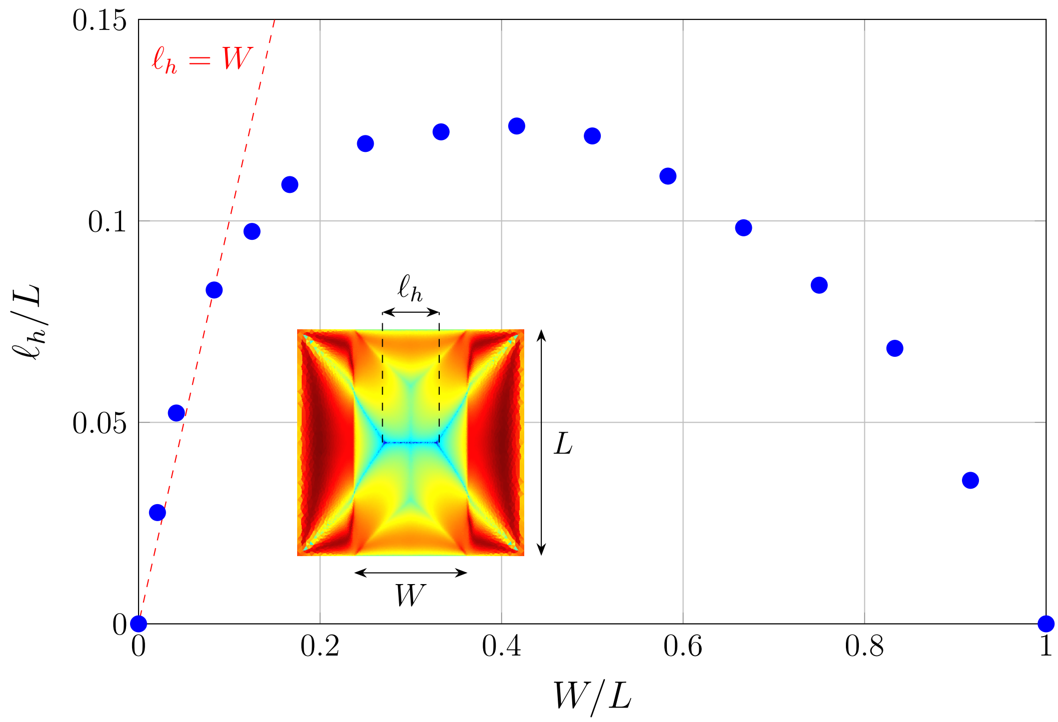

Figure 6.13: Dimensionless extension of the horizontal d-line, ℓ_h/L, as a function of the dimensionless width of the rectangular strip, W/L. The two-layer assemblies are in the remanent state after an initial magnetization from a virgin sample up to 500 Oe. For all values of W, the longest median of the rectangular strip is aligned with one median of the square film. The dashed line serves as a guide for the eye and corresponds to $\ell_h = W$. For all simulations, $L = 200$ μm, and $d = 300$ nm. The parameters of the generalized Kim law are $J_c(0) = 4$ MA/cm^2, $B_0 = 20$ mT and $\alpha = 1$.

median of the square. If the rectangular strip is moved to the right by a distance X_c, the total magnetic field to which the square film is subjected changes, since it includes the contribution of the reaction field coming from the rectangular film. Modifications of the critical-state structure in the two-layer assembly are therefore expected. Hence, this subsection focuses on the layout of the critical states in these off-centred geometries. To this aim, the width of the rectangular strip is set again to $W = L/2$. The out-of-plane component of the magnetic field in the square film, $\mu_0 H_z$, is represented in Figure 6.14 for $X_c = 10$, 20, 30 and 40 μm.

In all cases, one can clearly see the imprint of the d-lines arising in the square film, which consists in the deviated diagonals of the square that meet at the centre and form the horizontal line, and the one from the rectangular film, which is the 'double Y'-shaped set of d-lines. However, two distinct features can be highlighted with respect to the centred case. First, it appears that the horizontal line shrinks to zero as the lateral offset of the strip is increased. For $X_c = 40$ μm, it has almost completely vanished, and the d-lines originating from the corners of the square film coincide with the diagonals of the square. Second, the magnetic-field imprint of the thin strip is not a straight 'double Y', as it was the case in the centred case. Instead, one can note a slight bending of the vertical branch of the 'double Y' pattern. One can also observe that the H_z distributions are no longer symmetric with respect to the longest median of the overlap region, where, on average, the H_z levels are larger to the left than to the right of the vertical branch.

These simulations hence highlight the influence of the lateral position of the rectangular film on the magnetic interaction between the films, as it determines the exact three-dimensional shape of the magnetic field to which each film is subjected. Therefore, the role played by the magnetic coupling between films of different cross sections on the magnetic-field distributions in two-layer assemblies was once again underlined.

6.4 Magnetic response of three-layer assemblies

Finally, let us extend the study of the critical states in assemblies of superimposed films with different cross sections to the case of three-layer assemblies. By investigating three-layer arrangements of films, one is able to verify whether the critical structures in three-layer assemblies change with respect to those observed in two-layer assemblies, but also to visualize the effect of the out-of-plane film ordering on the d-line networks. In what follows, two different assemblies will be considered, both of them being sketched in Figure 6.15. The first assembly, which is depicted in panel (a) of Figure 6.15, consists in a square film that is sandwiched in between two rectangular strips. It will be referred to as the rectangle-square-rectangle (RSR) assembly. Proximity effects between the square film and the rectangular strips are avoided by depositing a SiO_2 layer between them. This layout is thus symmetric with respect to the x-y plane. The second assembly, which is represented in panel (b) of Figure 6.15, still involves a superconducting square film and two rectangular strips, but this time, the strips are placed on the same side of the square film. By contrast to the RSR assembly, the out-of-plane symmetry of the arrangement is therefore broken. This arrangement of films will be referred to as the square-rectangle-rectangle (SRR) assembly.

Whatever the configuration, all the superconducting films have the same thickness, $d =$ 300 nm, while the insulating layers have all the same thickness, $t_{\mathrm{SiO_2}} = 300$ nm. The square films consist in $L \times L$ films, with $L = 200$ μm, while the rectangular ones are $L \times W$ films, with $W = L/2$. The longest medians of the rectangular strips are here aligned with one of the medians of the square film, so that the assembly is symmetric with respect to the selected median. In these simulations, $J_c(0) = 4$ MA/cm^2, $B_0 = 20$ mT and $\alpha = 1$ in all films. The average mesh size is 1 μm in the whole strip and is relaxed back to 5 μm on the left and right edges of the square film.

The simulated distributions of B_z in each film and for each configuration are shown in Figure 6.16. The results for the RSR assembly are shown in the left column (panels (a), (c) and (e)), while those of the SRR assembly are shown in the right column (panels (b), (d) and (f)). As in the case of the two-layer assembly, the out-of-plane magnetic field remains the same in all the films, whatever the configuration. Barely noticeable variations of the maximal intensity occur from one film to another one. In the RSR configuration, the B_z distributions in the rectangular films are rigorously the same due to the out-of-plane symmetry of this layout. Moreover, a horizontal d-line is present in both cases. However, some differences can be noticed. First, in the SRR layout, two 'double Y'-shaped patterns appear at the center of each film, while a single magnetic-field footprint is observed in the

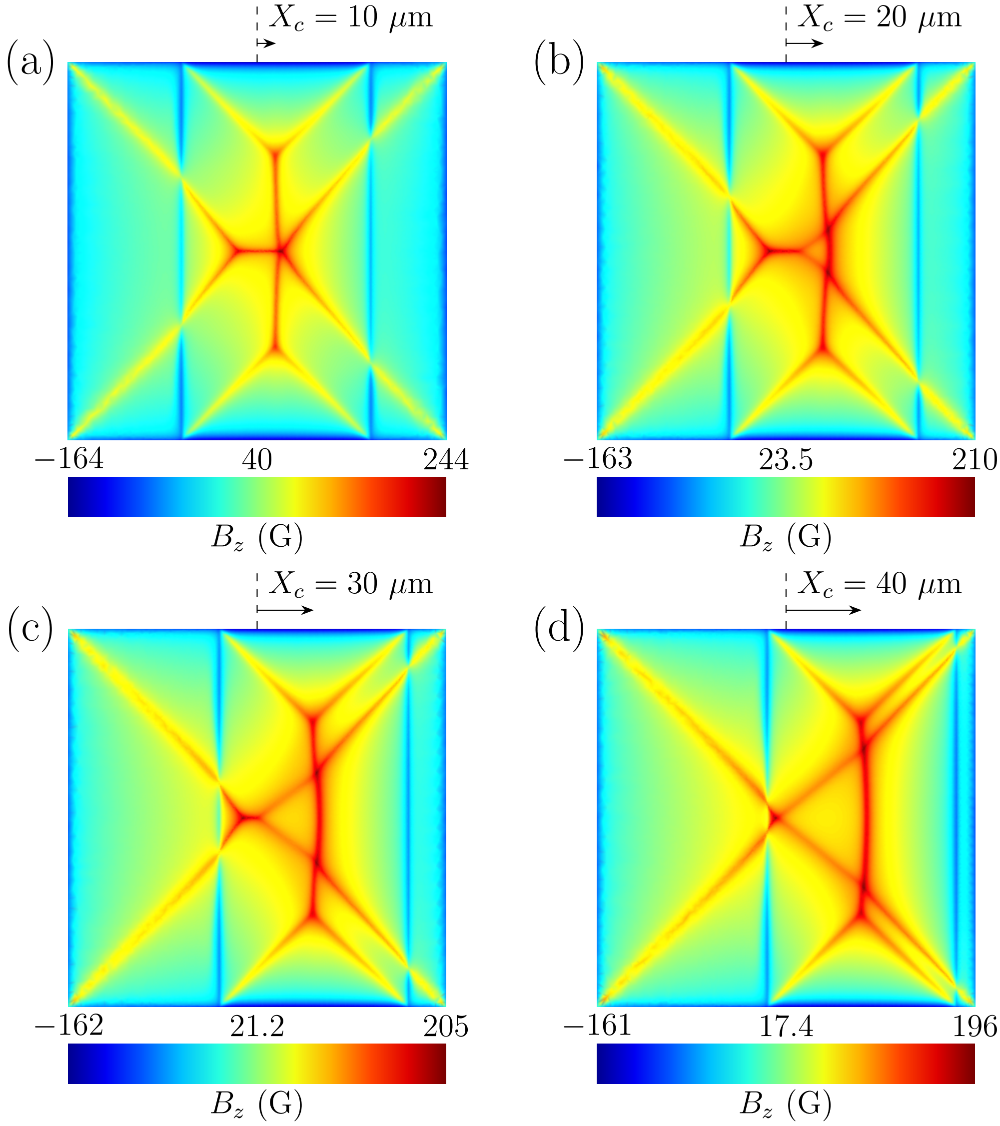

Figure 6.14: Distributions of B_z in the square film of a two-layer assembly made of a square and a rectangular film. The rectangular strip is off-centred by a horizontal distance X_c which is equal to (a) 10, (b) 20, (c) 30 and (d) 40 μm. The arrows above the upper side of each image represent the distance X_c from the vertical median of the square film, which is indicated by the dashed lines. The width of the rectangular film is $W = 100\ \mu$m, while the length and the thickness of both films are $L = 200\ \mu$m and $d = 300$ nm, respectively. The parameters of the generalized Kim law are $J_c(0) = 4$ MA/cm^2, $B_0 = 20$ mT and $\alpha = 1$.

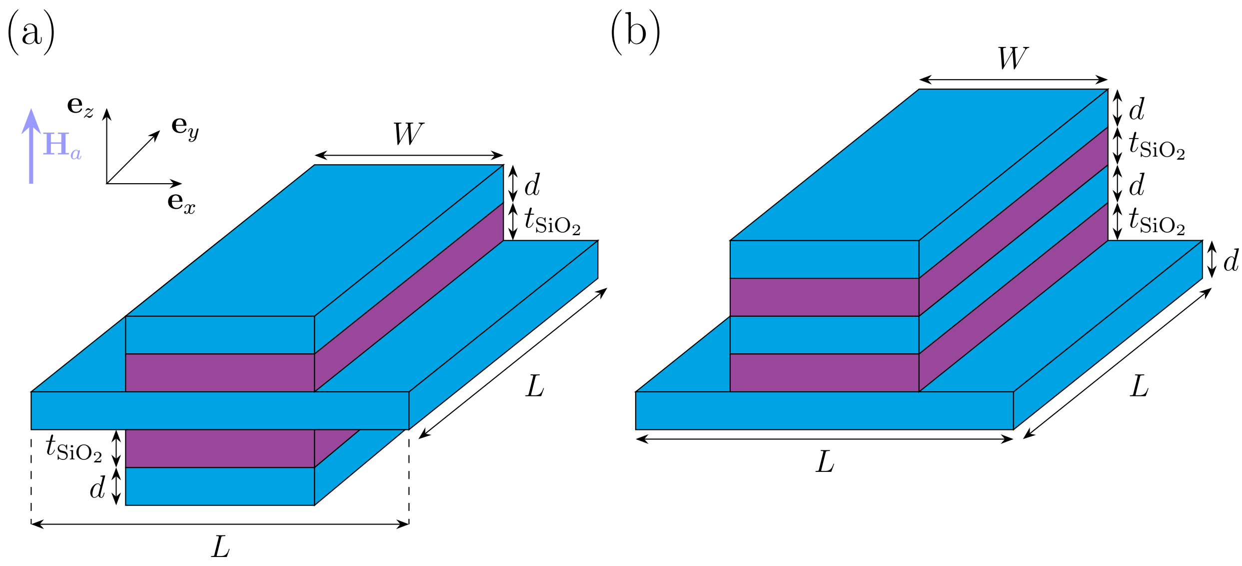

Figure 6.15: Geometries of three-layer assemblies made of two rectangular strips and one thin square film, where the rectangular films are either placed (a) on each side of the square film (RSR assembly), or (b) on the same side of the square film (SRR assembly). The applied field, $\mathbf{H}_a$, is perpendicular to the cross section of the films. The length of the square and the rectangular films is L, while the width of the rectangular film is W. The thickness of each film is d, and the thickness of each intermediate insulating $\mathrm{SiO_2}$ layer is equal to $t_{\mathrm{SiO_2}}$. The longest medians of the rectangular strips are aligned with one of the medians of the square film.

RSR assembly. In the SRR configuration, which is non-symmetric along the out-of-plane direction, two pairs of branches spread from the corners of the rectangular films, with an angle that differs from the $\pi/4$-angle that is observed in the two-layer and the RSR assemblies. Besides, the length of the horizontal line depends on the disposition of the films, as ℓ_h/L is equal to 0.17 and 0.19 in the RSR and SRR configurations, respectively. In the case of the centred ($X_c = 0$) two-layer assembly, $\ell_h/L = 0.12$, which is lower than in the two three-layer arrangements. Therefore, the number of films and their ordering has a tangible impact on the magnetic-field distribution in the films.

Considering equal spacing between successive films, the fact that ℓ_h is longer in three-layer assemblies than in two-layer assemblies can be understood in the light of the simplified model from Section **6.2.5**. In the remanent state, when another strip is added, the magnetic field that is trapped in the region where the films overlap is increased. As a consequence, the difference between $J_{c,s-\mathrm{int}}$ and $J_{c,s-\mathrm{ext}}$ is exacerbated, and ℓ_h increases, as indicated by Equation **6.4**.

Although the distributions of B_z in the rectangular and the square films are roughly the same for a given three-layer structure, one should expect different current-density patterns from one film to another. These differences can be explained as follows. Although the mechanism that is responsible for the apparition of the additional kinked d-lines stays the same as in the two-layer case, the relative positions between the different films influence the strength and the orientation of the total reaction field that threads a given film. For example in the RSR layout, the penetration of magnetic field in the square film is determined by the strength of the applied field, but also by the equal influence of each

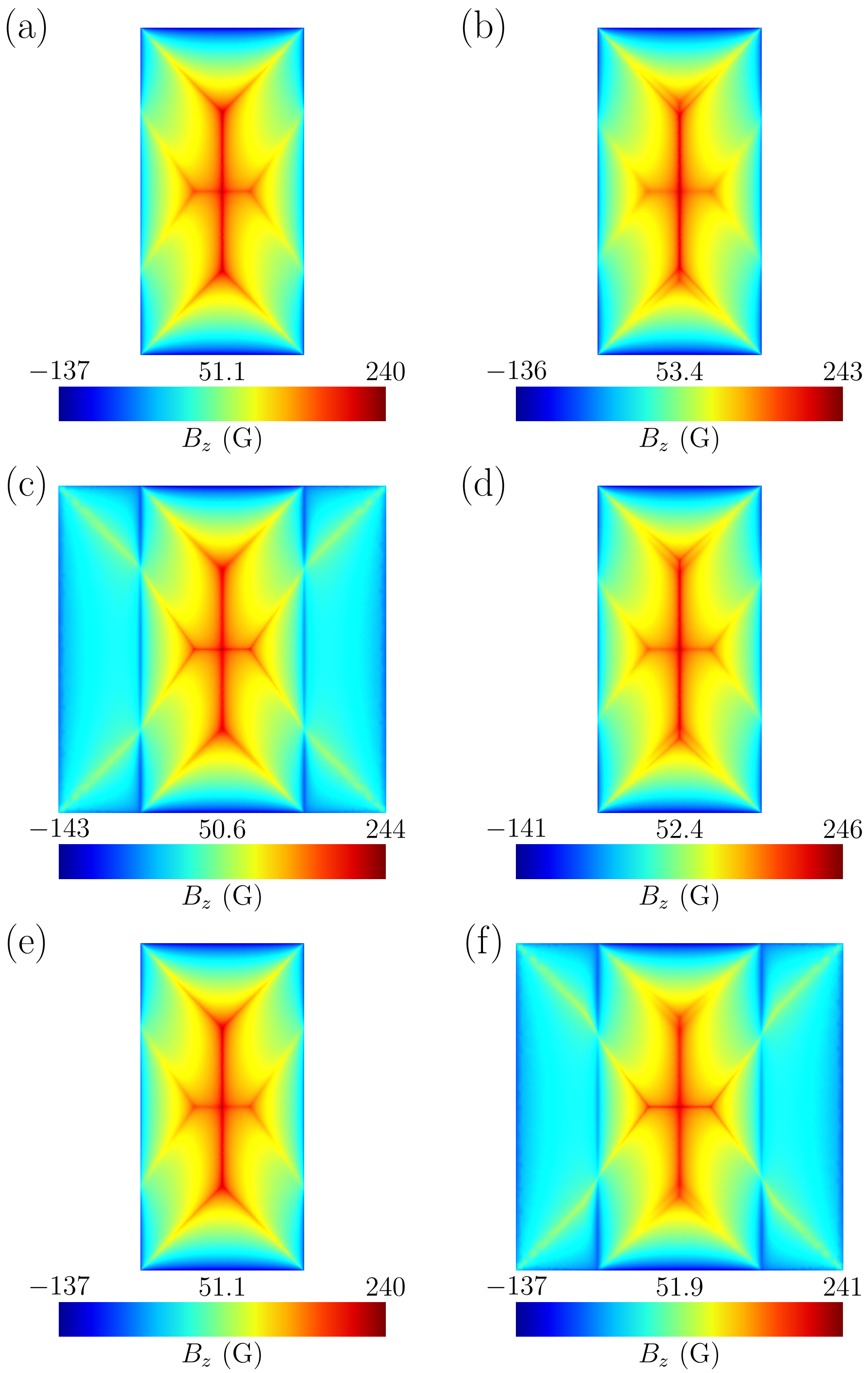

Figure 6.16: Distributions of B_z in the rectangular and square films in the three-layer RSR configuration (panels (a), (c) and (e)) or in the SRR configuration (panels (b), (d) and (f)), see panel (a) and (b) of Figure 6.15, respectively, for a visual description of the two assemblies. Panel (a) and (b) correspond to the uppermost rectangular films in the RSR and SRR layouts, respectively. The width of the rectangular films is $W = 100$ μm, while the length and the thickness of the films are $L = 200$ μm and $d = 300$ nm, respectively. The parameters of the generalized Kim law are $J_c(0) = 4$ MA/cm^2, $B_0 = 20$ mT and $\alpha = 1$.

equally distant rectangular strip. The magnetic-field penetration in the rectangular strips is instead feeling the influence of the square film predominantly, as the second rectangular strip lies further, meaning that its contribution to the reaction-field strength and direction is weakened. A similar argument can be enunciated to explain why the current-density distributions in the two rectangular films of the SRR disposition differ from each other. Therefore, the induced-current loops might become very complex, so that it is difficult to predict how the d-lines are organized inside multilayer samples. In any case, as it was already highlighted for the two-layer assembly, one cannot simply assume that the current-density patterns in these structures, where the cross sections of the films are dissimilar, will correspond to those of individual isolated films.

6.5 Conclusion

This chapter was devoted to the description of the critical states in three-dimensional assemblies made of a square film and a thin rectangular strip superimposed on top of each other. MOI has revealed non-trivial networks of d-lines that cannot be obtained by a simple superposition of the d-lines of each isolated film. Moreover, the d-line patterns are observed to vary with the applied field. More specifically, at the center of the assembly, a central d-line appears with a vertical orientation for increasing fields and a horizontal orientation for decreasing fields.

Numerical modelling then helped to emphasize the underlying phenomenology. First, the magnetic coupling between the rectangular strip and the square film induce the breaking of the C_4 symmetry of the square film. The films interact with each other through their reaction field, which influences the magnetic-field penetration. Then, most crucially, a magnetic-field dependence of the critical current density generates imbalances in the critical-current-density distribution within the square film, which in turn force the current to go along distorted loops to ensure current conservation.

Based on a simplified two-dimensional model constructed on the critical-state model, a systematic numerical study of the parameters that describe the magnetic-field dependence of the critical current density was then carried out. Despite being rudimentary, the simplified model gives significant insight on how the d-line networks are modified. Simple expressions of the lengths of the vertical or horizontal d-lines as a function of the mean values of the trapped field in the overlap and outer regions were derived in Appendix **C**.

Thereafter, an extended investigation of the role played by the magnetic coupling between the two films on the position of the d-lines was carried out. This was achieved by modifying some geometrical parameters of the assembly, such as the separation between the films, the width of the rectangular strip, and the lateral position of the strip. It was clearly shown that the closer the films, the more perturbed the d-line patterns. Besides, a vast and rich variety of critical-states patterns was displayed as the lateral position and the aspect ratio of the strip were changed. This allowed one to verify the importance of the magnetic coupling between the films on the shape of the d-line patterns, as the strength and the orientation of the reaction field that embraces each film were changed for each set of parameters.

Finally, the magnetic-flux penetration in three-layer assemblies that include two rectangular and one square films was also studied. Although the obtained critical states were close to those observed in the two-layer assemblies, it appeared that the ordering of the films in the out-of-plane direction was able to induce variations of the current loops from one film to another one. These tangible differences further corroborated the sensitivity of the d-line architecture to the shape of the reaction field that is perceived by each film in the assembly, when a magnetic-field dependence of the critical current density is accounted for.

The results of this chapter show how cautious one has to be when considering stacks of tapes with non-uniform cross sections, since the geometry of one layer could heavily perturb the magnetic-field and the current distributions across the various layers, forcing the current density to follow unexpected routes. However, to the best of my knowledge, the kind of critical states that were described here are not observed in stacks of films of identical cross sections, such as the commercial ones, given that they are subjected to a uniform out-of-plane magnetic field. Deviations of the current patterns in superconducting tapes subjected to the stray field of a rotating magnet have however been reported, even with constant J_c [258]. Besides, the spacing between the films also has a non negligible effect on the field distributions, as it fine-tunes the strength of the interaction between the different films. All of this calls for further investigation concerning the shape of the different films, their thickness, and their spacing, which could be used for heterostructures based on superconducting films, such as shifted strip arrays, magnetic cloaking, or fast logic devices [44].

Conclusions and perspectives

This thesis was devoted to the numerical investigation of the penetration of magnetic flux in structured systems made up of superconducting films and subjected to a uniform out-of-plane magnetic field. The focus was essentially put on elucidating the question of the physical or phenomenological origin of unexpected observed d-line patterns in several experiments. To this aim, numerical methods proved to be a crucial tool to test the validity of hypotheses and to collect insightful information on the electromagnetic fields, which would be otherwise complicated, or even impossible, to evaluate experimentally.

The numerical modelling of the magnetic field penetration in thin superconducting films was addressed by means of a finite-element method, based on the $\mathbf{H}$-ϕ formulation. This numerical method requires to mesh the non-conducting domain, which increases the number of degrees of freedom of the problem. Usually, a domain truncation is used to keep the non-conducting domain finite, at the cost of imposing a Dirichlet boundary condition at a finite distance of the conducting domain. By contrast, shell-transformation techniques map infinite domains onto finite ones, so that the Dirichlet boundary condition is correctly applied at an infinite distance from the superconductors. Therefore, it was investigated whether the latter approach could reduce the number of degrees of freedom in the non-conducting domain by reducing the size of the shell domain as much as possible, while achieving a given level of accuracy for the interpolation of the magnetic field and the induced currents. The optimal size and mesh quality for the shell domain were numerically investigated for single films with different aspect ratios, and recommendations were made for the choice of the transformation parameter. For thin superconducting disks, it was found that using a spherical shell transformation was the most beneficial shell-transformation shape, as the simulation time was reduced by 35% with respect to the truncation method. However, the spherical shell transformation only reduced the simulation time by 5% in the case of rectangular films. Unidirectional shell transformations, which were the most investigated shell transformation, did not reduce the simulation time significantly, and therefore appear to be of marginal interest. Besides, it was shown throughout the manuscript that the shell-transformation approach was as accurate as the method of truncation for a variety of film geometries and three-dimensional superconducting assemblies, independently of the choice of the constitutive laws, such as isotropic or anisotropic $\mathbf{E}$-$\mathbf{J}$ laws, or magnetic-field-dependent critical current density, $J_c(\mathbf{B})$.

The $\mathbf{H}$-ϕ formulation was then used to investigate the origins of the excess magnetic field penetrations and the temperature widening of the parabolic discontinuity lines that develop around edge indentations in thin niobium films. In particular, the plausibility of the suggestion of [41], which argues that the deviations from the Bean model stem from a depletion of the Bean-Livingston barrier at the tip of the indentation, was tested.

Surface barriers effects were included in the finite-element simulations by means of an artificial peripheral region of enhanced pinning. The numerical simulations then confirmed the phenomenology of the experiments, as the indentation indeed acted as a tiny flux faucet through which magnetic flux penetrates more easily, leading to enhanced excess penetration depths and wider parabolic discontinuity lines than what is predicted by the Bean model. However, unambiguous evaluation of the temperature dependence of the surface barriers at the indentation and away from it are currently lacking for niobium films. Further experimental work is therefore needed to conclude on the opening of the parabolic d-lines with increasing the temperature, which were observed in [41].

A major finding of this work concerns the fundamental influence that the magnetic field dependence of the critical current density can have on the critical states in systems made of superconducting thin films. Usually, the $J_c(\mathbf{B})$ dependence only influences the magnetic field and current density levels in the films, but the d-lines, which mark the position of the abrupt current density changes of orientation always coincide with symmetry lines that depend on the geometry of the sample and the distribution of the critical current density in the sample. Besides, once the system is fully penetrated, the d-line patterns no longer evolve. These two generally accepted principles were however found to be violated in two radically different cases.

The first case concerns thin square superconducting films which are pierced with a regular array of triangular antidots. The C_3 symmetry of the triangular holes breaks the C_4 symmetry of the square cross section of the sample. At the micro-scale, vortices escape more easily from the triangular holes through their vertices than through their flat edges, since current crowding is enhanced in the vicinity of the sharp tips of the triangular holes. The system is therefore inherently anisotropic. Moreover, time-dependent Ginzburg-Landau simulations revealed the magnetic field dependence of the system anisotropy. These observations were transposed at the macro-scale, by considering a magnetic-field-dependent anisotropic **E**-**J** law. Finite-element numerical simulations then highlighted critical state structures that change with the applied field, qualitatively reproducing the experimental observations.

The second category of systems consists in three-dimensional assemblies made of a rectangular film superimposed on a square film. In the region where the films overlap, the total field to which the square film is subjected includes the contribution of the reaction field emanating from the rectangular film and differs from that in the rest of the film. Hence, because of the $J_c(\mathbf{B})$ dependence, the critical current density in the overlap region differs from that in the region where the films do not overlap and the C_4 symmetry of the square sample is broken. This non-uniform distribution of the critical current density is at the origin of the applied-field-dependent critical states. Numerical modelling of these systems allowed one to evidence the role of the $J_c(\mathbf{B})$ dependence and to carry out a systematic investigation of the role of the magnetic coupling in these multilayer assemblies, in very good phenomenological and good qualitative agreement with the experimental observations.

In both cases, the metamorphosis of the d-lines are unambiguously illustrated with the reversal of an additional d-line that arises in the centre of the assembly. As the applied magnetic field is decreased back to zero after a first magnetization from a virgin state, it can in fact be observed that this central d-line goes from a vertical position to a horizontal one, or, by contrast, from a horizontal to a vertical position. Besides, it is worth noting that these critical states are not related to any kind of extrinsic anisotropy that would stem from applying an external in-plane field [97]. Instead, these peculiar critical states were reported in systems whose geometrical characteristics are non-symmetric, such as the array of triangular antidots or the different film cross sections in the three-dimensional assemblies. Therefore, it is not expected to observe such distortions of the critical states in stacks of identical centred tapes.

Besides, the magnetic field dependence of the critical current density not only influences the critical states that progressively develop during the smooth penetration of the magnetic field, but also impacts the regime of magnetic flux avalanches. The magnetic field dependence was suggested as a possible explanation for the triggering of flux avalanches along the smooth edges of niobium films, while they are expected to nucleate instead at the tip of the edge indentation, according to the literature. When the magnetic field dependence of the critical current density is accounted for, numerical modelling of the magnetic field penetration in a square film with a triangular indentation showed that, although the electric field is the highest at the indentation tip, the current density is depleted in the vicinity of the indentation. This contradicts the commonly accepted statement that current crowding occurs at the indentation tip. At the tip of the indentation, the combination of the electric field enhancement with the current density depletion can sometimes result in a lower threshold magnetic field along the smooth border than at the indentation, whereas this threshold field will always be lower at the indentation when the critical current density is assumed to be field-independent.

In its current form, the finite-element model could be improved on several aspects. For instance, in the simulations that were carried out in this thesis, the mesh across the thickness of the film is made of only one element. By doing so, the eddy currents generated by in-plane variations of the magnetic field are disregarded. This assumption also neglects the induced currents along the thickness of the film, which might be detrimental in more complex situations where the distribution of the magnetic field across the thickness must be determined with precision. In this case, the number of degrees of freedom in the conducting domains might become a limiting factor, numerically speaking. Therefore, approaches that reduce the number of degrees of freedom associated to the superconducting films might be required [259]. Besides, since the asymptotic behaviour of the magnetic potential scales as $\phi \sim Z^{-2}$, it would be interesting to test whether using second-order elements in the shell domain could reduce the number of degrees of freedom. Finally, it is worth stressing out that the mesh quality in the immediate vicinity of the superconducting films influences a lot the quality of the approximation of the magnetic field inside the films. For this reason, using fine structured meshes in the surroundings of the films is recommended.

The models could also be adapted to account for several phenomenological elements that were omitted. For example, the anisotropy that is induced by in-plane fields was not modelled in our simulations of the critical states in multilayer assemblies. Although the in-plane field that was applied in the experiments of [44] was not large enough to induce anisotropy in the film, it would be interesting to see if the critical states are significantly modified when a large enough in-plane field is applied. To this aim, one could use the anisotropic model of [108] to account for this additional phenomenon. Surface barriers could also be taken into account in the model, and it would be interesting to study how they influence the magnetic flux distributions in such assemblies and how the subsequent changes in the magnetic field levels modify the corresponding current density patterns.

Moreover, in the anisotropic model that was used for describing the magnetic flux penetration in films with the square array of triangular holes, the interstitial current density that flows in between the holes is not fully modelled, so that its influence on the magnetic field dependence of the anisotropic current density is not entirely described. Including this contribution in the anisotropic model could improve the quantitative comparison between simulations and the experiments. It is also worth noting that the macroscopic anisotropic **E**-**J** law does not exactly reflect the C_3 symmetry of the antidots. Adapting the shape of the critical curve to the symmetry of the holes must however conserve the convexity of the curve, so that more complex mathematical expressions than the ovoid-shaped critical curve should be considered. This would allow for a better estimation of the critical current densities when the current density is forced to flow along directions that are not aligned with the principal axes of the ovoid, i.e. for more elaborated film cross sections. In any case, the direct and naive approach, where the array of antidots is described explicitly, seems unrealistic, as meshing a very fine array of tiny triangular holes with enough resolution in the superconducting film is out of reach for nowadays computers.

Finally, it is worth stressing out that modelling surface barriers in three-dimensional geometries remains a challenge that needs to be tackled. The choice that was assumed in this work was to emulate the surface currents by means of a peripheral region of enhanced pinning. Although the approach reproduces quantitatively the expected behaviour of surface barriers, it does not capture the phenomenology entirely. On the one hand, the current model allows unphysical negative field values in the peripheral region. This is a consequence of the current density distribution that results from the delimitations of the regions with uneven critical current densities. Moreover, due to numerical issues, the dummy critical current density in the peripheral region could not be set to a value as high as the depairing current, while the actually realized value of the peripheral current density depends on the n-exponent of the **E**-**J** law. On the other hand, the delayed entrance of magnetic field that is concomitant with surface barriers also needs to be improved. A three-dimensional surface barrier model that replicates all the main characteristics of a non-uniform surface barrier is therefore still to be devised, and could be useful for practical reasons, since surface barriers were found to enhance the critical current density in superconducting films coupled with magnetic layers [260, 261], or to play a role in SQUIDs and single photons detectors [221, 222]. Coupling a complete surface barrier model to thermomagnetic simulations would also help to evidence whether surface barriers play a role on the onset of magnetic flux avalanches in superconducting films. Last, more accurate models of the geometrical variations of surface barriers could also be investigated and compared to the first-order approach that was selected here.

Despite these shortcomings, the numerical models that were developed in this thesis constitute a set of tools that can be used in future works in a more applicative context. The anisotropic feature that is induced by the arrays of triangular antidots could be exploited to fabricate single films with a slight flux-concentrating or flux-expulsion property, depending on the orientation of the triangular holes. For instance, by making all the triangular holes point towards the centre of the sample, the motion of the vortices would in principle be facilitated as they head towards the centre while their motion would be hindered as they leave the sample. The anisotropic model that was developed could therefore be adapted to the study of the macroscopic flux penetration in such systems.

Besides, the advantages of using thin films and tapes over bulk samples [8] could be considered for assemblies of films with different cross sections to design superconducting metamaterials [44, 256, 262] or magnetic flux concentrators [263, 264], which could in turn be combined with SQUIDs. More complex arrangements of films also seem to be beneficial for the performance of levitating devices [12]. For these kinds of applications, it would be interesting to investigate whether using films with non-identical cross sections would significantly impact their characteristics. Combining different planar geometries indeed influence the way magnetic field is distributed and penetrates in the assembly, so that it might be possible to come with material designs with a non-uniform magnetic permeability, concentrating the magnetic flux on given target areas. Numerical modelling would then reveal particularly useful for designing such materials, particularly if the $J_c(\mathbf{B})$ dependence must be accounted for in the films, since the current patterns might become complex.

Finally, the experimentally observed deflections of the critical states could be used for material characterization. For example, the extension of the horizontal line in bi-layer assemblies could give some information about the presence and the characteristics of the magnetic field dependence of the critical current density of a given superconducting wafer. Similarly, measuring the curvature of the parabolic d-lines around indentations could also provide information on surface barriers or on the nature of the surface defects.

Appendices

Appendix A

Newton-Raphson $\partial\mathbf{E}/\partial\mathbf{J}$ tensor

A.1 Isotropic superconductor

Consider the electrical resistivity of an isotropic superconductor, which is given by Equation 2.18. From this expression, one obtains the derivative of the component E_α with respect to J_β, where α and β can both be taken among x, y or z,

$$\begin{aligned}\frac{\partial E_\alpha}{\partial J_\beta} &= \frac{\partial}{\partial J_\beta}\left\{\frac{E_c}{J_c}\left(\frac{|\mathbf{J}|}{J_c}\right)^{n-1} J_\alpha\right\}\\ &= \frac{E_c}{J_c^n}\left\{|\mathbf{J}|^{n-1}\delta_{\alpha\beta} + (n-1)|\mathbf{J}|^{n-2}\frac{J_\beta}{|\mathbf{J}|}J_\alpha\right\}\\ &= \frac{E_c}{J_c}\left(\frac{|\mathbf{J}|}{J_c}\right)^{n-1}\delta_{\alpha\beta} + (n-1)\frac{E_c}{J_c^3}\left(\frac{|\mathbf{J}|}{J_c}\right)^{n-3} J_\alpha J_\beta,\end{aligned} \tag{A.1}$$

where $\delta_{\alpha\beta}$ is the Kronecker function. The expression of the $\partial\mathbf{E}/\partial\mathbf{J}$ tensor immediately follows

$$\frac{\partial\mathbf{E}}{\partial\mathbf{J}} = \frac{E_c}{J_c}\left(\frac{|\mathbf{J}|}{J_c}\right)^{n-1}\mathcal{I}_3 + (n-1)\frac{E_c}{J_c^3}\left(\frac{|\mathbf{J}|}{J_c}\right)^{n-3}\mathbf{J}\mathbf{J}^{\mathrm{T}}, \tag{A.2}$$

where $\mathbf{J}^T = (J_x, J_y, J_z)$ is the transpose of $\mathbf{J}$, and $\mathcal{I}_3$ is the 3×3 identity tensor.

A.2 Asymmetric anisotropic superconductor

Let us start from the generic phenomenological dissipation function, described by Equation 5.6, and a three-dimensional extension of Equation 5.7, Equation 5.8, and a generalized version of Equation 5.9, that are now written as

$$\mathcal{E} = \mathcal{E}_s + \mathcal{E}_a, \tag{A.3}$$

$$\mathcal{E}_s = \left(\frac{J_x}{J_{c,x}}\right)^2 + \left(\frac{J_y}{J_{c,y}}\right)^2 + \left(\frac{J_z}{J_{c,z}}\right)^2, \tag{A.4}$$

$$\mathcal{E}_a = -\frac{1}{\mathcal{E}_s^{1/2}}\left\{C_x\left(\frac{J_x}{J_{c,x}}\right)^3 + C_y\left(\frac{J_y}{J_{c,y}}\right)^3 + C_z\left(\frac{J_z}{J_{c,z}}\right)^3\right\} \equiv -\frac{\mathcal{W}_a}{\mathcal{E}_s^{1/2}}. \tag{A.5}$$

According to [108], the components of the electric field, $\mathbf{E}$, can be obtained as the derivatives of $\mathcal{F}$ with respect to the components of the current density, $\mathbf{J}$. Consequently, one can write

$$\frac{\partial\mathcal{E}_s}{\partial J_\alpha} = \frac{2}{J_{c,\alpha}}\frac{J_\alpha}{J_{c,\alpha}}, \tag{A.6}$$

$$\frac{\partial\mathcal{E}_a}{\partial J_\alpha} = -\frac{1}{J_{c,\alpha}}\frac{1}{\mathcal{E}_s^{3/2}}\left\{3C_\alpha\left(\frac{J_\alpha}{J_{c,\alpha}}\right)^2\mathcal{E}_s - \frac{J_\alpha}{J_{c,\alpha}}\mathcal{W}_a\right\}, \tag{A.7}$$

where α can be taken among x, y or z. Together, Equation A.6 and Equation A.7 yield

$$\begin{aligned} E_\alpha &= E_c\,\mathcal{E}^{\frac{n-1}{2}}\frac{J_{c,x}}{J_{c,\alpha}}\left[\frac{J_\alpha}{J_{c,\alpha}} - \frac{1}{\mathcal{E}_s^{3/2}}\left\{\frac{3}{2}C_\alpha\left(\frac{J_\alpha}{J_{c,\alpha}}\right)^2\mathcal{E}_s - \frac{1}{2}\frac{J_\alpha}{J_{c,\alpha}}\mathcal{W}_a\right\}\right] \\ &\equiv E_c\,\mathcal{E}^{\frac{n-1}{2}}\mathcal{V}_\alpha, \end{aligned} \tag{A.8}$$

where one has assumed $n = 2M - 1$ and $\mathcal{F}_0 = E_c J_{c,x}/2M$.

Now that $\mathbf{E} = (E_x, E_y, E_z)$ has been derived, one can calculate the $\partial\mathbf{E}/\partial\mathbf{J}$ tensor. One has, with α and β being both equivalent to one of the arbitrarily selected indices x, y or z,

$$\begin{aligned} \frac{\partial E_\alpha}{\partial J_\beta} = E_c\,\mathcal{E}^{\frac{n-1}{2}}\frac{J_{c,x}}{J_{c,\alpha}}&\left[\frac{\delta_{\alpha\beta}}{J_{c,\alpha}} + \frac{3}{\mathcal{E}_s^{5/2}}\frac{J_\beta}{J_{c,\beta}^2}\left\{\frac{3}{2}C_\alpha\left(\frac{J_\alpha}{J_{c,\alpha}}\right)^2\mathcal{E}_s - \frac{1}{2}\frac{J_\alpha}{J_{c,\alpha}}\mathcal{W}_a\right\}\right. \\ &-\frac{3C_\alpha}{\mathcal{E}_s^{3/2}}\left\{\frac{\delta_{\alpha\beta}}{J_{c,\alpha}}\frac{J_\alpha}{J_{c,\alpha}}\mathcal{E}_s + \frac{1}{J_{c,\beta}}\left(\frac{J_\alpha}{J_{c,\alpha}}\right)^2\frac{J_\beta}{J_{c,\beta}}\right\} \\ &\left.+\frac{1}{\mathcal{E}_s^{3/2}}\left\{\frac{1}{2}\frac{\delta_{\alpha\beta}}{J_{c,\alpha}}\mathcal{W}_a + \frac{3}{2}\frac{C_\beta}{J_{c,\beta}}\frac{J_\alpha}{J_{c,\alpha}}\left(\frac{J_\beta}{J_{c,\beta}}\right)^2\right\}\right] \\ &+\frac{E_c}{J_{c,x}}\frac{n-1}{2}\mathcal{E}^{\frac{n-3}{2}}\mathcal{V}_\alpha\mathcal{V}_\beta, \end{aligned} \tag{A.9}$$

where $\delta_{\alpha\beta}$ is the Kronecker function. Equation A.9 is a non-symmetric tensor, given that the parameters C_α and $J_{c,\alpha}$ are not equal. When the relations $J_{c,x} = J_{c,y} = J_{c,z}$ and $C_x = C_y = C_z = 0$ stand true, one recovers the symmetric tensor $\partial\mathbf{E}/\partial\mathbf{J}$ described by Equation A.2. In practice, the divergence that arises when $\mathbf{J} = 0$ is skirted by adding an extremely small offset $\sim 100\ \mu\mathrm{A/km}^2$ each time $\mathcal{E}_s$ appears at the denominator of a fractional expression.

Appendix B

Decay of the scalar magnetic potential as a function of the out-of-plane distance from the film

B.1 Out-of-plane decay of the scalar magnetic potential in a superconducting thin disk

The aim of this appendix is to determine how the scalar magnetic potential ϕ varies as a function of the out-of-plane distance from a thin superconducting film when it is fully penetrated. To this end, the following calculations are based on the thin-film approximation, which consists in approaching a thin film of thickness d as an infinitely thin sheet of current, J_s, which intensity is the integral of the current density over the thickness. This simplification is justified when one can assume that $L/d \gg 1$. In what follows, it will also be assumed that the current density is uniform in the whole film, and its value will be denoted by J_c. Consequently, when the sample is fully penetrated, the sheet current density is uniform across the thickness, and one can write $|\mathbf{J}_s| = J_c d$.

First, let us consider the case of a superconducting thin disk of radius R and thickness d. It is assumed that $R/d \gg 1$, see Figure B.1 for an illustration of the geometry. A reference Cartesian orthonormal basis will be used throughout the section. Its equivalent cylindrical basis is also shown for an arbitrary point which is rotated by an angle θ with respect to $\mathbf{e}_x$. Its origin, the point $O\,(0,0,0)$, corresponds to the centre of the thin disk. Biot-Savart law over the infinitely thin superconducting sheet, Ω_c, can be formulated in cylindrical coordinates, and takes the form

$$\mathbf{B}(\mathbf{r}) = \frac{\mu_0}{4\pi} \int_0^{2\pi} \int_0^{R} J_s(\mathbf{r}') \frac{\mathbf{dl} \times (\mathbf{r} - \mathbf{r}')}{|\mathbf{r} - \mathbf{r}'|^3}\, r \,\mathrm{d}r \,\mathrm{d}\theta, \tag{B.1}$$

where $\mathbf{r}$ stands for the cylindrical coordinates of a given point in the three-dimensional space, while $\mathbf{r}'$ summarizes the cylindrical coordinates of a point in Ω_c. $\mathbf{dl}$ is a vector that indicates the orientation of the sheet current density $\mathbf{J}_s$ at $\mathbf{r}'$ and $J_s(\mathbf{r}')$ is the sheet current density intensity at $\mathbf{r}'$. The integral is performed over the whole section of the film, which lies in the plane $Z = 0$.

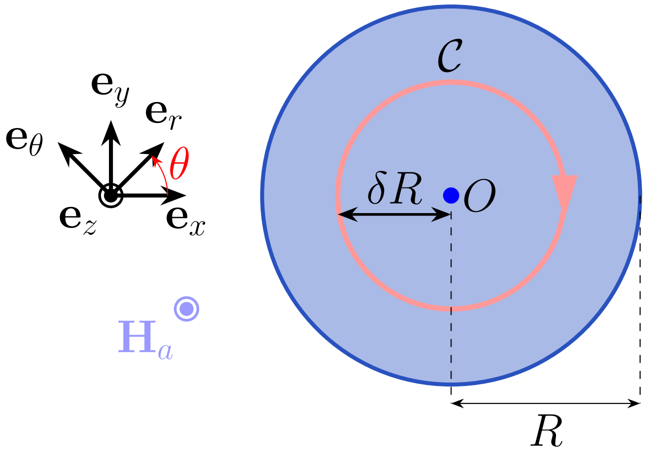

Figure B.1: Sketch of a random current loop, $\mathcal{C}$ in an infinitely thin superconducting disk of radius R. The loop lies in the plane $Z = 0$. The current density flows azimuthally so that $\mathcal{C}$ describes a circular pattern that is parallel to the edge of the film. The light red arrow shows the direction of the azimuthal induced current. A translated orthonormal basis is shown for the sake of clarity. Point $O\,(0,0,0)$, in dark blue, coincides with the centre of the film. δ is a parameter ranging from 0 to 1 labelling each current loop.

A few remarks allow one to simplify the following calculations. First, the observation point, P, may be located everywhere in the three-dimensional space. However, for the sake of the conciseness of the following calculations, it will be assumed that $P(0,0,Z)$, where Z is the distance from the thin-film surface, so that $\mathbf{r} = Z\,\mathbf{e_z}$. Second, since only the z dependence of ϕ is sought, the relation $\mathbf{H} = -\nabla\phi$ holding in the current-free regions implies that only the determination of B_z needs to be addressed. Therefore, not all components of Equation B.1 requires evaluation. In a fully penetrated superconducting disk, current density circulates parallel to the sample borders, i.e. it flows azimuthally. Thereby, one has $\mathbf{r}' = r\,\mathbf{e}_r$, and $\mathbf{dl} = \mathbf{e}_\theta$.

Based on these simplifications, one can recast Equation B.1 as

$$B_z(\mathbf{r}) = -\frac{\mu_0 J_c d}{4\pi}\int_0^{2\pi}\int_0^{R}\frac{r^2}{(r^2+Z^2)^{3/2}}\,\mathrm{d}r\,\mathrm{d}\theta. \tag{B.2}$$

Using the changes of variables $c = Z/R$ and $r = R\,\delta$, with $\delta \in [0,1]$, Equation B.2 is equivalent to

$$B_z(\mathbf{r}) = -\frac{\mu_0 J_c d}{2}\int_0^{1}\frac{\delta^2}{(\delta^2+c^2)^{3/2}}\,\mathrm{d}\delta. \tag{B.3}$$

The integral in Equation B.3 is solved by using the substitution $u = \sin(\arctan(\delta/c))$, which amounts to

$$\begin{aligned}\int\frac{\delta^2}{(\delta^2+c^2)^{3/2}}\,\mathrm{d}\delta &= \int\frac{u^2}{1-u^2}\mathrm{d}u\\ &= \frac{1}{2}\log\left|\frac{\sqrt{\delta^2+c^2}+\delta}{\sqrt{\delta^2+c^2}-\delta}\right| - \frac{\delta}{\sqrt{\delta^2+c^2}}.\end{aligned} \tag{B.4}$$

Substituting Equation B.4 in Equation B.3 leads to the analytical expression of B_z as a function of the out-of-plane distance from the centre of the disk

$$B_z(\mathbf{r}) = \frac{\mu_0 J_c d}{2}\left[-\frac{1}{2}\log\left|\frac{\sqrt{1+c^2}+1}{\sqrt{1+c^2}-1}\right| + \frac{1}{\sqrt{1+c^2}}\right]. \tag{B.5}$$

Once the Z dependence of B_z has been obtained, the out-of-plane variations of the scalar magnetic potential, ϕ, can be obtained from the relation $H_z = -\partial\phi/\partial Z$, by integrating by parts Equation B.5 with respect to Z and accounting for the boundary condition $\lim_{Z\to\infty}\phi(\mathbf{r}) = 0$. This gives

$$\phi(\mathbf{r}) = \frac{J_c d}{2}R\left[1 - \frac{c}{2}\log\left|\frac{\sqrt{1+c^2}+1}{\sqrt{1+c^2}-1}\right|\right], \tag{B.6}$$

where the integral from c to $+\infty$ of the second term of Equation B.5 cancels with the integration by parts of its first term, and where the limit

$$\lim_{c\to+\infty}\frac{c}{2}\log\left|\frac{\sqrt{1+c^2}+1}{\sqrt{1+c^2}-1}\right| = 1 \tag{B.7}$$

was used. Equation B.6 is represented in Figure 2.7 on a logarithmic-scale plot. In order to determine the value of A, which is the out-of-plane extension of the shell region, Ω_{sh}, one needs to determine the value at which ϕ/ϕ_0 is equal to $1/2$, in accordance with the criterion proposed in Chapter 2, and one finds $A \approx 0.23 \times R$.

B.2 Out-of-plane decay of the scalar magnetic potential in a rectangular superconducting thin film

Now, consider the case of a thin rectangular superconducting film of length L, width W, and thickness d. It is assumed that $L \geq W$ and $L/d \gg 1$, see Figure B.2 for a representation of the geometry and the set of axes that will be used in the rest of this section. The centre of the coordinate system, $O\,(0,0,0)$, lies at the intersection of the diagonals of the rectangular sample. Without loss of generality, the length of the rectangular film is supposed to be directed along the y-axis.

According to Bio-Savart law over the infinitely thin superconducting sheet, Ω_c,

$$\mathbf{B}(\mathbf{r}) = \frac{\mu_0}{4\pi}\int_\Omega J_s(\mathbf{r}')\frac{\mathbf{dl}\times(\mathbf{r}-\mathbf{r}')}{|\mathbf{r}-\mathbf{r}'|^3}\,\mathrm{d}x\,\mathrm{d}y. \tag{B.8}$$

In a fully penetrated rectangular superconducting sample, current density circulates parallel to the sample borders and makes sharp turns along the d-lines, as discussed in Chapter 1. The sample can then be divided in four sectors, labelled from 1 to 4, which exact shape depends on the length and width of the rectangular sample. Nevertheless, under these assumptions, a random current loop $\mathcal{C}$ always takes the shape of a rectangle that is parallel to the edges of the sample. Consequently, one can decompose $\mathcal{C}$ as $\mathcal{C}_1\cup\mathcal{C}_2\cup\mathcal{C}_3\cup\mathcal{C}_4$,

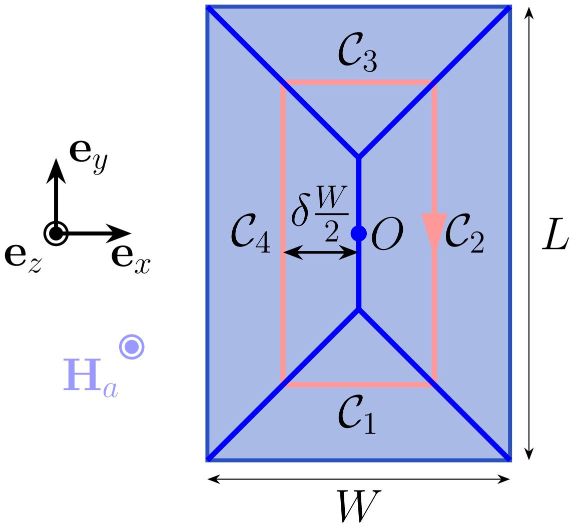

Figure B.2: Sketch of a random current loop $\mathcal{C}$ in an infinitely thin rectangular film of length L and width W. The film lies in the plane $z = 0$. The current density flows parallel to the sample border, and one can decompose the current loop $\mathcal{C}$ as $\mathcal{C}_1 \cup \mathcal{C}_2 \cup \mathcal{C}_3 \cup \mathcal{C}_4$, where $\mathcal{C}_1$, $\mathcal{C}_3$ are parallel to the x-axis and $\mathcal{C}_2$, $\mathcal{C}_4$ are parallel to the y-axis. The abrupt redirection of the current density is demarcated by d-lines, in dark blue. The light red arrow shows the direction of the induced current. A translated orthonormal basis is shown for the sake of clarity. Point $O\,(0,0,0)$, in dark blue, corresponds to the intersection of the diagonals of the film. δ is a parameter that ranges from 0 to 1 labelling each current loop.

as shown in Figure B.2, where $\mathbf{dl} = -\mathbf{e}_x$ on $\mathcal{C}_1$, $\mathbf{dl} = -\mathbf{e}_y$ on $\mathcal{C}_2$, $\mathbf{dl} = \mathbf{e}_x$ on $\mathcal{C}_3$ and $\mathbf{dl} = \mathbf{e}_y$ on $\mathcal{C}_4$. Finally, due to the symmetry of the rectangle, the contributions of $\mathcal{C}_1$ (resp. $\mathcal{C}_2$) and $\mathcal{C}_3$ (resp. $\mathcal{C}_4$) to B_z are identical. Hence, only the contributions of $\mathcal{C}_1$ and $\mathcal{C}_2$ are treated in what unfolds. Again, one notices that only the B_z component needs to be calculated, since it exclusively encompasses the variations of ϕ along the out-of-plane direction.

On $\mathcal{C}_1$, $\mathbf{r}'$ can be expressed as

$$\mathbf{r}' = x_1\mathbf{e}_x + y_1\mathbf{e}_y, \tag{B.9}$$

$$x_1 \in \left[-\delta\frac{W}{2}, \delta\frac{W}{2}\right], \tag{B.10}$$

$$y_1 = -\frac{L - W(1-\delta)}{2}, \tag{B.11}$$

where $\delta \in [0, 1]$. The integration of Biot-Savart law over sector 1 then yields, after a change of variables from y_1 to δ,

$$B_{z,1}(\mathbf{r}) = -\frac{\mu_0 J_c d}{4\pi}\frac{W}{2}\int_0^1\int_{-\delta\frac{W}{2}}^{\delta\frac{W}{2}} \frac{y_1}{\left(x_1^2 + y_1^2 + Z^2\right)^{3/2}}\,\mathrm{d}x_1\mathrm{d}\delta. \tag{B.12}$$

The solution of the integral with respect to x_1 in Equation B.12 can be obtained by substituting $\tan\theta = x_1/\sqrt{y_1^2+Z^2}$ and gives

$$\int \frac{\mathrm{d}x_1}{(x_1^2+y_1^2+Z^2)^{3/2}} = \frac{1}{y_1^2+Z^2}\sin\left(\arctan\left[\frac{x_1}{\sqrt{y^2+Z^2}}\right]\right) = \frac{1}{y_1^2+Z^2}\frac{x_1}{\sqrt{x_1^2+y_1^2+Z^2}}. \tag{B.13}$$

Hence, one can rewrite Equation B.12 in the light of Equation B.13, so that the contribution of sector 1 to the reaction field is given by

$$B_{z,1}(\mathbf{r}) = \frac{\mu_0 J_c d}{4\pi}\int_0^1 \frac{2}{(\delta+b)^2+c^2}\frac{\delta(\delta+b)}{\sqrt{\delta^2+(\delta+b)^2+c^2}}\,\mathrm{d}\delta, \tag{B.14}$$

where and $b \equiv (L-W)/W$ and $c \equiv 2Z/W$.

Similarly, on the path $\mathcal{C}_2$ the following relations hold

$$\mathbf{r}' = x_2\mathbf{e}_x + y_2\mathbf{e}_y, \tag{B.15}$$

$$x_2 = \delta\frac{W}{2}, \tag{B.16}$$

$$y_2 \in \left[-\frac{L-W(1-\delta)}{2}, \frac{L-W(1-\delta)}{2}\right]. \tag{B.17}$$

After a change of variables from x_2 to δ, the previous equations lead to an expression of the contribution of sector 2 to the reaction field, i.e.

$$B_{z,2}(\mathbf{r}) = \frac{\mu_0 J_c d}{4\pi}\frac{W}{2}\int_0^1\int_{-\frac{L-W(1-\delta)}{2}}^{\frac{L-W(1-\delta)}{2}} \frac{x_2}{(x_2^2+y_2^2+Z^2)^{3/2}}\,\mathrm{d}y_2\,\mathrm{d}\delta. \tag{B.18}$$

Following the same steps as in the integration of the Biot-Savart law over sector 1, Equation B.18 is equivalent to

$$B_{z,2}(\mathbf{r}) = \frac{\mu_0 J_c d}{4\pi}\int_0^1 \frac{2}{\delta^2+c^2}\frac{\delta(\delta+b)}{\sqrt{\delta^2+(\delta+b)^2+c^2}}\,\mathrm{d}\delta. \tag{B.19}$$

The out-of-plane dependence of the reaction field at the centre of the rectangular strip is thus obtained from the combination of Equation B.14 and Equation B.19, which yields, once the contributions of sector 3 and 4 have been added,

$$B_z(\mathbf{r}) = \frac{\mu_0 J_c d}{4\pi}\int_0^1 \left(\frac{4}{(\delta+b)^2+c^2}+\frac{4}{\delta^2+c^2}\right)\frac{\delta(\delta+b)}{\sqrt{\delta^2+(\delta+b)^2+c^2}}\,\mathrm{d}\delta. \tag{B.20}$$

Such integral cannot be solved analytically, with the noteworthy exception of the case of a square film, where $b = 0$. The resolution of Equation B.20 for $b > 0$ is handled by means of numerical integration. In the case $b = 0$, Equation B.20 becomes

$$B_z(\mathbf{r}) = \frac{\mu_0 J_c d}{4\pi}\int_0^1 \frac{8}{\delta^2+c^2}\frac{\delta^2}{\sqrt{2\delta^2+c^2}}\,\mathrm{d}\delta. \tag{B.21}$$

With the help of the substitution $u = \sin\left(\arctan\left(\sqrt{2}\delta/c\right)\right)$, the integral in Equation B.21 rewrites as

$$\begin{aligned}\int \frac{1}{\delta^2+c^2}\frac{\delta^2}{\sqrt{2\delta^2+c^2}}\mathrm{d}\delta &= \frac{1}{\sqrt{2}}\int \frac{u^2}{2-u^2}\frac{\mathrm{d}u}{1-u^2} \\ &= \frac{1}{2\sqrt{2}}\log\left|\frac{\sqrt{c^2+2\delta^2}+\sqrt{2}\delta}{\sqrt{c^2+2\delta^2}-\sqrt{2}\delta}\right| - \frac{1}{2}\log\left|\frac{\sqrt{c^2+2\delta^2}+\delta}{\sqrt{c^2+2\delta^2}-\delta}\right|. \end{aligned} \tag{B.22}$$

Thus, one finally obtains

$$B_z(\mathbf{r}) = \frac{\mu_0 J_c d}{\pi}\left(\frac{1}{\sqrt{2}}\log\left|\frac{\sqrt{c^2+2}+\sqrt{2}}{\sqrt{c^2+2}-\sqrt{2}}\right| - \log\left|\frac{\sqrt{c^2+2}+1}{\sqrt{c^2+2}-1}\right|\right). \tag{B.23}$$

The variations of ϕ with respect to the out-of-plane distance from the centre of the film is obtained by integrating with respect to Z the result of the numerical integration of Equation B.20 with respect to δ, accounting for the boundary condition $\lim_{Z\to\infty}\phi(\mathbf{r}) = 0$. In the case of the thin square film ($b = 0$) one can obtain $\phi(\mathbf{r})$ by integrating by parts Equation B.23, so that

$$\begin{aligned}\phi(\mathbf{r}) = \frac{J_c d}{\pi}\frac{W}{2}\Bigg(&\frac{c}{\sqrt{2}}\log\left|\frac{\sqrt{c^2+2}+\sqrt{2}}{\sqrt{c^2+2}-\sqrt{2}}\right| - c\log\left|\frac{\sqrt{c^2+2}+1}{\sqrt{c^2+2}-1}\right| \\ &-2\int_c^{\infty}\frac{1}{v^2+1}\frac{1}{\sqrt{v^2+2}}\mathrm{d}v\Bigg). \end{aligned} \tag{B.24}$$

The last integral in Equation B.24 can be solved with the help of the henceforth usual substitution $u = \sin\left(\arctan\left(v/\sqrt{2}\right)\right)$, which leads to

$$\int \frac{1}{v^2+1}\frac{1}{\sqrt{v^2+2}}\mathrm{d}v = \arctan\left(\frac{v}{\sqrt{v^2+2}}\right). \tag{B.25}$$

Substituting Equation B.25 into Equation B.24, one finally obtains the ultimate analytical form of the dependence of ϕ as a function of $c = 2Z/W$ from the centre of a thin square superconducting film

$$\begin{aligned}\phi(\mathbf{r}) = \frac{J_c d}{\pi}\frac{W}{2}\Bigg[&\frac{c}{\sqrt{2}}\log\left|\frac{\sqrt{c^2+2}+\sqrt{2}}{\sqrt{c^2+2}-\sqrt{2}}\right| - c\log\left|\frac{\sqrt{c^2+2}+1}{\sqrt{c^2+2}-1}\right| \\ &+2\arctan\left(\frac{c}{\sqrt{c^2+2}}\right) - \frac{\pi}{2}\Bigg], \end{aligned} \tag{B.26}$$

where the term $-\pi/2$ is the result of the limit to $+\infty$ of Equation B.25.

The variations of ϕ along the out-of-plane direction in a rectangular film are shown in Figure B.3 for various values of L/W. These curves were obtained by means of numerical integration. The determination of the value of A follows the same criterion as in Section B.1, which is $\phi/\phi_0 = 1/2$. The estimation of A is repeated for a fine equally spaced set of values of L/W, ranging from 1 to 10. The results are exposed in Figure 2.13.

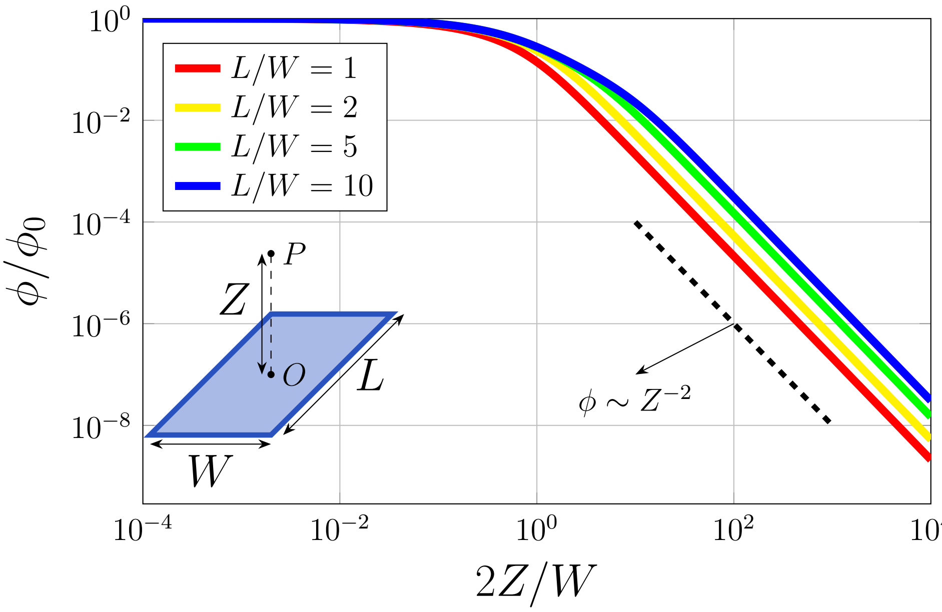

Figure B.3: Magnetic scalar potential, ϕ/ϕ_0, as a function of $2Z/W$, the out-of-plane distance from a superconducting thin strip of length L, width W and thickness d, on a logarithmic-scale plot, for various aspect ratios L/W. ϕ_0 is the scalar magnetic potential on the film surface. The dashed line is a guide to the eye indicating the Z^{-2} decay of ϕ far enough from the film surface.

Appendix C

Simplified critical state model of superposed films

This appendix aims at calculating the length of the additional central d-line in a three-dimensional assembly made of a thin superconducting square of length L on which a centred rectangular strip of length L and width W is superimposed. The thickness of both films is denoted by d. The complexity of the magnetic flux penetration and the coupling between the films do not allow for an easy model to be devised. Instead, a simplified two-dimensional model is used. This is motivated by the observation that the modifications of the d-lines that entail the additional vertical or horizontal d-line, of length ℓ_v and ℓ_h respectively, develop exclusively in the square film, while the current loops in the rectangular strip remain mostly invariable with respect to the d-line network in an isolated strip, as discussed in Subsection **6.2.4**.

A possible simplification that gives access to an analytical model consists in considering the average of the magnetic field in three rectangular sectors: a central rectangular band that matches the projection of the thin strip on the square film, and the two lateral regions that surround it. The average magnetic field in the central region (overlap region) is denoted by $\mathbf{B}_{int}$. In the two outer parts, due to the axial symmetry along the longest median of the strip, the average magnetic field levels are the same, and are labelled as $\mathbf{B}_{ext}$. The magnetic field is therefore assumed to vary discontinuously from one region to another. In other words, the sheet critical current density is constant within each sector, their value being denoted by $J_{c,s-int}$ and $J_{c,s-ext}$ in the overlap and outer regions, respectively. Based on this last assumption, analytical expressions of ℓ_v and ℓ_h in the scope of the critical state model (CSM) are derived.

C.1 Length of the additional vertical d-line in a fully penetrated thin square film ($J_{c,s-int} > J_{c,s-ext}$)

First, consider the case of a fully penetrated film. In this case, current lines are equidistant to each other. In fully penetrated samples, the magnetic field is higher in peripheral

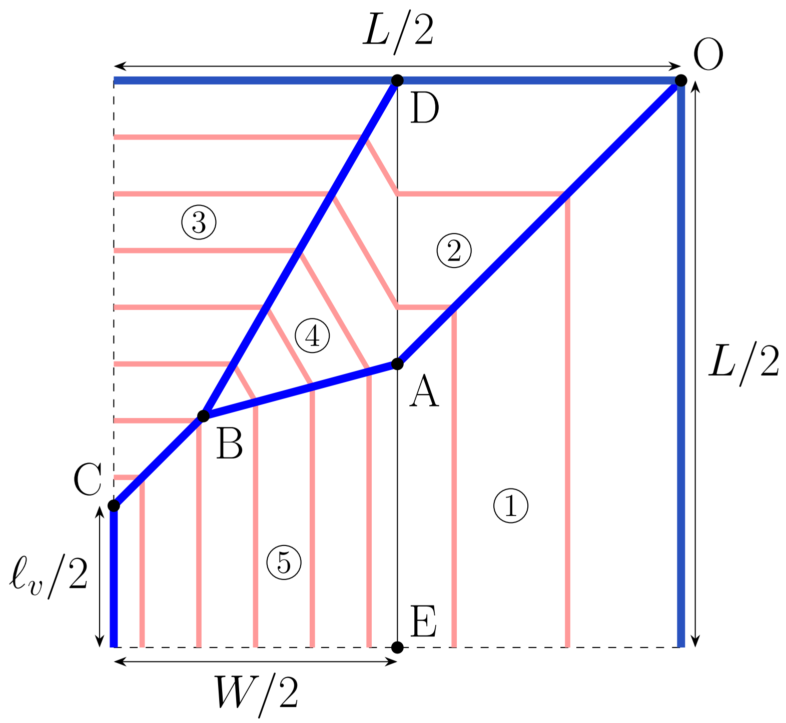

Figure C.1: Critical state in a fully penetrated square with non-uniform $J_{c,s}$, assuming $J_{c-\text{int}} = 2J_{c-\text{ext}}$ and $W = L/2$. Only the upper right part of the structure is shown. The other parts can be obtained by reflection symmetry, the axes of symmetry being highlighted with dashed lines. The dark blue lines correspond to the d-lines, while the light red lines show the current lines in the square film. The filled circles mark the locations where the d-lines abruptly change direction, and are labelled with capital letters. Circled numbers indicate the different sectors within which the orientation of the current density remains unchanged. The following annotations are used throughout Section C.1: $\angle BDA = \alpha$, $\angle BAE = \beta$, $\angle DOA = \pi/4$, $|BD| = L_1$, $|AB| = L_2$.

regions than in the central one, because vortices have first to engage through the borders before they reach the overlap region. On average, one has $|\mathbf{B}_{int}| < |\mathbf{B}_{ext}|$, and thus $J_{c,s-ext} < J_{c,s-int}$. For the sake of illustration, the current lines in the upper right quarter of the square film are depicted in Figure C.1, in the specific case of $W = L/2$ and $J_{c,s-int} = 2J_{c,s-ext}$. Nonetheless, the following developments are valid for other values of $W/L < 1$ and $J_{c,s-int}/J_{c,s-ext} > 1$. The remaining parts of the critical state can be obtained by reflection symmetry along the medians of the square. The notations that will be used throughout the calculations of this section are also indicated in Figure C.1.

The d-line patterns are governed by the conservation of current density, accounting for the non-uniform $J_{c,s}$ distribution. The current loops first progress parallel to the edges of the sample. In the outer regions, where the critical current density is uniform, a sharp change of the current orientation occurs between sectors 1 and 2 , both of them being separated by the d-line [OA], forming an $\pi/4$ angle with the upper edge, which coincides with the straight line OD. The vortices that have entered the sample through this side generate parallel current lines, but the condition $J_{c,s-ext} < J_{c,s-int}$ implies a higher current line density in the overlap region. According to current conservation, the current lines undergo a sharp change of orientation from sector 3 to sector 4. These two sectors are separated by another d-line, [BD], defining the angle $\angle BDA = \alpha$ with respect to the line AD. Similarly, current conservation implicates the d-line [AB] that separates sectors 4 and 5, where the current density flows again parallel to the vertical edge of the square film, and forming the angle $\angle BAE = \beta$ with the straight line DA. Finally, the transition from sector 3 to sector 5 is delimited by a d-line, [BC], which makes a $\pi/4$ angle with respect to the horizontal edge, so that the vertical current lines originating from the right edge meet the horizontal ones that are parallel to the top edge. C lies on the vertical median of the square, and a d-line of length $\ell_v/2$ extends from C to the center of the sample, separating currents that circulate in opposite directions, owing to the mirror symmetry of the system.

The change of the current line direction between sectors 3 and 4 and that between sectors 4 and 5 depend on $J_{c,s-ext}$ and $J_{c,s-int}$. Moreover, the mismatch between the current density in sector 2 and that in sector 3 is the reason for the existence of sector 4, where the orientation of the current lines is deflected by an angle 2α with respect to those in sector 2. α verifies current conservation across the line AD, so that [95]

$$\frac{J_{c,s-int}}{J_{c,s-ext}} = \frac{1}{\cos 2\alpha}. \tag{C.1}$$

The angle $\angle BAE = \beta$ can be found by a simple angle chasing, given that the current lines are horizontal in sector 3 and become vertical in sector 5. One has

$$\begin{aligned} \pi/2 + (\pi - 2\beta) + 2\alpha &= \pi \\ \Rightarrow \beta &= \frac{\pi}{4} + \alpha. \end{aligned} \tag{C.2}$$

The length ℓ_v is determined from the difference between the projections of the path OABC along the vertical and the horizontal directions, which yields

$$\ell_v = 2\left(\sin\beta - \cos\beta\right) L_2, \tag{C.3}$$

with $L_2 = |AB|$. The sine law in triangle ABD yields the value of L_2 as a function of $|AD| = L/2 - W/2$,

$$L_2 = \frac{\sin\alpha}{\sin\left(\beta - \alpha\right)}\left[\frac{L}{2} - \frac{W}{2}\right]. \tag{C.4}$$

Finally, substituting Equation C.1, Equation C.2 and Equation C.4 in Equation C.3 gives

$$\begin{aligned} \frac{\ell_v}{L} &= (1 - \cos 2\alpha)\left[1 - \frac{W}{L}\right] \\ \Leftrightarrow \frac{\ell_v}{L} &= \left(1 - \frac{J_{c,s-ext}}{J_{c,s-int}}\right)\left[1 - \frac{W}{L}\right]. \end{aligned} \tag{C.5}$$

In particular, if $W = L/2$, one recovers the result of Equation 6.4 i.e.

$$\frac{\ell_v}{L} = \frac{1}{2}\left(1 - \frac{J_{c,s-ext}}{J_{c,s-int}}\right). \tag{C.6}$$

It is worth stressing out that the previous developments are valid if and only if point B exists, i.e. that the projection of [BD] on the upper edge is less than $W/2$. In the extreme case $\alpha = \pi/4$ and thus $\beta = \pi/2$, B is located on the vertical median of the square and coincides with C. Sectors 4 and 5 merge, as the current lines do not change abruptly their direction from one sector to the other one any more. Hence, [BA] becomes horizontal but is no longer a d-line.

C.2 Length of the additional horizontal d-line in the thin square film in the remanent state ($J_{c,s-int} < J_{c,s-ext}$)

Now, let us turn to the case of the remanent state in the same model. Assuming that the maximal applied field is large enough to achieve a full magnetic field penetration, the current lines can be assumed to be equidistant to each other in the remanent state. However, one now has $|\mathbf{B}_{ext}| < |\mathbf{B}_{int}|$, and thus $J_{c,s-int} < J_{c,s-ext}$, because magnetic field mainly stays trapped around the center of the sample. Figure C.2 then shows the current loops and the subsequent sets of d-lines, in the specific case $W = L/2$ and $J_{c,s-int} = \sqrt{3}/2 J_{c,s-ext}$, although the upcoming developments remain valid for other values of $W/L < 1$ and $J_{c,s-int}/J_{c,s-ext} < 1$. Again, only the upper right quarter of the film is drawn. The current lines and d-lines can be extended to the rest of the film by reflection symmetry. The reader is invited to refer to Figure C.2 to access the necessary notations.

Similarly to the case of fully penetrated films, the following calculations rely on current conservation. Current lines that are parallel to the upper and right edges reunite along the d-line [OA], separating sector 1 from sector 2 and forming a $\pi/4$ angle with respect to both edges. Because of the relation $J_{c,s-int} < J_{c,s-ext}$, [OA] does not extend to the boundary of the overlap region. Indeed, consecutive current lines are now closer to each other in the outer regions than in the overlap one. Current density, which is divergence-free, entails an abrupt change of orientation from sector 2 to sector 4 to compensate the difference in flux penetration between sector 2 and sector 3. The non-uniform critical current density hence generates the d-lines [AB] and [AD], the former demarcating currents with different orientations in sector 4 and in sector 1. Finally, sector 3, where current lines are horizontal, and sector 5, where current lines are vertical, rejoin along [BC]. B is located at the limit between the outer and the overlap regions, while C lies on the horizontal median of the square. Owing to the mirror symmetry of the sample, a d-line of length $\ell_h/2$ going from C to the center of the sample appears, separating currents flowing in opposite directions. In what follows, let us define the angles $\angle ADB = \alpha$ and $\angle ABD = \beta$.

The steps are the same as in Section C.1. The unequal values of $J_{c,s-ext}$ and $J_{c,s-int}$ govern the changes of direction of the current lines occurring at the separation between sectors 1, 2 and 3 and sector 4, according to current conservation. For instance, the horizontal current lines are deflected by an angle 2α going from sector 3 to sector 4, so that current conservation along BD gives [95]

$$\frac{J_{c,s-ext}}{J_{c,s-int}} = \frac{1}{\cos 2\alpha}. \tag{C.7}$$

The current lines undergo two successive changes of orientation, in such a way that they go from flowing horizontally in sector 3 to flowing vertically in sector 1. These deflections

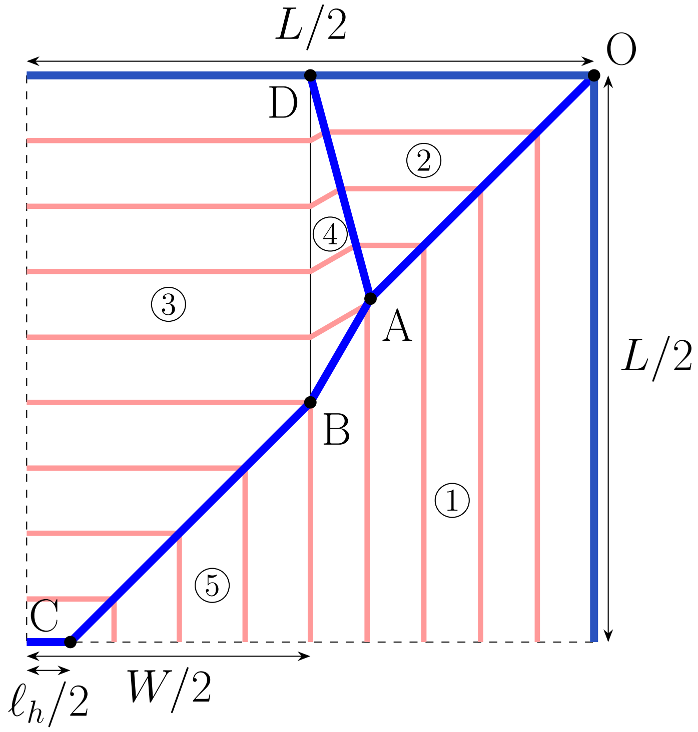

Figure C.2: Critical state in a square with non-uniform $J_{c,s}$ in the remanent state, assuming $J_{c,s-\mathrm{int}} = \sqrt{3}/2 \times J_{c,s-\mathrm{ext}}$ and $W = L/2$. Only the upper right part of the structure is shown. The other parts can be obtained by reflection symmetry, the axes of symmetry being highlighted with dashed lines. The dark blue lines correspond to the d-lines, while the light red lines show the current lines in the square film. The filled circles mark the locations where the d-lines abruptly change direction, and are labelled with capital letters. Circled numbers indicate the different sectors within which the orientation of the current density remains unchanged. The following annotations are adopted throughout Section C.2: $\angle BDA = \alpha$, $\angle ABD = \beta$, $\angle AOD = \pi/4$, $|AD| = L_1$, $|AB| = L_2$.

occur across [BD] and across [AB]. Taking into account the successive orientations of the current lines, one finds

$$\begin{aligned} 2\alpha - (\pi - 2\beta) &= -\pi/2 \\ \Rightarrow \beta &= \pi/4 - \alpha. \end{aligned} \tag{C.8}$$

The length ℓ_h is given by subtracting the projection of the path OABC on the horizontal median of the square from its projection on the vertical median, which reads as

$$\ell_h = 2\left(\cos\beta - \sin\beta\right) L_2. \tag{C.9}$$

Finding an expression of ℓ_h as a function of the critical current densities and the geometrical parameters of the assembly requires slightly more work than in the previous section. The sine law in triangle ABD yields $|\mathrm{AB}| = L_2$ as a function of $|AD| = L_1$, which is

$$L_2 = \frac{\sin\alpha}{\sin\beta} L_1. \tag{C.10}$$

Similarly, the sine law in triangle OAD allows to relate L_1 to $|OD| = L/2 - W/2$ as

$$L_1 = \frac{\sin\pi/4}{\sin\left(\pi/4 + \alpha\right)} \left[\frac{L}{2} - \frac{W}{2}\right]. \tag{C.11}$$

Combining Equation C.7, Equation C.8, Equation C.9, Equation C.10 and Equation C.11 allows for finding the final expression of ℓ_h, which is

$$\begin{aligned} \frac{\ell_h}{L} &= \left(\frac{1}{\cos 2\alpha} - 1\right)\left[1 - \frac{W}{L}\right] \\ \Leftrightarrow \frac{\ell_h}{L} &= \left(\frac{J_{c,s-ext}}{J_{c,s-int}} - 1\right)\left[1 - \frac{W}{L}\right]. \end{aligned} \tag{C.12}$$

In particular, if $W = L/2$, one recovers Equation 6.4, which is in this case

$$\frac{\ell_h}{L} = \frac{1}{2}\left(\frac{J_{c,s-ext}}{J_{c,s-int}} - 1\right). \tag{C.13}$$

These analytical developments are only valid when the segment [AB] intersects the boundary demarcating the regions with uneven critical current densities, i.e. BD. If not, B lies on the horizontal median of the square, outside the overlap region rather than inside it, and sector 5 disappears subsequently, invalidating Equation C.12. This condition is equivalent to

$$\cos 2\alpha > 1 - \frac{W}{L}, \tag{C.14}$$

which relates the critical current densities in each region to the geometrical parameters of the rectangular and square films, by virtue of Equation C.7. For the sake of illustration, if $W = L/2$, one must verify $\cos 2\alpha > 1/2$, i.e. $2J_{c,s-int} > J_{c,s-ext} > J_{c,s-int}$.

Bibliography

[1] E. A. Borodianskyi and V. M. Krasnov. Josephson emission with frequency span 1–11 THz from small $Bi_2Sr_2CaCu_2O_{8+\delta}$ mesa structures. *Nature Communications*, 8:1742, November 2017.

[2] M. I. Faley, E. A. Kostyurina, K. V. Kalashnikov, Yu. V. Maslennikov, V. P. Koshelets, and R. E. Dunin-Borkowski. Superconducting Quantum Interferometers for Nondestructive Evaluation. *Sensors*, 17(12):2798, December 2017.

[3] M. H. Devoret and R. J. Schoelkopf. Superconducting Circuits for Quantum Information: An Outlook. *Science*, 339(6124):1169–1174, March 2013.

[4] Frank Arute, Kunal Arya, Ryan Babbush, Dave Bacon, Joseph C. Bardin, Rami Barends, Rupak Biswas, Sergio Boixo, Fernando G. S. L. Brandao, David A. Buell, Brian Burkett, Yu Chen, Zijun Chen, Ben Chiaro, Roberto Collins, William Courtney, Andrew Dunsworth, Edward Farhi, Brooks Foxen, Austin Fowler, Craig Gidney, Marissa Giustina, Rob Graff, Keith Guerin, Steve Habegger, Matthew P. Harrigan, Michael J. Hartmann, Alan Ho, Markus Hoffmann, Trent Huang, Travis S. Humble, Sergei V. Isakov, Evan Jeffrey, Zhang Jiang, Dvir Kafri, Kostyantyn Kechedzhi, Julian Kelly, Paul V. Klimov, Sergey Knysh, Alexander Korotkov, Fedor Kostritsa, David Landhuis, Mike Lindmark, Erik Lucero, Dmitry Lyakh nad Salvatore Mandrà, Jarrod R. McClean, Matthew McEwen, Anthony Megrant, Xiao Mi, Kristel Michielsen, Masoud Mohseni, Josh Mutus, Ofer Naaman, Matthew Neeley, Charles Neill, Murphy Yuezhen Niu, Eric Ostby, Andre Petukhov, John C. Platt, Chris Quintana, Eleanor G. Rieffel, Pedram Roushan, Nicholas C. Rubin, Daniel Sank, Kevin J. Satzinger, Vadim Smelyanskiy, Kevin J. Sung, Matthew D. Trevithick, Amit Vainsencher, Benjamin Villalonga, Theodore White, Z. Jamie Yao, Ping Yeh, Adam Zalcman, Hartmut Neven, and John M. Martinis. Quantum supremacy using a programmable superconducting processor. *Nature*, 574:505–510, October 2019.

[5] Teng Tan, M. A. Wolak, X. X. Xi, T. Tajima, and L. Civale. Magnesium diboride coated bulk niobium: a new approach to higher acceleration gradient. *Scientific Reports*, 6:35879, October 2016.

[6] V. Selvamanickam, M. Heydari Gharahcheshmeh, A. Xu, Y. Zhang, and E. Galstyan. Critical current density above 15 MA cm^{-2} at 30 K, 3 T in 2.2 μm thick heavily-doped (Gd,Y)$Ba_2Cu_3O_x$ superconductor tapes. *Superconductor Science and Technology*, 28(7):072002, May 2015.

[7] Lucio Rossi and Carmine Senatore. HTS Accelerator Magnet and Conductor Development in Europe. *Instruments*, 5(1):8, February 2021.

[8] A. Dadhich and E. Pardo. Modeling cross-field demagnetization of superconducting stacks and bulks for up to 100 tapes and 2 million cycles. *Scientific Reports*, 10:19265, November 2020.

[9] D. Uglietti. A review of commercial high temperature superconducting materials for large magnets: from wires and tapes to cables and conductors. *Superconductor Science and Technology*, 32(5):053001, April 2019.

[10] Anup Patel, Algirdas Baskys, Tom Mitchell-Williams, Aoife McCaul, William Coniglio, Jens Hänisch, Mayraluna Lao, and Bartek A. Glowacki. A trapped field of 17.7 T in a stack of high temperature superconducting tape. *Superconductor Science and Technology*, 31(9):09LT01, July 2018.

[11] A. Patel, S. Hahn, J. Voccio, A. Baskys, S. C. Hopkins, and B. A. Glowacki. Magnetic levitation using a stack of high temperature superconducting tape annuli. *Superconductor Science and Technology*, 30(2):024007, December 2016.

[12] Zhaoxin Liu, Wenjiang Yang, Long Yu, Yu Ji, Mingliang Bai, Fawzi, and Xiaodong Li. Testing and Comparison of Levitation Forces and Rotational Friction in Different Superconducting Tape Stacks. *Journal of Superconductivity and Novel Magnetism*, 33:3035–3041, July 2020.

[13] Charalampos Manolopoulos, Matteo Iacchetti, Alexander Smith, Kévin Berger, Mark Husband, and Paul Miller. Stator Design and Performance of Superconducting Motors for Aerospace Electric Propulsion Systems. *IEEE Transactions on Applied Superconductivity*, 28(4):5207005, March 2018.

[14] Bin Liu, Rod Badcock, Hang Shu, and Jin Fang. A Superconducting Induction Motor with a High Temperature Superconducting Armature: Electromagnetic Theory, Design and Analysis. *Energies*, 11(4):792, March 2018.

[15] Enric Pardo, Francesco Grilli, Yingzhen Liu, Simon Wolftädler, and Thomas Reis. AC Loss Modelling in Superconducting Coils and Motors with Parallel Tapes as Conductor. *IEEE Transactions on Applied Superconductivity*, 29(5):5202505, April 2019.

[16] Francesco Grilli, Tara Benkel, Jens Hänisch, Mayraluna Lao, Thomas Reis, Eva Berberich, Simon Wolfstädter, Christian Schneider, Paul Miller, Chloe Palmer, Bartek Glowacki, Vicente Climente-Alarcon, Anis Smara, Lukasz Tomkow, Johannes Teigelkötter, Alexander Stock, Johannes Büdel, Loïc Jeunesse, Martin Staempflin, Guillaume Delautre, Baptiste Zimmermann, Ruud van der Woude, Ana Perez, Sergey Samoilenkov, Alexander Molodyk, Enric Pardo, Milan Kapolka, Shuo Li, and Anang Dadhich. Superconducting motors for aircraft propulsion: the Advanced Superconducting Motor Experimental Demonstrator project. *Journal of Physics: Conference Series*, 1590:012051, December 2020.

[17] Guanjie Liu, Guomin Zhang, Guole Liu, Haonan Wang, and Liwei Jing. Experimental and numerical study of high frequency superconducting air-core transformer. *Superconductor Science and Technology*, 34(8):085011, June 2021.

[18] Arsalan Hekmati and Rasoul Hekmati. Double pancake superconducting coil design for maximum magnetic energy storage in small scale SMES systems. *Cryogenics*, 80(1):74–81, December 2016.

[19] E. P. Krasnoperov, V. V. Sychugov, V. V. Guryev, S. V. Shavkin, V. E. Krylov, and P. V. Volkov. 2G HTS tape and double pancake coil for cryogen-free superconducting magnet. *Electrical Engineering*, 102:1769–1774, April 2020.

[20] Chandra M. Natarajan, Michael G. Tanner, and Robert H. Hadfield. Superconducting nanowire single-photon detectors: physics and applications. *Superconductor Science and Technology*, 25(6):063001, April 2012.

[21] WeiJun Zhang, LiXing You, Hao Li, Jia Huang, ChaoLin Lv, Lu Zhang, XiaoYu Liu, JunJie Wu, Zhen Wang, and XiaoMing Xie. NbN superconducting nanowire single photon detector with efficiency over 90% at 1550 nm wavelength operational at compact cryocooler temperature. *Science China Physics, Mechanics & Astronomy*, 60:120314, October 2017.

[22] Boris Korzh, Qing-Yuan Zhao, Jason P. Allmaras, Simone Frasca, Travis M. Autry, Eric A. Bersin, Andrew D. Beyer, Ryan M. Briggs, Bruce Bumble, Marco Colangelo, Garrison M. Crouch, Andrew E. Dane, Thomas Gerrits, Adriana E. Lita, Francesco Marsili, Galan Moody, Cristián Peña, Edward Ramirez, Jake D. Rezac, Neil Sinclair, Martin J. Stevens, Angel E. Velasco, Varun B. Verma, Emma E. Wollman, Si Xie, Di Zhu, Paul D. Hale, Maria Spiropulu, Kevin L. Silverman, Richard P. Mirin, Sae Woo Nam, Alexander G. Kozorezov, Matthew D. Shaw, and Karl K. Berggren. Demonstration of sub-3 ps temporal resolution with a superconducting nanowire single-photon detector. *Nature Photonics*, 14:250–255, March 2020.

[23] J. Brisbois, B. Vanderheyden, F. Colauto, M. Motta, W. A. Ortiz, J. Fritzsche, N. D. Nguyen, B. Hackens, O.-A. Adami, and A. V. Silhanek. Classical analogy for the deflection of flux avalanches by a metallic layer. *New Journal of Physics*, 16:103003, October 2014.

[24] J. Brisbois, V. N. Gladilin, J. Tempere, J. T. Devreese, V. V. Moshchalkov, F. Colauto, M. Motta, T. H. Johansen, J. Fritzsche, O.-A. Adami, N. D. Nguyen, W. A. Ortiz, R. B. G. Kramer, and A. V. Silhanek. Flux penetration in a superconducting film partially capped with a conducting layer. *Physical Review B*, 95(9):094506, March 2017.

[25] P. Mikheenko, J. I. Vestgården, S. Chaudhuri, I. J. Maasilta, Y. M. Galperin, and T. H. Johansen. Metal frame as local protection of superconducting films from thermomagnetic avalanches. *AIP Advances*, 6(3):035304, March 2016.

[26] D. C. Larbalestier, J. Jiang, U. P. Trociewitz, F. Kametani, C. Scheuerlein, M. Dalban-Canassy, M. Matras, P. Chen, N. C. Craig, P. J. Lee, and E. E. Hellstrom. Isotropic round-wire multifilament cuprate superconductor for generation of magnetic fields above 30 T. *Nature Materials*, 13:375–381, March 2014.

[27] Jérémy Brisbois, Maycon Motta, Jonathan I. Avila, Gorky Shaw, Thibaut Devillers, Nora M. Dempsey, Savita K. P. Veerapandian, Pierre Colson, Benoît Vanderheyden, Philippe Vanderbemden, Wilson A. Ortiz, Ngoc Duy Nguyen, Roman B. G.

Kramer, and Alejandro V. Silhanek. Imprinting superconducting vortex footsteps in a magnetic layer. *Scientific Reports*, 6:27159, June 2016.

[28] V. Vlasko-Vlasov, U. Welp, G. Karapetrov, V. Novosad, D. Rosenmann, M. Iavarone, A. Belkin, and W.-K. Kwok. Guiding superconducting vortices with magnetic domain walls. *Physical Review B*, 77(13):134518, April 2008.

[29] V. K. Vlasko-Vlasov, F. Colauto, A. I. Buzdin, D. Rosenmann, T. Benseman, and W.-K. Kwok. Magnetic gates and guides for superconducting vortices. *Physical Review B*, 95(14):144504, April 2017.

[30] A. P. Petrović, M. Raju, X. Y. Tee, A. Louat, I. Maggio-Aprile, R. M. Menezes, M. J. Wyszyński, N. K. Duong, M. Reznikov, Ch. Renner, M. V. Milošević, and C. Panagopoulos. Skyrmion-(Anti)Vortex Coupling in a Chiral Magnet-Superconductor Heterostructure. *Physical Review Letters*, 126(11):117205, March 2021.

[31] Raí M. Menezes, José F. S. Neto, Clécio C. de Souza Silva, and Milorad V. Milošević. Manipulation of magnetic skyrmions by superconducting vortices in ferromagnet-superconductor heterostructures. *Physical Review B*, 100(1):014431, July 2019.

[32] V. Rouco, R. Córdoba, J. M. De Teresa, L. A. Rodríguez, C. Navau, N. Del-Valle, G. Via, A. Sánchez, C. Monton, F. Kronast, X. Obradors, T. Puig, and A. Palau. Competition between Superconductor – Ferromagnetic stray magnetic fields in $YBa_2Cu_3O_{7-x}$ films pierced with Co nano-rods. *Scientific Reports*, 7:5663, July 2017.

[33] Alvaro Sanchez, Carles Navau, Jordi Prat-Camps, and Du-Xing Chen. Antimagnets: controlling magnetic fields with superconductor–metamaterial hybrids. *New Journal of Physics*, 13:093034, September 2011.

[34] Fedor Gömöry, Mykola Solovyov, Ján Šouc, Carles Navau, Jordi Prat-Camps, and Alvaro Sanchez. Experimental Realization of a Magnetic Cloak. *Science*, 335(6075):1466–1468, March 2012.

[35] Mykola Solovyov, Ján Šouc, and Fedor Gömöry. Magnetic Cloak for Low Frequency AC Magnetic Field. *IEEE Transactions on Applied Superconductivity*, 25(3):8800705, June 2015.

[36] Min Zhang and T. A. Coombs. 3D modeling of high-T_c superconductors by finite element software. *Superconductor Science and Technology*, 25(1):015009, December 2011.

[37] Sansheng Wang, Tongfu He, and Yiming Zhang. Research on a Superconducting Magnetic Flux Concentrator for a GMI-Based Mixed Sensor. *IEEE Transactions on Applied Superconductivity*, 24(5):1600305, October 2014.

[38] L. P. Ichkitidze, M. V. Belodedov, S. V. Selishchev, and D. V. Telishev. Magnetic Field Concentrator Based on the Superconducting Films with Nanosize Cuts. *Journal of Physics: Conference Series*, 1182:012007, September 2018.

[39] Jordi Prat-Camps, Carles Navau, and Alvaro Sanchez. A Magnetic Wormhole. *Scientific Reports*, 5:12488, August 2015.

[40] R. Zadorosny, F. Colauto, M. Motta, T. H. Johansen, R. Dinner, M. Blamire, G. W. Ataklti, V. V. Moshchalkov, A. V. Silhanek, and W. A. Ortiz. Morphology of Flux Avalanches in Patterned Superconducting Films. *Journal of Superconductivity and Novel Magnetism*, 26:2285–2288, June 2013.

[41] J. Brisbois, O.-A. Adami, J. I. Avila, M. Motta, W. A. Ortiz, N. D. Nguyen, P. Vanderbemden, B. Vanderheyden, R. B. G. Kramer, and A. V. Silhanek. Magnetic flux penetration in Nb superconducting films with lithographically defined microindentations. *Physical Review B*, 93(5):054521, February 2016.

[42] Anna Palau, Sergio Valencia, Nuria Del-Valle, Carles Navau, Matteo Cialone, Ashima Arora, Florian Kronast, D. Alan Tennant, Xavier Obradors, Alvaro Sanchez, and Teresa Puig. Encoding Magnetic States in Monopole-Like Configurations Using Superconducting Dots. *Advanced Science*, 3(11):1600207, November 2016.

[43] F. Colauto, D. Carmo, A. M. H. de Andrade, A. A. M. Oliveira, W. A. Ortiz, and T. H. Johansen. Anisotropic thermomagnetic avalanche activity in field-cooled superconducting films. *Physical Review B*, 96(6):060506, August 2017.

[44] T. Tamegai, A. Mine, Y. Tsuchiya, S. Miyano, S. Pyon, Y. Mawatari, S. Nagasawa, and M. Hidaka. Critical states and thermomagnetic instabilities in three-dimensional nanostructured superconductors. *Physica C: Superconductivity and its Applications*, 533:74–79, February 2017.

[45] G. Shaw, J. Brisbois, L. B. G. L. Pinheiro, J. Müller, S. Blanco Alvarez, T. Devillers, N. M. Dempsey, J. E. Scheerder, J. Van de Vondel, S. Melinte, P. Vanderbemden, M. Motta, W. A. Ortiz, K. Hasselbach, R. B. G. Kramer, and A. V. Silhanek. Quantitative magneto-optical investigation of superconductor/ferromagnet hybrid structures. *Review of Scientific Instruments*, 89(2):023705, February 2018.

[46] S. Blanco Alvarez, J. Brisbois, S. Melinte, R. B. G. Kramer, and A. V. Silhanek. Statistics of thermomagnetic breakdown in Nb superconducting films. *Scientific Reports*, 9:3659, March 2019.

[47] F. Colauto, M. Motta, and W. A. Ortiz. Controlling magnetic flux penetration in low-T_c superconducting films and hybrids. *Superconductor Science and Technology*, 34(1):013002, November 2020.

[48] M. Motta, L. Burger, Lu Jiang, J. D. González Acosta, Ž. L. Jelić, F. Colauto, W. A. Ortiz, T. H. Johansen, M. V. Milošević, C. Cirillo, C. Attanasio, Cun Xue, A. V. Silhanek, and B. Vanderheyden. Metamorphosis of discontinuity lines and rectification of magnetic flux avalanches in the presence of noncentrosymmetric pinning forces. *Physical Review B*, 103(22):224514, June 2021.

[49] D. A. D. Chaves, I. M. de Araújo, D. Carmo, F. Colauto, A. A. M. de Oliveira, A. M. H. de Andrade, T. H. Johansen, A. V. Silhanek, W. A. Ortiz, and M. Motta. Enhancing the effective critical current density in a Nb superconducting thin film by cooling in an inhomogeneous magnetic field. *Applied Physics Letters*, 119(2):022602, July 2021.

[50] Leon N. Cooper. Bound Electron Pairs in a Degenerate Fermi Gas. *Physical Review*, 104(4):1189, November 1956.

[51] F. London and H. London. The electromagnetic equations of the supraconductor. *Proceedings of the Royal Society A*, 149(866), March 1935.

[52] V. L. Ginzburg and L. D. Landau. On the theory of superconductivity. *Journal of Experimental and Theoretical Physics*, 20:1064–1082, 1950.

[53] M. Tinkham. *Introduction to superconductivity*. Dover Publications, second edition edition, June 2004.

[54] R. J. Watts-Tobin, Y. Krähenbühl, and L. Kramer. Nonequilibrium theory of dirty, current-carrying superconductors: phase-slip oscillators in narrow filaments near T_c. *Journal of Low Temperature Physics*, 42(5-6):459–501, March 1981.

[55] Tommy Sonne Alstrøm, Mads Peter Sørensen, Niels Falsig Pedersen, and Søren Madsen. Magnetic Flux Lines in Complex Geometry Type-II Superconductors Studied by the Time Dependent Ginzburg-Landau Equation. *Acta Applicandae Mathematicae*, 115:63–74, August 2010.

[56] L. P. Gor'kov and G. M. Eliashberg. Generalization of Ginzburg-Landau equations for non-stationary problems in the case of alloys with paramagnetic impurities. *Soviets Physics Journal of Experimental and Theoretical Physics*, 27(2):328–334, 1968.

[57] B. W. Maxfield and W. L. McLean. Superconducting penetration depth of niobium. *Physical Review*, 139(5):1515, August 1965.

[58] Z.-H. Sung, P. J. Lee, A. Gurevich, and D. C. Larbalestier. Evidence for preferential flux flow at the grainboundaries of superconducting RF-quality niobium. *Superconductor Science and Technology*, 31(4):045001, February 2018.

[59] S. J. Williamson. Bulk upper critical field of clean type-II superconductors: V and Nb. *Physical Review B*, 2(9):3545, November 1970.

[60] D. Larbalestier, A. Gurevich, and A. Feldmann, D. M. Polyanskii. High-T_c superconducting materials for electric power applications. *Nature*, 414:368–377, November 2001.

[61] L. Krusin-Elbaum, A. P. Malozemoff, Y. Yeshurun, D. C. Cronemeyer, and F. Holtzberg. Temperature dependence of lower critical fields in Y-Ba-Cu-O crystals. *Physical Review B*, 39(4):2936, February 1989.

[62] T. Sekitani, N. Miura, S. Ikeda, Y. H. Matsuda, and Y. Shiohara. Upper critical field for optimally-doped $YBa_2Cu_3O_{7-\delta}$. *Physica B: Condensed Matter*, 346:319–324, April 2004.

[63] Ruslan Prozorov and Russell W. Giannetta. Magnetic penetration depth in unconventional superconductors. *Superconductor Science and Technology*, 19(8):41–67, June 2006.

[64] C. J. Gorter and H. Casimir. On supraconductivity I. *Physica*, 1(1-6):306–320, 1934.

[65] J. Bardeen, L. N. Cooper, and J. R. Schrieffer. Theory of Superconductivity. *Physical Review*, 108(5), December 1957.

[66] G. M. Eliashberg, G. V. Klimovitch, and A. V. Rylyakov. On the temperature dependence of the London penetration depth in a superconductor. *Journal of Superconductivity*, 4(5):393–396, October 1991.

[67] W. N. Hardy, D. A. Bonn, D. C. Morgan, Ruixing Liang, and Kuan Zhang. Precision measurements of the temperature dependence of λin $YBa_2Cu_3O_{6.95}$: Strong evidence for nodes in the gap function. *Physical Review Letters*, 70(25):3999, June 1993.

[68] D. K. Finnemore, T. F. Stromberg, and C. A. Swenson. Superconducting Properties of High-Purity Niobium. *Physical Review*, 149(1):231, September 1966.

[69] R. A. French. Intrinsic type-2 superconductivity in pure niobium. *Cryogenics*, 8(5):301–308, October 1968.

[70] Yuji Asada and Hiroshi Nosé. Superconductivity of Niobium Films. *Journal of the Physical Society of Japan*, 26(2):347–354, August 1968.

[71] Cécile Delacour, Luc Ortega, Marc Faucher, Thierry Crozes, Thierry Fournier, Bernard Pannetier, and Vincent Bouchiat. Persistence of superconductivity in niobium ultrathin films grown on R-plane sapphire. *Physical Review B*, 83(14):144504, April 2011.

[72] J. Pearl. Current distribution in superconducting films carrying quantized fluxoids. *Applied Physics Letters*, 5(4):65, August 1964.

[73] I. Zaytseva, A. Abaloszew, B. C. Camargo, Y. Syryanyy, and M. Z. Cieplak. Upper critical field and superconductor-metal transition in ultrathin niobium films. *Scientific Reports*, 10:19062, November 2020.

[74] J. V. J. Congreve, Y. H. Shi, A. R. Dennis, J. H. Durrell, and D. A. Cardwell. Comparison of the superconducting properties of Y-Ba-Cu-O and Y-Ba-Cu-O-Ag bulksuperconductors. *IOP Conference Series: Materials Science and Engineering*, 502:012181, 2019.

[75] E. Stilp, A. Suter, T. Prokscha, Z. Salman, E. Morenzoni, H. Keller, C. Katzer, F. Schmidl, and M. Döbeli. Modifications of the Meissner screening profile in $YBa_2Cu_3O_{7-\delta}$ thin films by gold nanoparticles. *Physical Review B*, 89:020510, January 2014.

[76] Guanmei Wang, Mark J. Raine, and Damian P. Hampshire. How resistive must grain boundaries in polycrystalline superconductors be, to limit J_c? *Superconductor Science and Technology*, 30(10):104001, August 2017.

[77] John R. Clem. Simple model for the vortex core in a type II superconductor. *Journal of Low Temperature Physics*, 18:427–434, March 1975.

[78] D.-X. Chen, J. J. Moreno, A. Hernando, A. Sanchez, and B.-Z. Li. Nature of the driving force on an Abrikosov vortex. *Physical Review B*, 57(9):5059–5062, March 1998.

[79] A. L. Fetter, P. C. Hohenberg, and P. Pincus. Stability of a Lattice of Superfluid Vortices. *Physical Reveiw*, 147(1):140, July 1966.

[80] John Bardeen and M. J. Stephen. Theory of the Motion of Vortices in Superconductors. *Physical Review*, 140(4A):1197, November 1965.

[81] C. P. Bean. Magnetization of Hard Superconductors. *Physical Review Letters*, 8(6):250, March 1962.

[82] Charles P. Bean. Magnetization of High-Field Superconductors. *Reviews of Modern Physics*, 36(1):31, January 1964.

[83] X. Zhang, Z. Zhong, J. Geng, B. Shen, J. Ma, C. Li, H. Zhang, Q. Dong, and T. A. Coombs. Study of Critical Current and n-Values of 2G HTS Tapes: Their Magnetic Field-Angular Dependence. *Journal of Superconductivity and Novel Magnetism*, 31:3847–3854, April 2018.

[84] Y. B. Kim, C. F. Hempstead, and A. R. Strnad. Critical Persistent Currents in Hard Superconductors. *Physical Review Letters*, 9(7):306, October 1962.

[85] C. P. Bean and J. D. Livingston. Surface Barrier in Type-II Superconductors. *Physical Review Letters*, 12(1):14, January 1964.

[86] P. K. Mishra, G. Ravikumar, V. C. Sahni, M. R. Koblischka, and A. K. Grover. Surface pinning in niobium and a high-T_c superconductor. *Physica C: Superconductivity*, 269(1-2):71–75, September 1996.

[87] M. Konczykowski, L. I. Burlachkov, Y. Yeshurun, and F. Holtzberg. Evidence for surface barriers and their effect on irreversibility and lower-critical-field measurements in Y-Ba-Cu-O crystals. *Physical Review B*, 43(16):13707, June 1991.

[88] Th. Schuster, M. V. Indenbom, H. Kuhn, E. H. Brandt, and M. Konczykowski. Flux Penetration and Overcritical Currents in Flat Superconductors with Irradiation-Enhanced Edge Pinning: Theory and Experiment. *Physical Review Letters*, 73(10):1424, September 1994.

[89] E. Zeldov, A. I. Larkin, M. Konczykowski, B. Khaykovich, D. Majer, V. B. Geshkenbein, and V. M. Vinokur. Geometrical barriers in type II superconductors. *Physica C: Superconductivity*, 235-240(4):2761–2762, December 1994.

[90] M. Benkraouda and John R. Clem. Magnetic hysteresis from the geometrical barrier in type-II superconducting strips. *Physical Review B*, 53(9):5716, March 1996.

[91] E. H. Brandt. Geometric barrier and current string in type-II superconductors obtained from continuum electrodynamics. *Physical Review B*, 59(5):3369, February 1999.

[92] Maamar Benkraouda and John R. Clem. Critical current from surface barriers in type-II superconducting strips. *Physical Review B*, 58(22):15103, December 1998.

[93] Grigorii P. Mikitik and Ernst Helmut Brandt. Critical state in thin anisotropic superconductors of arbitrary shape. *Physical Review B*, 62(10):6800, September 2000.

[94] N. Pompeo, A. Alimenti, K. Torokhtii, E. Bartolomé, A. Palau, T. Puig, A. Augieri, V. Galluzzi, A. Mancini, and G. Celentano. Intrinsic anisotropy and pinning anisotropy in nanostructured $YBa_2Cu_3O_7$ from microwave measurements. *Superconductor Science and Technology*, 33(4):044017, March 2020.

[95] Th. Schuster, H. Kuhn, and M. V. Indenbom. Discontinuity lines in rectangular superconductors with intrinsic and extrinsic anisotropies. *Physical Review B*, 52(21):15621, December 1995.

[96] V. K. Vlasko-Vlasov, F. Colauto, A. A. Buzdin, D. Carmo, A. M. H. Andrade, A. A. M. Oliveira, W. A. Ortiz, D. Rosenmann, and W.-K. Kwok. Crossing fields in thin films of isotropic superconductors. *Physical Review B*, 94(18):184502, November 2016.

[97] Fabiano Colauto, Danusa do Carmo, Antonio M. H. de Andrade, Ana A. M. Oliveira, Wilson A. Ortiz, Yuri M. Galperin, and Tom H. Johansen. Anisotropic Flux Penetration in Superconducting Nb Films With Frozen-in In-plane Magnetic Fields. *IEEE Transactions on Applied Superconductivity*, 25(9):8002505, August 2019.

[98] John Bardeen. Critical Fields and Currents in Superconductors. *Reviews of Modern Physics*, 34(4):667, October 1962.

[99] É. A. Pashitskiĭ, V. I. Vakaryuk, S. M. Ryabchenko, and Yu. V. Fedotov. Temperature dependence of the critical current in high-T_c superconductors with low-angle boundaries between crystalline blocks. *Low Temperature Physics*, 27(2):96, February 2001.

[100] E. Zeldov, N. M. Amer, G. Koren, A. Gupta, M. W. McElfresh, and R. J. Gambino. Flux creep characteristics in high-temperature superconductors. *Applied Physics Letters*, 56(7):680, December 1989.

[101] Elia Zeldov. Flux creep and vortex potential well structure in high-temperature superconductors. *Physica A: Statistical Mechanics and its Applications*, 168(1):260–267, September 1990.

[102] P. W. Anderson. Theory of Flux Creep in Hard Superconductors. *Physical Review Letters*, 9(7):309, October 1962.

[103] R. G. Mints and E. H. Brandt. Flux jumping in thin films. *Physical Review B*, 54(17):12421, November 1996.

[104] Teruo Matsushita. Longitudinal Magnetic Field Effect in Superconductors. *Japanese Journal of Applied Physics*, 51(1R):010111, December 2011.

[105] John R. Clem, Marcus Weigand, J. H. Durrell, and A. M. Campbell. Theory and experiment testing flux-line cutting physics. *Superconductor Science and Technology*, 24(6):062002, March 2011.

[106] M. L. Amigó, V. Ale Crivillero, D. G. Franco, A. Badía-Majós, J. Guimpel, and G. Nieva. Vortex pinning by intrinsic correlated defects in $Fe_{1-y}Se$. *Journal of Physics: Conference Series*, 507:012001, 2014.

[107] E. H. Brandt and G. P. Mikitik. Unusual critical states in type-II superconductors. *Physical Review B*, 76(6):064526, August 2007.

[108] A. Badía-Majós and C. López. Modelling current voltage characteristics of practical superconductors. *Superconductor Science and Technology*, 28(2):024003, December 2014.

[109] H. Yamasaki and Y. Mawatari. Current-voltage characteristics and flux creep in melt-textured $YBa_2Cu_3O_{7-\delta}$. *Superconductor Science and Technology*, 13(2):202, 2000.

[110] W. J. Kossler, Nathan Abraham, C. E. Stronach, and Allan J. Greer. Magnetic Fields of Vortices in a Superconducting Thin Film. *Physics Procedia*, 30:241–244, 2012.

[111] D. Yu. Vodolazov and I. L. Maksimov. Distribution of the magnetic field and current density in superconducting films of finite thickness. *Physica C: Superconductivity*, 349(1-2):125–138, January 2001.

[112] P. N. Mikheenko and Yu. E. Kuzovlev. Inductance measurements of HTSC films with high critical currents. *Physica C: Superconductivity*, 204(3-4):229–236, January 1993.

[113] John R. Clem and Alvaro Sanchez. Hysteretic ac losses and susceptibility of thin superconducting disks. *Physical Review B*, 50(13):9335, October 1994.

[114] Ernst Helmut Brandt and Mikhail Indenbom. Type-II superconductor strip with current in a perpendicular magnetic field. *Physical Review B*, 48(17):12893, November 1993.

[115] Ernst Helmut Brandt. Thin superconductors in a perpendicular magnetic ac field: General formulation and strip geometry. *Physical Review B*, 49(13):9024, April 1994.

[116] Th. Schuster, M. V. Indenbom, M. R. Koblischka, H. Kuhn, and H. Kronmüller. Observation of current-discontinuity lines in type-II superconductors. *Physical Review B*, 49(5):3443, February 1994.

[117] E. H. Brandt. Electric field in superconductors with rectangular cross section. *Physical Review B*, 52(21):15442, December 1995.

[118] Henrik Jeldtoft Jensen. *Self-organized criticality: Emergent complex behavior in physical and biological systems*. Cambridge Lecture Notes in Physics. Cambridge University Press, 1998.

[119] J. I. Vestgården, D. V. Shantsev, Y. M. Galperin, and T. H. Johansen. Lightning in superconductors. *Scientific Reports*, 2(886), November 2012.

[120] B. Biehler, B.-U. Runge, P. Leiderer, and R. G. Mints. Ultrafast magnetic flux dendrite propagation into thin superconducting films. *Physical Review B*, 72(2):024532, July 2005.

[121] Igor S. Aranson, Alex Gurevich, Marco S. Welling, Rinke J. Wijngaarden, Vitalii K. Vlasko-Vlasov, Valerii M. Vinokur, and Ulrich Welp. Dendritic Flux Avalanches and Nonlocal Electrodynamics in Thin Superconducting Films. *Physical Review Letters*, 94(3):037002, January 2005.

[122] M. S. Welling, R. J. Westerwaal, W. Lohstroh, and R. J. Wijngaarden. Huge compact flux avalanches in superconducting Nb thin films. *Physica C: Superconductivity*, 411(1-2):11–17, September 2004.

[123] A. L. Rakhmanov, D. V. Shantsev, Y. M. Galperin, and T. H. Johansen. Finger patterns produced by thermomagnetic instability in superconductors. *Physical Review B*, 70(22):224502, December 2004.

[124] D. V. Denisov, A. L. Rakhmanov, D. V. Shantsev, Y. M. Galperin, and T. H. Johansen. Dendritic and uniform flux jumps in superconducting films. *Physical Review B*, 73(1):014512, January 2006.

[125] J. I. Vestgården, Y. M. Galperin, and T. H. Johansen. The Thermomagnetic Instability in Superconducting Films with Adjacent Metal Layer. *Journal of Low Temperature Physics*, 173:303–326, September 2013.

[126] D. V. Denisov, D. V. Shantsev, Y. M. Galperin, Eun-Mi Choi, Hyun-Sook Lee, Sung-Ik Lee, A. V. Bobyl, P. E. Goa, A. A. F. Olsen, and T. H. Johansen. Onset of Dendritic Flux Avalanches in Superconducting Films. *Physical Review Letters*, 97(7):077002, August 2006.

[127] J. M. D. Coey. *Magnetism and Magnetic Materials.* Cambridge University Press, May 2010.

[128] A. Y. Elezzabi and M. R. Freeman. Ultrafast magneto-optic sampling of picosecond current pulses. *Applied Physics Letters*, 68(25):3546, April 1996.

[129] Y. Hashimoto, A. R. Khorsand, M. Savoini, B. Koene, D. Bossini, A. Tsukamoto, A. Itoh, Y. Ohtsuka, K. Aoshima, A. V. Kimel, A. Kirilyuk, and T. Rasing. Ultrafast time-resolved magneto-optical imaging of all-optical switching in GdFeCo with femtosecond time-resolution and a µm spatial-resolution. *Review of Scientific Instruments*, 85(6):063702, June 2014.

[130] S. Blanco Alvarez. *Thermally and dynamically driven magnetic flux penetration in type-II superconductors.* phdthesis, Liège Université, Liège, October 2020.

[131] E. C. Stoner and E. P. Wohlfarth. A mechanism of magnetic hysteresis in heterogeneous alloys. *Philosophical Transactions of the Royal Society A*, 240(826):599–642, May 1948.

[132] J. Brisbois. *Magneto-optical investigation of superconducting hybrid structures.* phdthesis, Liège Université, October 2017.

[133] T. H. Johansen, M. Baziljevich, H. Bratsberg, Y. Galperin, P. E. Lindelof, Y. Shen, and P. Vase. Direct observation of the current distribution in thin superconducting strips using magneto-optic imaging. *Physical Review B*, 54(22):16264, December 1996.

[134] Ch. Jooss, J. Albrecht, H. Kuhn, S. Leonhardt, and H. Kronmüller. Magneto-optical studies of current distributions in high-T_c superconductors. *Reports On Progress in Physics*, 65(5):651, April 2002.

[135] M. Lüders, M. A. L. Marques, N. N. Lathiotakis, A. Floris, G. Profeta, L. Fast, A. Continenza, S. Massidda, and E. K. U. Gross. Ab-initio theory of superconductivity – I: Density functional formalism andapproximate functionals. *Physical Review B*, 72(2):024545, July 2005.

[136] M. A. L. Marques, M. Lüders, N. N. Lathiotakis, G. Profeta, A. Floris, L. Fast, A. Continenza, E. K. U. Gross, and S. Massidda. Ab initio theory of superconductivity. II. Application to elemental metals. *Physical Review B*, 72(2):024546, July 2005.

[137] William D. Gropp, Hans G. Kaper, Gary K. Leaf, David M. Levine, Mario Palumbo, and Valerii M. Vinokur. Numerical Simulation of Vortex Dynamics in Type-II Superconductors. *Journal of Computational Physics*, 123(2):254–266, February 1996.

[138] T. Winiecki and C. S. Adams. A Fast Semi-Implicit Finite-Difference Method for the TDGL Equations. *Journal of Computational Physics*, 179(1):127–139, June 2002.

[139] A. M. Campbell. A new method of determining the critical state insuperconductors. *Superconductor Science and Technology*, 20(3):292, February 2007.

[140] A. Badía-Majós and C. López. Electromagnetics close beyond the criticalstate: thermodynamic prospect. *Superconductor Science and Technology*, 25(10):104004, September 2012.

[141] E. H. Brandt, M. V. Indenbom, and A. Forkl. Type-II superconducting strip in perpendicular magnetic field. *Europhysics Letters*, 22(9):735, April 1993.

[142] Grigorii P. Mikitik and Ernst Helmut Brandt. Analytic solution for the critical state in superconducting elliptic films. *Physical Review B*, 60(1):592, July 1999.

[143] Ernst Helmut Brandt. Square and rectangular thin superconductors in a transverse magnetic field. *Physical Review Letters*, 74(15):3025, April 1995.

[144] E. H. Brandt. Vortices in thin flat superconductors with holes and slits. *Physica C: Superconductivity and its Applications*, 437-438:29–33, May 2006.

[145] Ernst Helmut Brandt. Theory of type-II superconductors with finite London penetration depth. *Physical Review B*, 64(2):024505, June 2001.

[146] Th. Schuster, H. Kuhn, E. H. Brandt, M. V. Indenbom, M. Kläser, G. Müller-Vogt, H.-U. Habermeier, H. Kronmüller, and A. Forkl. Current and field pattern in rectangular and inhomogeneous superconductors. *Physical Review B*, 52(14):10375, October 1995.

[147] Th. Schuster, H. Kuhn, E. H. Brandt, and S. Klaumünzer. Flux penetration into flat rectangular superconductors with anisotropic critical current. *Physical Review B*, 56(6):3413, August 1997.

[148] Rinke J. Wijngaarden, K. Heeck, H. J. W. Spoelder, R. Surdeanu, and R. Griessen. Fast determination of 2D current patterns in flat conductors from measurement of their magnetic field. *Physica C: Superconductivity*, 295(3–4):177–185, February 1998.

[149] J. I. Vestgården and T. H. Johansen. Modeling non-local electrodynamics insuperconducting films: the case of a rightangle corner. *Superconductor Science and Technology*, 25(10):104001, September 2012.

[150] F. Sirois, F. Roy, and B. Dutoit. Assessment of the Computational Performances of the Semi-Analytical Method (SAM) for Computing 2-D Current Distributions in Superconductors. *IEEE Transactions on Applied Superconductivity*, 19(3):3600–3604, June 2009.

[151] Leonid Prigozhin and Vladimir Sokolovsky. Fast Fourier transform-based solution of 2D and 3D magnetization problems in type-II superconductivity. *Superconductor Science and Technology*, 31(5):055018, April 2018.

[152] L. Prigozhin and V. Sokolovsky. Solution of 3D magnetization problems for superconducting film stacks. *Superconductor Science and Technology*, 31(12):125001, October 2018.

[153] James W. Cooley and John W. Tukey. An algorithm for the machine calculation of complex Fourier series. *Mathemetics of Computation*, 19:297–301, 1965.

[154] Leslie Greengard and June-Yub Lee. Accelerating the Nonuniform Fast Fourier Transform. *SIAM Review*, 46(3):443–454, July 2004.

[155] June-Yub Lee and Leslie Greengard. The type 3 nonuniform FFT and its applications. *Journal of Computational Physics*, 206(1):1–5, June 2005.

[156] Diego Ruiz-Antolín and Alex Townsend. A Nonuniform Fast Fourier Transform Based on Low Rank Approximation. *SIAM Journal on Scientific Computing*, 40(1):529–547, February 2018.

[157] Enric Pardo and Milan Kapolka. 3D computation of non-linear eddy currents: Variational method and superconducting cubic bulk. *Journal of Computational Physics*, 344:339–363, September 2017.

[158] E. Pardo and M. Kapolka. 3D magnetization currents, magnetization loop, and saturation field in superconducting rectangular prisms. *Superconductor Science and Technology*, 30(6):064007, May 2017.

[159] M. Kapolka, V. M. R. Zermeño, S. Zou, A. Morandi, P. L. Ribani, E. Pardo, and F. Grilli. Three-Dimensional Modeling of the Magnetization of Superconducting Rectangular-Based Bulks and Tape Stacks. *IEEE Transactions on Applied Superconductivity*, 28(4):1–6, June 2018.

[160] M. Kapolka, E. Pardo, F. Grilli, A. Baskys, V. Climente-Alarcon, A. Dadhich, and B. A. Glowacki. Cross-field demagnetization of stacks of tapes: 3D modeling and measurements. *Superconductor Science and Technology*, 33(4):044019, March 2020.

[161] Enric Pardo, Ján Šouc, and Lubomir Frolek. Electromagnetic modelling of superconductors with a smooth current–voltage relation: variational principle and coils from a few turns to large magnets. *Superconductor Science and Technology*, 28(4):044003, February 2015.

[162] J. Ruuskanen, A. Stenvall, V. Lahtinen, and E. Pardo. Electromagnetic nonlinearities in a Roebel-cable-based accelerator magnet prototype: variational approach. *Superconductor Science and Technology*, 30(2):024008, December 2016.

[163] Leonid Prigozhin and Vladimir Sokolovsky. Computing AC losses in stacks of high-temperature superconducting tapes. *Superconductor Science and Technology*, 24(7):075012, May 2011.

[164] Leonid Prigozhin. The Bean Model in Superconductivity: Variational Formulation and Numerical Solution. *Journal of Computational Physics*, 129(1):190–200, November 1996.

[165] A. Badía, C. López, and J. L. Giordano. Optimal control model for the critical state in superconductors. *Physical Review B*, 58(14):9440, October 1998.

[166] A. Badía and C. López. Vector magnetic hysteresis of hard superconductors. *Physical Review B*, 65(10):104514, February 2002.

[167] Z. Hong, A. M. Campbell, and T. A. Coombs. Numerical solution of critical state in superconductivity by finite element software. *Superconductor Science and Technology*, 19(12):1246, October 2006.

[168] Francesco Grilli, Roberto Brambilla, Frédéric Sirois, Antti Stenvall, and Steeve Memiaghe. Development of a three-dimensional finite-element model for high-temperature superconductors based on the H-formulation. *Cryogenics*, 53:142–147, January 2013.

[169] Víctor M. R. Zermeño and Francesco Grilli. 3D modeling and simulation of 2G HTS stacks and coils. *Superconductor Science and Technology*, 27(4):044025, March 2014.

[170] F. Sass, G. G. Sotelo, R. de Andrade Junior, and F. Sirois. H-formulation for simulating levitation forces acting on HTS bulks and stacks of 2G coated conductors. *Superconductor Science and Technology*, 28(12):125012, November 2015.

[171] M. P. Philippe, M. D. Ainslie, L. Wéra, J. F. Fagnard, A. R. Dennis, Y.-H. Shi, D. A. Cardwell, B. Vanderheyden, and P. Vanderbemden. Influence of soft ferromagnetic sections on the magnetic flux density profile of a large grain, bulk Y–Ba–Cu–O superconductor. *Superconductor Science and Technology*, 28(9):095008, July 2015.

[172] Junjie Zhao, Yingxu Li, and Yuanwen Gao. 3D simulation of AC loss in a twisted multi-filamentary superconducting wire. *Cryogenics*, 84:60–68, June 2017.

[173] Loïc Quéval, Kun Liu, Wenjiao Yang, Víctor M. R. Zermeño, and Guangtong Ma. Superconducting magnetic bearings simulation using an H-formulation finite element model. *Superconductor Science and Technology*, 31(8):084001, June 2018.

[174] Boyang Shen, Francesco Grilli, and Tim Coombs. Overview of H-Formulation: A Versatile Tool for Modeling Electromagnetics in High-Temperature Superconductor Applications. *IEEE Access*, 8:100403–100414, May 2020.

[175] A. Stenvall, V. Lahtinen, and M. Lyly. An H-formulation-based three-dimensional hysteresis loss modelling tool in a simulation including time varying applied field and transport current: the fundamental problem and its solution. *Superconductor Science and Technology*, 27(10):104004, August 2014.

[176] Alexandre Arsenault, Frédéric Sirois, and Francsesco Grilli. Implementation of the H-ϕ Formulation in COMSOL Multiphysics for Simulating the Magnetization of Bulk Superconductors and Comparison With the H-Formulation. *IEEE Transactions on Applied Superconductivity*, 31(2):6800111, March 2021.

[177] Julien Dular, Christophe Geuzaine, and Benoît Vanderheyden. Finite-Element Formulations for Systems With High-Temperature Superconductors. *IEEE Transactions on Applied Superconductivity*, 30(3):8200113, April 2020.

[178] Julien Dular, Mané Harutyunyan, Lorenzo Bortot, Sebastian Schöps, Benoît Vanderheyden, and Christophe Geuzaine. On the Stability of Mixed Finite-Element Formulations for High-Temperature Superconductors. *IEEE Transactions on Applied Superconductivity*, 31(6):8200412, September 2021.

[179] A. M. Campbell. A direct method for obtaining the critical state in two and three dimensions. *Superconductor Science and Technology*, 22(3):034005, January 2009.

[180] Gregory P. Lousberg, Marcel Ausloos, Christophe Geuzaine, Patrick Dular, Philippe Vanderbemden, and Benoît Vanderheyden. Numerical simulation of the magnetization of high-temperature superconductors: a 3D finite element method using a single time-step iteration. *Superconductor Science and Technology*, 22(5):055005, March 2009.

[181] Y. Komi, M. Sekino, and H. Ohsaki. Three-dimensional numerical analysis of magnetic and thermal fields during pulsed field magnetization of bulk superconductors with inhomogeneous superconducting properties. *Physica C: Superconductivity*, 469(15–20):1262–1265, October 2009.

[182] J. F. Fagnard, M. Morita, S. Nariki, H. Teshima, H. Caps, B. Vanderheyden, and P. Vanderbemden. Magnetic moment and local magnetic induction of superconducting/ferromagnetic structures subjected to crossed fields: experiments on GdBCO and modelling. *Superconductor Science and Technology*, 29(12):125004, October 2016.

[183] Masahiro Nii, Naoyuki Amemiya, and Taketsune Nakamura. Three-dimensional model for numerical electromagnetic field analyses of coated superconductors and its application to Roebel cables. *Superconductor Science and Technology*, 25(9):095011, July 2012.

[184] Naoyuki Amemiya, Shun-ichi Murasawa, Nobuya Banno, and Kengo Miyamoto. Numerical modelings of superconducting wires for AC loss calculations. *Physica C*, 310(1–4):16–29, December 1998.

[185] F. Grilli, S. Stavrev, Y. Le Floch and. M. Costa-Bouzo and. E. Vinot, I. Klutsch and. G. Meunier, P. Tixador, and B. Dutoit. Finite-element method modeling of superconductors: from 2-D to 3-D. *IEEE Transactions on Applied Superconductivity*, 15(1):17–25, March 2005.

[186] Huiming Zhang, Min Zhang, and Weijia Yuan. An efficient 3D finite element method model based on the T–A formulation for superconducting coated conductors. *Superconductor Science and Technology*, 30(2):024005, December 2016.

[187] V. Lahtinen, M. Lyly, A. Stenvall, and T. Tarhasaari. Comparison of three eddy current formulations for superconductor hysteresis loss modelling. *Superconductor Science and Technology*, 25(11):115001, September 2012.

[188] John W. Barrett and Leonid Prigozhin. Electric field formulation for thin film magnetization problems. *Superconductor Science and Technology*, 25(10):104002, September 2012.

[189] Leonid Prigozhin. Solution of Thin Film Magnetization Problems in Type-II Superconductivity. *Journal of Computational Physics*, 144(1):180–193, July 1998.

[190] Francesco Grilli, Enric Pardo, Antonio Morandi, Fedor Gömöry, Mykola Solovyov, Víctor M. R. Zermeño, Roberto Brambilla, Tara Benkel, and Nicolò Riva. Electromagnetic Modeling of Superconductors With Commercial Software: Possibilities With Two Vector Potential-Based Formulations. *IEEE Transactions on Applied Superconductivity*, 31(1):5900109, January 2021.

[191] P. Dular, C. Geuzaine, F. Henrotte, and W. Legros. A general environment for the treatment of discrete problems and its application to the finite element method. *IEEE Transactions on Magnetics*, 34(5):3395–3398, September 1998.

[192] Santiago Badia, Alberto F. Martín, and Javier Principe. FEMPAR: An Object-Oriented Parallel Finite Element Framework. *Archives of Computational Methods in Engineering*, 25(2):195–271, April 2018.

[193] Qiushi Chen and A. Konrad. A review of finite element open boundary techniques for static and quasi-static electromagnetic field problems. *IEEE Transactions on Magnetics*, 33(1):663–676, January 1997.

[194] Satoshi Tamitani, Tomoaki Takamatsu, Asuka Otake, Shinji Wakao, Akihisa Kameari, and Yasuhito Takahashi. Finite-Element Analysis of Magnetic Field Problem With Open Boundary Using Infinite Edge Element. *IEEE Transactions on Magnetics*, 47(5):1194–1197, May 2011.

[195] F. Henrotte, B. Meys, H. Hedia, P. Dular, and W. Legros. Finite element modelling with transformation techniques. *IEEE Transactions on Magnetics*, 35(3):1434–1437, May 1999.

[196] A. Bossavit. *Computational Electromagnetism: Variational Formulations, Complementarity, Edge Elements*. Electromagnetism. Academic Press, San Diego, 1998.

[197] M. Tinkham. Resistive transition of high-temperature superconductors. *Physical Review Letters*, 61(14):1658, October 1988.

[198] A. Bossavit. Magnetostatic problems in multiply connected regions: Some properties of the curl operator. *IEE Proceedings A*, 135(3):179–187, March 1988.

[199] P. Dular. *Modeling of magnetic field and eddy currents in three-dimensional nonlinear systems*. phdthesis, Université de Liège, November 1994.

[200] Patrick Dular. The benefits of nodal and edge elements coupling for discretizing global constraints in dual magnetodynamic formulations. *Journal of Computational and Applied Mathematics*, 168(1–2):165–178, July 2004.

[201] Marián Slodička and Edita Janíková. Convergence of the backward Euler method for type-II superconductors. *Journal of Mathematical Analysis and Applications*, 342(2):1026–1037, June 2008.

[202] S. Durand and M. Slodička. Convergence of the mixed finite element method for Maxwell's equations with nonlinear conductivity. *Mathematical Methods in the Applied Sciences*, 35(13):1489–1504, June 2012.

[203] Malabika Adak. *Comparison of Explicit and Implicit Finite Difference Schemes on Diffusion Equation*. Springer Singapore, Singapore, April 2020.

[204] J. E. Everett and J. E. Osemeikhian. Spherical coils for uniform magnetic fields. *Journal of Scientific Instruments*, 43(7):470, August 1966.

[205] Christophe Geuzaine and Jean-François Remacle. Gmsh: A 3-D finite element mesh generator with built-in pre- and post-processing facilities. *International Journla for Numerical Methods in Engineering*, 79(11):1309–1331, September 2009.

[206] Ernst Helmut Brandt. Superconductors of finite thickness in a perpendicular magnetic field: Strips and slabs. *Physical Review B*, 54(6):4246, August 1996.

[207] J. I. Vestgården, D. V. Shantsev, Y. M. Galperin, and T. H. Johansen. Flux penetration in a superconducting strip with an edge indentation. *Physical Review B*, 76(17):174509, November 2007.

[208] L. Burlachkov, Y. Yeshurun, M. Konczykowski, and F. Holtzberg. Explanation for the low-temperature behavior of H_{c1} in $YBa_2Cu_3O_7$. *Physical Review B*, 45(14):8193, April 1992.

[209] A. Buzdin and M. Daumens. Electromagnetic pinning of vortices on different types of defects. *Physica C: Superconductivity*, 294(3–4):257–269, January 1998.

[210] J. R. Clem. *A Model for Flux Pinning in Superconductors*. Springer, Boston, MA, 1974.

[211] Grigorii P. Mikitik and Ernst Helmut Brandt. Theory of the longitudinal vortex-shaking effect in superconducting strips. *Physical Review B*, 67(10):104511, March 2003.

[212] G. P. Mikitik. Critical current in thin flat superconductors with Bean-Livingston and geometrical barriers. *Physical Review B*, 104(9):094526, September 2021.

[213] R. Willa, V. B. Geshkenbein, and G. Blatter. Suppression of geometric barrier in type-II superconducting strips. *Physical Review B*, 89(10):104514, March 2014.

[214] B. L. T. Plourde, D. J. Van Harlingen, D. Yu. Vodolazov, R. Besseling, M. B. S. Hesselberth, and P. H. Kes. Influence of edge barriers on vortex dynamics in thin weak-pinning superconducting strips. *Physical Review B*, 64(1):014503, June 2001.

[215] Å. A. F. Olsen, H. Hauglin, T. H. Johansen, P. E. Goa, and D. Shantsev. Single vortices observed as they enter $NbSe_2$. *Physica C: Superconductivity*, 408–410:537–538, August 2004.

[216] J. Daams and J. P. Carbotte. Thermodynamic properties of superconducting niobium. *Journal of Low Temperature Physics*, 40:135–154, July 1980.

[217] L. Burlachkov, M. Konczykowski, Y. Yeshurun, and F. Holtzberg. Bean–Livingston barriers and first field for flux penetration in high-T_c crystals. *Journal of Applied Physics*, 70(10):5759, 1991.

[218] L. Burlachkov, A. E. Koshelev, and V. M. Vinokur. Transport properties of high-temperature superconductors: Surface vs bulk effect. *Physical Review B*, 54(9):6750, September 1996.

[219] H. Darhmaoui, J. Jung, J. Talvacchio, M. A.-K. Mohamed, and L. Friedrich. Temperature dependence of the magnetic-flux penetration into disk-shaped $YBa_2Cu_3O_{7-\delta}$ thin films. *Physical Review B*, 53(18):12330, May 1996.

[220] M. Ziese, P. Esquinazi, P. Wagner, H. Adrian, S. H. Brongersma, and R. Griessen. Matching and surface barrier effects of the flux-line lattice in superconducting films and multilayers. *Physical Review B*, 53(13):8658, April 1996.

[221] Gheorghe Stan, Stuart B. Field, and John M. Martinis. Critical Field for Complete Vortex Expulsion from Narrow Superconducting Strips. *Physical Review Letters*, 92(9):097003, March 2004.

[222] O. V. Dobrovolskiy, D. Yu Vodolazov, F. Porrati, R. Sachser, V. M. Bevz, M. Yu Mikhailov, A. V. Chumak, and M. Huth. Ultra-fast vortex motion in a direct-write Nb-C superconductor. *Nature Communications*, 11:3291, July 2020.

[223] D. Yu Vodolazov. Flux-flow instability in a strongly disordered superconducting strip with an edge barrier for vortex entry. *Superconductor Science and Technology*, 32(19):115013, October 2019.

[224] Alex Gurevich and Mark Friesen. Nonlinear transport current flow in superconductors with planar obstacles. *Physical Review B*, 62(6):4004, August 2000.

[225] Mark Friesen and Alex Gurevich. Nonlinear current flow in superconductors with restricted geometries. *Physical Review B*, 63(6):064521, February 2001.

[226] F. Ludwig and D. Drung. Low-frequency noise of improved direct-coupled high-T_c superconducting quantum interference device magnetometers in ac and dc magnetic fields. *Applied Physics Letters*, 75(18):2821, September 1999.

[227] M. Baziljevich, E. Baruch-El, T. H. Johansen, and Y. Yeshurun. Dendritic instability in $YBa_2Cu_3O_{7-\delta}$ films triggered by transient magnetic fields. *Applied Physics Letters*, 105(1):012602, June 2014.

[228] Honghai Song, Frank Hunte, and Justin Schwartz. On the role of pre-existing defects and magnetic flux avalanches in the degradation of $YBa_2Cu_3O_{7-x}$ coated conductors by quenching. *Acta Materialia*, 60(20):6991–7000, December 2012.

[229] Ze Jing and Mark D. Ainslie. Numerical simulation of flux avalanches in type-II superconducting thin films under transient AC magnetic fields. *Superconductor Science and Technology*, 33(8):084006, July 2020.

[230] Z. W. Zhao, S. L. Li, Y. M. Ni, H. P. Yang, Z. Y. Liu, H. H. Wen, W. N. Kang, H. J. Kim, E. M. Choi, and S. I. Lee. Suppression of superconducting critical current density by small flux jumps in MgB_2 thin films. *Physical Review B*, 65(6):064512, January 2002.

[231] P. Leiderer, J. Boneberg, P. Brüll, V. Bujok, and S. Herminghaus. Nucleation and growth of a flux instability in superconducting $YBa_2Cu_3O_{7-x}$ films. *Physical Review Letters*, 71(16):2646, October 1993.

[232] You-He Zhou, Cunhong Wang, Cong Liu, Huadong Yong, and Xingyi Zhang. Optically Triggered Chaotic Vortex Avalanches in Superconducting $YBa_2Cu_3O_{7-x}$ Films. *Physical Review Applied*, 13(2):024036, February 2020.

[233] Antonio Lara, Farkhad G. Aliev, Victor V. Moshchalkov, and Yuri M. Galperin. Thermally Driven Inhibition of Superconducting Vortex Avalanches. *Physical Review Applied*, 8(3):034027, September 2017.

[234] M. Motta, F. Colauto, J. I. Vestgården, J. Fritzsche, M. Timmermans, J. Cuppens, C. Attanasio, C. Cirillo, V. V. Moshchalkov, J. Van de Vondel, T. H. Johansen, W. A. Ortiz, and A. V. Silhanek. Controllable morphology of flux avalanches in microstructured superconductors. *Physical Review B*, 89(13):134508, April 2014.

[235] John R. Clem and Karl K. Berggren. Geometry-dependent critical currents in superconducting nanocircuits. *Physical Review B*, 84(17):174510, November 2011.

[236] Th. Schuster, H. Kuhn, and E. H. Brandt. Flux penetration into flat superconductors of arbitrary shape: Patterns of magneticand electric fields and current. *Physical Review B*, 54(5):3514, August 1996.

[237] Lu Jiang, Cun Xue, L. Burger, B. Vanderheyden, A. V. Silhanek, and You-He Zhou. Selective triggering of magnetic flux avalanches by an edge indentation. *Physical Review B*, 101(22):224505, June 2020.

[238] J. McDonald and John R. Clem. Theory of flux penetration into thin films with field-dependent critical current. *Physical Review B*, 53(13):8643, April 1996.

[239] Cun Xue, An He, Huadong Yong, and Youhe Zhou. Field-dependent critical state of high-T_c superconducting strip simultaneously exposed to transport current and perpendicular magnetic field. *AIP Advances*, 3(12):122110, November 2013.

[240] Peter Hänggi and Fabio Marchesoni. Artificial Brownian motors: Controlling transport on the nanoscale. *Reviews of Modern Physics*, 81(1):387, March 2009.

[241] Sven Matthias and Frank Müller. Asymmetric pores in a silicon membrane acting as massively parallel brownian ratchets. *Nature*, 424:53–57, July 2003.

[242] Peter Galajda, Juan Keymer, Paul Chaikin, and Robert Austin. A Wall of Funnels Concentrates Swimming Bacteria. *Journal of Bacteriology*, 189(23):8704, December 2007.

[243] Pulak K. Ghosh, Vyacheslav R. Misko, Fabio Marchesoni, and Franco Nori. Self-Propelled Janus Particles in a Ratchet: Numerical Simulations. *Physical Review Letters*, 110(26):268301, June 2013.

[244] A. Guidobaldi, Y. Jeyaram, I. Berdakin, V. V. Moshchalkov, C. A. Condat, V. I. Marconi, L. Giojalas, and A. V. Silhanek. Geometrical guidance and trapping transition of human sperm cells. *Physical Review E*, 89(3):032720, March 2014.

[245] Xingyu Jiang, Derek A. Bruzewicz, Amy P. Wong, Matthieu Piel, and George M. Whitesides. Directing cell migration with asymmetric micropatterns. *Proceedings of the National Academy of Sciences*, 102(4):975–978, January 2005.

[246] C.-S. Lee, B. Jankó, I. Derényi, and A.-L. Barabási. Reducing vortex density in superconductors using the 'ratchet effect'. *Nature*, 400:337–340, July 1999.

[247] J. E. Villegas, S. Savel'ev, F. Nori, E. M. Gonzalez, J. V. Anguita, R. García, and J. L. Vicent. A Superconducting Reversible Rectifier That Controls the Motion of Magnetic Flux Quanta. *Science*, 302(5648):1188–1191, November 2003.

[248] V. Rouco, A. Palau, C. Monton, N. Del-Valle, C. Navau, A. Sanchez, X. Obradors, and T. Puig. Geometrically controlled ratchet effect with collective vortex motion. *New Journal of Physics*, 17:073022, July 2015.

[249] J. Albrecht, A. T. Matveev, J. Strempfer, H.-U. Habermeier, D. V. Shantsev, Y. M. Galperin, and T. H. Johansen. Dramatic role of critical current anisotropy on flux avalanches in MgB_2 films. *Physical Review Letters*, 98(11):117001, March 2007.

[250] M. Menghini, J. Van de Vondel, D. G. Gheorghe, R. J. Wijngaarden, and V. V. Moshchalkov. Asymmetry reversal of thermomagnetic avalanches in Pb films with a ratchet pinning potential. *Physical Review B*, 78(18):184515, November 2007.

[251] D. Cerbu, V. N. Gladilin, J. Cuppens, J. Fritzsche, J. Tempere, J. T. Devreese, V. V. Moshchalkov, A. V. Silhanek, and J. Van de Vondel. Vortex ratchet induced by controlled edge roughness. *New Journal of Physics*, 15:063022, June 2013.

[252] L. E. Helseth, R. W. Hansen, E. I. Il'yashenko, M. Baziljevich, and T. H. Johansen. Faraday rotation spectra of bismuth-substituted ferrite garnet films with in-plane magnetization. *Physical Review B*, 64(17):174406, October 2001.

[253] J. Van de Vondel, V. N. Gladilin, A. V. Silhanek, W. Gillijns, J. Tempere, J. T. Devreese, and V. V. Moshchalkov. Vortex Core Deformation and Stepper-Motor Ratchet Behavior in a Superconducting Aluminum Film Containing an Array of Holes. *Physical Review Letters*, 106(13):137003, April 2011.

[254] A. Badía-Majós and C. López. Electric field in hard superconductors with arbitrary cross sectionand general critical current law. *Journal of Applied Physics*, 95(12):8035, June 2004.

[255] S. Nagasawa, K. Hinode, T. Satoh, H. Akaike, Y. Kitagawa, and M. Hidaka. Development of advanced Nb process for SFQ circuits. *Physica C: Superconductivity*, 412–414(2):1429–1436, October 2004.

[256] T. Tamegai, Y. Tsuchiya, S. Tada, J. Ibuka, A. Mine, S. Pyon, Y. Mawatari, S. Nagasawa, M. Hidaka, and M. Maezawa. Flux penetrations into two- and three-dimensional nanostructured superconductors. *Physica C: Superconductivity and its Applications*, 503:62–69, August 2014.

[257] Y. Tsuchiya, Y. Mawatari, J. Ibuka, S. Tada, S. Pyon, S. Nagasawa, M. Hidaka, M. Maezawa, and T. Tamegai. Flux avalanches in Nb superconducting shifted strip arrays. *Superconductor Science and Technology*, 26(9):095004, July 2013.

[258] Asef Ghabeli, Enric Pardo, and Milan Kapolka. 3D modeling of a superconducting dynamo-type flux pump. *Scientific Reports*, 11:10296, May 2021.

[259] Bruno de Sousa Alves, Valtteri Lahtinen, Marc Laforest, and Frédéric Sirois. Thin-shell approach for modeling superconducting tapes in the H-ϕ finite-element formulation. *Superconductor Science and Technology*, 35(2):024001, December 2021.

[260] D. Y. Vodolazov, B. A. Gribkov, S. A. Gusev, A. Yu. Klimov, Yu. N. Nozdrin, V. V. Rogov, and S. N. Vdovichev. Considerable enhancement of the critical current in a superconducting film by a magnetized magnetic strip. *Physical Review B*, 72(6):064509, August 2005.

[261] D. Y. Vodolazov, B. A. Gribkov, A. Yu. Klimov, V. V. Rogov, and S. N. Vdovichev. Strong influence of a magnetic layer on the critical current of Nb bridge in finite magnetic fields due to surface barrier effect. *Applied Physics Letters*, 94(1):012508, January 2009.

[262] J. B. Pendry, D. Schurig, and D. R. Smith. Controlling Electromagnetic Fields. *Science*, 312(5781):1780–1782, June 2006.

[263] T. Kiyoshi, S. Choi, S. Matsumoto, T. Asano, and D. Uglietti. Magnetic Flux Concentrator Using Gd-Ba-Cu-O Bulk Superconductors. *IEEE Transactions on Applied Superconductivity*, 19(3):2174 – 2177, June 2009.

[264] Z. Y. Zhang, S. Matsumoto, S. Choi, R. Teranishi, and T. Kiyoshi. A new structure for a magnetic field concentrator using NbTi sheet superconductors. *Physica C*, 471(21-22):1547–1549, November 2011.

List of publications

1. **Modelling the penetration of magnetic flux in thin superconducting films with shell transformations**
   L. Burger, C. Geuzaine, F. Henrotte, and B. Vanderheyden.
   COMPEL **38** (5), 1441-1452 (2019).

2. **Numerical investigation of critical states in superposed superconducting films**
   L. Burger, I. S. Veshchunov, T. Tamegai, A. V. Silhanek, S. Nagasawa, M. Hidaka, and B. Vanderheyden.
   Superconductor Science and Technology **32** (12), 125010 (2019).

3. **Magnetic Recording of Superconducting States**
   Gorky Shaw, Sylvain Blanco Alvarez, Jérémy Brisbois, **Loïc Burger**, Lincoln B. L. G. Pinheiro, Roman B. G. Kramer, Maycon Motta, Karl Fleury-Frenette, Wilson Aires Ortiz, Benoît Vanderheyden, and Alejandro V. Silhanek.
   Metals **9** (10), 1022 (2019)

4. **Selective triggering of magnetic flux avalanches by an edge indentation**
   Lu Jiang, Cun Xue, **L. Burger**, B. Vanderheyden, A. V. Silhanek, and You-He Zhou.
   Physical Review B **101** (22), 224505 (2020).

5. **Metamorphosis of discontinuity lines and rectification of magnetic flux avalanches in the presence of noncentrosymmetric pinning forces**
   M. Motta*, **L. Burger***, Lu Jiang*, J. D. González Acosta, Ž. L. Jelić, F. Colauto, W. A. Ortiz, T. H. Johansen, M. V. Milošević, C. Cirillo, C. Attanasio, Cun Xue, A. V. Silhanek, and B. Vanderheyden.
   Physical Review B **103** (22), 224514 (2021).
   * These authors contributed equally to this work.